Li-Containing Coloured Intermetallic Compounds and Chalcogenides

by

Mohammed Yagoub Ahmed Jomaa

A thesis submitted in partial fulfillment of the requirements for the degree of

Doctor of Philosophy

Department of Chemistry

University of Alberta

Abstract

This thesis describes the synthesis of Li-containing intermetallics and chalcogenides using high-temperature solid-state reactions and induction heating, with the aim of studying their structures, electronic properties, and optical properties to gain insights into their potential applications in jewellery and nonlinear optical devices.

The first part of this thesis focuses on coloured intermetallic compounds, which have a long history in decorative and jewellery applications, with gold and platinum-based alloys being among the very earliest examples. The objective was to identify new coloured substances based on non-precious and less expensive components. Several coloured Li-containing intermetallics were discovered, including purple Li_2ZnGa, light blue Li_2ZnIn, light blue LiMgCdGe. The colour can be controlled in the series of solid solutions $LiCu_2Al_{1-x}Ga_x$ and $LiCu_{2-y}Ni_yGa$. All of these compounds adopt cubic structures in different space groups, as determined by powder X-ray diffraction. To clarify ambiguities about the site distribution, ^{7}Li solid-state nuclear magnetic resonance spectroscopy was applied. The colours of these materials were quantified by extracting chromaticity coordinates from optical reflectance spectra. Electronic structure calculations indicate that these compounds are metallic. The observed colours are proposed to arise from interband transitions.

The second part of this thesis tests the hypothesis that incorporating a mixture of Li and Ag atoms into commercially available NLO materials, such as $AgGaS_2$ and $AgGaSe_2$, could result in solid solutions with a balanced set of properties. Complete substitution of Li atoms for Ag atoms was achieved in $AgAlSe_2$, $AgGaSe_2$, and $AgInSe_2$, resulting in the solid solutions $Li_xAg_{1-x}AlSe_2$, $Li_xAg_{1-x}GaSe_2$, and $Li_xAg_{1-x}InSe_2$. The crystal structures of solid solutions were determined by single-crystal X-ray diffraction and solid-state ^{7}Li nuclear magnetic resonance

spectroscopy. The Ga-containing solid solution retains a tetragonal $CuFeS_2$-type structure (space group $I\bar{4}2d$) throughout the entire range of Li content, whereas the Al and In-containing solid solutions transform from this tetragonal structure to an orthorhombic β-$NaFeO_2$-type structure (space group $Pna2_1$) as Li content increases past $x = 0.50$. The optical band gaps can be tuned to desired values. The second harmonic generation responses were comparable to benchmark materials. All compounds melt congruently at accessible temperatures. Electronic structure calculations were carried out to quantify the bonding in these compounds.

Preface

This thesis presents the results of my research work during my graduate studies from September 2018 to March 2023, which was conducted at the Department of Chemistry, University of Alberta under the supervision of Prof. Arthur Mar. My contributions are summarized briefly below. Dr. A. Mar, the corresponding author, was involved in all stages of manuscript preparation and submission.

Chapter 2 of this thesis has been published as Jomaa, M.; Mishra, V.; Mumbaraddi, D.; Chaudhary, M.; Dmytriv, G.; Michaelis, V. K.; Mar, A. Coloured intermetallic compounds Li_2ZnGa and Li_2ZnIn. *J. Solid State Chem.* **2022**, *306*, 122792. My contribution includes synthesis, data collection, analysis, characterization, and preparing the draft for the manuscript. Dr. V. Mishra assisted with electronic structure calculations, D. Mumbaraddi assisted with synthesis, M. Chaudhary assisted in NMR data collection and analysis, Dr. G. Dmytriv proposed the project, and Dr. V. K. Michaelis assisted with NMR data analysis.

Chapter 3 has been published as Jomaa, M.; Mishra, V.; Chaudhary, M.; Mumbaraddi, D.; Michaelis, V. K.; Mar, A. True colours shining through: Determining site distributions in coloured Li-containing quaternary Heusler compounds. *J. Solid State Chem.* **2022**, *314*, 123372. My contribution includes conceptualization, synthesis, data collection, analysis, characterization, and preparing the draft for the manuscript. Dr. V. Mishra assisted with electronic structure calculations, D. Mumbaraddi assisted with synthesis, M. Chaudhary assisted in NMR data collection and analysis, and Dr. V. K. Michaelis assisted with NMR data analysis.

Chapter 4 has been prepared as a draft for publication as Jomaa, M.; Mumbaraddi, D.; Mishra, V.; Chaudhary, M.; Mah, B.; Delaruelle, D.; Michaelis, V. K.; Mar, A. Investigating the phase behaviours and optical properties of $LiCu_2Al_{1-x}Ga_x$ and $LiCu_{2-y}Ni_yGa$ solid solutions. My

contribution includes conceptualization, synthesis, data collection, analysis, characterization, and preparing the draft for the manuscript. D. Mumbaraddi assisted with synthesis, Dr. V. Mishra assisted with electronic structure calculations, M. Chaudhary assisted in NMR data collection and analysis, B. Mah and D. Delaruelle assisted with synthesis, and Dr. V. K. Michaelis assisted with NMR data analysis.

Chapter 5 has been accepted as Jomaa, M.; Mishra, V.; Mumbarradi, D.; Sikdar, R.; Sarkar, D.; Sun, M.; Yao, J.; Michaelis, V. K.; Mar, A. Structure and Optical Properties of $Li_xAg_{1-x}GaSe_2$ and $Li_xAg_{1-x}InSe_2$. *Inorg. Chem.* **2023**. My contribution includes conceptualization, synthesis, data collection, analysis, characterization, and preparing the draft for the manuscript. Dr. V. Mishra assisted with electronic structure calculations, D. Mumbaraddi assisted with single crystal determination, R. Sikdar assisted with synthesis, D. Sarkar assisted in NMR data collection, M. Sun and Dr. J. Yao assisted with NLO measurements, and Dr. V. K. Michaelis assisted with NMR data analysis.

Chapter 6 has been prepared as a draft for publication as Jomaa, M.; Mishra, V.; Sarkar, D.; Sun, M.; Yao, J.; Michaelis, V. K.; Mar, A. Structure and Optical Properties of $Li_xAg_{1-x}AlSe_2$. My contribution includes conceptualization, synthesis, data collection, analysis, characterization, and preparing the draft for the manuscript. Dr. V. Mishra assisted with electronic structure calculations, D. Sarkar assisted in NMR data collection, M. Sun and Dr. J. Yao assisted with NLO measurements, and Dr. V. K. Michaelis assisted with NMR data analysis.

Dedication

It is my genuine gratefulness and warmest regard that I dedicate this work to my beloved parents, my supportive wife, my adorable daughter, and my amazing siblings

Acknowledgements

First and foremost, I am deeply grateful to my supervisor, Prof. Arthur Mar, for his continuous support, guidance, and encouragement throughout my PhD program. He has been an inspiring teacher and mentor who always gives you not only the freedom and flexibility of choosing and managing your projects but his appreciation of the work you do, which has benefited me in developing unique learning and research skills and given me self-confidence during my PhD program. I am genuinely thankful to you, you are such a wise, hard-working, friendly, and understanding supervisor and I could not have asked for better role models. I am also thankful to my supervisory and examining committee members, Prof. Yunjie Xu, Prof. Lingzi Sang, Prof. Mariusz Klobukowski, and Prof. Jennifer Aitken for providing invaluable feedback and insights. I would also like to thank Prof. Vladimir Michaelis, Prof. Jonathan Veinot and Prof. Josef Takats for their assistance in my candidacy exam.

I extend my sincere appreciation to the technical and support staff of the University of Alberta, Chemistry Department, including Dr. Mike Ferguson, Dr. Wayne Moffat, Dr. Guibin Ma, Dr. Nathan Gerein, Jennifer Jones, Rebecca Funk, Jason Dibbs, and Ryan Lewis, as well as the machine shop and electronics shop staff. Their expertise, patience, and professionalism have made research possible and enjoyable.

I am grateful to my colleagues in the Mar group, both past and present, for their support, and intellectual exchange. In particular, I would like to acknowledge Anton Oliynyk, Yuqiao Zhou, Lawrence Adutwum, Frank Stegemann, Hussien Osman, Balaranjan Selvaratnam, Maxwell Wallace, Brett Duell, Volodymyr Gvozdetskyi, Alexander Gzyl, Dong Zhang, Vidyanshu Mishra, Dundappa Mumbaraddi, Amit Bhattacharya, Fuwei Wen, Arkadii Pominov, Ritobroto Sikdar and

Trinanjan Dey. My time at the University of Alberta would not have been nearly as enjoyable without you and I feel lucky to have spent my PhD getting to know you all.

I also express my deepest gratitude to my family, including my parents for their endless love, support, and encouragement throughout my entire life, no matter how far I am. I would like to express my most sincere gratitude to my supportive wife, my little princess Yaqeen, my brothers, and my sisters for their unconditional love, encouragement, and sacrifices.

I must not forget to thank Dr. Yoram Apelblat for his mentorship during my teaching assistantship, Anita and Laura for their administrative support. I am also grateful to my collaborators, Dr. Jiyong Yao, Sun Mengran, Madhusudan, and Diganta for their contributions to my research.

Finally, I would like to acknowledge the funding support from the University of Alberta and the Natural Sciences and Engineering Research Council of Canada (NSERC). I am also thankful to all the internship students who have assisted me during my research.

Thank you all for your contributions, guidance, and support throughout my journey.

Table of Contents

List of Tables

List of Figures

List of Symbols and Abbreviations

1D, 2D, 3D	One-, two-, three-dimensional
$a\ b\ c\ \alpha\ \beta\ \gamma$	Unit cell parameters
Å	Angstrom
BSE	Backscattered electrons
CIE	Commission Internationale de l'Eclairage
Ch	Chalcogenides
COBI	Crystal orbital bond index
COHP	Crystal orbital Hamilton population
CPA	Coherent potential approximation
°C	Degree Celsius
d_{hkl}	d-spacing
DOS	Density of states
DSC	Differential scanning calorimetry
E	Electric field
EDX	Energy dispersive X-ray
ELF	Electron localization functions
E_g	Band gap
eV	Electron volt
F_{hkl}	Structure factor
GGA	Generalized gradient approximation
hkl	Miller indices
IR	Infrared

LDA	Local density approximation
LDT	Laser damage threshold
MAS	Magic-angle spinning
μm	Micrometre
NCS	Non-centrosymmetric
NLO	Nonlinear optics
NMR	Nuclear magnetic resonance
nm	Nanometer
N_{val}	Number of valance electrons
PAW	Projected augmented wave
PM	Phase matchable
P	Induced polarization
SE	Secondary electrons
SEM	Scanning electron microscopy
SHG	Second harmonic generation
TPA	Two-photon absorption
VASP	Vienna ab initio simulation package
XRD	X-ray diffraction
Z	Atomic number
λ	Wavelength
α	Absorption coefficient (Kubelka-Munk)
δ	Chemical shift
ΔE	Energy difference

Δl	Change in orbital quantum number
χ	Susceptibility coefficient
ω	Frequency
θ	Angle of diffraction

Chapter 1.

Introduction

1.1 Solid state substances

The solid state is one of the fundamental states of matter. Solid state chemistry is a branch of chemistry that examines the synthesis, structure, chemical bonding, properties, and applications of solids. Depending on the arrangement of constituent particles (atoms, ions, or molecules), solids can be classified as crystalline, in which the particles are arranged regularly in a well defined repeating structure with long-range order, or amorphous, in which the particles are arranged randomly without long-range order. Crystalline solids can be further classified by the types of forces holding the particles together. In molecular solids, discrete molecules are held together by weak intermolecular forces, such as dipole-dipole or dispersion forces. In extended (or non-molecular) solids, atoms or ions are held together by strong bonding forces, namely some combination of ionic, covalent, and metallic bonds. Perhaps the most fascinating aspect of solid state chemistry is that understanding the detailed structures and learning how to modify them allows physical properties to be controlled. In this regard, extended solids are particularly interesting because they possess interesting properties beyond those intrinsic to discrete molecules, including magnetism, superconductivity, colour, and band gaps.

The use of solid-state materials that contain lithium is an area of significant research and practical interest because of their unique properties and applications in various technologies. The most widespread application is in lithium-containing batteries, which are used extensively in electronic devices, such as cell phones, computers, and medical implants including cardiac pacemakers.[1,2] These batteries are now increasingly used in military, aerospace, and electric

vehicles.[3,4] However, there exist many other lithium-containing compounds whose potential has yet to be met because their properties have not been evaluated thoroughly. The primary theme of this thesis is to focus on such lithium-containing materials. The first part deals with Li-based intermetallic compounds with the unusual property that they exhibit colour, a feature that could be valuable for the jewellery industry. The second part deals with Li-based chalcogenides that could be good nonlinear optical (NLO) materials, which are used in infrared lasers for medical, environmental, and military applications.

1.2 Intermetallic compounds

Intermetallic compounds (or intermetallics, in short) have been identified as promising materials for a variety of applications throughout history.[5] They are defined as compounds consisting of two or more metals or metalloids with a definite composition.[6] They could be binary compounds consisting of two elements such as brass (Cu–Zn), ternary compounds consisting of three elements such as stainless steel (Fe–Cr–Ni), or more complicated multinary compounds.[7,8] Sometimes the distinction is not so clear between intermetallic compounds, which have a definite composition and usually have an ordered arrangement of atoms, and alloys, which are solid solutions of metals and have a random arrangement of atoms.[9,10] The condition that intermetallic compounds must have a definite composition can be relaxed, because they do often exhibit partial disorder or vacancies; when some variability in composition is observed, we say that there is a narrow phase width and that the compounds are nonstoichiometric. However, the key criterion remains that intermetallic compounds have a different crystal structure from those of their constituent components.

Unlike other kinds of solids (such as ionic compounds and Zintl phases), the structures of intermetallic compounds do not usually follow simple valence rules. Their bonding is complex and cannot be easily rationalized according to classical bonding theories, such as the octet rule and the 18-electron rule, which were developed for molecular substances and assume that covalent bonding is the dominant interaction. Notwithstanding their name, intermetallic compounds need not exhibit solely metallic bonding.[10] It could be argued that covalent and metallic bonding is part of a continuum, depending on the degree of electron delocalization. In polar intermetallics, ionic bonding is an important contribution. Many intermetallics are hard, tough, wear-resistant, corrosion-resistant, and high-melting.[12,13] They have found diverse applications in various fields. For example, $Nd_2Fe_{12}B$ is widely used as a permanent magnet, Nb_3Sn is a superconductor found in NMR spectrometers, PdIn is a catalyst for many reactions, and TiNi is a shape memory material used in medical implants.[14–17] Less well known, a very small number of intermetallics exhibit the highly unusual property of exhibiting colour in the visible spectrum, such as $AuAl_2$ and $AuGa_2$, making them valuable for applications in jewellery (Figure 1-1).[18]

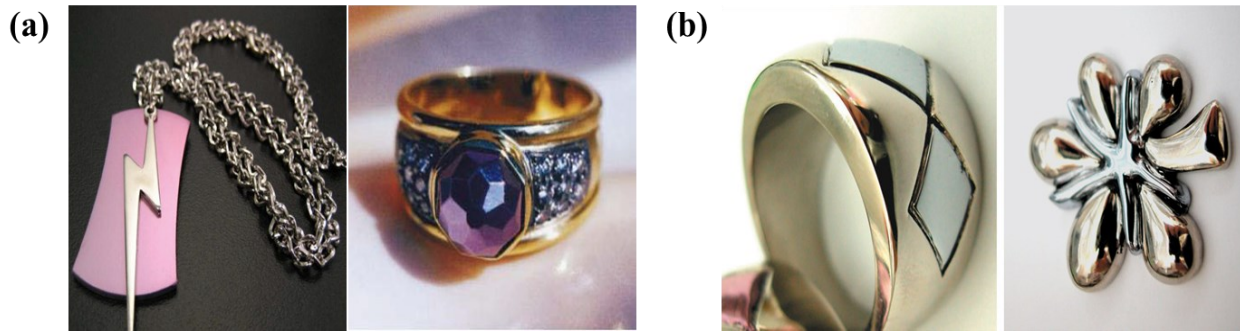

Figure 1-1. Jewellery items produced by (a) purple gold $AuAl_2$ and (b) blue gold $AuGa_2$ coating.

1.3 Solid solutions

The significance of alloying, the process of adding one metal to another, has been recognized since ancient times.[19] Understanding the roles played by each constituent element in

the design of alloys is crucial.[20] In some cases, adding a second metal forms a new phase with a different structure and significant change in properties. In other cases, adding a second metal up to a limiting concentration retains the same structure of the first metal, resulting in a solid solution. This is usually done by preparing a molten mixture of the two metals, followed by cooling. In a substitutional solid solution, solute atoms are randomly substituted for solvent atoms in the crystal structure. In an interstitial solid solution, solute atoms are small enough to randomly occupy interstitial sites within the crystal structure.[21,22]

According to the Hume-Rothery rules, the degree of solubility in a substitutional solid solution depends on several factors.[23] The solute and solvent components should have similar atomic radii (differing by up to 15%), similar electronegativity, identical valence, and similar crystal structures. If the solid solution $A_{1-x}B_x$ undergoes a linear change in a unit cell parameter a as a function of the mole fraction x, we say that Vegard's law is followed:

$$a_{\mathrm{A}_{(1-x)}\mathrm{B}_x} = (1-x)a_A + xa_B \qquad \textbf{Equation 1-1.}$$

Different scenarios for a binary alloy are illustrated in Figure 1-2. A substitutional solution forms when the grey solute atoms have similar size as the yellow solvent atoms, both having the same structure. The substitution could be complete (0 to 100%) or partial. An interstitial solution forms when the small pink solute atoms fit into interstices between the yellow atoms. Sometimes, the solute atoms are arranged in an ordered manner, resulting in a well defined structure that is of its own type; in this case, we tend to endow it with the description as an intermetallic compound.

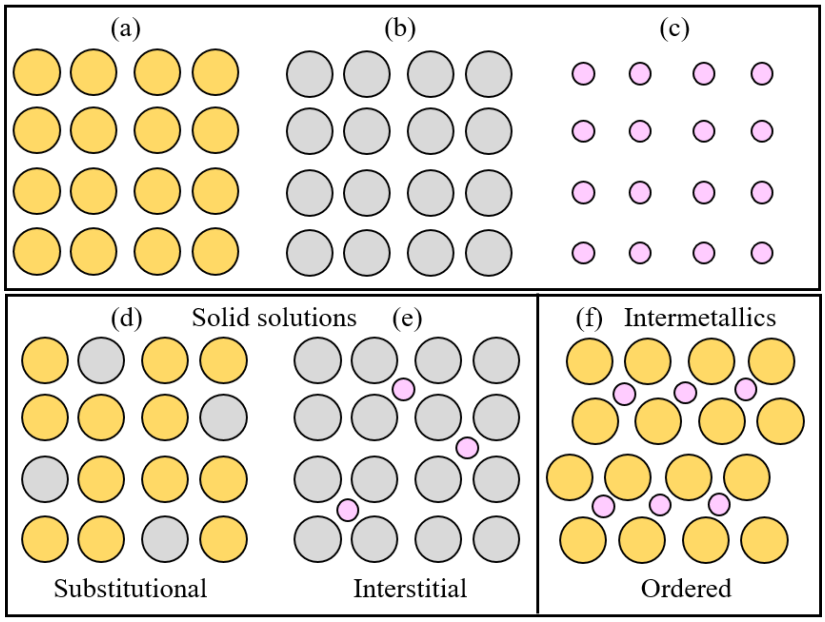

Figure 1-2. Structure of binary alloys: (a), (b) and (c) represent three elements, (d) substitutional solid solution (e) interstitial solid solution, and (f) intermetallic compound.

1.4 Colour of metallic compounds

Colour can be commonly observed in many semiconductors if the energy gap separating valence and conduction bands falls in the visible region (1.7–3.0 eV),[25] but not in metals because the absence of an energy gap allows absorption and reflection at all wavelengths.[26,27] Among metallic elements, gold and copper are the only two that exhibit colour.[28,29] A very small number of intermetallic compounds are coloured because there may be maxima in the density of states (DOS) separated by a pseudogap, permitting prominent interband transitions in the visible region (Figure 1-3).

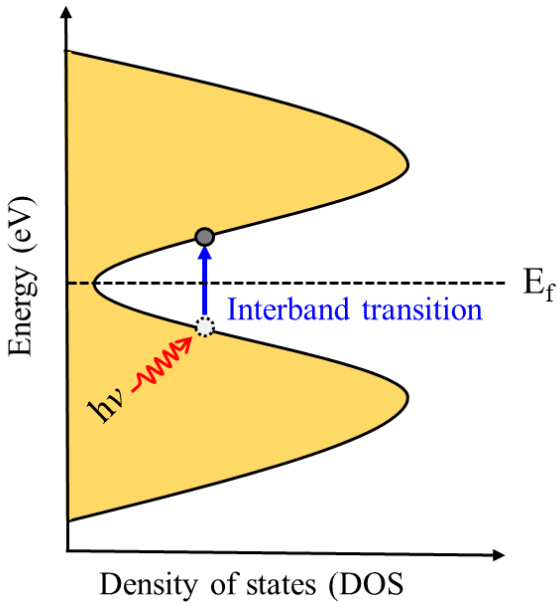

Figure 1-3. Schematic representation of interband transition in metallic substances.

Steinemann has proposed that high symmetry structures tend to lead to distinct features in the DOS, so it is no surprise that the vast majority of coloured intermetallics are cubic.[25,31] Many of them are binary compounds with simple formulas, *AB* or AB_2, where *A* is a late transition metal (Pd, Pt, Ag, Au) and *B* is a post-transition metal or metalloid (Al, Ga, In, Si, Ge, Sn, Pb). Within a Pettifor structure map,[34] these compounds are dominated by two structure types, CsCl or CaF_2.[25,32] Ternary and quaternary coloured intermetallics often contain Li or Mg, with cubic structures derived from CsCl or CaF_2 (Figure 1-4).[35–38] Given the dipole selection rule for electronic transitions ($\Delta l = \pm 1$), it is also desirable to have strong covalent bonding, so that metal *d* states are hybridized with metal or metalloid *sp* states.[25,26,31] The presence of late transition metals tends to give electron counts that place the Fermi level within a pseudogap in the DOS.

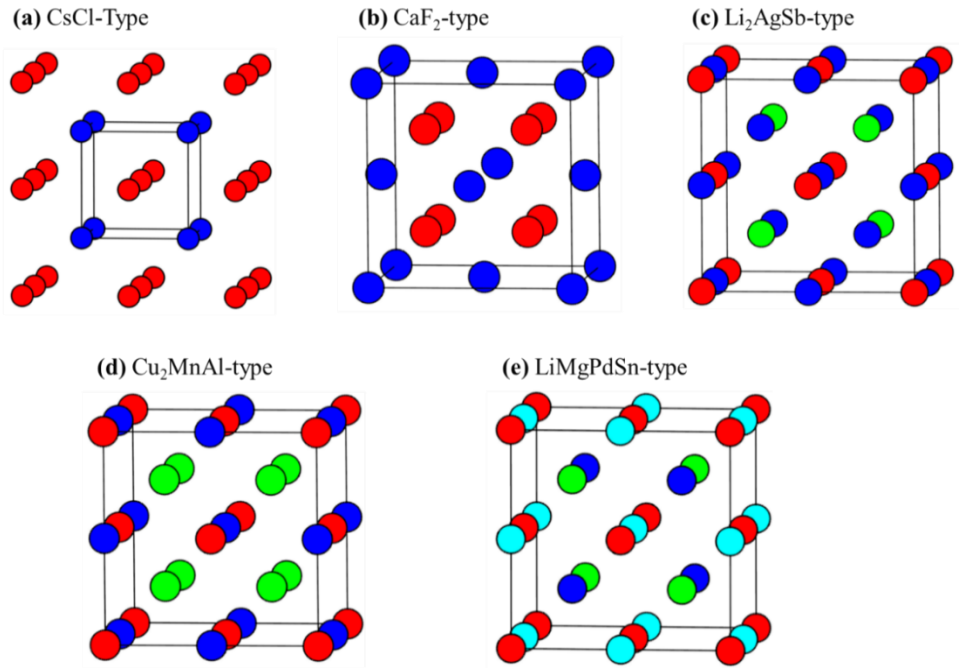

Figure 1-4. Cubic crystal structures models of coloured intermetallic compounds.

The ternary and quaternary coloured intermetallics are interesting because they can be considered to be Zintl phases, which are a subset of polar intermetallics that follow valence rules. Eberz has suggested that such compounds will be coloured if the number of valence electrons *N* per formula unit is equal to or smaller than seven, provided that late transition metals (Fe, Co, Ni, Ru, Rh, Pd, Ir, Pt) are assigned a count of zero electrons (Ekman's rule).[31,39] This principle seems to be satisfactory, although there are exceptions (Sb-containing phases, disilicides) where the number of valence electrons exceeds seven (Table 1-1).[40]

Table 1-1. Selected ternary and quaternary coloured intermetallic compounds.

Compound	Structure type	Space group	Colour	*N*
$LiCu_2Si$	Cu_2MnAl	$Fm\bar{3}m$	red-violet	7
Li_2CuGe	Cu_2MnAl	$Fm\bar{3}m$	bright red	7
Li_2AgAl	Li_2AgSb	$F\bar{4}3m$	yellow-pink	6
Li_2AuIn	Li_2AgSb	$F\bar{4}3m$	green-yellow	6
Li_2PdAl	Li_2AgSb	$F\bar{4}3m$	violet	5
Li_2PdSb	Li_2AgSb	$F\bar{4}3m$	brass-yellow	7
LiMgPdSn	LiMgPdSn	$F\bar{4}3m$	red-violet	7
LiMgPtSb	Li_2AgSb	$F\bar{4}3m$	red violet	8

The criteria for coloured intermetallics seem to be quite restrictive. As another approach to imparting colour to metallic substances, their surfaces can be coated or modified through chemical and physical techniques, including oxidization, anodization, nitrogen coating, and direct surface nanopatterning.[41–43] They present some drawbacks, such as weak resistance to light and weather, which could lead to loss of colour or physical damage. Moreover, the colour may be inhomogeneous or may deteriorate over time.[25] It is worthwhile to search for metallic substances that exhibit intrinsic colour, which number only a few hundred to date. In the first part of this thesis, the aim to discover new ternary and quaternary coloured intermetallic compounds that do not contain expensive precious metals.

1.5 Metal chalcogenides

Chalcogenides refer to compounds containing the group 16 elements (O, S, Se, Te). Because oxygen is considerably more electronegative (Pauling electronegativity of 3.4) than the

other elements (Pauling electronegativity of 2.1 to 2.6), oxides have more ionic character in their bonding and are usually treated separately.[44] Chalcogenides have a wide range of applications in semiconductors, optoelectronics, and catalysis. The second part of this thesis explores a series of noncentrosymmetric lithium-containing chalcogenides. The focus is on tuning optical band gaps to enhance their performance as nonlinear optical (NLO) materials operating in the infrared region.

1.6 Nonlinear optical phenomena

Light interacts with matter in various ways, such as refraction, reflection, diffraction, or absorption, when it has weak or moderate intensity. These kinds of interactions occur in the linear domain, which means the optical response of the material scales linearly with light intensity; moreover, when photons of different frequencies meet in a medium, they do not interact with each other.[45] However, when the light intensity exceeds a certain threshold, the situation is changed, and the optical response of the material is no longer proportional to the light intensity. In this way, we enter the exciting world of nonlinear optics (NLO), a term which describes the study of the interaction of intense light with matter to produce modified fields that are different from the input field in phase, frequency, or amplitude.[46,47] A very strong electric field is required to modify the optical properties of a material and induce these nonlinear effects, and therefore the development of NLO followed closely after the invention of the laser.[45]

When an electric field E of incident light is applied, a material develops an induced polarization P, which is the dipole moment per unit volume. In conventional optics, the light is not intense and the polarization depends linearly on the electric field, scaled by linear electric susceptibility $\chi^{(1)}$:

$$P = \chi^{(1)} E \qquad \textbf{Equation 1-2.}$$

In nonlinear optics, the dependence is expressed as a power series:

$$P = P^{(1)} + P^{(2)} + P^{(1)} + \cdots = \chi^{(1)}E^{(1)} + \chi^{(2)}E^{(2)} + \chi^{(3)}E^{(3)} + \cdots \quad \textbf{Equation 1-3.}$$

where $\chi^{(2)}$ and $\chi^{(3)}$ are the second- and third-order nonlinear electric susceptibility coefficients, respectively. A nonzero quadratic term is responsible for the phenomenon known as frequency doubling process or second harmonic generation (SHG), in which two photons of the frequency ω are phase matched and summed to produce a single photon of frequency 2ω (Figure 1-5). The process occurs within a nonlinear medium, usually a crystal. SHG was first observed by Franken in 1961 when light from a ruby laser (with frequency of 694.3 nm) was directed onto a single crystal of quartz, an NLO material. Two components were produced by the quartz crystal: the fundamental frequency (694.3 nm) without any change and a second component appearing with twice (347.15 nm) the fundamental frequency.[48]

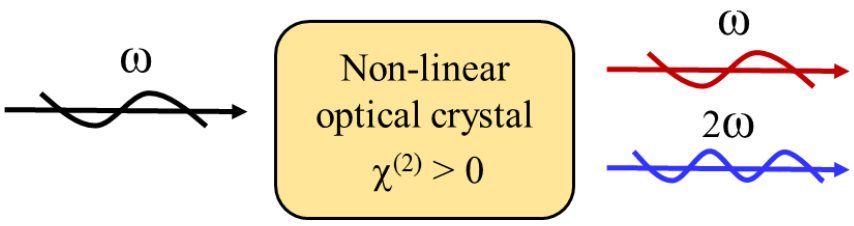

Figure 1-5. A nonlinear crystal converts light of frequency (ω) to the second harmonics (2ω).

1.7 Nonlinear optical materials

Infrared nonlinear optical (IR NLO) materials play an essential role in various applications, including laser communication and environmental monitoring, as they can convert laser frequency to more favourable frequencies where the normal lasers perform poorly.[49,50,51] Many NLO crystals have been discovered over the past few decades, but for practical applications, several crucial criteria have to be satisfied simultaneously.[52] Besides a high-quality crystal that can be easily grown, a wide band gap (E_g) is necessary to achieve a high laser damage threshold. The material

must be sufficiently transparent with high optical transmittance at both the fundamental and the doubled frequency.[53,54]

From a crystallographic perspective, a non-centrosymmetric (NCS) structure, that is, one that lacks a centre of inversion, is required.[52] From symmetry considerations, all components of even-order susceptibilities are zero in a centrosymmetric medium,[50,55] so if an electric field inversion is applied, a corresponding polarization inversion will occur. Because the susceptibility component $\chi^{(n)}$ represents a physical property, it should not change sign under inversion:

$-P^{(n)} = P^{(n)}$ and $\chi^{(n)}(E^{(n)}) = \chi^{(n)}(-E^{(n)})$ where $n = 1, 2, 3,\ldots$ **Equation 1-4.**

The odd-order terms are independent of the crystal orientation.[55] Consequently, the nonlinear polarization produced by SHG is expressed as:

$\chi^{(2)}(-E^{(2)}) = \chi^{(2)}(E^{(2)})$, but $-P^{(2)} = P^{(2)}$ is only possible if $\chi^{(2)} = 0$. **Equation 1-5.**

Furthermore, it is essential for the material to be type I phase matchable (PM). This occurs in a second harmonic generating crystal in which the refractive index of the fundamental wave $n(\omega)$ and second-harmonic wave $n(2\omega)$ are equal ($n(\omega) = n(2\omega)$). The determination of phase matching behavior can be achieved by measuring the SHG intensity at a specific wavelength as a function of particle size.[56] A type I phase matching material is characterized by a rising trend in SHG intensity with increasing particle size, followed by a plateau at the maximum value (Figure 1-6(a)). If phase matching behaviour does not occur, the SHG intensity will fall off after reaching the maximum value, as the particle size increases (Figure 1-6(b)).[57] It is important to note that the plots below are not the result of actual experimental data of $LiNbO_3$ and SiO_2.

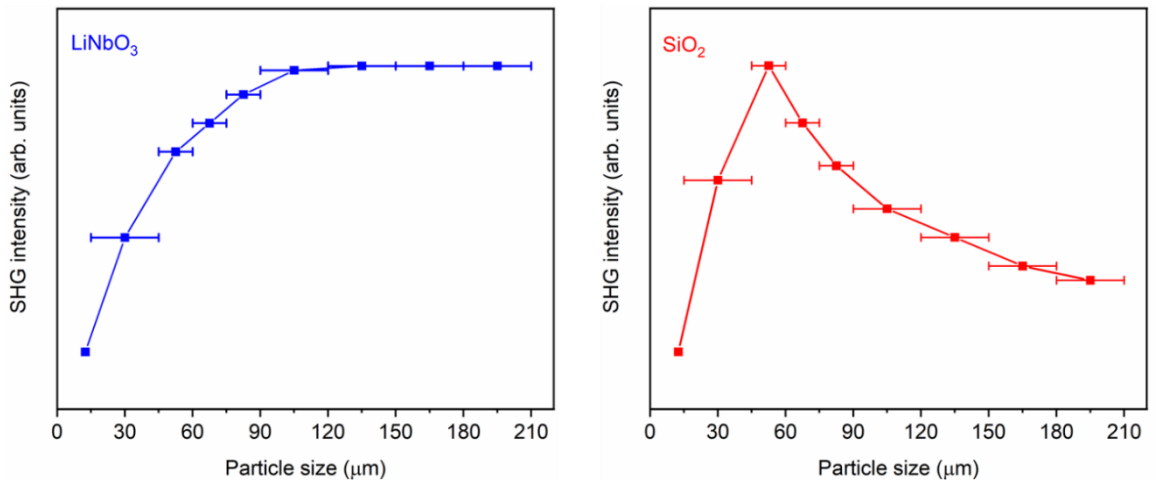

Figure 1-6. Phase-matchable ($LiNbO_3$) and non-phase matchable (SiO_2) curves from powder SHG measurements.

Significant effort has been made to evaluate IR NLO materials possessing the aforementioned characteristics. Oxides, pnictides, and chalcogenides with remarkably high SHG response have been discovered.[51,58,59] Most oxides have a limited range of transparency (<5 μm), which hinders them to be good candidates.[60] Chalcogenides and pnictides remain the most promising materials for many IR applications because of their structural flexibility and good optical transparencies within the IR range.[61] Nevertheless, the few commercially available materials are limited to $AgGaS_2$, $AgGaSe_2$, and $ZnGeP_2$.[62–64] These materials are still associated with some drawbacks that greatly restrict their practical use. For example, both $AgGaS_2$ and $AgGaSe_2$ have a low laser-damage threshold, while $AgGaSe_2$ is not phase-matchable at 1 μm. On the other hand, $ZnGeP_2$ exhibits strong two-photon absorption of the conventional 1–2 μm laser-pumping sources.[65–69] It is valuable to discover new IR NLO candidates to overcome those problems, but this is challenging because a high SHG response typically correlates with a low laser-damage threshold.

Based on the performance of these commercial materials, it is worthwhile to examine how other ternary and quaternary NLO materials can be derived by using compounds of the formula

A^{I}–B^{III}–C_2^{VI} as a template. For instance, substituting appropriate alkali or alkaline-earth metals could increase the band gaps. Many Li-containing ternary chalcogenides Li*MCh*$_2$ (*M* = In, Ga; *Ch* = S, Se, Te) and quaternary chalcogenides Li_2Cd*MCh*$_4$, Li_2Mn*MCh*$_4$, Li_2Zn*MCh*$_4$, Li_2Zn*MCh*$_4$ (*M* = Ge, Sn; *Ch* = S, Se), and Li_2In_2*MCh*$_6$ (*M* = Si, Ge; *Ch* = S, Se) for NLO exhibit wide band gaps and nonlinear susceptibilities similar to those of $AgGaS_2$ and $AgGaSe_2$.[70–76]

This thesis examines the hypothesis that solid solutions based on the ternary compounds Ag*M*Se_2 and Li*M*Se_2 (*M* = Al, Ga, In) could provide greater compositional flexibility to allow tuning of physical properties. All of these compounds are constructed from metal-centred tetrahedra. Substitution of Li for Ag atoms enlarges the band gaps (e.g. 1.8 eV for $AgGaSe_2$ and 3.4 eV for $LiGaSe_2$). As a result, $LiGaSe_2$ has a larger laser damage induced threshold for the near IR pumping laser than $AgGaSe_2$, but its NLO coefficient is relatively small, compared to other IR NLO materials. Thus, there is still much work to be done in the search for new IR NLO materials with better overall properties. The focus in this part of the thesis is on the synthesis, crystal structure, optical, thermal, and electronic properties of Li-containing selenides in order to achieve a desired balance between a large NLO coefficient and a high laser induced damage threshold.

Characterization of the optical second-harmonic generation behaviour was performed in collaboration with Prof. Jiyong Yao at the Technical Institute of Physics and Chemistry, Chinese Academy of Sciences.

1.8 Solid-state synthesis

Solid-state reactions may not be very familiar to readers who have not been exposed to the diversity of techniques beyond conventional molecular chemistry. These reactions are driven by the migration or diffusion of ions from the reactants to the other interface, which usually requires high temperatures. Several methods are used for the synthesis of intermetallic compounds and

chalcogenides. The most widely used and reliable preparative method of solid-state compounds is by heating the solid starting materials together at elevated temperatures, typically around 1000 °C, to produce a new phase. The reactants are mixed and ground to obtain a homogeneous mixture, which is then pressed into pellets to encourage intimate contact between reactants before being heated at a controlled temperature for a specific time. In some cases, the synthesis may involve regrinding and pelletizing to bring fresh surfaces in contact, which speeds up the reaction. This approach involves careful consideration of specific mixing, heating and cooling rates, heating atmospheres, and crucibles for certain types of targeted compounds. The appropriate container dependes on factors like reactivity, strength, ductility, and cost. Generally, fused silica ("quartz" SiO_2) is the most commonly used container because of its compatibility with many reactants and its reasonable price. However, highly electropositive metals like alkali and alkaline earth metals may reacts with SiO_2 to form very stable oxides and silicates.[77] Alumina (Al_2O_3) and zirconia (ZrO_2) crucibles or welded niobium (Nb) or tantalum (Ta) tubes can be used in the presence of these active metals, provided they are jacketed by an outer silica tube and evacuated. When Nb or Ta tubes are used, induction heating can be a convenient, fast method of melting the components under a controlled atmosphere. In this method, an electrically conducting sample is subjected to a rapidly changing magnetic field producing an induced current that causes the heating effect. Optical pyrometers are used to monitor the temperature during the induction heating process.

To prepare Li-containing intermetallic compounds in this thesis, induction heating in niobium tubes was used (Figure 1-7). The tubes were cleaned by soaking in hexane, rinsed with distilled water, dried, crimped on one end, and sealed by arc welding in an argon atmosphere. High-purity constituent elements were then weighed out in appropriate stoichiometric ratios and loaded into the niobium tubes. The tubes were then transferred into a glove box where Li metal is

kept. The Li ribbon was freshly cleaned by scraping the surface and cut into small pieces within the argon-filled glove box and mixed with other components. The other end of the tubes was sealed by arc welding in an argon atmosphere and placed within a 5-cm diameter copper coil in a water-cooled Ambrell EASYHEAT 560LI 6.0-kW induction heater where they were subjected to a frequency of approximately 157 kHz and a current of around 139 A under an argon atmosphere following a suitable temperature profile. The corresponding temperature was estimated to be between 800 and 900 °C using an optical pyrometer.

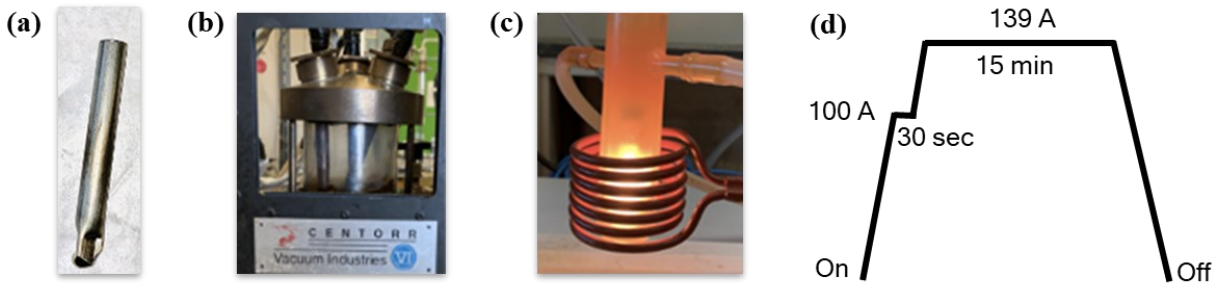

Figure 1-7. Synthesis of coloured intermetallic phases: (a) niobium tube, (b) arc-welder, (c) induction heating furnace, (d) heating profile.

Induction heating is not suitable for preparing Li-containing chalcogenides because Nb and Ta metal tubes are not compatible with S, Se, and Te and can form stable metal chalcogenides. Fused silica could be an option, but since we are dealing with electropositive lithium, precautions have to be taken. The inner surface of the fused silica tubes were coated with carbon (through pyrolysis of acetone), which acts as a protective layer.[78] Then, appropriate amounts of the starting materials were mixed and transferred into carbon-coated silica tubes, which were then evacuated and placed in computer-controlled furnaces (Figure 1-8). High-quality single crystals were obtained by slowly cooling of the samples.

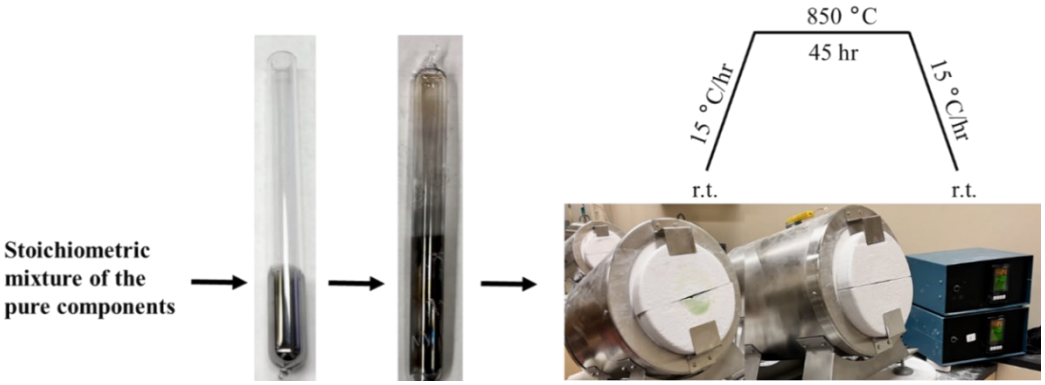

Figure 1-8. Synthesis of Li-containing chalcogenides by direct heating.

All starting elements used in the syntheses were obtained from commercial sources. Their forms, sources, purity, melting, and boiling points are listed (Table 1-2). Most of these elements were used as received, except for the lithium ribbon, whose surface was scraped to eliminate any potential contaminants.

Table 1-2. Starting elements used in the syntheses.

Element	Form	Source	Purity (%)	mp (°C)	bp (°C)
Li	ribbon	Aldrich	99.9	180	1347
Mg	turnings	Aldrich	98	649	1090
Ni	powder	Cerac	99.9	1453	2732
Cu	shot	Alfa Aesar	99.5	1085	2567
Zn	powder	Onyxmet	99.8	419	907
Pd	powder	Alfa Aesar	99.95	1552	2927
Ag	powder	Aldrich	99.9	961	2212
Cd	shot	Alfa Aesar	99.95	321	765
Pt	sponge	Aldrich	99.9	1772	3827
Al	powder	Alfa Aesar	99.5	660	2467
Ga	ingot	Alfa Aesar	99.99	30	2403
In	powder	Alfa Aesar	99.9	157	2000
Ge	pieces	Alfa Aesar	99.999	937	2830
Sn	powder	Onyxmet	99.9	232	2270
Se	powder	Onyxmet	99.5	217	685

1.9 Characterization

When a new compound is synthesized, it is important to characterize it. Foremost is the crystal structure, which is essential for understanding the properties. Single-crystal X-ray diffraction methods provide the most detailed information about atomic positions and bond lengths. In this thesis, the major techniques used are X-ray diffraction, energy-dispersive X-ray spectroscopy, nuclear magnetic resonance spectroscopy (NMR), and diffuse reflectance spectroscopy.

1.9.1 X-ray diffraction methods

Investigating the structure of matter at the atomic level became possible with the discovery of X-rays by Roentgen in 1895, whose short wavelengths (~1 Å) were suitable for diffraction experiments on crystals. X-rays are a form of high-energy electromagnetic radiation. Hard X-rays, which have photon energies above 5–10 keV, are highly penetrating and have a wide range of uses in medical, industrial, and research fields. They are typically generated through a process called electron bombardment, which involves directing a high-energy beam of accelerated electrons emitted from a heated filament onto a metal target, usually Cu or Mo. This process results in the emission of two types of radiation. The first is a broad continuous spectrum, known as white radiation or Bremsstrahlung, which is produced by inelastic collisions when the electrons come extremely close to the nucleus of the target atoms, causing a deceleration or deflection, converting the kinetic energy to electromagnetic radiation. The second is characterized by sharp and intense characteristic lines that arise from elastic collisions when the incident electrons eject an electron from the *K*-shell of the target atoms and leave a vacancy; the resultant vacancy is filled by electrons from higher energy levels corresponding to $L \rightarrow K$ or $M \rightarrow K$ electronic transitions, giving rise to the intense K_α and K_β lines, respectively (Figure 1-9).

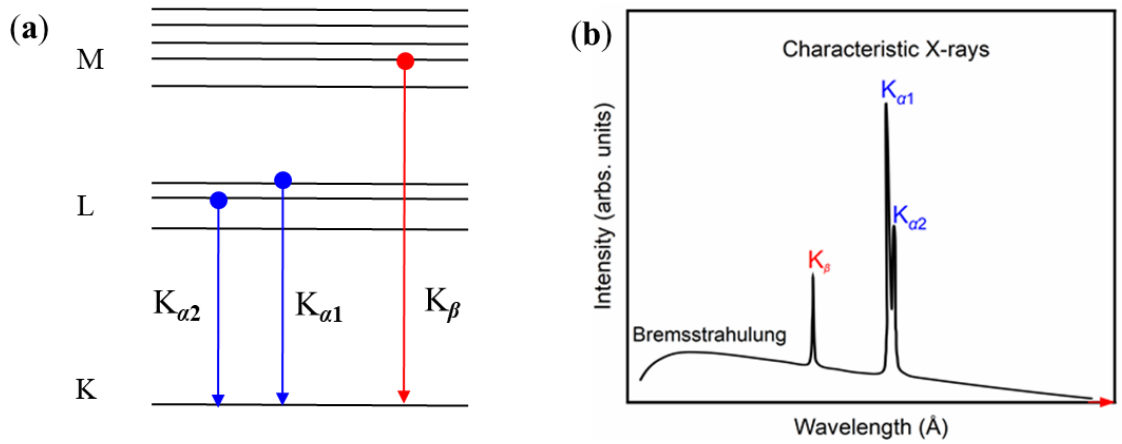

Figure 1-9. Schematic representation of (a) X-ray generation and (b) emission spectrum.

As the emission spectrum consists of different characteristic X-rays, we can select a monochromatic beam, usually the K_{α} line, while the continuous radiation and the less intense K_{β} line can be removed by using an appropriate filter, chosen to be an element with an absorption edge lying at a lower wavelength beside the unwanted line. It is common practice to use a filter of element (Z–1) for an element with an atomic number of Z. For example, a Ni filter is used for a Cu source, and an Nb filter is used for a Mo source.

To describe how diffraction occurs, we must first define the crystal structure, which is an arrangement of atoms that repeats periodically. The translational symmetry of such arrangements can be described using the concepts of lattice and basis. A lattice is a set of points within the crystal that have identical environments, while a basis is the set of atoms associated with each lattice point. Diffraction occurs when the X-ray strikes a set of lattice planes within a crystal with spacing d, similar in order of magnitude to the X-ray wavelength. The incident beams are scattered due to their interaction with the electron density of atoms in the crystal, and scattered X-rays from different parts of the atoms interfere either constructively or destructively. For constructive interference to occur, the path difference between neighbouring deflected X-rays must be an

integral number of the wavelength λ. This is known as Bragg's condition and is expressed as $n\lambda = 2d \sin\theta$ (Figure 1-10).[79]

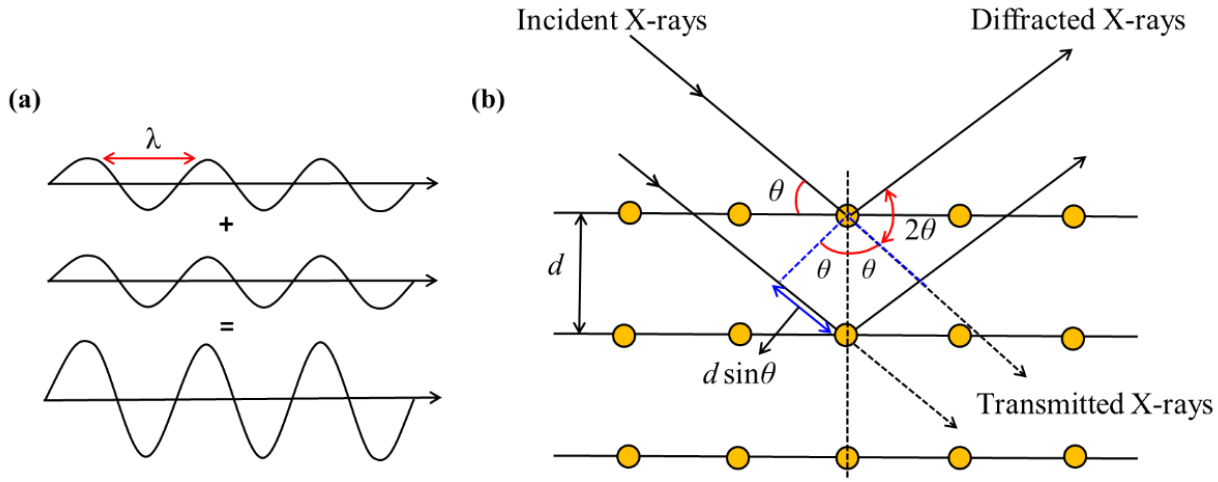

Figure 1-10. (a) Constructive interference. (b) Bragg's law for X-ray diffraction.

The Laue conditions provide a more general description of how X-rays can scatter within a three-dimensional arrangement of atoms. When X-rays are scattered from a crystal with a single scattering center, the difference in path length between two adjacent scattered X-rays will depend on both the incident angle μ and the scattered angle v (Figure 1-11(a)). Since X-rays can be scattered in all directions at any given point, this will result in a diffraction cone. In a three-dimensional scenario, three equations must apply simultaneously to define the direction of an incident and diffracted X-rays, satisfying the condition that the three Laue cones must intersect one another in a single line (Figure 1-11(b)).

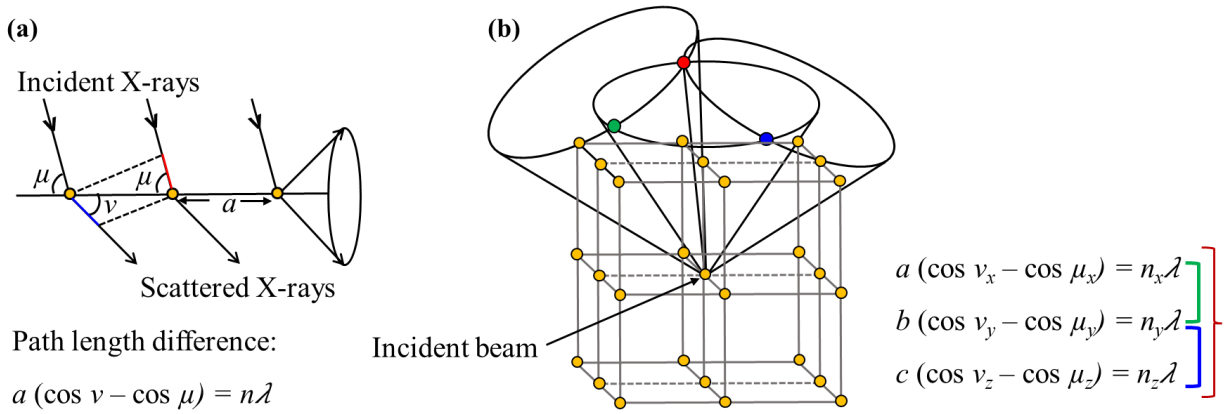

Figure 1-11. Laue conditions for X-ray diffraction.

1.9.1.1 Single crystal X-ray diffraction

The process of structure determination using single-crystal X-ray diffraction begins with the growth of high-quality single crystals, which is often the most challenging step. In the past, relatively large crystal sizes were required for diffraction measurements. However, with modern X-ray diffractometers, small crystals with dimensions of less than 0.1 mm can now be measured accurately. After a suitable crystal is selected, it is glued to the tip of a glass fiber which is then placed on a goniometer on a Bruker PLATFORM diffractometer equipped with a SMART APEX II CCD area detector and a graphite-monochromated Mo K_α radiation source. The intensity of each diffraction spot is recorded as the crystal is rotated. A complete dataset is typically collected using ω scans at different ϕ angles with a frame width of 0.3° and an exposure time of 10–15 s per frame (Figure 1-12), resulting in several thousand reflections *hkl*. These reflections are then averaged to obtain more accurate intensities I_{hkl}. These measured intensities are corrected by applying numerical face-indexed absorption corrections.

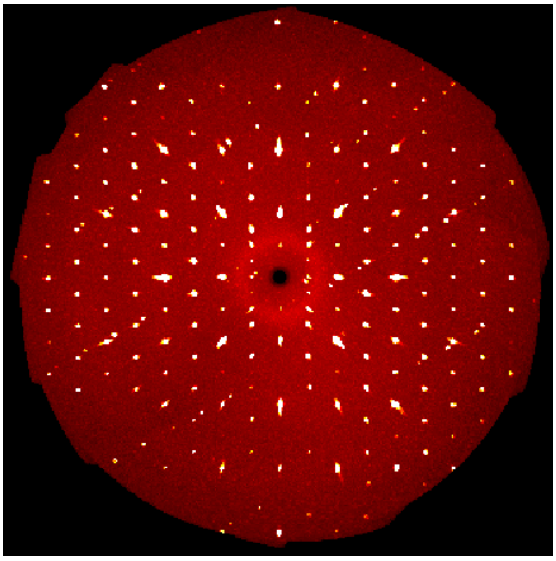

Figure 1-12. A precession image of reflections in reciprocal space collected from $Li_{0.25}Ag_{0.75}AlSe_2$ single crystal.

The intensity of a reflection *hkl* is proportional to the square of the structure factor F_{hkl}, which is complex-valued and depends on various factors including the positions and scattering ability of atoms as well as other parameters such as thermal displacements and site occupancies. The electron density function ρ_{xyz}, which is interpreted as the crystal structure, is obtained by a Fourier transform of the structure factors F_{hkl}.[80] However, this requires information on phases of structure factors, which cannot be measured experimentally.[81] To get around this phase problem, the most commonly used approach relies on direct methods, in which the phases of a few strong reflections are guessed based on probability theories. The phases are then improved until a consistent set is obtained where calculated and observed structure factors agree well. The agreement is evaluated by the agreement or residual factor (*R*-factor) and the goodness of fit.

1.9.1.2 Powder X-ray diffraction

Single crystals may not always be of appropriate size and quality to be analyzed by single-crystal X-ray diffraction, but samples are often available in the form of powders containing many

microcrystallites with random orientations. In such cases, powder X-ray diffraction (XRD) can be performed. It is primarily used for identifying phases by comparing experimental patterns with patterns simulated from known phases. If necessary, structural information can also be extracted using Rietveld profile refinement.

For this thesis work, a Bruker D8 Advance diffractometer equipped with a SSD160 detector a Cu K_α radiation source operated at 40 kV and 40 mA was used. Air-sensitive samples were finely ground inside an argon-filled glove box and mixed with mineral oil to minimize surface oxidation. The powder XRD patterns were analyzed and compared with the simulated pattern generated using the program PowderCell (version 2.4) (Figure 1-13).[82] To refine and extract cell parameters for certain compounds, the TOPAS software was used.[83]

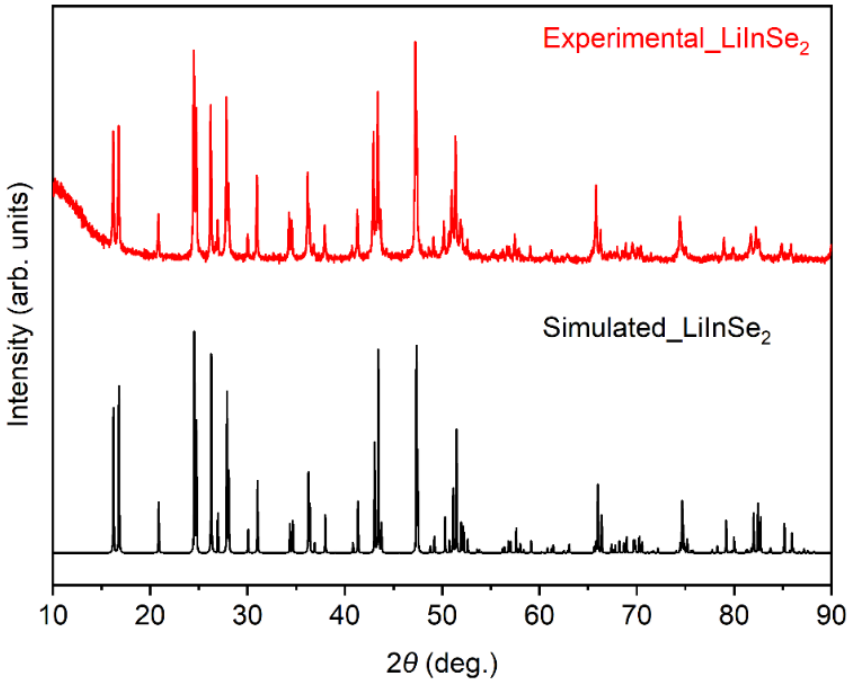

Figure 1-13. Experimental powder XRD pattern (red), compared with a pattern simulated from a structural model (black).

1.9.2 Energy dispersive X-ray (EDX) spectroscopy

Energy dispersive X-ray spectroscopy is widely used to identify and quantify the chemical composition of solid surfaces. Typically, EDX detectors are attached to a scanning electron microscope (SEM) or a transmission electron microscope (TEM). When an electron beam strikes the surface of a sample, many interactions can occur, generating different signals. Among these are secondary electrons (SE), backscattered electrons (BSE), characteristic X-rays, Auger electrons, and photons of various energies.[84] The region in which such interactions occur is called the "interaction volume"; it is proportional to the energy of the primary electron beam and the atomic number of the specimen. The secondary electrons, backscattered electrons, and characteristic X-rays provide information about composition (Figure 1-14).

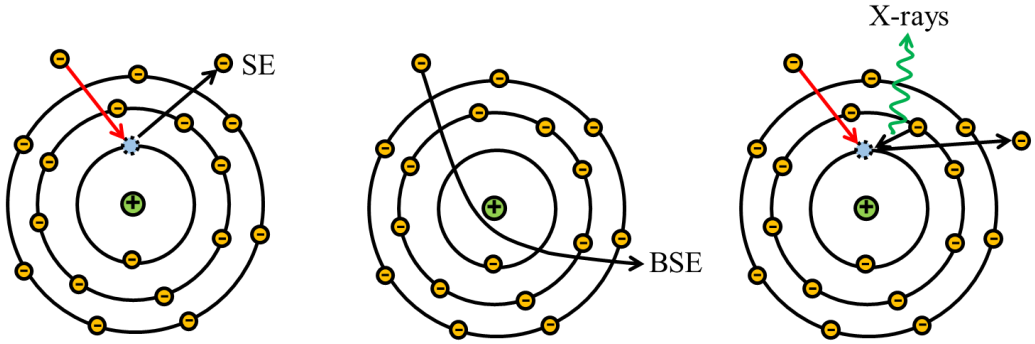

Figure 1-14. Specimen-beam interactions at an atomic level: secondary electrons, backscattered electron, and characteristic X-rays.

Secondary electrons are low-energy electrons produced from the surface or near-surface regions of the sample through inelastic interactions between the incident electron and the sample. Because of their low energy (~5 eV), they are useful for inspecting the topography of the sample's surface. In contrast, backscattered electrons are reflected when elastic scattering occurs. Because they originate from deeper areas of the sample, they are utilized to distinguish between different phases in a sample. Different regions of the sample appear brighter or darker, depending on the atomic numbers of elements present.[85]

EDX is based on the emission of characteristic X-rays which are produced when core electrons are ejected from an atom. This process leaves behind a hole that can be filled by a higher energy electron, resulting in the emission of an X-ray with an energy equal to difference between the two levels. The energy released during this process is unique to each element (Figure 1-15). EDX spectroscopy can only be used to detect elements that have an atomic number $Z > 4$ because the characteristic X-rays are too low in energy to be detected for light elements. Another problem is that it is difficult to distinguish between elements of similar atomic numbers because their peaks may overlap.[86]

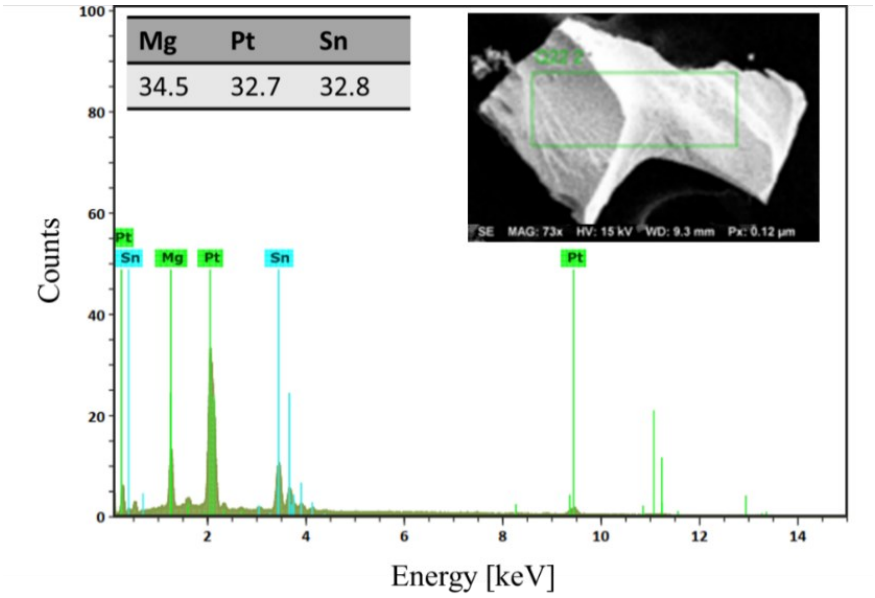

Figure 1-15. EDX spectrum of LiMgPtSn crystal, shown in a secondary electron image in inset.

All samples synthesized in this thesis contain Li, which cannot be detected by EDX spectroscopy. The amounts of other elements present were determined on a Zeiss Sigma 300 VP field-emission scanning electron microscope or a JEOL JSM-6010 LA InTouchScope scanning electron microscope, both operated with an accelerating voltage of 15–25 kV. The resulting data were analyzed and complemented by ^{7}Li NMR spectroscopy, which was used to probe the Li atoms in the samples.

1.9.3 Solid-state nuclear magnetic resonance (NMR) spectroscopy

Complementing diffraction techniques, solid state NMR spectroscopy is an effective method that can probe local atomic environments and dynamics within many solids, both crystalline and amorphous, and encompassing many types of materials (intermetallic compounds, non-linear optical crystals, battery materials, and glass-ceramics).[87–90] Most NMR active atomic nuclei have a spin number larger than 1/2. Lithium has two naturally occurring isotopes which are NMR-active, ^{6}Li (7.59 %) and ^{7}Li (92.41%), both are having a spin number I greater than 1/2.[91] In solution NMR, the spectra consist of a series of very sharp transitions because the dipolar interactions and chemical shift anisotropy are averaged out due to the rapid tumbling of the molecules in solution.[92] However, in solid-state NMR, molecules are randomly oriented and experience anisotropic interactions, so that the resonances are much broader compared to solution NMR.[93] To obtain site-resolved spectra, the anisotropic contribution can be removed by magic-angle spinning (MAS), in which the sample is rapidly rotated around an axis at an angle of 54.74° with respect to the external magnetic field.[94,95] Even though ^{7}Li has a nuclear spin of I = 3/2, its quadrupole moment is very small and has a negligible impact on the central transition under typical NMR magnetic fields, such that it can be treated effectively as a spin-1/2 nucleus.[96] Because of these advantages, ^{7}Li MAS NMR is used to determine the sites occupation in both Li-containing coloured intermetallic compounds and chalcogenides. These ^{7}Li NMR studies were performed in collaboration with Prof. Vladimir Michaelis research group at the University of Alberta. The experiments were carried out on either a Bruker 500 MHz (B_0 = 11.75 T) Avance NEO or a 400 MHz (B_0 = 9.4 T) Avance III HD NMR spectrometer, equipped with a 4-mm double resonance H-X MAS probe.

1.9.4 Differential scanning calorimetry

Thermal stability is an important property that affects the suitability of materials for specific applications. Differential scanning calorimetry (DSC) is used to investigate how materials respond to heat and to detect thermal processes such as glass transition, melting, and crystallization. In a DSC experiment, the sample is enclosed in a suitable pan, while a separate empty pan serves as a reference. Both the sample and reference are heated at the same linear rate. As the temperature changes, the sample may undergo a thermal event, and the amount of heat absorbed (endothermic process) or released (exothermic process) by the sample is measured based on a temperature difference between the sample and reference materials.

In this thesis, DSC measurement for Li-containing chalcogenides was performed in collaboration with Prof. Wenlong Yin at the Institute of Chemical Materials, China Academy of Engineering Physics, to evaluate the thermal stability and melting behaviour of the synthesized crystals. The samples were ground and placed in quartz tubes, which were evacuated to 10^{-3} Pa and sealed.

1.9.5 Diffuse reflectance spectroscopy

When light falls onto a sample surface, it can be reflected in two ways: specular reflection and diffuse reflection (Figure 1-16). Specular reflection occurs when light reflects off a smooth surface, such as a mirror or polished object, at an angle equal to the incident angle. In contrast, diffuse reflection occurs when light is reflected off rough surfaces in all directions.[97]

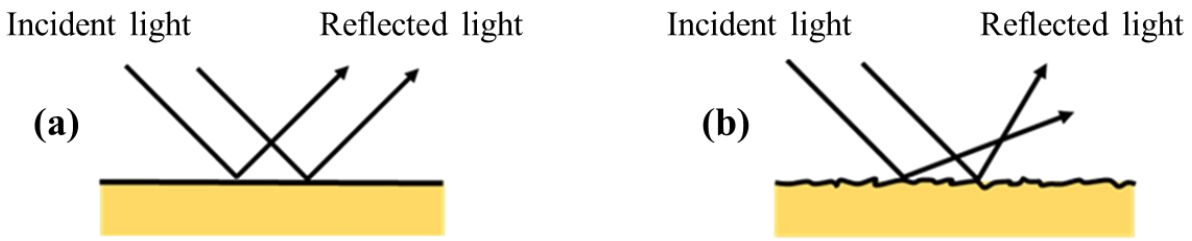

Figure 1-16. (a) Specular and (b) diffuse reflectance from a solid surface.

Diffuse reflectance spectrophotometry is a useful technique for measuring the colour of metallic compounds and determining the experimental energy band gap (E_g) of semiconductors. There is no standardized method for preparing powder samples for diffuse reflectance measurements. Typically, powder samples are placed in a sample holder with a surface of a few square millimeters, forming a layer that is 1–3 mm thick. This ensures that all incident light is either absorbed or scattered before reaching the back surface of the sample. All measurements are baseline corrected and run over the range of 200 to 1200 nm. A compacted pellet of $BaSO_4$ or polytetrafluoroethylene is used to collect 100% reflectance.

1.9.6 Colour determination in intermetallic compounds

The colour of a sample is perceived by shining a light source (illuminant) on it; those wavelengths that are not absorbed, but reflected, reach the observer's eyes. The problem is that people's sensitivity to colours can vary, and the perception of colours can differ between normal and dark lighting environments, which often leads to inconsistencies in colour evaluation. To address this, the International Commission on Illumination (CIE) standardized the way in which the colour of an object is measured to ensure that colour perceptions are not specific to an individual observer.[98,99] To establish the standard observers, a colour-matching experiment was conducted independently by Wright and Guild to find the colour-matching functions (CMF) for

red, green, and blue (RGB) primaries, which were obtained by averaging the judgements of 17 observers.[100,101] The observers looked through a small hole with a 2-degree field of view and matched each colour in the spectrum by additive mixing of three primaries lights. Based on the responses in this experiment, values were then averaged and plotted to create a representation of how the average human eye perceives colours in the spectrum. These resulting functions, known as CIE $\bar{x}$, $\bar{y}$, and $\bar{z}$ colour matching functions, represent the perceptions of an average observer (Figure 1-17).

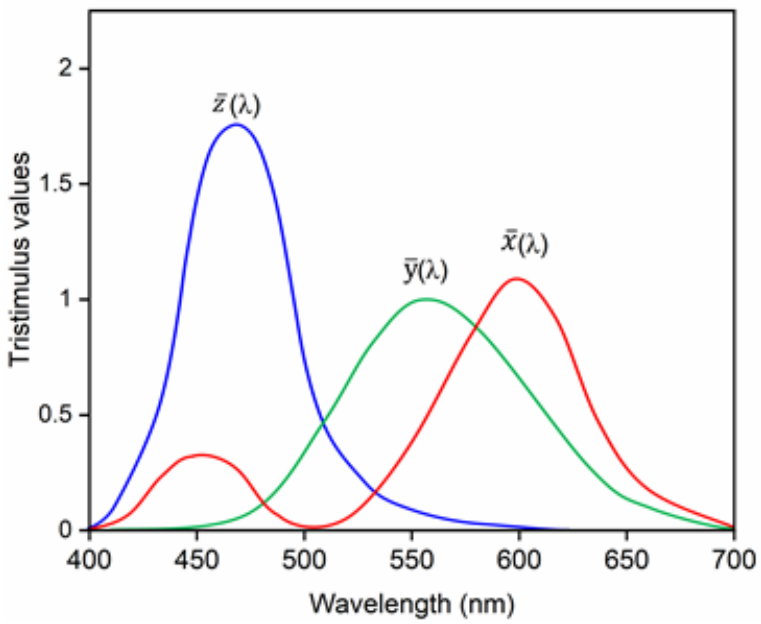

Figure 1-17. CIE 1931, 2° colour matching functions.

For colorimetric purposes, the CIE has proposed several spectral power distributions (SPD), which are known as CIE standard illuminants. By using the SPDs of these illuminants, the CIE-XYZ tristimulus values can be obtained from the colour-matching functions. If we replace our eyes with an instrument, it will perceive colour the same way our eyes do by gathering the wavelengths of reflected light from a sample as numeric values. These values can be recorded as

points across the visible spectrum and represented as a spectral curve to determine the colour of the substance. An example of this is shown in the spectral curve for pure gold (Figure 1-18).

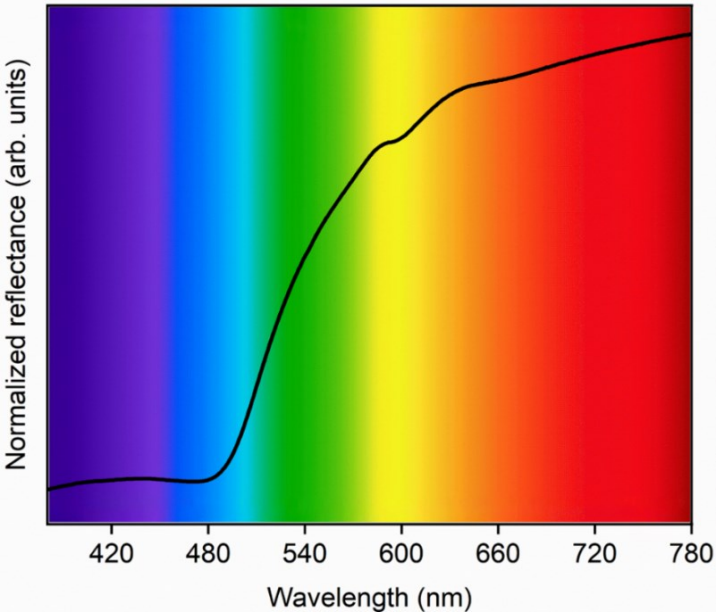

Figure 1-18. Spectral curve of pure gold (99.999%).

Once the spectral curve is measured, the tristimulus XYZ values can be obtained by multiplying the reflectance data with the colour-matching functions. The chromaticity coordinates are obtained x and y, which can specify a colour numerically by normalizing the XYZ by intensities:

$$x = \frac{X}{(X+Y+Z)}; \qquad y = \frac{Y}{(X+Y+Z)}; \qquad z = \frac{Z}{(X+Y+Z)} \qquad \textbf{Equation 1-6.}$$

where $x + y + z = 1$; thus, with only two components x and y which are the normalized values, the chromaticity of colour is defined (Figure 1-19). Pure and saturated colours are found along the curved boundary, and the colours become less saturated on moving toward the middle of the curve.

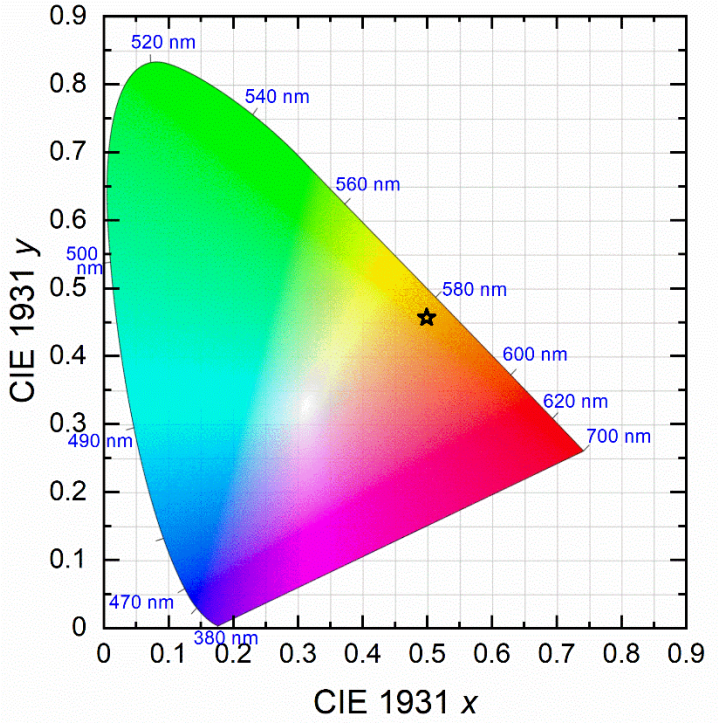

Figure 1-19. Normalized CIE 1931 ($x = 0.4991$, $y = 0.45652$) coordinates for pure gold (99.99%).

In this work, a spectral calculator designed for 5-nm sample intervals across the visible spectrum was used to calculate x and y chromaticity coordinates.[102]

1.9.7 Band gap measurement in semiconductors

The band gap energy (or band gap, E_g) of a semiconductor, which is the energy needed to promote an electron from the valence band to the conduction band, can be estimated from diffuse reflectance spectra of a powder sample.[103] An accurate determination of the band gap energy is critical for evauating the applicability and performance of semiconductors in many fields.[104] Generally, to measure the experimental optical energy gap of any material, the reflectance spectra are converted to the corresponding absorption spectra by applying the Kubelka–Munk function (Equation 1-7).[105] This function describes the behaviour of the light path through a dispersing medium as a function of the scattering and absorption coefficients:

$$F(R) = \frac{(1-R)^2}{2R} = \frac{K}{S} = \alpha$$ **Equation 1-7.**

where $F(R)$ denotes the ratio of absorption coefficient K and scattering coefficient S, and R is the reflectance. Then the energy band gap is usually evaluated from the Tauc representation by replacing $F(R)$ with α.[106,107]

$$(\alpha \cdot h\nu)^{1/\gamma} = (F(R) \cdot h\nu)^{1/\gamma} = B\left(h\nu - E_g\right)$$ **Equation 1-8.**

where h is the Planck constant, ν is the photon's frequency, and B is a constant. The γ factor depends on the nature of the electron transition; it is equal to 1/2 for a direct band gap or 2 for an indirect band gap. The E_g values can then be obtained by extrapolating the absorption edge to the baseline of a plot of $(F(R) \cdot h\nu)^{1/\gamma}$ vs. $h\nu$ (Figure 1-20).

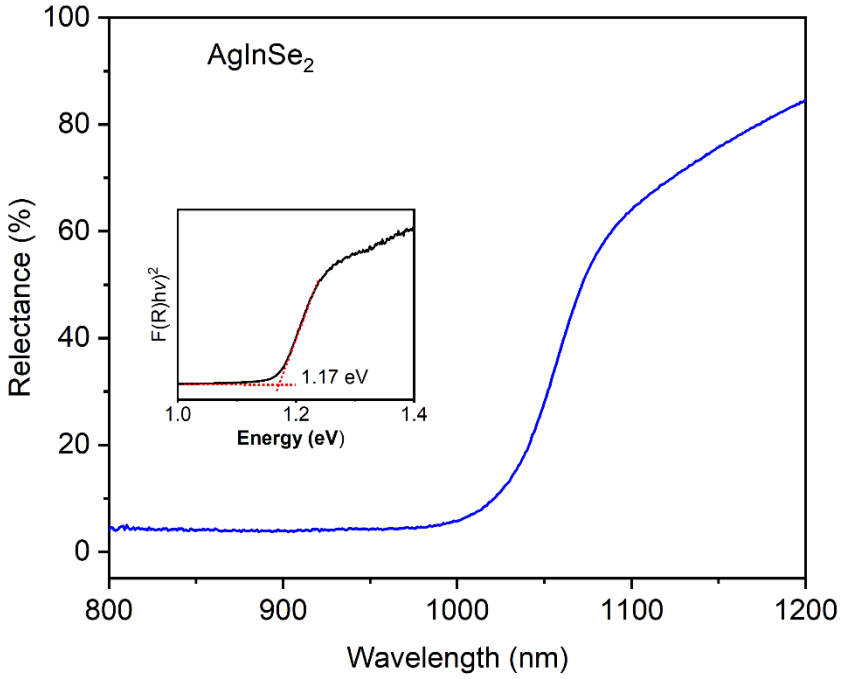

Figure 1-20. Diffuse reflectance spectrum of $AgInSe_2$. The inset is a Tauc plot showing the determination of the optical bandgap value.

1.10 Band structure calculations

Calculating the electronic structure of crystalline extended solids allows many important properties to be rationalized or predicted. Unlike molecular solids, where few atoms interact to result in a finite number of energy levels in a molecular orbital diagram, extended solids contain a periodic arrangement of a very large number of atoms that interact so that the energy levels are no longer discrete but instead form bands with numerous closely spaced energy levels. These energy levels correspond to the extended overlap of atomic orbitals, consistent with the symmetry of the crystal structure. It is impractical to solve the Schrödinger equation exactly for extended solids, which are composed of many electrons. The presence of electron-electron Coulomb repulsion term in the Hamiltonian term comes into play, but there are some approximations that can simplify this equation. Instead of considering all possible interactions simultaneously, it is assumed that all electrons are independent, each moving in a local effective external potential. The Schrödinger equation can now be solved by Kohn-Sham equation, which has the sums of the Coulomb potential, the Hartree potential, and the exchange-correlation potential.[108,109] Just as molecular orbitals are formed by combining atomic orbitals in a linear manner, electronic wavefunctions in extended solids are also linear combinations of atomic orbitals.[110] Taking advantage of translational periodicity, which is characteristic of crystal lattices, will further simplify the problem. As a result, solving the Schrödinger equation becomes tractable, and the resulting wavefunctions are called Bloch functions. For a simple 1D crystal, these Bloch functions are expressed as:

$$\psi_{(k)} = \sum_n e^{ikna} x_n \qquad \textbf{Equation 1-9.}$$

where a is the unit cell length and the wavevector k measures momentum and is quantized in reciprocal space. The unit cell in reciprocal space is called the first Brillouin zone and lies within the interval $-\frac{\pi}{a} \leq k \leq \frac{\pi}{a}$. The Bloch functions at the centre and edge of the Brillouin zone are:

$$k = 0 \qquad \psi_{(0)} = \sum_n e^0 x_n = x_0 + x_1 + x_2 + x_3 + \cdots \qquad \textbf{Equation 1-10.}$$

$$k = \frac{\pi}{a} \qquad \psi_{(\frac{\pi}{a})} = \sum_n e^{i\pi n} x_n = x_0 - x_1 + x_2 - x_3 + \cdots \qquad \textbf{Equation 1-11.}$$

A plot of energy as a function of k is called a band dispersion diagram (Figure 1-21(a)). Because the energy is symmetrical around the centre of the Brillouin zone, we only need to plot over the positive range, $0 \leq k \leq \frac{\pi}{a}$. Although k is quantized, the bands are drawn as continuous lines because the energy levels are spaced so closely together. In real 3D crystals, the band structures are much more complex, of course. Instead of showing bands, it is convenient to plot the density of state (DOS), which is the number of states over an infinitesimal increment of energy (Figure 1-21(b)). For a single band, the DOS is inversely proportional to the slope of the band. The interaction between the orbitals of two neighbouring atoms is described by their Hamiltonian matrix element. Multiplying the DOS by the corresponding element of the Hamiltonian results in the crystal orbital Hamilton population (COHP), which serves as a quantitative measure of bonding strength (Figure 1-21(c)).[111,112]

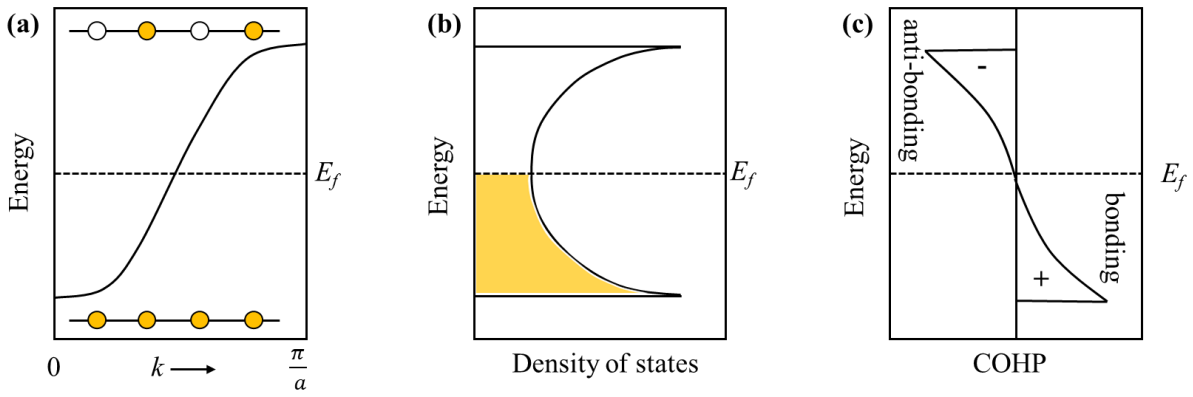

Figure 1-21. (a) Band dispersion, (b) density of states, and (c) crystal orbital Hamiltonian population for a 1D chain of s-orbitals.

In this work, band structures and density of states of Li_2ZnX (X = Ga, In) were performed using the program Akai-KKR,[113] which uses the Korringa-Kohn-Rostoker Green function method combined with the local density approximation (LDA) and the coherent potential approximation (CPA), suitable for treating the site disorder of Zn and Ga or In atoms occurring in these compounds. For quaternary intermetallics and chalcogenides, calculations were performed using the projected augmented wave (PAW) method as implemented in the Vienna ab initio simulation package (VASP version 5.4.4),[114–116] with the generalized gradient approximation (GGA) parameterized by PBE to treat exchange and correlation.[108,117–118] Electron localization functions (ELF), projected crystal orbital Hamilton populations (−pCOHP), and crystal orbital bond index (COBI) were determined using the program LOBSTER (version 4.1.0).[112,119–122]

1.11 Research motivation

The primary objective of this research is to discover new intermetallics and chalcogenides containing lithium and to evaluate their crystal structures, optical and electronic properties comprehensively to establish a correlation between these characteristics. The study aims to gain insights into the underlying mechanisms responsible for colours in metallic substances. Moreover,

the incorporation of lithium into existing chalcogenide NLO materials is expected to enhance their second harmonic generation responses, which play a critical role in various technological applications.

The first part of this thesis is motivated by the search for new ternary and quaternary coloured intermetallics, which remain very rare, accounting for less than 1% of known intermetallic compounds, and mostly limited to combinations with very expensive precious metals like Au and Pt. These compounds exhibit colour, but not through the typical mechanisms, such as band gaps, charge transfer, or d-d/f-f transitions, encountered in other inorganic semiconductors or insulators. Because these vivid colours are combined with attractive metallic lustre, these coloured intermetallics are desirable for decorative coatings, jewelry, and plasmonic materials. The hypothesis is that Li-containing intermetallics synthesized with less expensive elements such as Cu and Zn would possess similar crystal and electronic structures as the previously known analogues, making them promising targets for new, more affordable coloured intermetallics. Furthermore, mixing two different coloured phases can result in permanent colour variations which could be an additional method for controlling colour in metallic materials and expanding their use in various applications.

This second part of the thesis is motivated by the search for new IR NLO crystals with a large SHG response and wide band gap, resulting in a high laser damage threshold. The focus is on modifying the known ternary chalcogenides $AgAlSe_2$, $AgGaSe_2$, and $AgInSe_2$, which have smaller band gaps compared to their Li-containing analogues. Although these compounds have been extensively studied, scant attention has been given to the investigating solid solutions based on them to form quaternary compounds with diverse properties. Many interpretations of their structure-property relationships have been previously made based on uncertain structures,

typically assumed through powder XRD data alone. The hypothesis is that substituting Ag with Li would allow for the optical properties of the crystal be appropriately tuned, resulting in a balance between a large SHG response and a wide bandgap. Solid state ^{7}Li NMR spectroscopy was also exploited to clarify ambiguities about the detailed arrangement of metal cations.

1.12 References

(1) Castillo, S.; Ansart, F.; Laberty-Robert, C.; Portal, J. *J. Power Sources* **2002**, *112*, 247–254.

(2) Greatbatch, W.; Holmes, C. F. *Pacing Clin. Electrophysiol.* **1992**, *15*, 2034–2037.

(3) Lavernia, E. J.; Grant, N. J. *J. Mater. Sci.* **1987**, *22*, 1521–1529.

(4) Kostrivas, A.; Lippold, J. C. *Int. Mater. Rev*. **1999**, *44*, 217–237.

(5) Schetky, L. M. *MRS Bull.* **1996**, 50–55.

(6) Deevi, S. C.; Sikka, V. K. *Intermetallics* **1996**, *4*, 357–375.

(7) Takano, K. *J. Phys. Soc. Japan* **1969**, *26*, 362–370.

(8) Ohara, S.; Komura, S.; Taked, T. *J. Phys. Soc. Japan* **1973**, *34*, 1472–1476.

(9) Scanlon, W. W. *Science* **1963**, *142*, 1265–1269.

(10) Antolini, E. *Appl. Catal. B Environ*. **2017**, *217*, 201–213.

(11) Jiang, Y.; He, Y.; Liu, C. T. *Intermetallics* **2018**, *93*, 217–226.

(12) Nakamura, M. *MRS. Bull*. **1995**, *20*, 33–39.

(13) Cinca, N.; Lima, C. R. C.; Guilemany, J. M. *J. Mater. Res. Technol*. **2013**, *2*, 75–86.

(14) Herbst, J. F.; Croat, J. J.; Pinkerton, F. E.; Yelon, W. B. *Phys Rev*. *B* **1984**, *29*, 4176–4178.

(15) Mathias, B. T.; Geballe, T. H.; Geller, S.; Corenzwit, E. *Phys. Rev*. **1954**, *95*, 1435.

(16) Furukawa, S.; Komatsu, T. *ACS. Catal*. **2017**, *7*, 735–765.

(17) Gil, F. J.; Planell, J.A. *J .Eng. Med*. **1998**, *212*, 473–488.

(18) Vishnubhatla, S. S.; Jan, J. P. *Philos. Mag*. **1967**, *16*, 45–50.

(19) Chatterjee, B. Diverse Topics in Science and Technology, AuthorHouse, UK, 2013.

(20) Wang, M.X.; Zhu, H.; Yang, G. J.; Liu, K.; Li, J. F.; Kong, L. T. *Mater. Des*. **2021**, *198*, 109359.

(21) Walter, R. *Nature* **1923**, *112*, 832–834.

(22) Liu, C.; Lu, W.; Xia, W.; Chang Liu, Du, C.; Rao, Z.; Best, J. P.; Brinckmann, S.; Lu, J.; Gault, B.; Dehm, G.; Wu,G.; Li, Z.; Raabe, D. *Nat. Commun*. **2022**, *13*, 1–9.

(23) Zhang, Y.; Zhou, Y. J.; Lin, J. P.; Chen, G. L.; Liaw, P. K. *Adv. Eng. Mater*. **2008**, *10*, 534–538.

(24) Kempter, C. P. *Phys. Status Solidi B* **1966**, *18*, K117–K118.

(25) Steinemann, S. G.; Wolf, W.; Podloucky, R. Color and Optical Properties. In: J. H. Westbrook, R. L. Fleischer (Eds.), *Intermetallic Compounds, Principles and Practice*. Vol 3, Weily, New York, 2002, 231–244.

(26) Mishra, V.; Iyer, A. K.; Mumbaraddi, D.; Oliynyk, A. O.; Zuber, G.; Boucheron, A.; Dmytriv, G.; Bernard, G. M.; Michaelis, V. K.; Mar, A. *J. Solid State Chem*. **2020**, *292*, 121703.

(27) Jomaa, M.; Mishra, V.; Mumbaraddi, D.; Chaudhary, M.; Dmytriv, G.; Michaelis, V. K.; Mar, A. *J. Solid State Chem*. **2022**, *306*, 122792.

(28) Gardam, G. E. *Trans IMF*. **1966**, *44*, 186–188.

(29) Cretu, C.; Van Der Lingen, E. *Gold Bull*. **1999**, *32*, 115–126.

(30) Saeger, K. E.; Rodies, J. *Gold Bull*. **1977**, *10*, 10–14.

(31) Steinemann, S. G.; Anongba, P. N. B. Podloucky, R. *J. Phase Equilibria* **1997**, *18*, 655–662.

(32) Van Der Lingen, E. *J. South. Afr. Inst. Min. Metall*. **2014**, *114*,137–144.

(33) Nomerovannaya, L. V.; Kirillova, M. M.; Shaikin, A. B. *Phys. Status Solidi B* **1980**, *102*, 715–720.

(34) Ranganathan, S.; Inoue, A. *Acta. Mater*. **2006**, *54*, 3647–3656.

(35) Eberz, U.; Seelentag, W.; Schuster, H.-U. *Z. Naturforsch*. **1980**, *35 b*, 1341–1343.

(36) Drews, J.; Eberz, U.; Schuster, H.-U. *J. Less Common Met.* **1986**, *116*, 271–278.

(37) Czybulka, A.; Petersen, A.; Schuster, H.-U. *J. Less Common Met.* **1990**, *161*, 303–312.

(38) Dmytriv, G.; Pauly, H.; Ehrenberg, H.; Pavlyuk, V.; Vollmar, E. *J. Solid State Chem*. **2005**, *178*, 2825–2831.

(39) Burstein, E.; Brotman, A.; Apell, P. *J. De. Phys*. **1983**, *44*, C10-429–C10-439.

(40) Villars, P.; Cenzual, K. *Pearson's Crystal Data–Crystal Structure Database for Inorganic Compounds*, (on DVD), Release 2022/23, ASM International, Materials Park, OH, USA.

(41) Jeong, Y. B.; Kim, J. T.; Hong, S. H.; Lee, H. D.; Choi, S. Y.; Kim, K. B. *Mater. Des*. **2019**, *175*, 107814.

(42) Supansomboon, S.; Dowd, A.; Van Der Lingen, E.; Keast, V. J.; Cortie, M. B. (Ed.) Howard, P.; Huggett, P.; Evans, D. *Mater. Forum* **2013**, *37*, 1–5.

(43) Seo, M.; Lee, M. *Acta Mater*. **2018**, *159*, 1–7.

(44) Makovicky, E. Rev. *Mineral Geochemistry* **2006**, *61*, 7–125

(45) Bergman, J. G.; Kurtz, S. K.; *Mater. Sci. Eng*. **1970**, *5*, 235–250.

(46) Shcherbakov, M. R.; Neshev, D. N.; Hopkins, B.; Shorokhov, A. S.; Staude, I.; Melik-Gaykazyan, E. V. ; Decker,M.; A. Ezhov, A. A.; Miroshnichenko, A. E.; Brener, I.; Fedyanin, A. A.; Kivshar, Y. S. *Nano Lett*. **2014**, *14*, 6488–6492.

(47) Sutherland, R. L.; Mclean, D.G.; Kirkpatrick, S. *Handbook of Nonlinear Optics with Contributions*. Marcel Dekker: New York, 2003.

(48) Boyd, R. W. *Nonlinear Optics*. 3rd ed. Rochester, Elsiver: New York, 2007.

(49) Luo, X.; Li, Z.; Guo, Y.; Yao, J.; Wu.; Y. *J. Solid State Chem*. **2019**, *270*, 674–687.

(50) Galanty, M.; Shavit, O.; Weissman, A.; Aharon, H.; Gachet, D.; Segal, S.; Salomon, A. *Light Sci. Appl*. **2018**, *7*, 1–8.

(51) Guo, S. P.; Chi, Y.; Guo, G. C. *Coord. Chem. Rev*. **2017**, *335*, 44–57.

(52) Halasyamani, P. S.; Rondinelli, J. M. *Nat. Commun*. **2018**, *9*, 1–4.

(53) Liu, B. W.; Zeng, H. Y.; Jiang, X. M.; Guo, G. C. *CCS. Chem*. **2021**, *3*, 964–973.

(54) Kang, L.; Zhou, M.; Yao, J.; Lin, Z.; Wu, Y.; Chen, C. *J. Am. Chem. Soc*. **2015**, *137*, 13049–13059.

(55) Guidotti, D.; Driscoll, T. A.; Gerritsen, H. J. *Solid State Commun*. **1983**, *46*, 337–340.

(56) Zhang, W.; Yu, H.; Wu, H.; Halasyamani, P. S. *Chem. Mater*. **2017**, *29*, 2655–2668.

(57) Ok, K. M.; Chi, E. O.; Halasyamani, P. S. *Chem. Soc. Rev*. **2006**, *35*, 710–717.

(58) Abudurusuli, A.; Li, J.; Pan, S. *Dalt. Trans*. **2021**, *50*, 3155–3160.

(59) Jiang X.-M.; Guo, S.-P.; Zeng, H.-Y.; Zhang, M.-J.; Guo. G.-C. *Structure-Property Relationships in Non-Linear Optical Crystals II: The IR Region*. Springer, Berlin, 2012.

(60) Chen, J.; Jiang, X.; Wu, Q.; Lin, Z.; Luo, M.; Ye, N. *J. Alloys Compd*. **2022**, *901*, 163384.

(61) Lin, H.; Chen, H.; Zheng, Y. J.; Yu, J. S.; Wu, X. T.; Wu, L. M. *Dalt. Trans*. **2017**, *46*, 7714–7721.

(62) Elsaesser, T.; Seilmeier, A.; Kaiser, W.; Koidl, P.; Brandt, G. *Appl. Phys. Lett*. **1984**, *44*, 383–385.

(63) Catella, G. C.; Shiozawa, L. R.; Hietanen, J. R.; Eckardtet R. C.; Route, R. K.; Feigelson, R. S.; Cooper, D. G.; Marquardt, C. L. *Appl. Opt*. **1993**, *32*, 3948–3951.

(64) Boyd, G. D.; Buehler, E.; Storz, F. G. *Appl. Phys. Lett*. **1971**, *18*, 301–304.

(65) Isaenko, L.; Yelisseyev, A.; Lobanov, S.; Petrov, V.; Rotermund, F.; Slekys, G.; Zondy. J. -J. *J. Appl. Phys*. **2002**, *91*, 9475–9480.

(66) Cai, W.; Abudurusuli, A.; Xie, C.; Tikhonov, E.; Li, J. Pan, S.; Yang, Z. *Adv. Funct. Mater.* **2022**, 2200231.

(67) Yin, W.; Feng, K.; He, R.; Mei, D.; Lin, Z.; Yao, J.; Wu, Y. *Dalt. Trans*. **2012**, *41*, 5653–5661.

(68) Geng, L.; Cheng, W. -D.; Lin, C. -S.; Zhang, W. -L.; Zhang, H.; He, Z. -Z. *Inorg. Chem*. **2011**, *50*, 5679–5686.

(69) Guo, Y.; Liang, F.; Li, Z.; Xing, W.; Lin, Z. -S.; Yao, J.; Mar. A.; Wu, Y. *Inorg. Chem*. **2019**, *58*, 10390–10398.

(70) Isaenko, L.; Yelisseyev, A.; Lobanov, S.; Titov, A.; Petrov, V.; Zondy, J. -J.; Krinitsin, P.; Merkulov, A.; Vedenyapin, V.; Smirnova, *J. Cryst. Res. Technol.* **2003**, *38*, 379–387.

(71) Yelisseyev, A.; Liang, F.; Isaenko, L.; Lobanov, S.; Goloshumova, A.; Lin, Z. S. *Opt. Mater*. **2017**, *72*, 795–804.

(72) Kumar, V.; Chandra, S.; Santosh, R. *J. Electron. Mater*. **2018**, *47*, 1223–1231.

(73) Lekse, J. W.; Moreau, M. A.; McNerny, K. L.; Yeon, J.; Halasyamani, P. S.; Aitken, J. A. *Inorg. Chem*. **2009**, *48*, 7516–7518.

(74) Brant, J. A.; Clark, D. J.; Kim, Y.S.; Jang, J. I.; Weiland, A.; Aitken, J. A. *Inorg. Chem*. **2015**, *54*, 2809–2819.

(75) Zhang, J. -H.; Clark, D. J.; Brant, J. A.; Sinagra, C. W.; Kim, Y. S.; Jang, J. I.; Aitken, J. A. *Dalt. Trans.* **2015**, *44*, 11212–11222.

(76) Yin, W.; Feng, K.; Hao, W.; Yao, J.; Wu, Y. *Inorg. Chem.* **2012**, *51*, 5839−5843.

(77) Cheetham, A. K.; Day. P. Solid State Chemistry, Clarendon: Oxford, 1988, 1–398.

(78) Harrison, M. J.; Graebner, A. P.; McNeil, W. J.; McGregor, D. S. *J. Cryst. Growth* **2006**, *290*, 597–601.

(79) Massa, W. *Crystal Structure Determination*, 2nd ed.; Springer: Berlin, 2004.

(80) Lynn, F.; Eyck, T. *Meth. Enzymol.* **1985**, *115*, 324–337.

(81) Cowtan, K. *Phase Problem in X -ray Crystallography, and Its Solution*, in *eLS*, Wiley: Chichester, UK, 2003.

(82) Kraus, W.; Nolze, G. *J. Appl. Crystallogr*. **1966**, *29*, 301–303.

(83) Coelho, A. A. *TOPAS–Academic, Version 6*, Coelho Software, Brisbane, Australia, 2007.

(84) Saghiri, M. A.; Asgar, K.; Lotfi, M.; Karamifar, K.; Saghiri, A. M.; Neelakantan, P.; Gutmann, J. L.; Sheibaninia, A. *Acta. Odontol. Scand*. **2012**, *70*, 603–609.

(85) Kowoll, T.; Müller, E.; Fritsch-Decker, S.; Hettler, S.; Störmer, H.; Weiss, C.; Gerthsen, D. *Scanning* **2017**, *2017*, 1–12.

(86) Heslop-Harrison, J.S. Energy Dispersive X-Ray Analysis. In: Linskens, HF., Jackson, J.F. (eds) *Physical Methods in Plant Sciences. Modern Methods of Plant Analysis*, vol 11, Springer, Berlin, Heidelberg, 1990, 244–277.

(87) Reif, B.; Ashbrook, S. E.; Emsley, L.; Hong, M. *Nat. Rev. Methods Primers* **2021**, *1*, 1–23.

(88) Dupke, S.; Eckert, H.; Winter, F.; Pöttgen, R. *Prog. Solid State Chem*. **2014**, *42*, 57–64.

(89) Youngman, R. *Materials* **2018**, *11*, 1–24.

(90) Lim, A. R.; Yoon, C. S. *Mater. Chem. Phys*. **2014**, *147*, 644–648.

(91) Chandran, C. V.; Heitjans, P. *Annu. Rep. NMR. Spectrosc.* **2016**, *89*, 1–102.

(92) Ganesh, K. N.; *Curr. Sci.* **1982**, *51*, 866–874.

(93) Sakellariou, D. Brown, S. P.; Lesage, A.; Hediger, S.; Bardet, M.; Meriles, C. A.; Pines, A.; Emsley, L. *J. Am. Chem. Soc*. **2003**, *125*, 4376–4380.

(94) Andrew, E. R.; Bradbury, A.; Eades, R. G. *Nature* **1958**, *182*, 4376–4380.

(95) Alia, A.; Ganapathy, S.; de Groot H. J. M. *Photosyn. Res*. **2009**, *102*, 415–425.

(96) Michaelis, V. K.; Levin, K.; Germanov, Y.; Kroeker, S. *Chem. Mater.* **2018**, *30,* 5521−5526.

(97) Janecek, M.; Moses, W. W. *IEEE. Trans. Nucl. Sci*. **2008**, *55*, 2432–2437.

(98) International Commission on Illumination. Commission internationale de l'éclairage, huitième session, Cambridge, Cambridge,1931.

(99) Smith, T.; Guild, J. *Trans. Opt. Soc*. **1931**, *33*, 74–134.

(100) Wright, W. D. *Trans. Opt. Soc.* 1**929**, *30*, 141–164.

(101) Guild, J. *Philos. Trans. Royal Soc. A* **1931**, *230*, 149–187.

(102) http://www.brucelindbloom.com/ (Accessed Jan 01, 2021).

(103) Makuła, P.; Pacia, M.; Macyk, W. *J. Phys. Chem. Lett*. **2018**, *9*, 6814–6817.

(104) Dolgonos, A.; Mason, T. O. *J. Solid State Chem*. **2016**, *240*, 43–48.

(105) Kubelka, P.; Munk, F. *Fuer. Tekn. Phys.* **1931**, *12*, 593–609.

(106) Tauc, J.; Grigorovici, R .; Vancu, A. *phys. stat. sol*. **1966**, *15*, 627–637.

(107) Zanatta, A.; Chambouleyron, I. *Phys. Rev. B* **1996**, *53*, 3833–3836.

(108) Kohn, W.; Sham, L. J. *Phys. Rev*. **1965**, *140*, A1133–A1138.

(109) Rindt, C. C. M., Gaastra-Nedea, S. V. Modeling thermochemical reactions in thermal energy storage systems. *Advances in Thermal Energy Storage Systems*. Woodhead Publishing, 2015, 375–415.

(110) Hoffmann, R. *Angew. Chem*. **1987**, *26*, 846–878.

(111) Dronskowski, R.; Blöchl, P. E. *J. Phys. Chem*. **1993**, *97*, 8617–8624.

(112) Deringer, V. L.; Tchougréeff, A. L.; Dronskowski, R. *J. Phys. Chem. A* **2011**, *115*, 5461–5466.

(113) Long, N. H.; Akai, H. *J. Phys. Condens. Matter*. **2007**, *19*, 365232.

(114) Kresse, G.; Furthmüller, J. *Phys. Rev. B* **1996**, *54*, 11169–11185.

(115) Kresse, G.; Joubert, D. *Phys. Rev. B* **1999**, *59*, 1758–1775.

(116) Blöchl, P. E. *Phys. Rev. B* **1994**, *50*, 17953–17979.

(117) Perdew, J. P.; Burke, K.; Ernzerhof, M. *Phys. Rev. Lett*. **1996**, *77*, 3865–3868.

(118) Hohenberg, P. *Phys. Rev*. **1964**, *136*, B864–B870.

(119) Grin, Y.; Savin, A.; Silvi B. The ELF Perspective of Chemical Bonding. *In The Chemical Bond: Fundamental Aspects of Chemical Bonding*, Frenking, G.; Shaik, S., Eds.; Wiley-VCH: Weinheim, 2014, pp 345–382.

(120) Dronskowski, R.; Festkbrperforschung, M.; Blochl, P. E. *J. Phys. Chem*. **1993**, *97*, 8617–8624.

(121) Maintz, S.; Deringer, V. L.; Tchougréeff, A. L. *J. Comput. Chem*. **2013**, *34*, 2557–2567.

(122) Maintz, S.; Deringer, V. L.; Tchougréeff, A. L.; Dronskowski, R. *J. Comput. Chem.* **2016**, *37*, 1030–1035.

Chapter 2.

Coloured intermetallic compounds Li_2ZnGa and Li_2ZnIn

A version of this chapter has been published.

Jomaa, M.; Mishra, V.; Mumbaraddi, D.; Chaudhary, M.; Dmytriv, G.; Michaelis, V. K.; Mar, A. J. Solid State Chem. **2022**, *306*, 1–6.

2.1 Introduction

Metallic substances normally have high optical reflectivity of all wavelengths within the visible region. There are much fewer (~10^2) examples of metallic substances that exhibit an absorption edge of 1.5–3.0 eV so that they possess the unusual property of appearing coloured.[1] They consist of some elemental metals (Cu, Au),[2] alloys (various Au-containing ones),[3,4] and intermetallic compounds,[5,6] including Laves phases[7] (the most well known being "purple plague" $AuAl_2$)[8–10] and Zintl phases.[11] These coloured metals are greatly valued in jewellery.[3,4,6,12] The brittleness and low ductility frequently shown by intermetallics presents challenges in processing,[13] but combining them in a matrix with better mechanical properties[14,15] or fabricating them as thin films have been proposed as possible solutions.[16] As an ambitious application, coloured intermetallics have been suggested as plasmonic materials.[17]

Most coloured intermetallics contain late transition metals (often precious metals such as Pd, Pt, Ag, Au) and p-block metalloids (Al, Ga, In; Si, Ge, Sn; Sb), and adopt simple structures based on cubic aristotypes such as CsCl, ZnS, and CaF_2.[1] Further, when these elements are combined with Li or Mg, ternary or quaternary coloured intermetallics are known.[11,18–20] These

compositions accord with principles first proposed by Steinemann for the appearance of colour in intermetallics: high-symmetry structures giving rise to sharp peaks in the density of states, electron counts imparted by late transition metals to place the Fermi level near a pseudogap, and mixing of metal d and metalloid s/p states to satisfy the dipole selection rule ($\Delta l = \pm 1$) for electronic transitions.[1] In general, a valence electron count per formula unit of 7 or less also seems to be a requirement for colour in these compounds, provided that metals in groups 8 to 10 are assigned an electron count of zero.

Coloured intermetallics that could be prepared without precious metals would be attractive candidates for applications. Recently, we have identified the new compounds $LiCu_2Al$ (red) and $LiCu_2Ga$ (yellow).[21] Related ternary Li-containing representatives that are coloured and consist of less expensive metals are uncommon; they include $LiNi_2X$ (X = Ge, Sn),[22,23] $LiCu_2X$ (X = Si, Ge, Sn),[24,25] Li_2CuX (X = Ge, Sn),[24,25] and Li_2ZnSi.[26]

Here, we investigate the Li–Zn–X (X = Ga, In) system and report the synthesis and characterization of the new ternary compounds $LiZn_2Ga$ and Li_2ZnIn, which are coloured. Because Li atoms are difficult to locate by X-ray diffraction methods, solid-state ^{7}Li NMR spectra were collected. Optical reflectance measurements and electronic structure calculations were carried out.

2.2 Experimental

2.2.1 Synthesis

Starting materials were Li ribbon (99.9%, Aldrich), Zn powder (99.8%, Onyxmet), Ga ingot (99.99%, Alfa Aesar), and In powder (99.9%, Alfa Aesar). The Li ribbon was handled and cut within an argon-filled glove box, and its surface was scraped to remove surface contaminants prior to use. Mixtures of Li, Zn, and Ga or In were combined in a molar ratio of 2:1:1 in a total

mass of 0.200 g, which were then placed within niobium tubes. The tubes were welded shut in a Centorr 5TA tri-arc furnace on a water-cooled copper hearth under high-purity argon atmosphere. The samples were heated for 15 min under argon atmosphere within a copper coil (5-cm diameter) of a water-cooled Ambrell EASYHEAT 560LI 6.0 kW induction heater, set to a frequency of 157 kHz and a current of 138 A. The reaction temperature was determined to be between 1070 and 1170 K, as measured by an optical pyrometer. The samples were cooled to room temperature by switching off the power to the induction heater. The tubes were opened within a glove box to extract the samples, which were stored under an inert atmosphere.

Other combinations of elements with various loading compositions Li_2MX, LiM_2X, and $LiMX_2$ (M = Fe, Co, Ni, Cu, Zn; X = Al, Ga, In) were also investigated. In general, most of these reactions tended to yield products that are grey and the targeted ternary phases were not obtained. Besides Li_2ZnGa and Li_2ZnIn, as well as the previously reported phases $LiCu_2Al$ and $LiCu_2Ga$,[21] the other coloured samples were "$LiFe_2Al$" and "$LiCo_2Al$," which were light yellow, but their extreme ductility made it difficult to grind them for further diffraction analysis.

2.2.2 Characterization

Energy-dispersive X-ray (EDX) analysis, which was performed on a Zeiss EVO scanning electron microscope, indicated a ratio of 1:1 for Zn:(Ga or In) for the Li_2ZnGa and Li_2ZnIn samples. To minimize surface oxidation, the samples were finely ground in an argon-filled glove box and mixed with mineral oil prior to powder X-ray diffraction (XRD) analysis, which was performed on a Bruker D8 Advance powder diffractometer, equipped with a SSD160 detector and a Cu K_α radiation source operated at 40 kV and 40 mA. The experimental XRD patterns were compared to simulated ones based on possible structural models using the program PowderCell

(version 2.4).[27] Pawley refinements were performed, with the background modeled by a twelve-term polynomial function, using the TOPAS Academic software package.[28]

Optical reflectance spectra were measured from 200 nm (6.2 eV) to 800 nm (1.5 eV) on an Agilent Cary 5000 UV-vis-NIR spectrophotometer equipped with a reflectance accessory. The spectra for Li_2ZnGa and Li_2ZnIn were compared with those of elemental gold (99.999%, Materion) and several coloured Ag–Au–Cu alloys,[3] which were prepared by arc-melting reactions of the elements in appropriate ratios under an argon atmosphere in an Edmund Bühler MAM-1 arc melter. The spectra were normalized, with a compacted pellet of polytetrafluoroethylene used as a 100% reflectance standard. Chromaticity coordinates in the CIE 1931 colour space (with standard illuminant E) were extracted from the optical reflectance spectra.[29]

Solid-state ^{7}Li nuclear magnetic resonance (NMR) experiments were performed on a Bruker 500 MHz (B_0 = 11.75 T) Avance NEO NMR spectrometer, equipped with a 4-mm double resonance H-X magic angle spinning (MAS) probe. The samples were ground, diluted with dry silica (50% by mass), and packed into ZrO_2 rotors (4 mm o.d.) which were sealed with a Kel-F cap in an argon-filled glove box. The ^{7}Li MAS NMR spectra were acquired using a Bloch decay pulse sequence ($\gamma B_1/2\pi$ of 71 kHz), recycle delays of 2–120 s (optimized for each sample), 16–64 co-added transients, and a spinning frequency of 14 kHz. The NMR spectra were referenced to 0.0 ppm (1.0 M LiCl(aq) solution).

2.2.3 Electronic structure calculations

First-principles electronic structure calculations were carried out with the program Akai-KKR,[30] which uses the Korringa-Kohn-Rostoker Green function method combined with the local density approximation and the coherent potential approximation, suitable for treating the site

disorder of Zn and Ga or In atoms occurring in these compounds. The number of *k*-points in the first Brillouin zone was 400 and the condition for convergence was 1×10^{-6} eV for the total energy.

2.3 Results and discussion

Li_2ZnGa and Li_2ZnIn were prepared by high-frequency induction heating of the elements placed in niobium tubes. They are new ternary intermetallic phases in the Li–Zn–Ga and Li–Zn–In systems, for which no phase diagram information is known and only three other phases [$Li_{68}Zn_{16}Ga_{133}$ and $Li_{38}(Ga_xZn_{1-x})_{101}$ with complex cluster framework structures and $Li_2ZnGa_{3.2}$] have been previously reported.[31–33] Both compounds are coloured: Li_2ZnGa is purple, and Li_2ZnIn is light blue (Figure 2-1). When the samples were exposed to air, the colours degraded after one to two days, and the powder XRD patterns showed small additional peaks appearing after one week, likely an indication of oxidized products. Attempts to prepare Li_2ZnAl under the same conditions as above also resulted in a coloured sample that is light blue, but deleterious reactions with the niobium tube had occurred, as signalled by the detection of Nb from EDX analysis and the presence of Nb_3Al as a secondary phase.

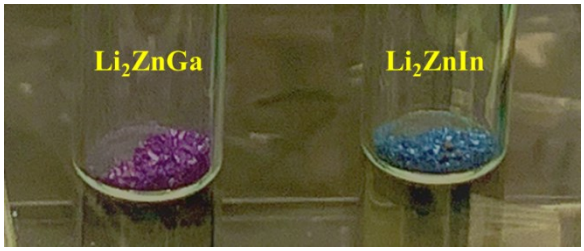

Figure 2-1. Samples of Li_2ZnGa and Li_2ZnIn.

Powder XRD patterns revealed the samples are nearly phase-pure (Figure 2-2). These simple patterns can be indexed to a face-centred cubic lattice. Based on the compositions of Li_2ZnGa and Li_2ZnIn, the most likely structural assignments are Cu_2MnAl-type (or full-Heusler)

in space group $Fm\bar{3}m$, Li_2AgSb-type (or inverse Heusler) in space group $F\bar{4}3m$, or NaTl-type in space group $Fd\bar{3}m$ (Figure 2-3). For the Cu_2MnAl-type model, the Li atoms could occupy the 8*c* sites exclusively, which leads to a simulated pattern (not shown) in severe disagreement with the experimental pattern, or they could be distributed over the 8*c* (disordered with Ga or In atoms) and 4*b* sites as shown (analogous to the structure reported for Li_2AgSn), which leads to a reversal in the relative intensities of the 111 and 220 peaks compared to the experimental pattern. The Li_2AgSb-type model, which assumes complete ordering of all atoms, gives a simulated pattern that seems to match reasonably well with the experimental pattern for Li_2ZnGa, but predicts a moderate 200 peak at 27° in 2θ which does not appear for Li_2ZnIn. Finally, the NaTl-type model invokes disorder of Zn with Ga or In atoms. It gives a nearly indistinguishable pattern from the Li_2AgSb-type model for Li_2ZnGa because Zn and Ga atoms have similar X-ray scattering factors, but agrees very well with the experimental pattern for Li_2ZnIn, for which Zn and In atoms can be differentiated. Pawley refinements of the powder XRD patterns gave satisfactory residuals (Figure A1-1).

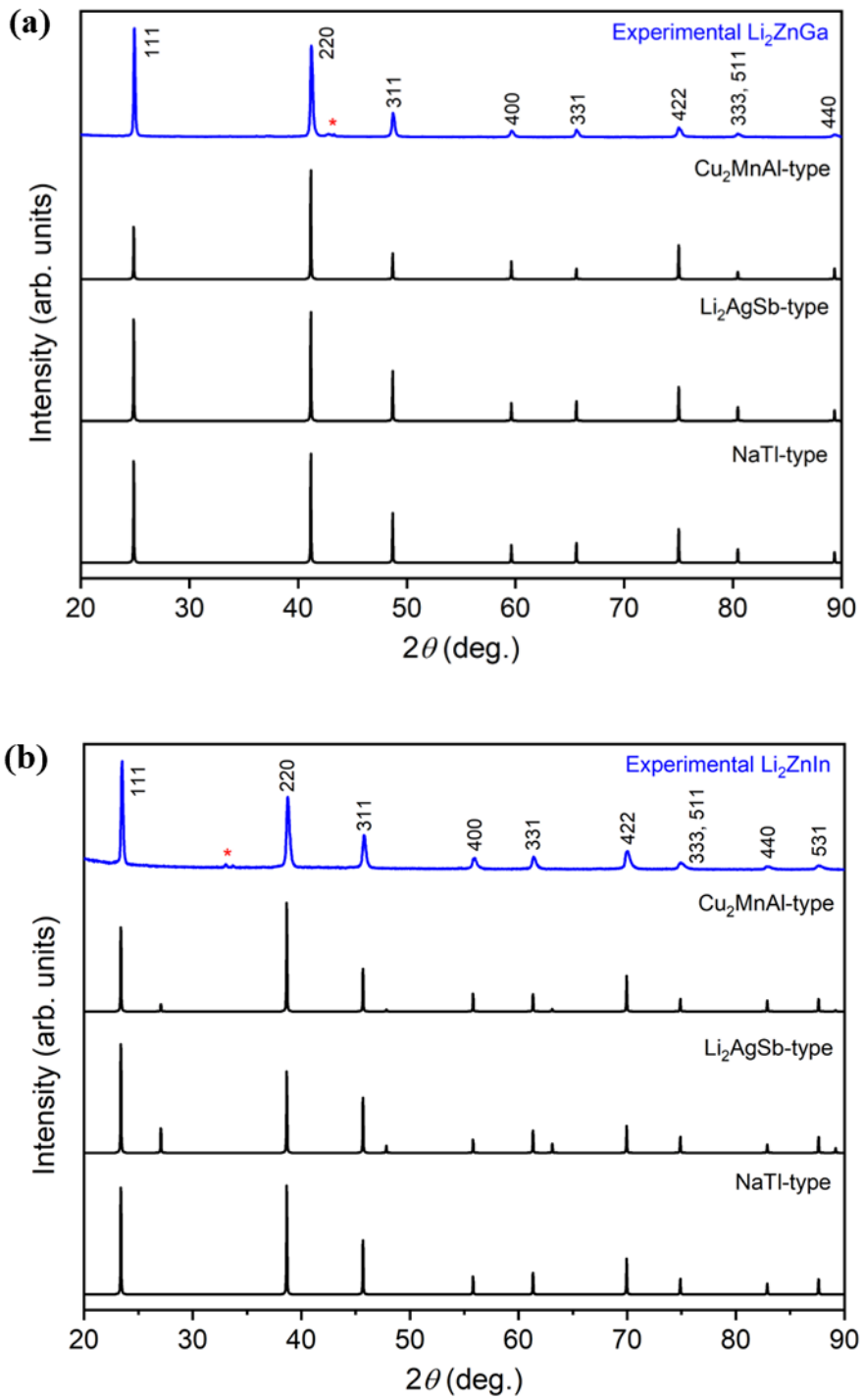

Figure 2-2. Experimental powder XRD patterns (blue) for (a) Li_2ZnGa and (b) Li_2ZnIn, compared with calculated patterns (black) based on possible structural models. The asterisks mark additional peaks arising from small amounts of impurities (Li_2O in the case of the Li_2ZnIn sample).

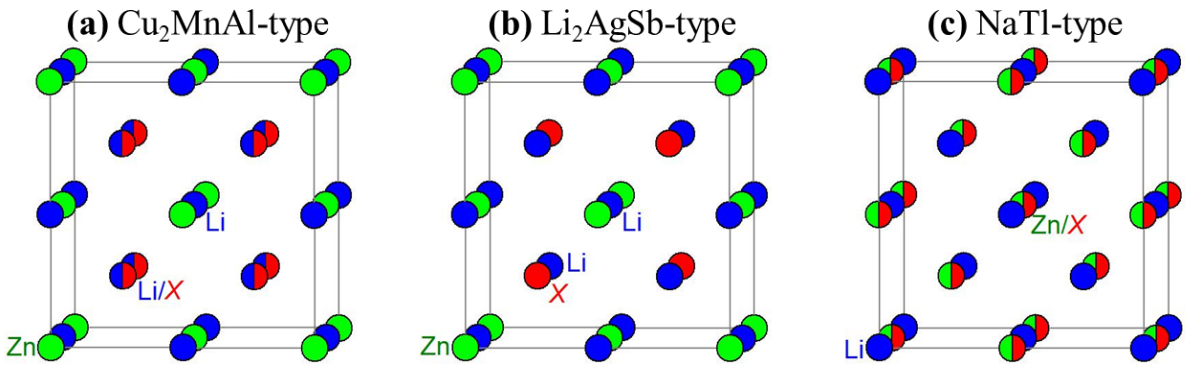

Figure 2-3. Structural models for Li_2ZnGa and Li_2ZnIn.

Crystal data are listed assuming the assignment of the NaTl-type structure (Table 2-1). The 8*a* sites at (0, 0, 0) are occupied by the Li atoms and the 8*b* sites at (½, ½, ½) are occupied by a disordered mixture of Zn and Ga or In atoms. [Equivalently, the assignment of these sites could be interchanged, or in an alternative setting, the origin of the unit cell could be shifted by (1/8, 1/8, 1/8) so that the 8*a* sites are at (1/8, 1/8, 1/8) and the 8*b* sites at (3/8, 3/8, 3/8).] A diamond-like substructure is formed by the Zn and Ga or In atoms, arranged in a framework of corner-sharing tetrahedra. Within this framework, the bond distances are 2.684 Å in Li_2ZnGa or 2.851 Å in Li_2ZnIn. Comparison to the sum of metallic radii (Zn, 1.31 Å; Ga, 1.26 Å; In, 1.44 Å)[34] suggests that both homoatomic and heteroatomic contacts are possible in Li_2ZnGa, whereas In–In contacts are probably less likely in Li_2ZnIn. The NaTl-type structure formed by Li_2ZnGa and Li_2ZnIn is a reasonable result given that it is also adopted by the binary compounds LiZn, LiGa, and LiIn.[35] Moreover, the similar sizes and electronegativities of Zn, Ga, and In atoms suggest that solid solutions $Li_2(Zn_{1-x}Ga_x)_2$ and $Li_2(Zn_{1-x}In_x)_2$ may be possible.

Table 2-1. Crystallographic data for Li_2ZnGa and Li_2ZnIn.

Crystal data		
formula	$LiZn_{0.5}Ga_{0.5}$	$LiZn_{0.5}In_{0.5}$
formula mass (amu)	74.50	97.04
space group	$Fd\bar{3}m$ (No. 227)	$Fd\bar{3}m$ (No. 227)
a (Å)	6.1978(3)	6.5833(4)
V (Å^3)	238.1(3)	285.3(5)
Z	8	8
ρ_{calcd} (g cm^{-3})	4.16	4.52
Site occupations		
8*a* (0, 0, 0)	1.0 Li	1.0 Li
8*b* (½, ½, ½)	0.5 Zn, 0.5 Ga	0.5 Zn, 0.5 In

The ^{7}Li MAS NMR spectra were collected for Li_2ZnGa and Li_2ZnIn, as well as a commercial sample of Li_2O (Figure 2-4). The ^{7}Li MAS NMR spectrum for Li_2ZnGa exhibits a dominant resonance with a centre-of-gravity chemical shift (δ_{cgs}) of 28.9 ppm and a full-width-half-maximum (fwhm) of 6 kHz, consistent with the occupation of a single site in the crystal structure. The ^{7}Li MAS NMR spectrum of Li_2ZnIn is shifted to a lower frequency with a δ_{cgs} of 18.0 ppm and a fwhm of 2.3 kHz. Both spectra contain a resonance located at ~2.8 ppm, which is attributed to Li_2O present as an impurity phase. This impurity has been tracked to the gradual oxidation of the parent phases, whereby Li_2O forms as an oxidation product when the samples are handled outside of an inert atmosphere, as confirmed by powder XRD patterns collected immediately after the NMR measurements (Figure A1-2). The chemical shifts for Li_2ZnGa and Li_2ZnIn are found at higher frequency than typical values for ionic compounds of Li (~0 ppm), while appearing well below that for Li metal (~260 ppm), implying that there is some influence from paramagnetic hyperfine interactions in these compounds.[21,36–40] The resonances do narrow

under MAS (attenuation of the dipolar interaction) and the residual breadth is inconsistent with second order quadrupolar broadening (due to the small ^{7}Li quadrupolar moment).[41] One possible explanation is that the Li atoms experience a randomly disordered local chemical environment within the crystal structure (such as mixing of Zn with In or Ga atoms), while electron-nuclear dipolar interactions, Knight shift contributions, and crystallite size can further contribute to this observed broadening.[36] Unfortunately, further insight was not possible because of the associated challenges in maintaining stable fast sample spinning at the magic angle and preventing sample degradation through oxidation.

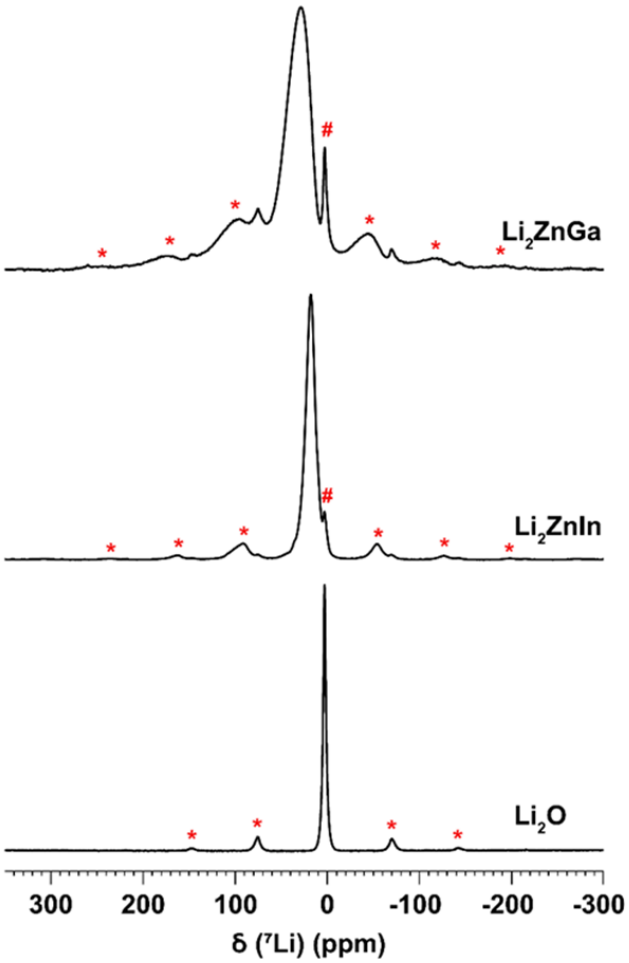

Figure 2-4. ^{7}Li MAS NMR spectra of Li_2ZnGa (top), Li_2ZnIn (middle), and Li_2O (bottom). The asterisks (*) denote spinning sidebands, and the hash symbols (#) denote Li_2O oxidation impurities in the parent samples.

To characterize the colours of Li_2ZnGa and Li_2ZnIn on a more quantitative basis, optical reflectance spectra were measured on the as-prepared ingots and compared with high purity gold as a reference (Figure 2-5). For Li_2ZnGa, the reflectance is strongest in the red region and moderate in the blue region, accounting for its appearance as a non-spectral colour of purple (or perhaps magenta). For Li_2ZnIn, the reflectance is high in the blue region, and then gradually decreases on proceeding to longer wavelengths (lower energy), consistent with the appearance of a light blue colour. Chromaticity coordinates x and y were extracted from the spectra to map onto the CIE 1931 colour space (with standard illuminant E), with the colours of Li_2ZnGa and Li_2ZnIn compared to those of gold and various gold-containing alloys (Figure 2-6). Based on these coordinates, the colours of Li_2ZnGa ($x = 0.329$, $y = 0.309$) and Li_2ZnIn ($x = 0.309$, $y = 0.315$) lie in a similar region in the diagram, the latter being displaced toward a bluish hue, and are significantly different from those of Au ($x = 0.430$, $y = 0.405$) and coloured gold alloys. Note that small shifts in the CIE coordinates can lead to striking differences in visual perception of colours.

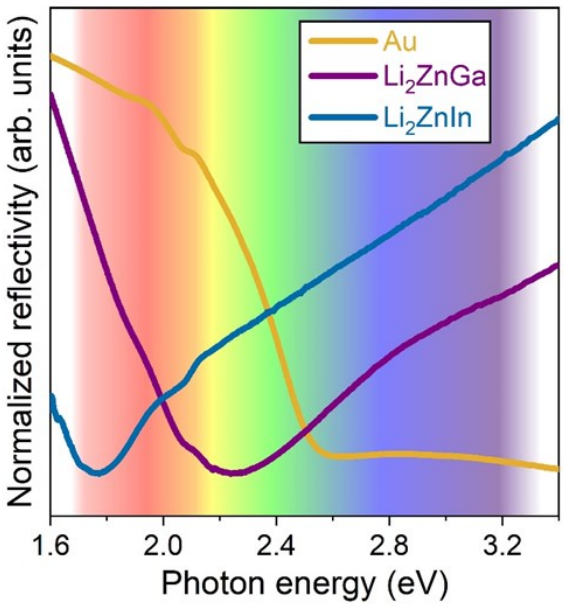

Figure 2-5. Optical reflectivity spectra for Li_2ZnGa, Li_2ZnIn, and high purity Au (99.999%).

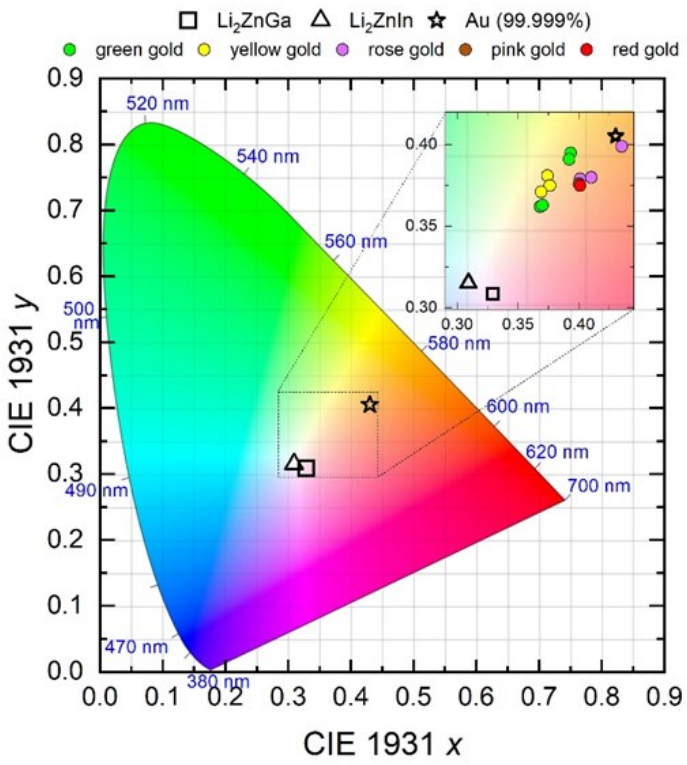

Figure 2-6. CIE 1931 coordinates for Li_2ZnGa, Li_2ZnIn, Au, and gold-containing alloys.

Electronic structure calculations were carried out on Li_2ZnGa and Li_2ZnIn, assuming disorder of Zn with Ga or In atoms. The density of states (DOS) curves are similar for these compounds, with no energy gap at the Fermi level, consistent with metallic behaviour for these compounds (Figure 2-7). A large narrow peak below –7 eV, derived from the filled 3d states of the Zn atoms, is superimposed on much more disperse bands extending to well above the Fermi level that result from mixing of Li 2s, Zn 4s/4p, and Ga 4s/4p (or In 5s/5p) states. There is a minimum in the DOS just above 1 eV, and it can be proposed that the electronic transitions responsible for the colour take place between the local maxima just below (–2 eV) and just above the Fermi level (2 eV). The electron counts for Li_2ZnGa and Li_2ZnIn [2(1) + 2 + 3 = 7 per formula unit] are typical of other ternary coloured intermetallic compounds Li–M–X (M = late transition metal; X = group 13 to 15 element).[1] If solid solutions $Li_2(Zn_{1-x}Ga_x)_2$ and $Li_2(Zn_{1-x}In_x)_2$ are

possible, increasing the Ga or In content would increase the electron count, raising the Fermi level so that it lies closer to the DOS minimum. Because the local maxima consist of contributions from all three elements, it is difficult to predict the effect on the resulting colour. However, preliminary experiments suggest that greater amounts of Ga in $Li_2(Zn_{1-x}Ga_x)_2$ or In in $Li_2(Zn_{1-x}In_x)_2$ shifts the colour to blue or lighter shades of blue.[42]

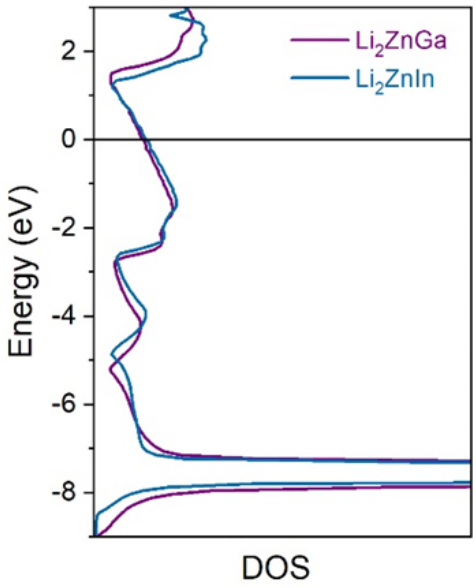

Figure 2-7. DOS curves for Li_2ZnGa and Li_2ZnIn.

2.4 Conclusions

Purple Li_2ZnGa and light blue Li_2ZnIn are new representatives of coloured intermetallic compounds, which are still relatively uncommon. The factors that determine the appearance of colour remain poorly understood, and more examples are needed to provide greater clarity. Toward this end, preparation of the solid solutions $Li_2(Zn_{1-x}Ga_x)_2$ and $Li_2(Zn_{1-x}In_x)_2$ would be helpful in revealing the effect of electron count. Preliminary results suggest that limited phase widths in these solid solutions are possible,[42] and further investigations are in progress to relate specific compositions to their colours.

2.5 References

(1) Steinemann, S. G.; Wolf, W.; Podloucky; R. *Color and optical properties*, in: J. H. Westbrook, R.L. Fleischer (Eds.), Intermetallic Compounds, Vol. 3, Principles and Practice, Wiley, New York, 2002, 231–244.

(2) Saeger, K. E.; Rodies; J. *Gold Bull*. **1977**, *10*, 10–14.

(3) Cretu, C.; van der Lingen, E. *Gold Bull*. **1999**, *32*,115–126.

(4) Corti, C. W.; Black, blue and purple! The special colours of gold, in: E. Bell (Ed.), The Santa Fe Symposium on Jewelry Manufacturing Technology, *Met-Chem. Research*, Albuquerque, 2004, 121–134.

(5) Hurly, J.; Wedepohl, P. T. *J. Mater. Sci*. **1993**, *28*, 5648–5653.

(6) van der Lingen, E. *J. South. Afr. Inst. Min. Metall.* **2014**, *114*, 137–144.

(7) Jeong, Y. B.; Kim, J. T.; S. Hong, H.; Lee, H. D.; Choi, S.Y.; Kim, K. B. *Mater. Des*. **2019**, *175*, 107814-1–107814-11.

(8) Cahn, R. W. *Nature* **1998**, *396*, 523–524.

(9) Keast, A. V. J.; Birt, K.; Koch, C. T.; Supansomboon, S.; Cortie, M. B. *Appl. Phys. Lett*. **2011**, *99*, 111908-1–111908-3.

(10) Furrer, A.; Seita, M.; Spolenak, R. *Acta Mater.* **2013**, *61*, 2874–2883.

(11) Eberz, U.; Seelentag, W.; Schuster, H.-U. *Z. Naturforsch*. *B* **1980**, *35*, 1341–1343.

(12) Supansomboon, S.; Maaroof, A.; Cortie; M. B. *Gold Bull*. **2008**, *41*, 296–304.

(13) Klotz; U. E. *Gold Bull.* **2010**, *43*, 4–10.

(14) Na, J. H.; Han, K. H.; Garrett, G. R.; Launey, M. E.; Demetriou, M. D.; Johnson, W. L. *Sci. Rep*. **2019**, *9*, 3269-1–3269-8.

(15) Mun, S. C.; Kang, G. C.; Jeong, Y. B.; Park, H. J.; Kim, Y. S.; Hong, S. H.; Song, G.; Kim, K. B. *Mater. Des.* **2021**, *200*, 109449-1–109449-8.

(16) Liu, J.; Liu, Y.; Gong, P.; Li, Y.; Moore, K. M.; Scanley, E.; Walker, F.; Broadbridge, C. C.; Schroers; J. *Gold Bull*. **2015**, *48*, 111–118.

(17) Blaber, M. G.; Arnold, M. D.; Ford, M. J. *J. Phys. Condens. Matter.* **2009**, *21*, 144211-1–144211-8.

(18) Drews, J.; Eberz, U.; Schuster, H.-U. *J. Less-Common Met.* **1986**, *116*, 271–278.

(19) Czybulka, A.; Petersen, A.; Schuster, H.-U. *J. Less-Common Met.* **1990.** *161*, 303–312.

(20) Dymtriv, G.; Pauly, H.; Ehrenberg, H.; Pavlyuk, V.; Vollmar, E. *J. Solid State Chem*. **2005**. *178*, 2825–2831.

(21) Mishra, V.; Iyer, A. K.; Mumbaraddi, D.; Oliynyk, A. O.; Zuber, G., Boucheron, A.; Dmytriv, G.; Bernard, G. M.; Michaelis, V. K.; Mar, A. *J. Solid State Chem*. **2020**, *292*, 121703.

(22) Schuster, H.-U.; Mewis, A. *Z. Naturforsch. B* **1969**, *24*, 1190.

(23) Mewis, A.; Schuster, H.-U. *Z. Naturforsch*. *B* **1971**, *26*, 62.

(24) Schuster, H.-U.; Thiedemann, D.; Schonemann, H. *Z. Anorg. Allg. Chem*. **1969**, *370*, 160–170.

(25) Fürtauer, S.; Effenberger, H. S.; Flandorfer, H. *J. Solid State Chem*. **2014**, *220*, 198–205.

(26) Schönemann, H.; Jacobs, H.; Schuster. H.-U. *Z. Anorg. Allg. Chem*. **1971**, *382*, 40–48.

(27) Kraus, W.; Nolze, G. *J. Appl. Crystallogr*. **1996**. *29*, 301–303.

(28) Coelho, A. A. *TOPAS-Academic, version 6, Coelho Software*, Brisbane, Australia, 2007.

(29) Hunt, R. W. G.; Pointer, M. R. Measuring Colour, 4th Ed., Wiley, Chichester, 2011.

(30) Long, N. H.; Akai, H. *J. Phys. Condens. Matter.* **2007**, *19*, 365232-1–365232-8.

(31) Tillard-Charbonnel, M.; Chahine, A.; Belin, C. *Mater. Res. Bull*. **1993**, *28*, 1285−1294.

(32) Tillard-Charbonnel, M.; Chouaibi, N.; Belin, C. *Eur. J. Solid State Inorg. Chem*. **1992**, *29*, 347−359.

(33) Kinzhibalo, V. V.; Mel'nyk, E. V.; Petrus, I. L. *Visn. L'viv. Derzh. Univ., Ser. Khim*. **1981**, *23*, 23−26.

(34) Pauling, L.; Kamb, B. *Proc. Natl. Acad. Sci. USA.* **1986**, *83*, 3569−3571.

(35) Villars, P.; Cenzual, K. *Pearson's Crystal Data – Crystal Structure Database for Inorganic Compounds*, (on DVD), Release 2021/22, ASM International, Materials Park, OH, USA.

(36) Bekaert, E.; Robert, F.; Lippens, P. E.; Menetrier, M. *J. Phys. Chem.* **2010**, *C114*, 6749−6754.

(37) Trease, N. M.; Zhou, L.; Chang, H. J.; Zhu, B. Y.; Grey, C. P. *Solid State Nucl. Magn. Reson*. **2012**, *42*, 62−70.

(38) Winter, F.; Dupke, S.; Eckert, H.; Rodewald, U. Ch.; Pöttgen, R. *Z. Anorg. Allg. Chem*. **2013**, *639*, 2790−2795.

(39) Dupke, S.; Eckert, H.; Winter, F.; Pöttgen, R. *Prog. Solid State Chem*. **2014**, *42*, 57−64.

(40) Hu, J. Z.; Zhao, Z.; Hu, M. Y.; Feng, J.; Deng, X.; Chen, X.; Xu, W.; Liu, J.; Zhang, J.-G. *J. Power Sources* **2016**, *304*, 51−59.

(41) Michaelis, V. K.; Levin, K.; Germanov, Y.; Lelong, G.; Kroeker, S. *Chem. Mater*. **2018**, *30*, 5521−5526.

(42) Dmytriv, G.; Pavlyuk, V.; Ehrenberg, H. *Unpublished results*.

Chapter 3.

True colours shining through: Determining site distributions in coloured Li-containing quaternary Heusler compounds

A version of this chapter has been published.

Jomaa, M.; Mishra, V.; Chaudhary, M.; Mumbaraddi, D.; Michaelis, V. K.; Mar, A. J. Solid State Chem. ***2022****, 314, 123372.*

3.1 Introduction

A prominent group of intermetallic compounds, called Heusler compounds, have long been investigated primarily as magnetic materials, as well as in newer applications such as thermoelectric materials, superconductors, topological insulators, and catalysts.[1,2] Less well appreciated is that some Heusler compounds exhibit colour in the visible region.[3–5] Of course, the attractive colours of metallic substances such as gold, copper, and its alloys are familiar and valued for coatings, decorations, and jewellery.[6–14] It is also possible to apply chemical and physical techniques, such as nanopatterning, to express different colours on metallic substances.[15–17] As in other surface modification approaches, the colour may be inhomogeneous or risks deterioration if the surface is physically damaged through environmental exposure. Thus, finding metallic materials that exhibit intrinsic chromatic colour (i.e., reflecting a predominant wavelength) would be valuable, but they are extremely rare. Among ternary or quaternary intermetallic compounds, only ~100 have been reported to be coloured, and most of them contain Li or Mg, or both, often in combination with a precious metal (Pd, Pt, Au).[3–5,18–20] Most Heusler compounds are ternary

phases with a composition of 1:1:1, corresponding to the half-Heusler structure (MgAgAs-type), or 2:1:1, corresponding to the full-Heusler (Cu_2MnAl-type) or inverse Heusler structure (Li_2AgSb-type, also called Hg_2CuTi-type in older literature).[1,2] Over 10^3 ternary Heusler compounds have now been synthesized, out of $>10^5$ combinations of three metallic components.[21] Quaternary Heusler compounds with a composition of 1:1:1:1 are also known, adopting the LiMgPdSn-type structure.[3,4,22–24] Here, the realm of possibilities has barely been scratched, with <30 equiatomic quaternary Heusler compounds assigned to this structure type characterized to date, out of $>10^6$ combinations of four metallic components.[21] The situation is complicated by the occurrence of substitutional disorder and vacancies, which leads to the formation of solid solutions, for example, between half- and full-Heusler end-members.[25]

Because the structures of Heusler compounds are relatively simple, all being derived by occupying sites within a cubic lattice (Figure 3-1(a)), it has become de rigueur to apply high-throughput density functional theory (DFT) calculations to propose new candidates, which are often touted as being "discovered" or "designed."[26–29] Indeed, the number of such hypothetical compounds far exceeds the number of Heusler compounds that have actually been synthesized. In our opinion, these types of computational studies are incomplete unless the predictions are experimentally tested, and it is premature to declare a compound to be "discovered" without confirmation by synthesis. Equally serious, the DFT calculations depend on structural models in which the site distribution of atoms is often assumed by analogy to existing compounds; if this assumption is incorrect or if alternative site distributions are not considered, the predictions about physical properties are suspect. Unfortunately, determining the site distributions in Heusler compounds by experimental methods is often fraught with ambiguity. For example, the powder X-ray diffraction (XRD) patterns for LiMgPdSn itself, which serves as the prototype structure for

quaternary Heusler compounds, are essentially indistinguishable among several models involving different site distributions as well as the possibility for disorder between Li and Mg atoms, or between Pd and Sn atoms (Figure 3-1(b)). With terminology borrowed from graph theory, this "colouring problem" of elucidating site preferences within a crystal structure is a pervasive theme in solid state chemistry.[30,31] Empirical guidelines and, more recently, machine-learning approaches have been applied to help solve this problem in ternary half-Heusler compounds, for which structural information is plentiful.[1,2,32] In contrast, hardly any experimental structural studies have been carried out in detail for quaternary Heusler compounds to allow generalizations to be formulated.

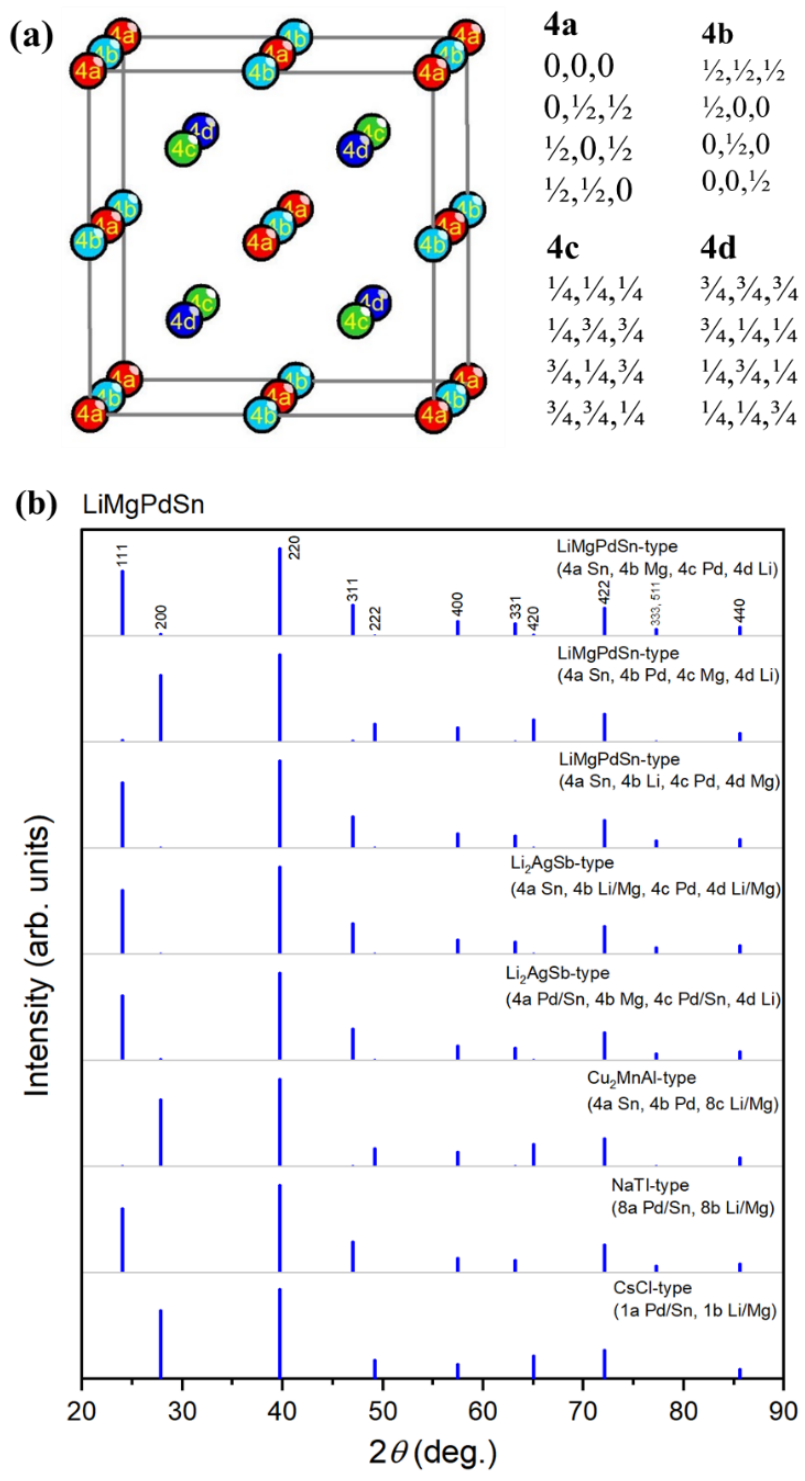

Figure 3-1. (a) Structures of most Heusler compounds are based on occupying sites within a cubic cell in space group $F\bar{4}3m$ (for LiMgPdSn-, Li_2AgSb-, and MgAgAs-type) or $Fm\bar{3}m$ (for Cu_2MnAl-type, with 4c and 4d merging into 8c). (b) Simulated powder XRD patterns for LiMgPdSn assuming different structural models.

This study has several objectives. First, we revisit the structures of LiMgPdSn and LiMgPtSn, which were among the earliest quaternary Heusler compounds reported. By applying ^{7}Li solid-state nuclear magnetic resonance (NMR) spectroscopy, we hope to clarify the site distributions in these compounds. Second, we wish to test some of the predictions obtained by high-throughput computations, which assert the existence of thermodynamically stable Li-containing quaternary Heusler compounds. Third, we embark on a general search for new Li-containing quaternary Heusler compounds that are coloured, preferably containing non-precious metals, with detailed characterization of the chromaticity coordinates extracted from optical reflectance measurements.

3.2 Experimental

3.2.1 Synthesis

Starting materials were Li ribbon (99.9%, Aldrich); Mg turnings (98%, Aldrich); various transition metals, including Pd powder (99.95%, Alfa Aesar), Pt sponge (99.9%, Aldrich), and Cd shot (99.95%, Alfa Aesar); and various p-block metals, including Ge pieces (99.999%, Alfa Aesar) and Sn powder (99.9%, Onyxmet). The Li ribbon was scraped to remove surface contaminants and cut into small pieces within an argon-filled glove box. Equimolar mixtures of Li, Mg, transition metal (M = Pd, Pt, Cd), and p-block metal (X = Ge, Sn) with a total mass of 400 mg were loaded into niobium tubes, which were welded shut in a Centorr 5TA triarc furnace on a water-cooled copper hearth under argon atmosphere. The niobium tubes were then placed within a 5-cm diameter copper coil in a water-cooled Ambrell EASYHEAT 560LI 6.0 kW induction heater where they were subjected to a frequency of 157 kHz and a current of 139 A for 15 min under argon atmosphere. The corresponding temperature was estimated to be between 800 and

900 °C using an optical pyrometer. The samples were cooled to room temperature by switching off the power to the induction heater. The niobium tubes were then placed within fused-silica tubes (12-mm diameter, 15-cm length), which were evacuated and sealed. They were placed within a furnace to undergo an annealing treatment at 600 °C for 7 d, followed by cooling to room temperature over 5 h. The niobium tubes were opened within a glove box, and the samples were stored under an inert atmosphere. Other combinations of elements (Li and Mg with transition metals Cr, Fe, Co, Ni, Cu, Ag, Zn and p-block metals or metalloids Al, Ga, In, Si, Ge, Sn, Pb, Sb) were also investigated. Most of these reactions led to samples that are grey-coloured and contained a mixture of phases without the desired quaternary Heusler compound.

3.2.2 Characterization

Energy-dispersive X-ray (EDX) analysis was performed on a Zeiss Sigma 300 VP field-emission scanning electron microscope, which was equipped with dual silicon drift detectors, or on a JEOL JSM-6010 LA InTouchScope scanning electron microscope, both operated with an accelerating voltage of 15 kV. Elemental compositions were determined on several points of multiple samples, with acquisition time of 60 s. Powder XRD patterns were collected on a Bruker D8 Advance powder diffractometer, equipped with a SSD160 detector and a Cu radiation source ($K\alpha_1$ = 1.54056 Å) operated at 40 kV and 40 mA. Samples were finely ground inside an argon-filled glove box and mixed with mineral oil to minimize surface oxidation. The powder XRD patterns were analyzed using the program PowderCell (version 2.4).[33] Optical reflectance spectra were measured from 200 nm (6.2 eV) to 800 nm (1.5 eV) on an Agilent Cary 5000 UV–vis–NIR spectrophotometer equipped with a reflectance accessory. A compacted pellet of polytetrafluoroethylene was used as a 100% reflectance standard. The spectra for the synthesized

samples were compared to that of elemental gold (99.999%, Materion). Chromaticity coordinates in the CIE 1931 colour space (with standard illuminant E) were extracted from the normalized optical reflectance spectra.[34]

^{7}Li NMR experiments were performed on either a Bruker 500 MHz (B_0 = 11.75) Avance NEO or a 400 MHz (B_0 = 9.4 T) Avance III HD NMR spectrometer, equipped with a 4-mm double resonance H-X magic angle spinning (MAS) probe. The samples were ground inside an argon-filled glove box, diluted with dry silica (50% by mass), and packed into ZrO_2 rotors (4-mm o.d.), which were sealed with a Kel-F cap. The ^{7}Li MAS NMR spectra were acquired using a Bloch decay pulse sequence with $\pi/2$ pulses optimized for each sample, under the conditions listed in (Table 3-1), with a spinning frequency of 14 kHz. The NMR spectra were referenced to 0.0 ppm for a 1.0 M LiCl(aq) solution. Data were processed with the TopSpin software package.

Table 3-1. Experimental conditions for acquisition of ^{7}Li NMR spectra

sample	LiMgPdSn	LiMgPtSn	LiMgPdGe	LiMgCdGe
B_0 (T)	9.4	9.4	9.4	11.75
$\pi/2$ pulse (μs)	3.0	3.5	3.1	2.0
recycle delay (s)	20	12	8	2
co-added transients	16	32	2048	256

3.2.3 Electronic structure calculations

The electronic band structure and density of states (DOS) were calculated on ordered models of the LiMg*MX* compounds using the projected augmented wave (PAW) method as implemented in the Vienna ab initio simulation package (VASP version 5.4.4), with the generalized gradient approximation parameterized by PBE to treat exchange and correlation.[35–38] The recommended standard PAW potentials (Li_sv, Mg, Ge_d, Sn_d, Cd, Pd, and Pt) were used,

with the plane-wave basis cutoff energy set to 650 eV. The first Brillouin zone was sampled by a 16 × 16 × 16 gamma-centred *k*-point grid. The convergence criteria were set to 10^{-8} eV for electronic optimization, and $|-2 \times 10^{-2}|$ eV for ionic relaxation.

3.3 Results and discussion

Quaternary equiatomic intermetallic compounds LiMgMX, where M is a transition metal and X is a p-block metal or metalloid, were targeted by reaction of the elements by high-frequency induction heating within niobium tubes, followed by annealing at 600 °C for 7 d. The results are summarized in Table 3-2. Most of these reactions yielded mixtures of known binary and ternary phases. Among known quaternary phases, LiMgPdSn and LiMgPtSn were successfully reproduced, but we were unable to obtain LiMgPdSb and LiMgPtSb, which were previously reported to form under similar heating conditions (reaction of the elements at 1030 °C for 0.5 h, followed by annealing at 630 °C but over a much shorter period of 6–20 h).[3,4] A possible explanation is that these antimonides may be metastable phases which do not survive prolonged heat treatment, which would favour thermodynamically stable phases. The new quaternary germanides LiMgPdGe and LiMgCdGe were discovered. All of these quaternary phases show visible colour: LiMgPdSn is red-violet, LiMgPtSn is red, LiMgPdGe is red-violet, and LiMgCdGe is light blue. It is noteworthy that LiMgCdGe is the first example of a coloured quaternary Heusler compound that does not involve a precious metal element (like Pd or Pt).

Table 3-2. Results of reactions targeting formation of LiMg*MX* (*M* = transition metal, rows; *X* = p-block metal or metalloid, columns) [a]

	Al	Ga	In	Si	Ge	Sn	Pb	Sb
Cr					–	–		
Fe						–		
Co	–	–	–	–	–	–	–	
Ni	–	–		–	–	–	–	
Pd				–	+	+	–	–
Pt				–	–	+	–	–
Cu	–	–	–	–	–	–	–	
Ag	–	–		–	–	–	–	
Zn	–	–		–	–	–	–	
Cd				–	+	–	–	

[a] Quaternary phase LiMg*MX* formed (+) or did not form (–). Blank entries indicate that the reaction was not attempted.

EDX analyses of these LiMgMX samples indicated the presence of 31–35% Mg, 30–34% M, and 29–36% X, in reasonable agreement with the equiatomic composition, but Li is undetectable by this technique. Powder XRD patterns revealed that the quaternary compounds were already formed after induction heating, but in the presence of secondary phases (Figure 3-2). After annealing, the samples became nearly phase pure. As indicated later by the NMR results, Li_2O is also present but in trace amounts not detectable in the powder XRD patterns. The blue colour of the LiMgCdGe sample becomes more apparent after the annealing treatment, which helps remove impurity phases. The patterns can be indexed to face-centred cubic lattices, for which cell parameters were refined (Table 3-3). If the site distribution reported for the LiMgPdSn-type structure,[3] is accepted at face value for these LiMgMX compounds (Li at 4d, Mg at 4b, M at 4c, X at 4a), then the experimental patterns are consistent with the simulated patterns. The calculated

intensity of the superlattice reflection 200, which appears near 28–29 in 2θ, is only about 1–2% that of the strongest principal reflection 220.[39,40] Although weak, this peak is unmistakeably detected in all experimental patterns except for LiMgPdSn, where it is barely visible above the background, if present. As indicated in the introduction, however, other structural models cannot be definitively ruled out in which the positions of the Li and Mg atoms are interchanged, or disorder is taking place. Even in a single-crystal structure determination, as was originally performed for LiMgPdSn, it would not be easy to exclude the possibility of Li–Mg disorder, especially given that the coordination geometries around all sites are similar.[3] The existence of a complete solid solution $Li_{2-x}Mg_xPdSn$ implies that such disorder is possible; however, the trend in cell parameters deviates from linearity and shows a break at the equiatomic composition.[4] Finally, inspection of bond lengths gives little guidance, because the typical interatomic distances for possible contacts among Li, Mg, Pd, and Sn atoms overlap within similar ranges of 2.7–3.2 Å.[21]

Table 3-3. Crystal data for LiMg*MX*, in space group $F\bar{4}3m$ (No. 216) with $Z = 4$

	LiMgPdSn	LiMgPtSn	LiMgPdGe	LiMgCdGe
formula mass (amu)	256.38	345.03	210.31	216.30
a (Å)	6.4118(3)	6.3682(4)	6.1682(1)	6.4160(1)
V (Å^3)	263.60(8)	258.26(12)	234.68(3)	264.12(3)
ρ_{calcd} (g cm^{-3})	6.46	8.87	5.95	5.44

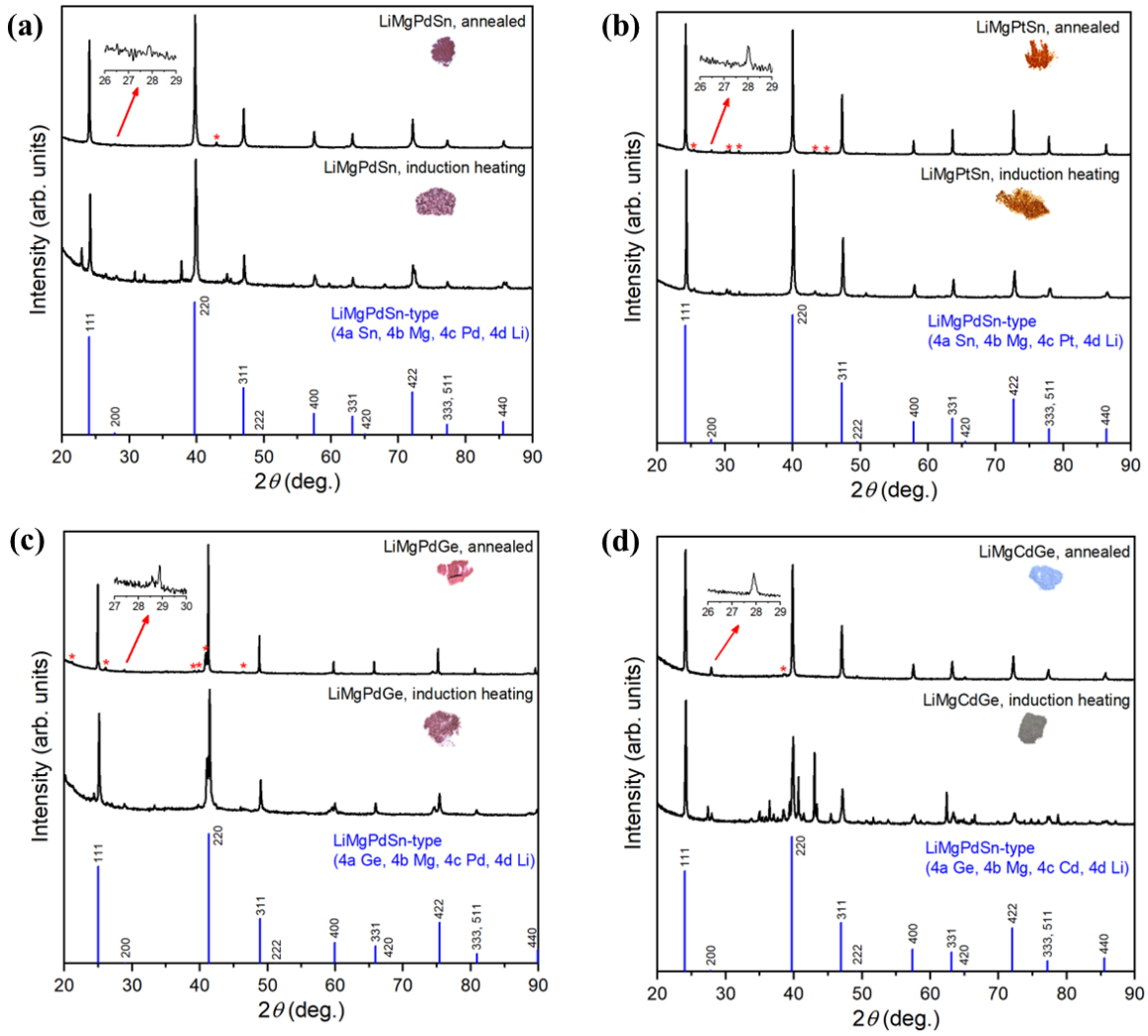

Figure 3-2. Powder XRD patterns for LiMgMX. The simulated patterns based on the previously reported site distribution for the LiMgPdSn-type structure (bottom) are compared with experimental patterns of samples after induction heating (middle) and annealing (top). Asterisks mark peaks belonging to secondary phases, including trace amounts of tin in the LiMgPtSn sample, but unidentified in the other samples.

To help resolve lingering doubts about the site distribution in LiMgPdSn and related compounds, ^{7}Li NMR spectra were collected. Although ^{7}Li is a quadrupolar nucleus (I = 3/2, natural abundance of 92.4%, Ξ = 38.9%), its small quadrupolar moment contributes virtually no second-order broadening to the central transition at high magnetic fields.[41] The breadths of ^{7}Li NMR peaks are often attributed to strong dipolar coupling which can be partially averaged under

the MAS conditions routinely applied. Hence, ^{7}Li behaves like a pseudo-half-spin system so that the NMR spectra are well resolved. The ^{7}Li NMR spectra show single resonances for LiMgPdSn (5.6 ppm, FWHM = 0.5 kHz), LiMgPtSn (28 ppm, FWHM = 1.5 kHz), and LiMgCdGe (7.7 ppm, FWHM = 0.06 kHz) (Figure 3-3(a)-3(c)). Trace amounts of Li_2O, presumably resulting from minor oxidation of the samples, were detected at 2.8 ppm; this impurity appears as a shoulder to the main resonance in LiMgPdSn. The peak for LiMgCdGe is narrow but asymmetrical; given its narrow linewidth of 60 Hz, the broadening at the low frequency site may be due to disorder within neighbouring sites (e.g., Cd and Ge within 4a and 4c), resulting in associated chemical shift changes in the environment of the parent Li atoms. Altogether, these results support the occurrence of a unique Li site in LiMgPdSn, LiMgPtSn, and LiMgCdGe. Note, however, that this can still be accommodated by several structural models. For example, in LiMgPdSn and LiMgPtSn, the Li and Mg sites could be interchanged, and disorder between Pd/Pt and Sn atoms cannot be ruled out (Figure 3-1(b)); similarly, in LiMgCdGe, disorder between Cd and Ge could still be occurring. The Gaussian broadening observed for some of the resonances could be explained by different degrees of this additional disorder.

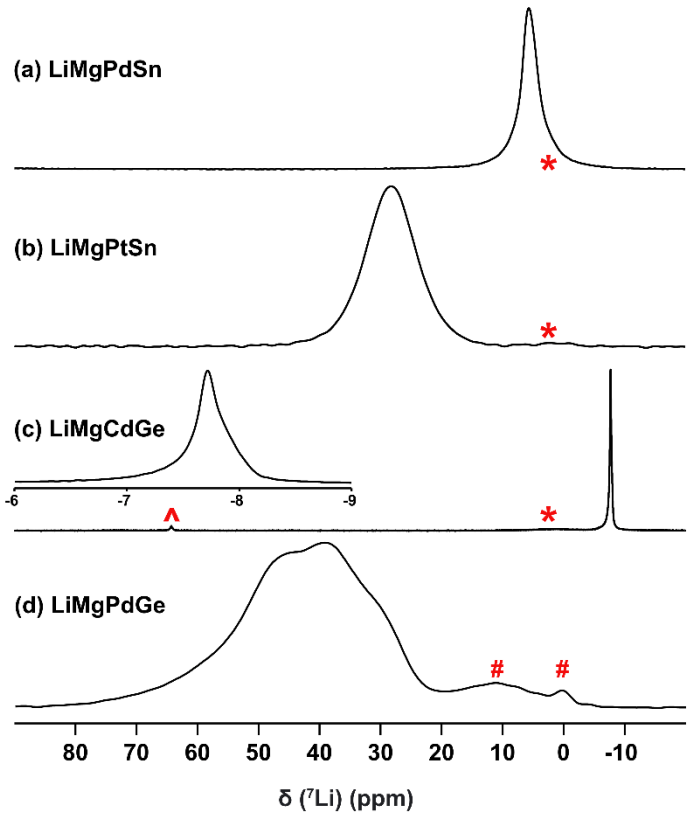

Figure 3-3. ^{7}Li MAS NMR spectra of LiMgMX compounds. The asterisks (*) mark peaks arising from trace amounts of Li_2O (<1%), the hash marks (#) mark unidentified impurities, and the caret (^) marks a first-order spinning sideband.

In contrast, the spectrum for LiMgPdGe shows three broad but distinguishable resonances at 47, 39, and 30 ppm, with a combined FWHM of 3.8 kHz (Figure 3-3(d)). Minor impurities account for the resonances between 20 and 0 ppm, likely binary or ternary phases, as well as an oxide phase near 0 ppm, consistent with the presence of small unassigned peaks seen in the powder XRD pattern (Figure 3-2(c)). These results indicate an atomic arrangement in which Li occupies more than one site. One possibility is a Li_2AgSb-type (inverse Heusler) structure in which Li and Mg atoms are disordered over two sites (4b and 4d), which would give a powder XRD pattern nearly indistinguishable from that of the ordered LiMgPdSn-type structure. The Li atoms in these two sites would experience different local environments in a cubic geometry, $Li@(Li_{0.5}Mg_{0.5})_4Pd_4$

and $Li@(Li_{0.5}Mg_{0.5})_4Ge_4$, and the random heterogenous distribution of surrounding Li and Mg atoms accounts for the considerably broadened ^{7}Li NMR resonances. We cannot rule out even more complex site distributions involving uneven occupation of the Li and Mg atoms within the 4b and 4d sites, or partial disorder of Pd and Ge atoms. It is interesting that the unit cell is significantly smaller for LiMgPdGe (a = 6.17 Å) compared to the other three compounds (a = 6.37–6.42 Å). We speculate that the disorder between Li and Mg atoms occurs here because of the inability to achieve optimal Li–Ge and Mg–Ge contacts in the alternative ordered structure.

Although the primary motivation for the present work was to search for coloured intermetallic compounds, the attempted preparation of these compounds serves as a test for recent reports that predict the existence of new quaternary Heusler compounds through machine learning and high-throughput DFT calculations.[26–29] In an initial study restricted to Li-containing candidates having an electron count of 18, a total of 99 candidates were predicted to be thermodynamically stable; none of these contained a combination of Li and Mg, so a comparison could not be made to our results.[26] In a similar subsequent study with no such restrictions applied, a total of 55 candidates were proposed, of which 43 are Li-containing.[27] Among these candidates, the first on the list is LiMgPtSn, which is not new, but rather one of the oldest known quaternary Heusler compounds,[3] whose synthesis was reproduced here. The new germanides LiMgPdGe and LiMgCdGe synthesized here were not among the proposed candidates, and represents a failure of the machine-learning model to predict true positives. Conversely, although "LiMgAgAl" was proposed to be stable, we were unable to prepare it, so this prediction appears to be a false positive. However, this does not preclude the possibility that the target compounds could be obtained as metastable phases through other synthetic routes that involve use of different precursors or heat treatments.

Of course, the compositions of the LiMgMX compounds prepared here were chosen precisely because they were chemically reasonable objectives, based on existing precedents (sometimes this commonsense approach is described in fancy terminology as a "strategy" or a "design"). As a fair test of the machine-learning model, it would be interesting to target less obvious candidates that are chemically distant from known compounds. For this purpose, by analogy to LiMgPtSn, the predicted compound "LiMgPtZn" was chosen for attempted synthesis because one would not normally expect isostructural compounds to be formed with Sn vs. Zn. (Disorder between Sn and Zn atoms has been observed in some intermetallic compounds, but this is not common.) Under the same conditions of induction heating and annealing as before, LiMgPtZn was successfully prepared as a new quaternary Heusler compound, as confirmed by its powder XRD pattern (Figure A2-1).

The intrinsic visible colours exhibited by LiMgPdSn, LiMgPtSn, LiMgPdGe, and LiMgCdGe are unusual, and they were further characterized by measuring optical reflectance spectra, referenced to elemental gold (Figure 3-4). LiMgPdSn and LiMgPdGe have similar profiles, with relatively sharp absorption edges near 2.3 eV. They reflect strongly in the red region, and slightly in the violet region, consistent with their appearance of red-violet. The absorption edge is shifted to higher energy, near 2.5 eV, for LiMgPtSn, so that the increased contribution of a yellow hue makes it appear light red. In contrast, the spectrum for LiMgCdGe is quite different, with strong reflectance in the blue to violet region. Accordingly, LiMgCdGe appears light blue. The normalized reflectance data were converted to chromaticity coordinates x and y mapped onto the CIE 1931 colour space, with standard illuminant E (Figure 3-5). LiMgPdSn, LiMgPdGe, and LiMgPtSn are clustered within the same general area of the colour space, whereas LiMgCdGe lies in the outlying blue area.

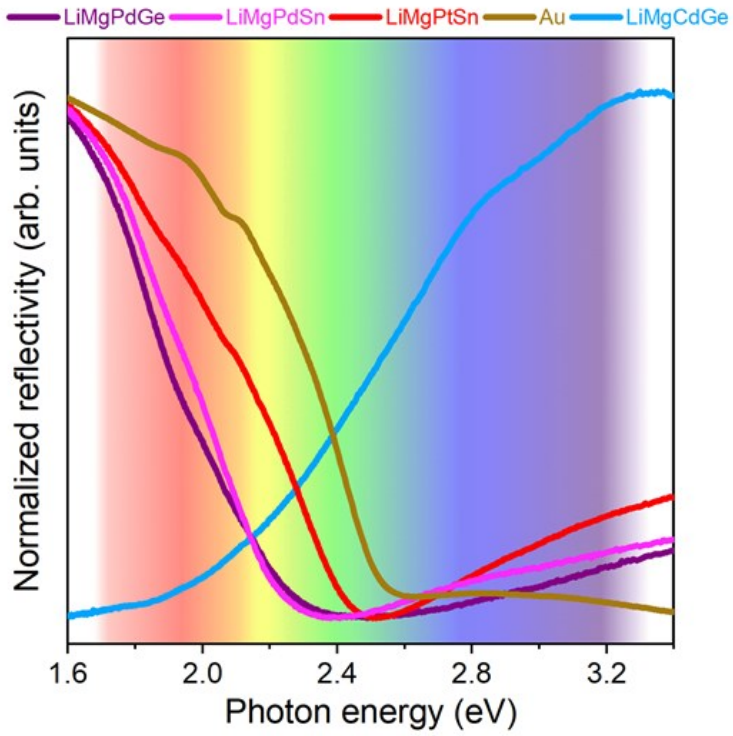

Figure 3-4. Optical reflectivity spectra for LiMgMX compounds and Au.

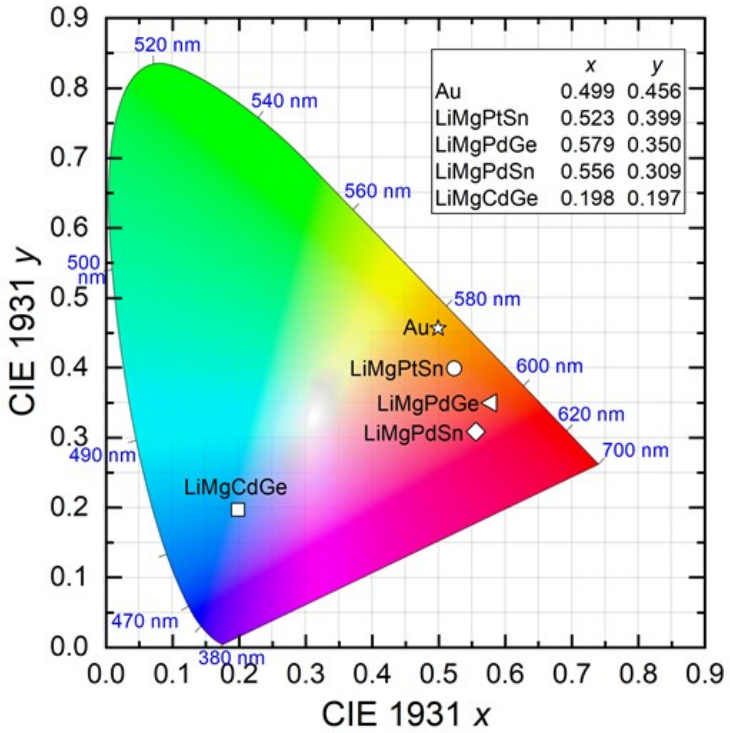

Figure 3-5. CIE 1931 coordinates for LiMgMX compounds and Au.

Electronic structure calculations were performed on ordered models of LiMgMX with Li in 4d, Mg in 4b, M in 4c, and X in 4a, in accordance with the reported site distribution of the LiMgPdSn-type structure.[3] The band dispersion and DOS curves are similar for LiMgPdSn, LiMgPtSn, and LiMgPdGe, which show a dense manifold of Pd 4d or Pt 5d states clustered around 3 to 4 eV, superimposed on very disperse bands formed by mixing Li 2s, Mg 3s, and Sn 5s/5p or Ge 4s/4p states (Figure 3-6(a)-6(c)). The continuous DOS curves, with no energy gap at the Fermi level, are typical of metallic substances. However, there is a shallow energy minimum located slightly higher in energy, near 1 eV. This feature is characteristic of other coloured intermetallic compounds, and a range of electronic transitions from filled to empty states (e.g., maximum near 2 eV) can be proposed to account for the red colours observed.

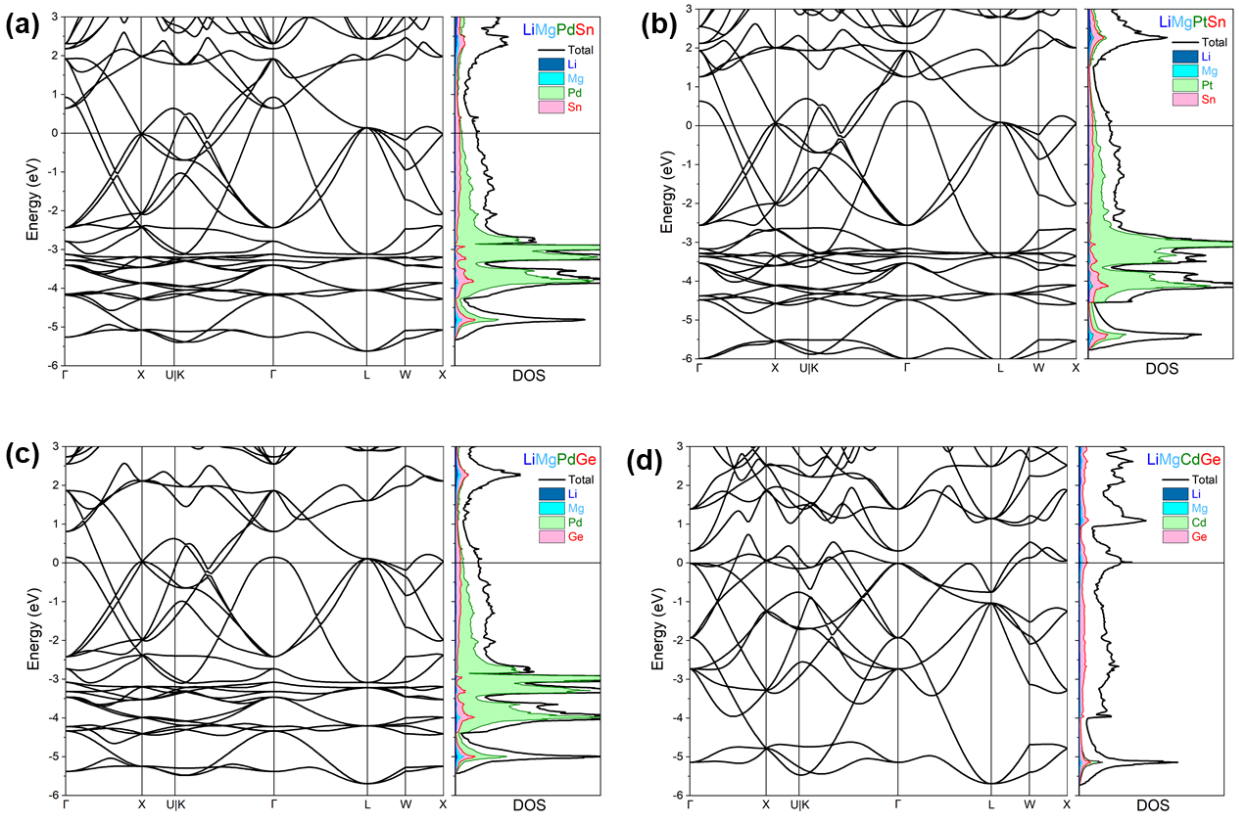

Figure 3-6. Electronic band structures and DOS plots for LiMgMX compounds, assuming ordered LiMgPdSn-type structures.

Recall that for LiMgPdSn and LiMgPtSn, the ^{7}Li NMR spectra suggest the presence of one Li site but the powder XRD patterns cannot distinguish between the possibilities of Li and Mg atoms being interchanged. Thus, the electronic calculations were repeated to determine the total energies of these two site distributions (Li in 4d and Mg in 4b, as in the reported structure of LiMgPdSn, vs. Li in 4b and Mg in 4d). In both cases, the site distribution with Li in 4d and Mg 4b was found to be more stable than the alternative, by 1.9 eV/cell for LiMgPdSn and 2.6 eV/cell for LiMgPtSn. In contrast, the energy difference is significantly smaller, about 1.1 eV/cell, for these two site distributions in LiMgPdGe, which would tend to favour disorder of Li and Mg atoms and which accounts for the observation of multiple Li sites seen in the ^{7}Li NMR spectra.

The electronic structure of LiMgCdGe, if it is assumed to have a similar site distribution as LiMgPdSn, shows clear differences from the other compounds. Although many bands remain the same, the Cd 5d states appear much lower in energy (at 9 eV, beyond the scale of the plot) and the Fermi level is raised relative to the other compounds because the Cd substitution increases the electron count (Figure 3-6(d)). The appearance of a local maximum in the DOS curve at the Fermi level is a signature of an electronic instability, indicating that LiMgCdGe may not have a strictly ordered site distribution. This result supports the interpretation from the ^{7}Li NMR spectra that although the Li atoms are likely occupying one site, disorder involving the other atoms may be occurring.

3.4 Conclusions

It was important to verify the site distribution for LiMgPdSn because it represents the parent structure type for equiatomic quaternary Heusler compounds, and any errors in the structure assignment could create unwelcome confusion in subsequent investigations. An ordered distribution with Li occupying one site (Li in 4d, Mg in 4b, Pd in 4a, Sn in 4c) is supported by the

combined results from powder XRD, ^{7}Li NMR spectroscopy, and electronic structure calculations. For LiMgPtSn, a similarly ordered site distribution can be confidently assigned, but for LiMgCdGe, the possibility of disorder between Cd and Ge atoms cannot be ruled out. In contrast, for LiMgPdGe, the evidence suggests that Li atoms occupy more than one site, likely disordering with Mg atoms in 4d and 4b. These results serve as an experimental test set for previous machine-learning models that predict the formation of ordered quaternary Heusler compounds. The performance is disappointing, given the occurrence of a false positive (LiMgAgAl was predicted to exist but could not be prepared) and two false negatives (LiMgPdGe and LiMgCdGe were not predicted to exist but could be prepared), but one true positive was subsequently found (LiMgPtZn was predicted and could be prepared). The attractive visible colours observed for LiMgPdSn, LiMgPtSn, LiMgPdGe, and LiMgCdGe show promise for finding other coloured intermetallics among quaternary Li-containing Heusler compounds.

3.5 References

(1) Graf, T.; Felser, C.; Parkin, S. S. P. *Prog. Solid State Chem*. **2011**, *39*, 1–50.

(2) Felser, C.; Hirohata, A. (Eds.). Heusler Alloys: Properties, Growth, Applications, Springer, Cham, Switzerland, 2016.

(3) Eberz, U.; Seelentag, W.; Schuster, H.-U. *Z. Naturforsch. B* **1980**, *35*, 1341–1343.

(4) Drews, J.; Eberz, U.; Schuster, H.-U. *J. Less Common Met*. **1986**, *116*, 271–278.

(5) Steinemann, S. G.; Wolf, W.; Podloucky, R. Color and optical properties, in: Westbrook, J. H.; Fleischer, R. L. (Eds.), *Intermetallic Compounds, Principles and Practice*, vol. 3, Wiley, New York, 2002, 231–244.

(6) Cretu, C.; van der Lingen, E. *Gold Bull*. **1999**, *32*, 115–126.

(7) Klotz, U. E. *Gold Bull*. **2010**, *43*, 4–10.

(8) Supansomboon, S.; Dowd, A.; van der Lingen, E.; Keast, V. J.; Cortie, M. B. *Mater. Forum* **2013**, *37*, 1–6.

(9) van der Lingen, E. *J. South. Afr. Inst. Min. Metall*. **2014**, *114*, 137–144.

(10) Liu, J.; Liu, Y.; Gong, P.; Li, Y.; Moore, K. M.; Scanley, E.; Walker, F.; Broadbridge, C. C.; Schroers, J. *Gold Bull*. **2015**, *48*, 111–118.

(11) Jeong, Y. B.; Kim, J. T.; Hong, S. H.; Lee, H. D.; Choi, S. Y.; Kim, K. B. *Mater. Des*. **2019**, *175*, 107814-1–107814-11.

(12) Prandini, G.; Rignanese, G.-M.; Marzari, N. *npj. Comput. Mater*. **2019**, *5*, 129-1–129-12.

(13) Mecking, O. *J. Archaeol. Sci*. **2020**, *121*, 105199-1–105199-16.

(14) Hong, S. H.; Mun, S. C.; Kang, G. C.; Park, H. J.; Jeong, Y. B.; Song, G.; Ki, K. B. *Prog. Mater. Sci*. **2022**, *123*, 100811-1–108111-18.

(15) Seo, M.; Lee; M. *Acta Mater*. **2018**, *159*, 1–7.

(16) Na, J. H.; Han, K. H.; Garrett, G. R.; Launey, M. E.; Demetriou, M. D.; Johnson, W. L. *Sci. Rep*. **2019**, *9*, 3269-1–3269-8.

(17) Mun, S. C.; Kang, G. C.; Jeong, Y. B.; Park, H. J.; Kim, Y. S.; Hong, S. H.; Song, G.; Kim, K. B. *Mater. Des*. **2021**, *200*, 109449-1–109449-8.

(18) Heletta, L.; Stein, S.; Pottgen, R. *Z. Naturforsch*. *B* **2018**, *73*, 739–747.

(19) Mishra, V.; Iyer, A. K.; Mumbaraddi, D.; Oliynyk, A. O.; Zuber, G.; Boucheron, A.; Dmytriv, G.; Bernard, G. M.; Michaelis, V. K.; Mar, A. *J. Solid State Chem*. **2020**, *292*, 121703-1–121703-5.

(20) Jomaa, M.; Mishra, V.; Mumbaraddi, D.; Chaudhary, M.; Dmytriv, G.; Michaelis, V. K.; Mar, A. *J. Solid State Chem*. **2022**, *306*, 122792.

(21) Villars, P.; Cenzual, K. *Pearson's Crystal Data – Crystal Structure Database for Inorganic Compounds*, (On DVD), Release 2021/22, ASM International, Materials Park, OH, USA.

(22) Özdoğan, K.; Şaşıoğlu, E.; Galanakis, I. *J. Appl. Phys*. **2013**, *113*, 193903-1–193903-5.

(23) Bainsla, L.; Suresh, K. G. *Appl. Phys. Rev*. **2016**, *3*, 031101-1–031101-21.

(24) Barman, C. K.; Mondal, C.; Pathak, B.; Alam, A. *Phys. Rev*. *B* **2019**, *99*, 045144-1–045144-6.

(25) Gzyl, A. S.; Oliynyk, A. O.; Mar, A. *Cryst. Growth Des*. **2020**, *20*, 6469–6477.

(26) He, J.; Naghavi, S. S.; Hegde, V. I.; Amsler, M.; Wolverton, C. *Chem. Mater*. **2018**, *30*, 4978–4985.

(27) Kim, K.; Ward, L.; He, J.; Krishna, A.; Agrawal, A.; Wolverton, C. *Phys. Rev*. *B* **2018**, *2*, 123801-1–123801-9.

(28) Gao, Q.; Opahle, I.; Zhang, H. *Phys. Rev. Mater*. **2019**, *3*, 024410-1–024410-12.

(29) Jiang, S.; Yang, K. *J. Alloys Compd*. **2021**, *867*, 158854-1–158854-14.

(30) Burdett, J. K.; Lee, S. L.; McLarnan, T. J. *J. Am. Chem. Soc*. **1985**, *107*, 3083–3089.

(31) Miller, G. J. *Eur. J. Inorg. Chem*. **1998**, 523–526.

(32) Gzyl, A. S.; Oliynyk, A. O.; Adutwum, L. A.; Mar, A. *Inorg. Chem*. **2019**, *58*, 9280–9289.

(33) Kraus, W.; Nolze, G. *J. Appl. Crystallogr*. **1996**, *29*, 301–303.

(34) Hunt, R. W. G.; Pointer, M. R. *Measuring Colour*, 4th ed., Wiley, Chichester, 2011.

(35) Kresse, G.; Furthmüller, J. *Phys. Rev*. *B* **1996**, *54*, 11169–11186.

(36) Kresse, G.; Joubert, D. *Phys. Rev*. *B* **1999**, *59*, 1758–1775.

(37) Blochl, P. E. *Phys. Rev*. *B* **1994**, *50*, 17953–17979.

(38) Perdew, J. P.; Burke, K.; Ernzerhof, M. *Phys. Rev. Lett*. **1996**, *77*, 3865–3868.

(39) Webster, P. J. *Contemp. Phys*. **1969**, *10*, 559–577.

(40) Webster, P. J.; Ziebeck, K. R. A. *J. Phys. Chem. Solid* **1973**, *34*, 1647–1654.

(41) Michaelis, V. K.; Levin, K.; Germanov, Y.; Lelong, G.; Kroeker, S. *Chem. Mater*. **2018**, *30*, 5521–5526.

Chapter 4.

Investigating the Phase Behaviours and Optical Properties of $LiCu_2Al_{1-x}Ga_x$ and $LiCu_{2-y}Ni_yGa$ Solid Solutions

Manuscript in preparation.

Jomaa, M.; Mumbaraddi, D.; Mishra, V.; Chaudhary, M.; Mah, B.; Delaruelle, D.; Michaelis, V. K.; Mar, A.

4.1 Introduction

The appearance of colour in metallic substances is highly prized and appealing for many applications such as consumer electronics, art, decoration, and interior design.[1–5] The colour can be expressed by surface modification through oxidization, anodization, nitrogen coating, and nanopatterning,[6–10] or by coating with thin layers of pigments.[11] Although these routes can overlay various chromatic colours, they present some limitations, such as poor resistance to light and weather, resulting in fading and physical degradation of the colour, as well as colour inhomogeneity.[2,12,13] Therefore, metallic substances that exhibit intrinsic colour would be valuable, but they remain unusually rare. Coloured intermetallics typically contain precious metals, such as $AuAl_2$, Li_2AuIn, $LiPtGa_2$, and LiMgPdSb.[14–17] Recently we have initiated the search for analogous compounds that are coloured but contain less expensive metals, including Li_2ZnGa, Li_2ZnIn, LiMgCdGe, $LiCu_2Al$, and $LiCu_2Ga$.[18–20] They are based on cubic structures that may differ in atomic site distributions. For example, red $LiCu_2Al$ adopts the CsCl-type and yellow $LiCu_2Ga$ adopts the Cu_2MnAl-type (full Heusler) structure.

To control the colour on a finer level, we hypothesize that a solid solution between two coloured end-members such as $LiCu_2Al$ and $LiCu_2Ga$ may produce a range of colours. It seems reasonable to expect that there will be a high degree of solid solubility in $LiCu_2Al_{1-x}Ga_x$, given that Al and Ga differ in atomic size by less than 4% and their electronegativities are comparable (Pauling electronegativities of 1.6 for Al and 1.8 for Ga), in accordance with the classical Hume-Rothery rules. However, because $LiCu_2Al$ and $LiCu_2Ga$ have different structures, a phase transition may be anticipated at some point. Other substitutions, such as Cu with Ni or Zn, may also be expected to shift the absorption edge or change the degree of reflectivity. These investigations were performed here, with characterization by powder X-ray diffraction (XRD), ^7Li solid-state nuclear magnetic resonance (NMR) spectroscopy, and optical reflectance measurements. Electronic structures were also calculated to understand the origin of colour in these compounds.

4.2 Experimental

4.2.1 Synthesis

Starting materials were Li ribbon (99.9%, Aldrich), Cu shot (99.5%, Alfa Aesar), Ni powder (99.9%, Cerac), Al powder (99.97%, Cerac), and Ga ingot (99.99%, Alfa Aesar). The Li ribbon was handled and cut within an argon-filled glove box, and its surface was scraped to remove surface contaminants prior to use. Members of the solid solutions $LiCu_2Al_{1-x}Ga_x$ and $LiCu_{2-y}Ni_yGa$ were prepared from mixtures of Li, Cu, Al or Ni, and Ga combined in appropriate molar ratios with a total mass of 200 mg, which were then placed within niobium tubes. The tubes were welded shut in a Centorr 5TA tri-arc furnace on a water-cooled copper hearth under argon atmosphere. The samples were heated for 15 min under argon atmosphere within a copper coil (5-cm diameter) of a water-cooled Ambrell EASYHEAT 560LI 6.0 kW induction heater, set to a

frequency of 157 kHz and a current of 139 A. The reaction temperature was determined to be between 800 and 900 °C, as measured by an optical pyrometer. The samples were allowed to cool to room temperature by switching off the power. The tubes were opened inside the glove box to extract the samples, which were stored under inert atmosphere. Attempts were also made to prepare the solid solutions $LiCu_{2-y}Ni_yAl$, $LiCu_{2-y}Zn_yAl$, and $LiCu_{2-y}Zn_yGa$ following the same procedure as above, but they were unsuccessful, resulting in mixtures of phases.

4.2.2 Characterization

Energy-dispersive X-ray (EDX) analysis, which was performed on a Zeiss EVO scanning electron microscope, confirmed the presence of all elements (except for Li, whose characteristic X-ray emission lines are too low in energy to detect) within members of the solid solutions $LiCu_2Al_{1-x}Ga_x$ and $LiCu_{2-y}Ni_yGa$ (Table A3-1). The compositions agree well with expectations, taking into account that the precision is affected by overlapping emission peaks for Cu, Ni, and Ga atoms.

Samples which were ground inside a glove box and mixed with mineral oil as a precaution against surface oxidation. Powder XRD patterns were collected on a Bruker D8 Advance powder diffractometer, equipped with a SSD160 detector and a Cu Kα radiation source operated at 40 kV and 40 mA. The experimental XRD patterns were analyzed with use of the TOPAS Academic software package and PowderCell (version 2.4).[21,22] The background was modeled by a twelve-term polynomial function and Pawley fittings were applied for all samples of $LiCu_2Al_{1-x}Ga_x$ and $LiCu_{2-y}Ni_yGa$ (Figure A3-2 and Figure A3-3).

Optical reflectance spectra were measured from 200 nm (6.2 eV) to 800 nm (1.5 eV) on an Agilent Cary 5000 UV-vis-NIR spectrophotometer equipped with a reflectance accessory. The

spectra for $LiCu_2Al_{1-x}Ga_x$ and $LiCu_{2-y}Ni_yGa$ were compared with that of elemental gold (99.999%, Materion). The optical reflectance spectra were normalized using a compacted pellet of polytetrafluoroethylene as a 100% reflectance standard. The chromaticity x and y coordinates in the CIE 1931 colour space, using standard illuminant E, were obtained from the normalized spectra.

Solid-state ^{7}Li nuclear magnetic resonance (NMR) experiments were performed on a Bruker 500 MHz (B_0 = 11.75) Avance NEO NMR spectrometer, equipped with a 4-mm double resonance H-X magic angle spinning (MAS) probe. The samples were ground, diluted with 50% (by mass) of dry silica, and packed into ZrO_2 rotors (4-mm o.d.) which were sealed with a Kel-F cap in an argon-filled glove box. All the spectra were acquired using a Bloch decay pulse sequence with pulses of 2 μs (optimized π/2 pulse of 4 μs for solution), recycle delays of 2–4 s, and a spinning frequency of 14 kHz for 256 scans. The spectra were referenced to the ^{7}Li peak, set to 0.0 ppm, for a 1.0-M LiCl(aq) solution, and they were processed with the TopSpin software package.

4.2.3 Electronic structure calculations

Electronic structure calculations were performed using the projected augmented wave (PAW) method as implemented in Vienna Ab initio Simulation Package (VASP).[23] The generalized gradient approximation, as parameterized by Perdew, Burke, and Ernzerhof, was used to treat exchange and correlation.[24] Three random 2 × 2 × 2 supercells were created to treat the disorder for $LiCu_2Al_{1-x}Ga_x$ (x = 0, 0.5, 1) and $LiCu_{2-y}Ni_yGa$ (x = 0.5, 1). Standard PAW potentials (Li_sv, Al, Ni, Cu, and Ga_d) were used, with the plane-wave basis cutoff energy set to 650 eV. The convergence criteria were set to 10^{-8} eV for electronic optimization and -2×10^{-2} eV for ionic relaxation. The density of states (DOS) was calculated by sampling the first Brillouin zone with

an 8 × 8 × 8 k-mesh for $LiCu_2Al$, a 17 × 17 × 17 k-mesh for $LiCu_2Ga$, and a 4 × 4 × 4 k-mesh for $LiCu_{2-y}Ni_yGa$ (x = 0.5, 1) and $LiCu_2Al_{0.5}Ga_{0.5}$.

4.3 Results and discussion

4.3.1 Structure

Powder XRD patterns for the solid solution $LiCu_2Al_{1-x}Ga_x$ and $LiCu_{2-y}Ni_yGa$ were analyzed (Figure 4-1(a)). All samples were single-phase. By considering simulated patterns for possible models (Figure A3-1), the structures could be assigned (Figure 4-2 and Table 4-1).

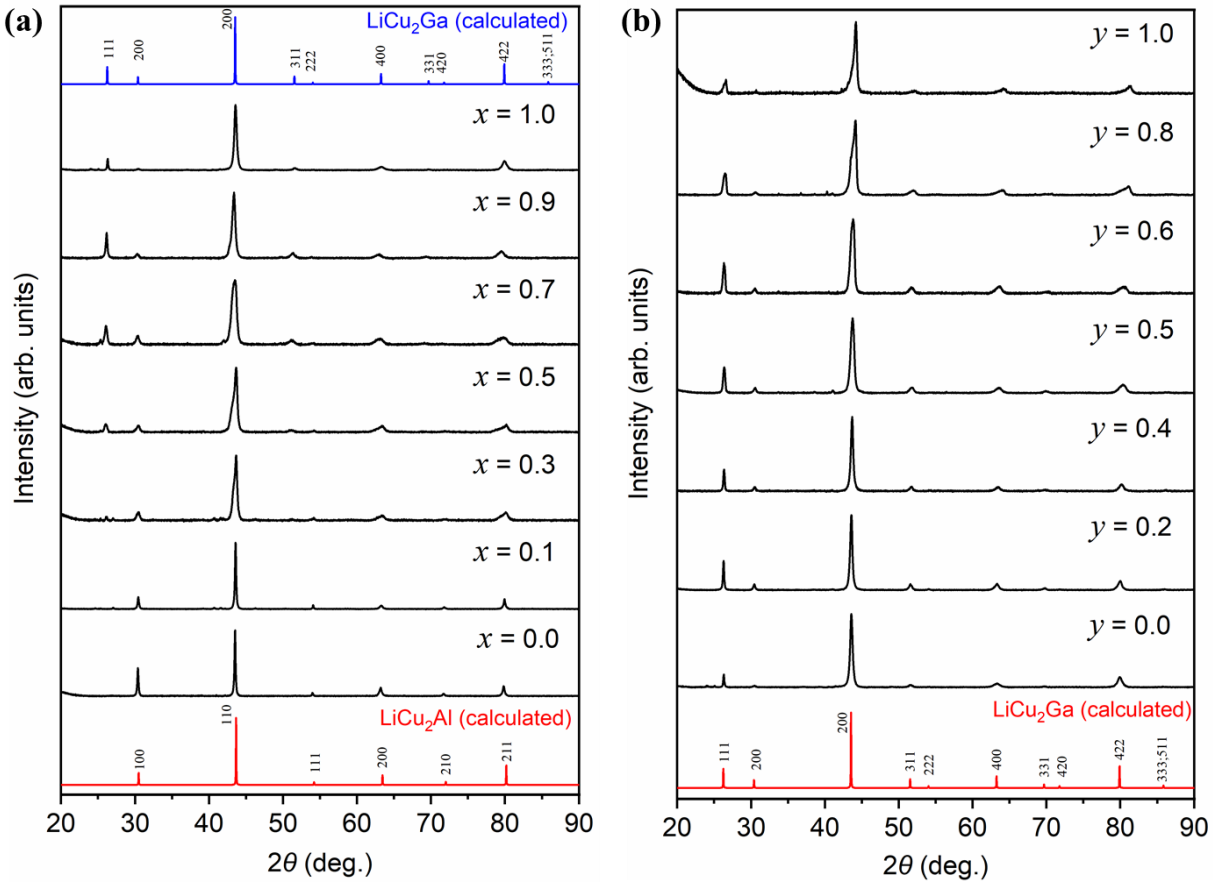

Figure 4-1. Powder XRD patterns for (a) $LiCu_2Al_{1-x}Ga_x$ and (b) $LiCu_{2-y}Ni_yGa$ solid solutions.

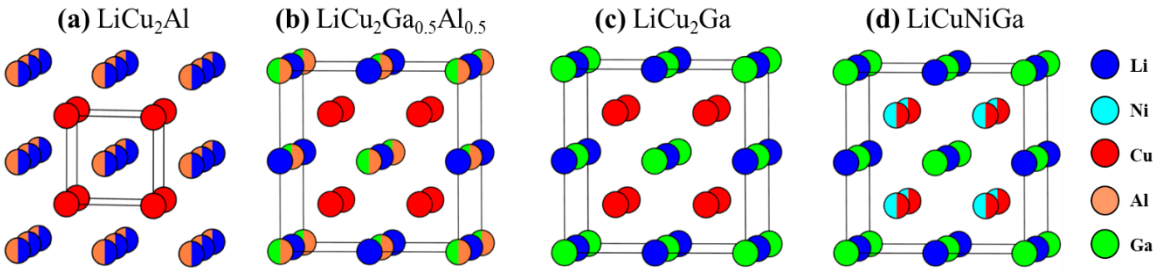

Figure 4-2. Structural models for $LiCu_2Al$, $LiCu_2Al_{0.5}Ga_{0.5}$, $LiCu_2Ga$, LiCuNiGa.

Table 4-2. Crystallographic data for $LiCu_2Al$, $LiCu_2Ga_{0.5}Al_{0.5}$, $LiCu_2Ga$, and LiCuNiGa.

Crystal data				
Formula	$Li_{0.5}CuAl_{0.5}$	$LiCu_2Al_{0.5}Ga_{0.5}$	$LiCu_2Ga$	LiCuNiGa
Formula mass (amu)	80.51	182.34	203.76	198.90
Space group	$Pm\bar{3}m$ (No. 221)		$Fm\bar{3}m$ (No. 225)	
a (Å)	2.9415(0)	5.8538(2)	5.8843(3)	5.8207(2)
V (Å^3)	25.45(0)	200.59(6)	203.74(9)	197.21(6)
Z	1	4	4	4
Site occupations				
1a (0, 0, 0)	1.0 Cu	–	–	–
1b (½, ½, ½),	0.5 Li, 0.5 Al	–	–	–
4b (½, ½, ½)	–	1.0 Li	1.0 Li	1.0 Li
8c (¼, ¼, ¼)	–	1.0 Cu	1.0 Cu	0.5 Cu, 0.5 Ni
4a (0, 0, 0)	–	0.5 Ga, 0.5 Al	1.0 Ga	1.0 Ga

The end-member $LiCu_2Al$ adopts the cubic CsCl-type structure (space group $Pm\bar{3}m$), in which Cu atoms occupy the 1a site at the corners of the unit cell, while Li and Al atoms are disordered over the 1b site at the centre of the unit cell (Figure 4-2(a)).[20] Substitution of a small amount of Ga is possible, up to $LiCu_2Al_{0.9}Ga_{0.1}$ (x = 0.1), while retaining this structure. As the Ga content increases (x = 0.3 to 1.0), a compositionally induced phase transition occurs, resulting in

the Cu_2MnAl-type (full-Heusler) structure (space group $Fm\bar{3}m$), as evidenced by the appearance of the 111 and 311 diffraction peaks at 26° and 52°, respectively. In this structure, adopted by the other end-member $LiCu_2Ga$, the Cu atoms occupy the 8*c* site at ¼, ¼, ¼, while Li and Ga atoms are ordered over the 4*b* and 4*a* sites located at the edges, centre, and corners of the unit cell (Figure 4-2(c)).[20] Within this range of the solid solution $LiCu_2Al_{1-x}Ga_x$, the Al and Ga atoms are disordered over the 4*a* site (Figure 4-2(b)). The cubic unit cell volume increases monotonically with greater Ga content in $LiCu_2Al_{1-x}Ga_x$, consistent with the larger atomic radius of Ga compared to Al (Figure 4-3(a)). Similar behaviour in related types of solid solutions has been reported previously.[25–30]

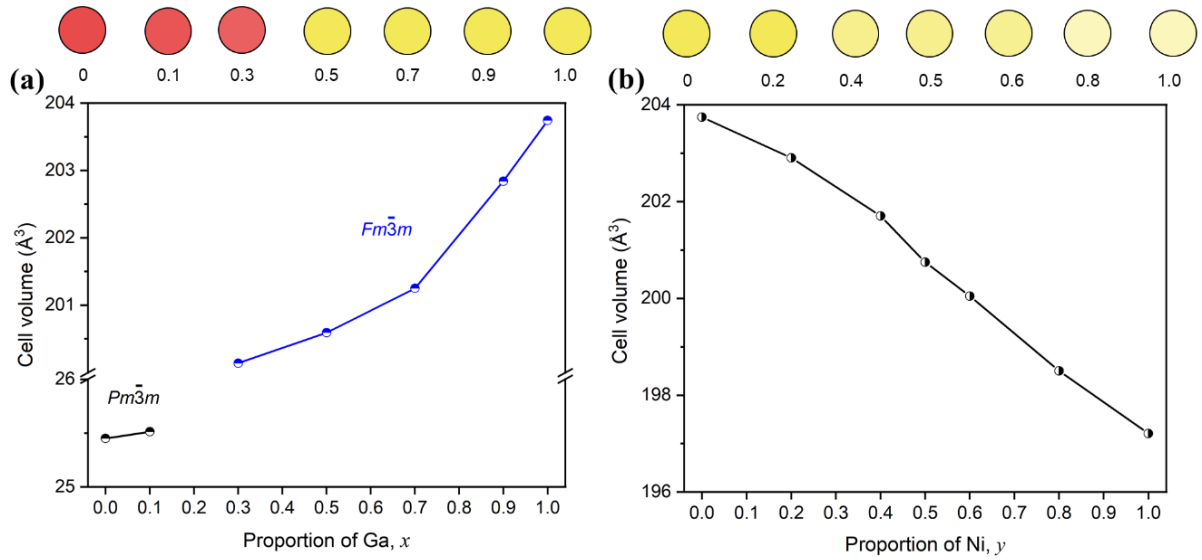

Figure 4-3. Variation in unit cell parameters in (a) $LiCu_2Al_{1-x}Ga_x$ and (b) $LiCu_{2-y}Ni_yGa$. The top panel simulates colours (based on their CIE coordinates) observed for these samples.

According to the classical Hume-Rothery rules for the formation of substitutional solid solutions, the replacement of Cu with the first row transition elements (e.g. Fe, Co, Ni, and Zn) should be possible due to their similar atomic radii. Therefore, solid solutions were investigated in which Cu atoms in $LiCu_2Ga$ were gradually substituted by Ni atoms. Single-phase samples for $LiCu_{2-y}Ni_yGa$ were obtained up to $y = 1.0$; that is, up to half of the Cu atoms could be substituted

by Ni, and beyond this point, multiphase mixtures were obtained (Figure 4-1(b)). The Cu and Ni atoms are disordered over the 8*c* site at ¼, ¼, ¼, while Li and Ga atoms are ordered over the 4*b* and 4*a* sites, as in the parent compound $LiCu_2Ga$ (Figure 4-2(d)). The cell volume shrink following a linear trend with partial Ni substitution, consistent with the smaller atomic radius of Ni (Figure 4-3(b)).[31,32]

4.3.2 ^{7}Li NMR spectroscopy

A series of ^{7}Li NMR spectra were acquired for the solid solution $LiCu_2Al_{1-x}Ga_x$ (Figure 4-4(a)). For both end-members, $LiCu_2Al$ (CsCl-type) and $LiCu_2Ga$ (Cu_2MnAl-type), the Li atoms occupy a single site ($m\bar{3}m$ symmetry) surrounded by eight nearest neighbour Cu atoms in a cubic environment. Given the small quadrupolar moment of ^{7}Li and the high magnetic fields, no significant second order quadrupolar interactions are expected to broaden the linewidths. Hence, the ^{7}Li MAS NMR spectra display a single Gaussian-like resonance with isotropic chemical shifts (δ_{iso}) of 51 ppm for $LiCu_2Al$ and 49 ppm for $LiCu_2Ga$. The linewidths, as gauged by the full-width-half-maximum (FWHM), are 2.2 kHz for $LiCu_2Al$ and 1.9 kHz for $LiCu_2Ga$. These resonances are shifted to higher frequency compared to other diamagnetic Li-containing ionic compounds ($\delta_{iso} \approx 4$ to -2 ppm), but to lower frequency compared to Li metal ($\delta_{iso} \approx 260$ ppm), suggesting some influence from conduction electrons within $LiCu_2Al_{1-x}Ga_x$ (i.e., Knight shift).[33–37] These results are consistent with previous analysis of non-spinning NMR of the end-members $LiCu_2Al$ and $LiCu_2Ga$.[20] There is a small resonance (~5%) that is located near 4 ppm, which is likely due to an oxide-containing side product, presumably formed by reaction with residual oxygen present during handling the starting materials or while transferring and welding the tube from the inert glove box.

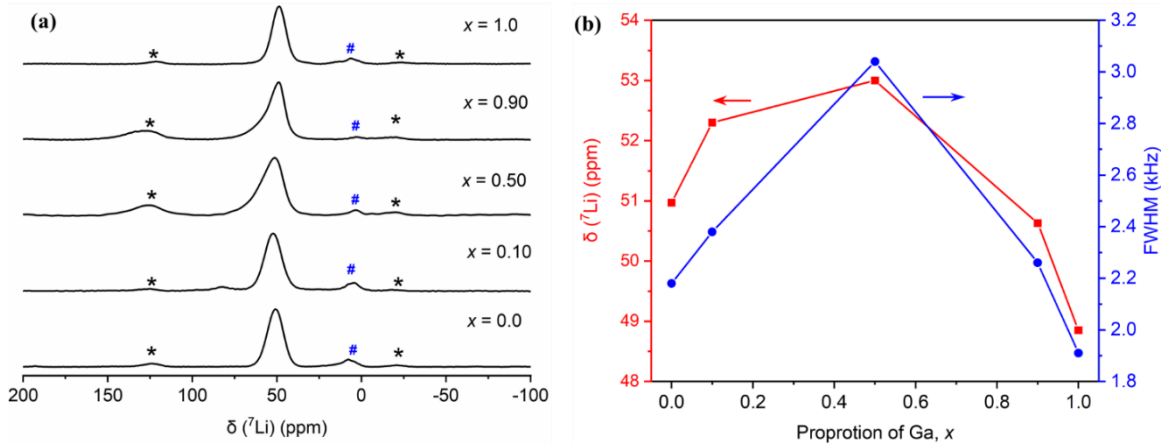

Figure 4-4. (a) ^{7}Li MAS NMR spectra of $Li_2CuAl_{1-x}Ga_x$. (b) Dependence of the centre of gravity shift and FWHM on Ga content. In (a), the asterisks (*) denote spinning sidebands, and the hash symbols (#) mark oxidation impurities.

Upon Ga incorporation from x = 0 to 0.1, the resonance shifts to higher frequency and broadens slightly (Figure 4-4(b)). This can be attributed to the increase in Ga/Al disorder within the second coordination sphere around the Li atoms. Starting at x = 0.3, the transition from CsCl-type to Cu_2MnAl-type structure occurs. Line broadening is maximized at $LiCu_2Al_{0.5}Ga_{0.5}$, consistent with the highest degree of Al/Ga disorder at the 4*a* site, which leads to the most varied distribution of chemical environments around the Li atoms. For the Ga-rich members, the resonances begin to narrow until end-member $LiCu_2Ga$ is reached. The slightly greater linewidth for $LiCu_2Al$ compared to $LiCu_2Ga$ is consistent with the occurrence of Li/Al disorder. Attempts were also made to collect ^{7}Li MAS NMR spectra for $LiCu_{2-y}Ni_yGa$, but these were unsuccessful because the samples are paramagnetic.

4.3.3 Optical reflectance

Within the solid solutions prepared here, the samples show a gradual change in colour from red to yellow as the Ga content increases in $LiCu_2Al_{1-x}Ga_x$, and from yellow to pale yellow as the Ni content increases in $LiCu_{2-y}Ni_yGa$ (Figure 4-5). The parent compound $LiCu_2Al$ is well known

for its bright red colour and high reflectivity, with an absorption edge located around 2.4 eV.[20] The optical reflectance spectra show that this edge shifts toward higher energy as the Ga content increases, until it reaches 2.7 eV for the end-member $LiCu_2Ga$ (Figure 4-5(a)). To assess the observed colours quantitatively, the spectral data were converted to coordinates in CIE 1931 colour space system, with standard illuminant E, and then mapped onto a chromaticity diagram (Figure 4-5(b)). The CIE *x* and *y* coordinates confirm the shift from the red to yellow region as the Ga content increases, matching the observed colours.

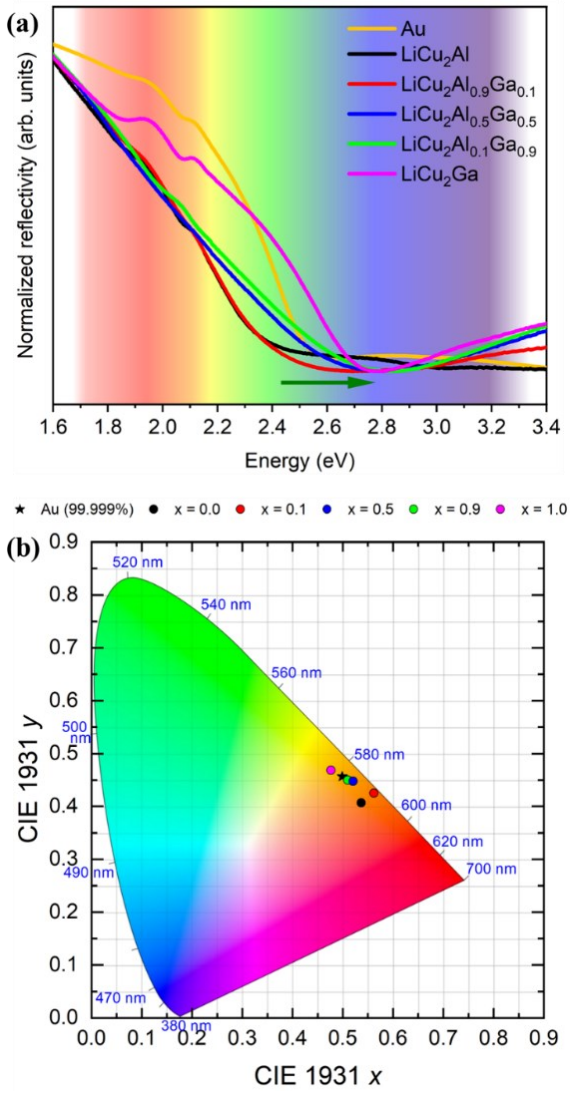

Figure 4-5. (a) Optical reflectivity spectra and (b) CIE 1931 coordinates for of $LiCu_2Al_{1-x}Ga_x$ and Au (99.999%).

Substituting Cu with Ni in $LiCu_{2-y}Ni_yGa$ shows the effect of decreasing the electron count. The absorption edge shifts over a narrower range, from 2.7 to 2.9 eV (corresponding to a change in wavelength from 460 to 430 nm), within the blue-violet region of the visible spectrum (Figure 4-6(a)). Despite this shift, the samples still appear yellow, which is the complementary colour of blue. However, the relative reflectivity gradually becomes less intense, so that the yellow colour becomes lighter. A similar behaviour was observed when the Ni content was increased in Au–Ni alloys, and when the Pd content was increased in Au–Pd alloys.[38,39] The CIE diagram shows the shift from the edge, where colours are intense, toward the central white region (Figure 4-6(b)).

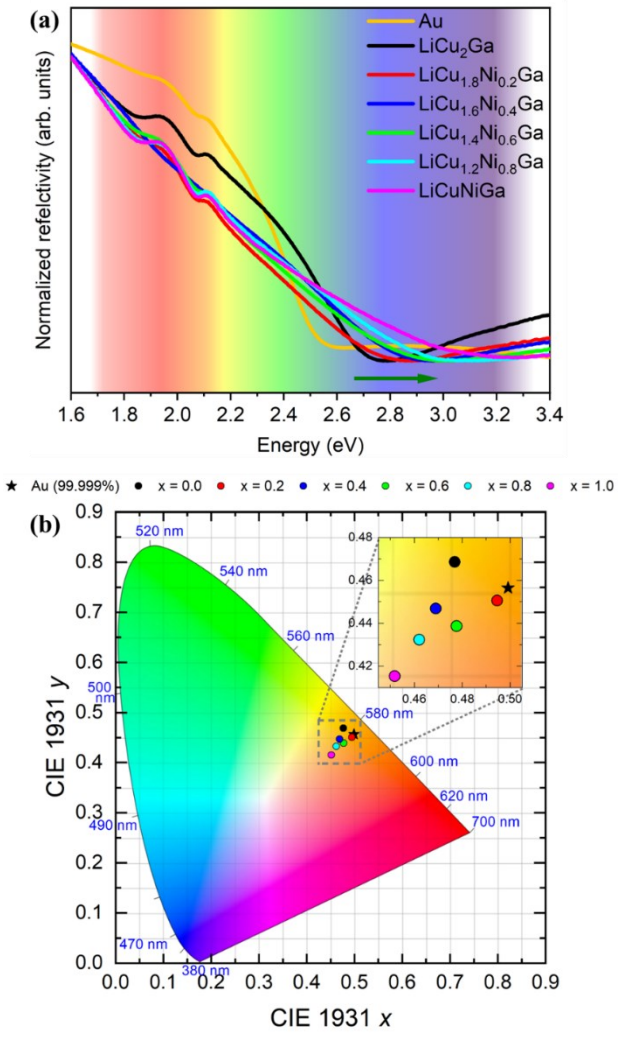

Figure 4-6. (a) Optical reflectivity spectra and (b) CIE 1931 coordinates for of $LiCu_{2-y}Ni_yGa$ and Au (99.999%).

Electronic structure calculations were carried out on $LiCu_2Al$, $LiCu_2Ga_{0.5}Al_{0.5}$, $LiCu_2Ga$, $LiCu_{1.5}Ni_{0.5}Ga$, and LiCuNiGa to understand their electronic and optical properties (Figure 4-7). In all compounds, there is no energy gap or pseudogap in the DOS curves. This differs from the expectation of a pseudogap predicted for Zintl phases that follow normal valence rules. The DOS curves are similar for $LiCu_2Al$, $LiCu_2Al_{0.5}Ga_{0.5}$, and $LiCu_2Ga$. The band dispersion diagrams show a dense manifold of states within a small energy range between –2.5 and –4.5 eV associated with the filled 3d states of Cu atoms, giving rise to the sharp spike in the DOS. These narrow bands are superimposed on disperse bands formed by mixing Li 2s, Cu 4s/4p, Al 3s/3p, and Ga 4s/4p states. When Ni is incorporated in $LiCu_{1.5}Ni_{0.5}Ga$ and LiCuNiGa, the Ni 3d states contribute to a similar spike in the DOS at slightly higher energy, between –1.0 and –2.5 eV, above the Cu 3d states.

The colour of these compounds could be explained by interband transitions from the filled Cu 3d states and the empty states above the Fermi level, similar to the process in elemental copper and gold.[38] The top of Cu 3d band is located approximately 2.2 to 2.5 eV below the Fermi level, which is in good agreement with the optical reflectance spectra absorption edges of 2.4 eV for $LiCu_2Al$ and 2.7 eV for $LiCu_2Ga$. For the Ni-containing compounds, an interband transition from the top on Ni 3d band may occur, but the energy of this transition is about 1.2 eV, which does not lie in visible region. Instead, the visible colour is probably still attributed to transitions from the top of the Cu 3d band, with an energy close to the observed absorption edges of 2.7–2.9 eV.

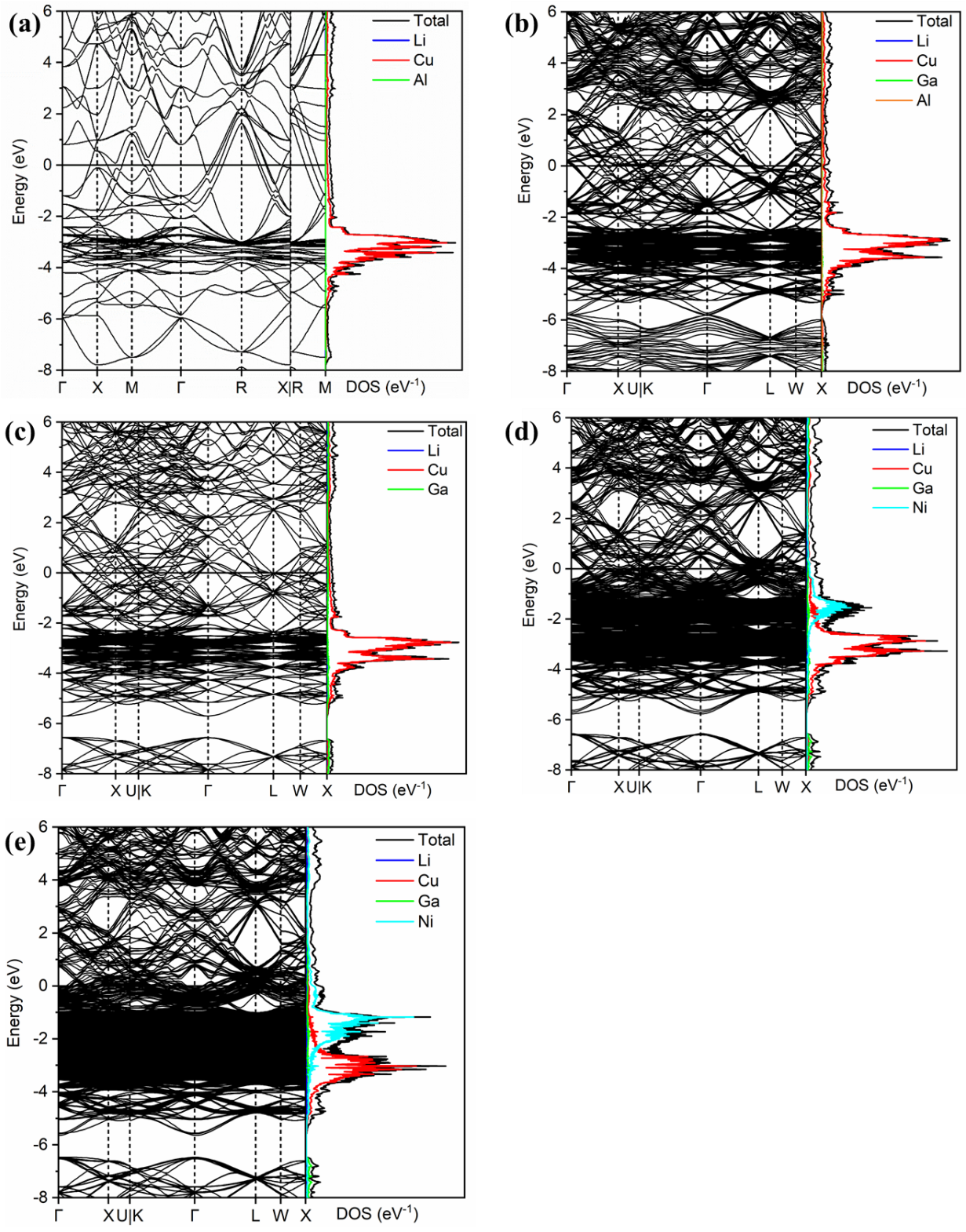

Figure 4-7. Band dispersion and DOS for (a) $LiCu_2Al$, (b) $LiCu_2Ga_{0.5}Al_{0.5}$, (c) $LiCu_2Ga$, (d) $LiCu_{1.5}Ni_{0.5}Ga$, and (e) LiCuNiGa.

4.4 Conclusion

The solid solutions $LiCu_2Al_{1-x}Ga_x$ and $LiCu_{2-y}Ni_yGa$ adopt cubic structures, as determined by powder XRD analysis. The Li atoms occupy a single site, as confirmed by ^7Li NMR spectra. As Ga substitutes for Al in $LiCu_2Al_{1-x}Ga_x$, the colour changes from red to yellow because of a shift in the absorption edge to higher energy. As Ni substitutes for Cu in $LiCu_{2-y}Ni_yGa$, the colour remains yellow becomes lighter, mainly because the relative reflectivity becomes less intense. The CIE colour coordinates indicate that some of these compounds, especially the Ga-rich members of $LiCu_2Al_{1-x}Ga_x$, are very similar to that of elemental gold, making them potential valuable candidates as decorative materials.

4.5 References

(1) Steinemann, S. G.; Wolf, W.; Podloucky; R. Color and optical properties, in: J. H. Westbrook, R.L. Fleischer (Eds.), *Intermetallic Compounds*, Vol. 3, Principles and Practice, Wiley, New York, 2002, 231–244.

(2) Jeong, Y. B.; Kim, J. T.; S. Hong, H.; Lee, H. D.; Choi, S.Y., Kim, K. B. *Mater. Des.* **2019**, *175*, 107814-1–107814-11.

(3) Prandini, G.; Rignanese, G. M.; Marzari, N. *npj. Comput. Mater.* **2019**, *5*, 129.

(4) Wu, H.; Fan, G. *Prog. Mater. Sci.* **2020**, *113*, 100675.

(5) Hong, S. H.; Mun, S. C.; Kang, G. C.; Park, J. J.; Jeong, Y. B.; Song, G.; Ki Buem Kim,K. B. *Prog. Mater. Sci.* **2021**, *113*, 100811.

(6) Esparza-Contro, C.; Berthomé, G.; Renou, G.; Robaut, F.; Coindeau, S.; Vachey, C.; Cambin, J.; Mantel, M.; Latu-Romain. L. *Surf. Coatings .Technol.* **2020**, *389*, 125643.

(7) Runge, J. M. The Metallurgy of Anodizing Aluminum: Connecting Science to Practice. Chicago, IL, USA, 2018, 1–473.

(8) Caicedo, J. C. *J. Alloys Compd.* **2019**, *770*, 875–885.

(9) Niyomsoan, S.; Grant, W.; Olson, D. L.; Mishra, B. *Thin Solid Films* **2002**, *415*, 187–194.

(10) Ma, J.; Yi, J.; Zhao, D. Q.; Pan, M. X.; Wang, W. H. *J. Appl. Phys.* **2012**, *112*, (2012).

(11) Pfaff, G. *ChemTexts.* **2022**, *8*, 1–17.

(12) Supansomboon, S.; Dowd, A.; van der Lingen, E.; Keast, V. J.; Cortie, M. B. **2013**, *37*, 1–5.

(13) Seo, M.; Lee, M. *Acta Mater.* **2018**, *159*, 1–7.

(14) Vishnubhatla, S. S.; Jan, J. P. *Philos. Mag.* **1967**, *16*, 45–50.

(15) Pauly, H.; Weiss, A.; Witte, H. *Int. J. Mater. Res.* **1968**, *59*, 47–58.

(16) Czybulka, A.; Petersen, A.; Schuster, H.-U. *J. Less-Common Met.* **1990**, *161*, 303–312.

(17) Drews, J.; Eberz, U.; Schuster, H.-U. *J. Less-Common Met.* **1986**, *116*, 271–278.

(18) Jomaa, M.; Mishra, V.; Mumbaraddi, D.; Chaudhary, M.; Dmytriv, M.; Michaelis, V. K. Mar. A. *J. Solid State Chem.* **2022**, *306*, 122792.

(19) Jomaa, M.; Mishra, V.; Chaudhary, M.; Mumbaraddi, D.; Michaelis, V. K. Mar. A. *J. Solid State Chem.* **2022**, *314*, 123372.

(20) Mishra, V.; Iyer, A. K.; Mumbaraddi, D.; Oliynyk, A. O.; Zuber, G., Boucheron, A.; Dmytriv, G.; Bernard, G. M.; Michaelis, V. K.; Mar, A. *J. Solid State Chem*. **2020**, *292*, 121703-1–121703-5.

(21) Coelho, A. A. *TOPAS-Academic, version 6, Coelho Software*, Brisbane, Australia, 2007.

(22) Kraus, W.; Nolze, G. *J. Appl. Crystallogr.* **1996**, *29*, 301–303.

(23) Allouche, A. *J. Comput. Chem.* **2012**, *32*, 174–182.

(24) Perdew, J. P.; Burke, K.; Ernzerhof, M. *Phys. Rev. Lett.* **1996**, *77*, 3865–3868.

(25) Slater, J. C. *J. Chem. Phys.* **1964**, *41*, 3199–3204.

(26) Talik, E.; Heimann, J.; Chelkowski, A. *J. Less-Common Met.* **1986**, *124*, L13–L16.

(27) Kimura, H.; Maeda, H.; Sato, M. *J. Cryst. Growth* **1986**, *74*, 187–190.

(28) Yamane, H.; Sakamoto, T.; Kubota, S.; Shimada, M. *J. Mater. Sci.* **2001**, *36*, 307–311.

(29) Fang, M. H., Fang, M-H.; Meng, S.-Y.; Majewska, N.; Leśniewski, T.; Mahlik, S.; Marek Grinberg, M.; Sheu, H.-S.; Liu, R.-S. *Chem. Mater.* **2019**, *31*, 4614–4618.

(30) Kominami, H.; Imagawa, K.; Matsuura, T.; Hara, K.; Kurowasa, S. *1st Int. Vac. Nanoelectron Conf.* **2018**, 1–2.

(31) Kumar, G. R.; Kumar, K. V.; Venudhar, Y. C. *Mater. Sci. Appl.* **2012**, *3*, 87–91.

(32) Kaleva, G. M.; Politova, E. D.; Ivanov, S. A.; Mosunov, A. V.; S. Stefanovich, Y.

Sadovskaya, N. V.; Mathieu, R.; Nordblad, P. *Inorg. Mater.* **2011**, *47*, 1132–1140.

(33) Michaelis, V. K.; Levin, K.; Germanov, Y.; Lelong, G.; Kroeker, S. *Chem. Mater.* **2018**, *30*, 5521–5526.

(34) Bekaert, E.; Robert, F.; Lippens, P. E.; Ménétrier, M. *J. Phys. Chem. C* **2010**, *114*, 6749–6754.

(35) Trease, N. M.; Zhou, L.; Chang, H. J.; Zhu, B. Y.; Grey, C. P. *Solid State Nucl. Magn. Reson.* **2012**, *42*, 62–70.

(36) Winter, F.; Dupke, S.; Eckert, H.; Rodewald, U. C.; Pöttgen, R. *Z. Anorg. Allg. Chem.* **2013**, *639*, 2790–2795.

(37) Dupke, S.; Eckert, H.; Winter, F.; Pöttgen, R. *Prog. Solid State Chem.* **2014**, *42*, 57–64.

(38) Hu, J. Z.; Zhao, Z.; Hu, M. Y.; Feng, J.; Deng, X.; Chen, X.; Xu, W.; Liu, J.; Zhang, J.-G. *J. Power Sources* **2016**, *304*, 51–59.

(39) Saeger, K. E.; Rodies, J. *Gold Bull.* **1977**, *10*, 10–14.

(40) Arrowsmith, D. J. *Gold Bull.* **1986**, *19*, 117–122.

Chapter 5.

Structure and Optical Properties of $Li_xAg_{1-x}GaSe_2$ and $Li_xAg_{1-x}InSe_2$

A version of this chapter has been submitted.

Jomaa, M.; Mishra, V.; Mumbaraddi, D.; Sikdar, R.; Sarkar, D.; Sun, M.; Yao, J.; Michaelis, V. K.; Mar. A. Inorg. Chem. ***2023****.*

5.1 Introduction

Solid state lasers that operate in the mid-infrared range have important applications such as non-invasive surgery, environmental monitoring, and military equipment.[1] The frequency conversion processes occurring in these lasers rely on non-oxide nonlinear optical (NLO) crystals.[2–9] Many IR NLO materials, including those that are most commonly encountered in commercial use (e.g., $AgGaS_2$, $AgGaSe_2$, $ZnGeP_2$), are derived from chalcopyrite and related structures, generally referred to as diamond-like semiconductors.[10–14] Their performance depends on many competing factors which must be balanced, foremost among which are a strong second harmonic generation (SHG) response and a high laser-induced damage threshold. Herculean efforts have been expended to evaluate other candidates, often predicated on enthusiastic claims of rational design, but to date, none have really threatened to displace the few existing commercial materials. For this reason, there has been interest in revisiting the original chalcopyrite-type compounds, including $AgGaS_2$ and $AgGaSe_2$, which still serve as benchmarks for IR NLO materials.

$AgGaS_2$ and $AgGaSe_2$ have relatively high second-order NLO coefficients but low laser-induced damage thresholds; in contrast, the Li-containing counterparts $LiGaS_2$ and $LiGaSe_2$, which are good IR NLO materials in their own right, have lower second-order NLO coefficients but higher laser-induced damage thresholds.[15] These properties are correlated to crystal structures and band gaps. The Ag-containing compounds adopt the tetragonal $CuFeS_2$-type structure (chalcopyrite, a superstructure of sphalerite, in space group $I\bar{4}2d$), whose higher symmetry is partly responsible for the stronger SHG response, whereas the Li-containing compounds adopt the orthorhombic β-$NaFeO_2$-type structure (a superstructure of wurtzite, in space group $Pna2_1$). Conversely, the larger band gaps of the Li-containing compounds lead to higher laser-induced damage thresholds than in the Ag-containing compounds. It is natural to hypothesize that solid solutions containing a mixture of Li and Ag atoms could lead to the desired balance of properties. This was recently achieved through the preparation of the solid solutions $Li_xAg_{1-x}GaS_2$ ($CuFeS_2$-type for x = 0–0.60; two-phase region for x = 0.60–0.70; β-$NaFeO_2$-type for x = 0.70–1.00)[16] and $Li_xAg_{1-x}GaSe_2$ ($CuFeS_2$-type for x = 0–0.90; β-$NaFeO_2$-type for x = 0.98–1.00).[17,18] Similar studies have been extended to the In-containing solid solution $Li_xAg_{1-x}InSe_2$, with two members $Li_{0.37}Ag_{0.63}InSe_2$ ($CuFeS_2$-type) and $Li_{0.55}Ag_{0.45}InSe_2$ (β-$NaFeO_2$-type) having been identified.[19] Similar approaches have been applied to mix Li into other Ag-containing chalcogenides, which serve as a rich source of potential NLO materials.[20,21]

The end-members of the selenide solid solution $Li_xAg_{1-x}GaSe_2$ are interesting. Although the stable form of $AgGaSe_2$ is well known to have the tetragonal $CuFeS_2$-type structure, nanocrystals of this compound can be prepared as the lower symmetry orthorhombic β-$NaFeO_2$-type polymorph.[22] On the other hand, $LiGaSe_2$ normally adopts the orthorhombic form, but can also be prepared as the tetragonal polymorph, which has been reported to exhibit a strong SHG

response (twice as large as $AgGaS_2$ at 2090 nm for particle sizes of 180–212 μm).[23] These observations exemplify the complex phase transformations that can take place among diamond-like semiconductors; they also illustrate the need for careful structural analysis, because the polymorphism largely relates to subtle differences in the ordering arrangements of the metal cations. Indeed, calculated formation energies may be very similar among different polymorphs, and metastable phases may be more easily accessible than assumed.[24]

Given this background, it appears possible to target a complete selenide solid solution $Li_xAg_{1-x}GaSe_2$ in which the same structure is retained for the entire breadth. The corresponding In-containing solid solution $Li_xAg_{1-x}InSe_2$ also deserves fuller investigation. Because Li atoms are often problematic to locate by X-ray diffraction methods alone, solid-state ^{7}Li nuclear magnetic resonance (NMR) spectroscopy may prove valuable in supporting the structure determinations of these compounds, especially with regards to the detailed arrangement of metal cations. Preliminary optical and thermal measurements are carried out to evaluate the potential of these solid solutions as IR NLO materials.

5.2 Experimental Section

5.2.1 Synthesis

Starting materials were Li ribbon (99.9%, Aldrich), Ag powder (99.9%, Aldrich), Ga ingot (99.99%, Alfa-Aesar), In powder (99.9%, Alfa-Aesar), and Se powder (99.5%, Onyxmet). The Li ribbon was handled and cut within an argon-filled glove box, and its surface was scraped to remove any oxidized contaminants prior to use.

Members of the solid solutions $Li_xAg_{1-x}GaSe_2$ and $Li_xAg_{1-x}InSe_2$ were prepared from stoichiometric mixtures of the elements with a total mass of 0.400 g. For $Li_xAg_{1-x}GaSe_2$, mixtures

of Ag and Se powders were ground together, pressed into pellets, and loaded into carbon-coated fused-silica tubes. Next, Ga was added to the tubes, which were transferred to the glove box, and then Li was added to the tubes. For $Li_xAg_{1-x}InSe_2$, mixtures of Ag, In, and Se powders were ground together, pressed into pellets, and loaded into carbon-coated fused-silica tubes, which were then transferred to the glove box so that Li could be loaded into them. The tubes were evacuated, sealed, and placed in a furnace, where they were heated to 850 °C (at a rate of 15 °C/h), held there for 45 h, cooled to 400 °C, and then immediately removed from the furnace at this stage.

Within the solid solution $Li_xAg_{1-x}GaSe_2$, this heating procedure affords the tetragonal polymorph of $LiGaSe_2$ (space group $I\bar{4}2d$). After careful investigation of varied synthetic conditions, it was determined that the orthorhombic polymorph of $LiGaSe_2$ (space group $Pna2_1$) can be prepared following the same temperature profile, except for the crucial difference that the tubes must be slowly cooled to room temperature at a rate of 15 °C/h.

Powder X-ray diffraction (XRD) patterns of ground samples were collected on a Bruker D8 Advance powder diffractometer, equipped with a SSD160 detector and a Cu $K\alpha$ radiation source operated at 40 kV and 40 mA. The experimental powder XRD patterns were analyzed with use of the TOPAS Academic software package.[25] The background was modeled by a twelve-term polynomial function. Pawley fits were applied and cell parameters were refined from these patterns.

Crystal extracted from the samples were examined on a Zeiss Sigma 300 VP field emission scanning electron microscope, operated with an accelerating voltage of 15 kV and equipped with a Bruker Quantax 600 system with dual X-Flash 6/60 detectors. Elemental compositions (except for Li, whose characteristic X-ray emission lines are too low in energy to detect) were determined by energy-dispersive X-ray (EDX) analyses performed on several areas of these samples.

5.2.2 Structure Determination

Various crystals within the solid solutions $Li_xAg_{1-x}GaSe_2$ and $Li_xAg_{1-x}InSe_2$ were screened for suitability to be analyzed by single-crystal X-ray diffraction. Intensity data were collected at room temperature on a Bruker PLATFORM diffractometer equipped with a SMART APEX II CCD area detector and a graphite-monochromated Mo $K\alpha$ radiation source, using ω scans at 4–8 different ϕ angles with a frame width of 0.3° and an exposure time of 15 s per frame. Face-indexed numerical absorption corrections were applied. Structure solution and refinement were carried out with use of the SHELXTL (version 2018/3) program package.[26]

Four crystals within $Li_xAg_{1-x}GaSe_2$ (x = 0.25, 0.50, 0.75, 1.00) and two crystals within $Li_xAg_{1-x}InSe_2$ (x = 0.25, 0.75) were examined. On the basis of Laue symmetries, intensity statistics, and systematic absences, the tetragonal space group $I\bar{4}2d$ was appropriate for all crystals except $Li_{0.75}Ag_{0.25}InSe_2$, which adopts the orthorhombic space group $Pna2_1$. All atomic sites were initially located by direct methods, and their positions were standardized with the program STRUCTURE TIDY.[27] When Li atoms were not included in the structural models, the Ag sites exhibited significantly elevated displacement parameters compared to other sites, implying that Li atoms disorder with Ag atoms. Refinements were performed in which the Li and Ag atoms disorder within the same site, with the constraints that their occupancies to sum to unity and that they have equal displacement parameters. For all crystals, the refined compositions agreed well with expectations, to within 0.1 in x (e.g., $Li_{0.35}Ag_{0.65}GaSe_2$ for the crystal with nominally loaded composition of $Li_{0.25}Ag_{0.75}GaSe_2$). Because these space groups are noncentrosymmetric, the correct absolute structure was determined by refining the Flack parameter; in a few cases, the initial structural model had to be inverted. The final refinements led to reasonable displacement

parameters for all atoms, sensible bond lengths, excellent agreement factors, and featureless difference electron density maps. Details of the crystallographic data have been deposited.

5.2.3 Solid-state ^{7}Li NMR Spectroscopy

Solid-state ^{7}Li NMR spectra were collected on either a Bruker 500 MHz (B_0 = 11.75 T, $\omega_0/2\pi(^7\text{Li})$ = 194.4 MHz) Avance NEO or a 400 MHz (B_0 = 9.4 T, $\omega_0/2\pi(^7\text{Li})$ = 155.6 MHz) Avance III HD NMR spectrometer, equipped with a 4 mm double resonance H-X magic angle spinning (MAS) probe. Ground samples with total mass of 50–100 mg were packed into ZrO_2 rotors (4 mm outer diameter) and sealed with Kel-F caps. The spectra were acquired using a Bloch decay sequence with a 4.0 μs π/2 pulse ($\omega_1/2\pi$ = 62.5 kHz), an optimized recycle delay of 100 s, 4 to 128 co-added transients, and a MAS frequency of 14 kHz.[28] All spectra were referenced to 1 M LiCl (aq.) solution at $\delta(^7\text{Li})$ = 0.0 ppm. The spectra were processed using the Bruker TopSpin 4.1.3 software package.

5.2.4 Optical Measurements

Optical diffuse reflectance spectra were measured from 200 nm (6.2 eV) to 1500 nm (0.8 eV) on an Agilent Cary 5000 UV-vis-NIR spectrophotometer equipped with a diffuse reflectance accessory. A compacted pellet of polytetrafluoroethylene was used as a reflectance standard. The reflectance spectra were converted to optical absorption spectra using the Kubelka–Munk function, $F(R) = \alpha/S = (1-R)^2/2R$, where α is the Kubelka–Munk absorption coefficient, S is the scattering coefficient, and R is the reflectance.[29]

Transmission IR spectra were measured from 400 cm^{-1} to 4000 cm^{-1} on an Excalibur 3100 Fourier transform IR spectrometer. The samples were ground with KBr powder in a mass ratio of 1:100.

Optical SHG intensities were estimated using the Kurtz-Perry technique,[30,31] using light with a fundamental wavelength of 2090 nm, generated by a Q-switched Ho:Tm:Cr:YAG laser. Ground samples were sieved into particle sizes in the ranges of 20–50, 50–90, 90–125, 125–150, and 150–200 μm, and then loaded into custom holders with a thickness of 0.5 mm. Ground microcrystals of $AgGaS_2$ with the same ranges of particle sizes served as the reference.

5.2.5 Thermal Analysis

Differential scanning calorimetry (DSC) was performed on a Setaram Labsys TGA-DTA 1600 thermal analyzer. Ground samples with total mass of 20 mg were placed in fused silica tubes, which were evacuated and sealed. The samples were heated and cooled at a rate of 20 °C/min, reaching a maximum temperature of 1000 °C.

5.2.6 Electronic Structure Calculations

Ordered models for various members of the solid solutions $Li_xAg_{1-x}GaSe_2$ and $Li_xAg_{1-x}InSe_2$ were generated using the program Supercell (version 2.0).[32] Electronic structure calculations were performed using the projected augmented wave (PAW) method as implemented in the Vienna ab initio simulation package (VASP version 5.4.4).[33] Exchange and correlation were treated in this density functional theory (DFT) method by the generalized gradient approximation, as parameterized by Perdew, Burke, and Ernzerhof.[34] The recommended standard PAW potentials (Li_sv, Ag, Ga_d, In_d, and Se) were used, with the plane-wave basis cutoff energy set to 650 eV. The first Brillouin zone was sampled by a 17 × 17 × 9 *k*-point grid to calculate the density of states (DOS). The convergence criteria were set to 10^{-8} eV for electronic optimization and $|-2 \times 10^{-2}|$ eV for ionic relaxation. Electron localization functions (ELF) were evaluated. Projected crystal

orbital Hamilton populations (–pCOHP), and crystal orbital bond indices (COBI) were calculated using the program LOBSTER (version 4.1.0).[35–38]

5.3 Results and Discussion

5.3.1 Structural Analysis

The solid solutions $Li_xAg_{1-x}GaSe_2$ and $Li_xAg_{1-x}InSe_2$ were prepared by reaction of the elements at 850 °C. Pawley fittings were applied to all powder XRD patterns (Figure A4-1 and Figure A4-2). These patterns reveal that all samples are phase-pure, with a gradual evolution in the positions and intensities of peaks (Figure 5-1). Cell parameters were refined from these patterns (Table 5-1 and Table 5-2). On progressing from the Ag-containing to the Li-containing end-members, the cell parameters decrease gradually, consistent with the relative ionic radii (cf. Shannon IR values of 1.00 Å for Ag^+ and 0.59 Å for Li^+ in CN4).[39] Plots of the cell volume show a strongly linear dependence on the Li content, in accordance with Vegard's law (Figure 5-2).

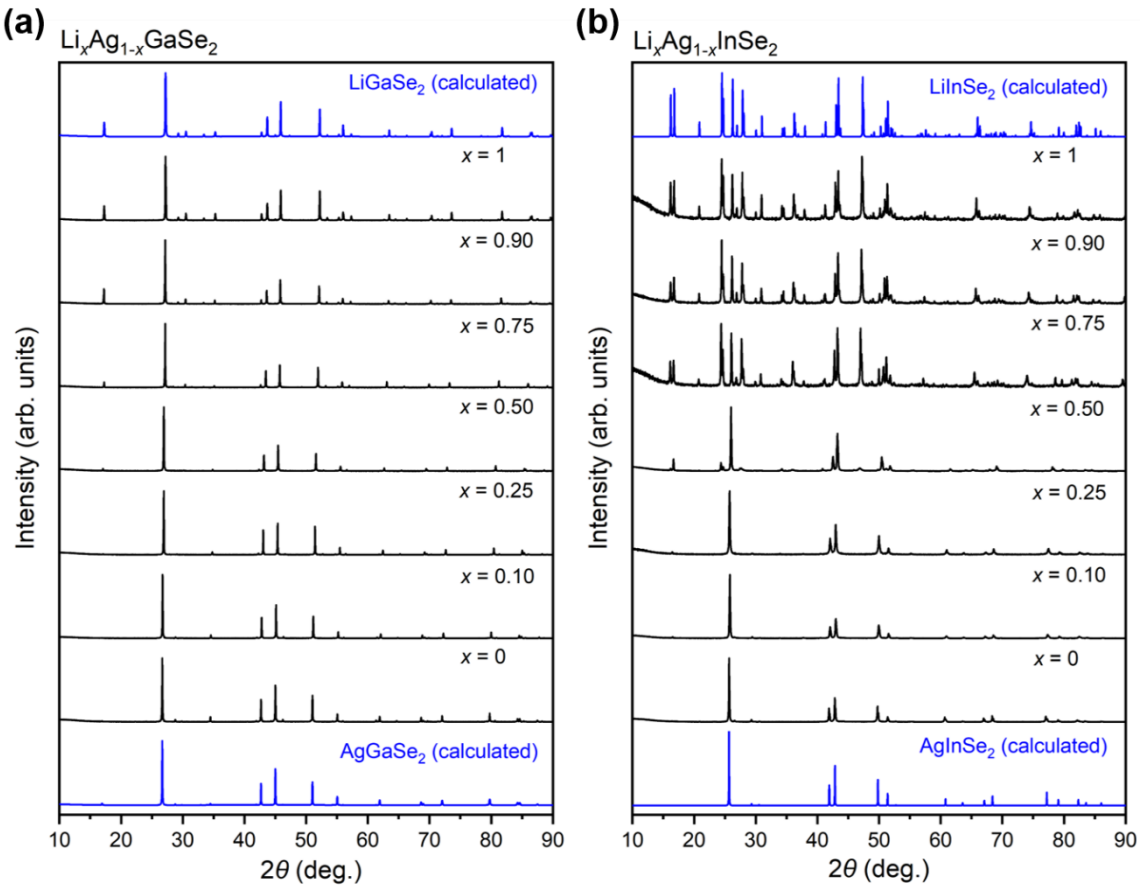

Figure 5-1. Powder XRD patterns for (a) $Li_xAg_{1-x}GaSe_2$ and (b) $Li_xAg_{1-x}InSe_2$.

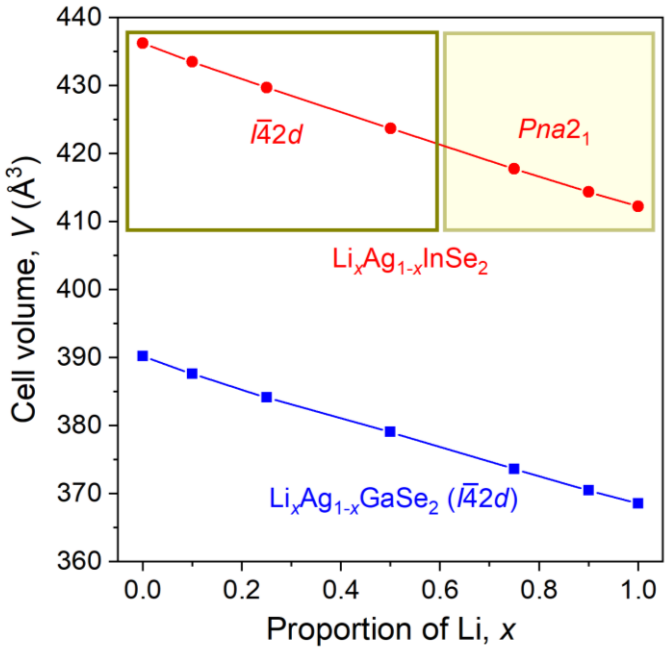

Figure 5-2. Dependence of unit cell volume on Li content for $Li_xAg_{1-x}GaSe_2$ and $Li_xAg_{1-x}InSe_2$.

Table 5-1. Cell Parameters and Refinement Results for $Li_xAg_{1-x}GaSe_2$ [a]

compound	a (Å)	c (Å)	V (Å^3)	$\eta = c / 2a$	R_p	R_{wp}
$AgGaSe_2$	5.9897(6)	10.880(1)	390.33	0.9082	0.079	0.112
$Li_{0.10}Ag_{0.90}GaSe_2$	5.9758(1)	10.8550(1)	387.63	0.9082	0.079	0.109
$Li_{0.25}Ag_{0.75}GaSe_2$	5.956(4)	10.8291(4)	384.14	0.9091	0.062	0.088
$Li_{0.50}Ag_{0.50}GaSe_2$	5.927(1)	10.789(2)	379.07	0.9101	0.082	0.111
$Li_{0.75}Ag_{0.25}GaSe_2$	5.894(4)	10.757(6)	373.65	0.9126	0.092	0.119
$Li_{0.90}Ag_{0.10}GaSe_2$	5.8729(1)	10.7417(1)	370.49	0.9145	0.079	0.109
$LiGaSe_2$	5.8611(3)	10.728(1)	368.55	0.9152	0.086	0.118

[a] All compounds adopt the tetragonal $CuFeS_2$-type structure in space group $I\bar{4}2d$.

Table 5-2. Cell Parameters and Refinement Results for $Li_xAg_{1-x}InSe_2$

compound	space group	a (Å)	b (Å)	c (Å)	V (Å^3)	R_p	R_{wp}
$AgInSe_2$	$I\bar{4}2d$	6.104(1)		11.707(2)	436.23	0.082	0.105
$Li_{0.10}Ag_{0.90}InSe_2$	$I\bar{4}2d$	6.089(2)		11.692(4)	433.49	0.065	0.086
$Li_{0.25}Ag_{0.75}InSe_2$	$I\bar{4}2d$	6.068(4)		11.670(1)	429.74	0.060	0.076
$Li_{0.50}Ag_{0.50}InSe_2$	$I\bar{4}2d$	6.0294(2)		11.6553(7)	423.71	0.108	0.169
$Li_{0.75}Ag_{0.25}InSe_2$	$Pna2_1$	7.222(4)	8.454(8)	6.842(7)	417.76	0.058	0.079
$Li_{0.90}Ag_{0.10}InSe_2$	$Pna2_1$	7.2064(1)	8.4384(4)	6.8147(3)	414.41	0.068	0.086
$LiInSe_2$	$Pna2_1$	7.195(5)	8.4254(5)	6.800(3)	412.24	0.067	0.086

For $Li_xAg_{1-x}GaSe_2$, the tetragonal $CuFeS_2$-type structure ($I\bar{4}2d$) is retained for the entire breadth of the solid solution. This is remarkable because the end-member $LiGaSe_2$ has normally been reported to adopt the orthorhombic β-$NaFeO_2$-type structure ($Pna2_1$).[40] The key step in the

synthesis to form the tetragonal polymorph of $LiGaSe_2$ was a relatively fast cooling rate (by removing the samples immediately from the furnace from 400 °C, effectively equivalent to quenching to room temperature), in contrast to the slow cooling used previously. Indeed, it was determined that cooling at a much slower rate of 15 °C/h does afford the orthorhombic polymorph of $LiGaSe_2$. In contrast, for $Li_xAg_{1-x}InSe_2$, a transition from the tetragonal to orthorhombic forms occurs on proceeding from $x = 0.5$ to $x = 0.75$, despite using the same temperature profile. The linear relationship of the cell parameters for $Li_xAg_{1-x}InSe_2$ may seem surprising given the occurrence of this structural transition (Figure 5-2), but it can be understood when the structural similarity is appreciated, as noted later.

Crystals selected from all samples were confirmed by EDX analysis to exhibit the expected chemical compositions, although Li is too light to be detected by this technique (Table A4-1). Representative crystals were chosen for single-crystal structure determination. Table 5-3 and Table 5-4 list crystal data, Table 5-5 lists atomic and displacement parameters, and Table 5-6 lists interatomic distances.

Table 5-3. Crystallographic Data for $Li_xAg_{1-x}GaSe_2$

nominal formula	$Li_{0.25}Ag_{0.75}GaSe_2$	$Li_{0.50}Ag_{0.50}GaSe_2$	$Li_{0.75}Ag_{0.25}GaSe_2$	$LiGaSe_2$
formula mass (amu)	310.28	285.05	259.81	234.58
refined composition	$Li_{0.350(3)}Ag_{0.650(3)}GaSe_2$	$Li_{0.525(3)}Ag_{0.475(3)}GaSe_2$	$Li_{0.727(4)}Ag_{0.273(4)}GaSe_2$	$LiGaSe_2$
space group	$I\bar{4}2d$ (no. 122)	$I\bar{4}2d$ (no. 122)	$I\bar{4}2d$ (no. 122)	$I\bar{4}2d$ (no. 122)
a (Å)	5.9529(5)	5.9293(5)	5.9008(5)	5.8627(6)
c (Å)	10.8194(14)	10.7902(13)	10.7639(9)	10.7317(16)
V (Å^3)	383.41(8)	379.35(8)	374.79(7)	368.86(10)
Z	4	4	4	4
T (K)	296(2)	296(2)	296(2)	296(2)
ρ_{calcd} (g cm^{-3})	5.375	4.991	4.604	4.224
crystal dimensions (mm)	0.07 × 0.07 × 0.06	0.19 × 0.11 × 0.09	0.10 × 0.08 × 0.06	0.17 × 0.11 × 0.10
μ(Mo $K\alpha$) (mm^{-1})	29.62	28.68	27.76	26.92
transmission factors	0.261–0.372	0.128–0.218	0.195–0.314	0.111–0.198
2θ limits	7.81–58.51°	7.84–58.37°	7.88–58.61°	7.92–58.67°
data collected	$-8 \le h \le 8$, $-8 \le k \le 8$, $-14 \le l \le 14$	$-8 \le h \le 8$, $-8 \le k \le 8$, $-14 \le l \le 14$	$-8 \le h \le 8$, $-8 \le k \le 8$, $-14 \le l \le 14$	$-8 \le h \le 8$, $-8 \le k \le 8$, $-14 \le l \le 14$
no. of data collected	1936	1931	1939	1914
no. of unique data, including $F_o^2 < 0$	262 (R_{int} = 0.024)	262 (R_{int} = 0.027)	262 (R_{int} = 0.020)	261 (R_{int} = 0.019)
no. of unique data, with $F_o^2 > 2\sigma(F_o^2)$	244	248	248	244
no. of variables	13	13	13	12
Flack parameter	0.07(4)	0.12(5)	0.12(6)	0.08(7)
$R(F)$ for $F_o^2 > 2\sigma(F_o^2)$ [a]	0.016	0.014	0.014	0.012
$R_w(F_o^2)$ [b]	0.041	0.035	0.031	0.028
goodness of fit	1.10	1.10	1.15	1.15
$(\Delta\rho)_{max}$, $(\Delta\rho)_{min}$ (e Å^{-3})	0.38, –0.51	0.43, –0.32	0.37, –0.26	0.35, –0.55

[a] $R(F) = \sum||F_o| - |F_c|| / \sum|F_o|$.

[b] $R_w(F_o^2) = [\sum[w(F_o^2 - F_c^2)^2] / \sum wF_o^4]^{1/2}$; $w^{-1} = [\sigma^2(F_o^2) + (Ap)^2 + Bp]$, where $p = [\max(F_o^2,0) + 2F_c^2] / 3$.

Table 5-4. Crystallographic Data for $Li_xAg_{1-x}InSe_2$

nominal formula	$Li_{0.25}Ag_{0.75}InSe_2$	$Li_{0.75}Ag_{0.25}InSe_2$
formula mass (amu)	355.38	285.05
refined composition	$Li_{0.347(4)}Ag_{0.653(4)}InSe_2$	$Li_{0.799(3)}Ag_{0.201(3)}InSe_2$
space group	$I\bar{4}2d$ (no. 122)	$Pna2_1$ (no. 33)
a (Å)	6.0615(7)	7.2212(6)
b (Å)	6.0615(7)	8.4668(7)
c (Å)	11.670(2)	6.8405(6)
V (Å^3)	428.76(12)	418.23(6)
Z	4	4
T (K)	296(2)	296(2)
ρ_{calcd} (g cm^{-3})	5.505	4.842
crystal dimensions (mm)	0.09 × 0.08 × 0.05	0.08 × 0.07 × 0.07
μ(Mo $K\alpha$) (mm^{-1})	25.58	23.95
transmission factors	0.254–0.426	0.241–0.401
2θ limits	7.58–67.46°	7.42–58.62°
data collected	$-9 \le h \le 9$, $-9 \le k \le 9$, $-17 \le l \le 17$	$-9 \le h \le 9$, $-11 \le k \le 11$, $-9 \le l \le 9$
no. of data collected	3028	4219
no. of unique data, including $F_o^2 < 0$	427 (R_{int} = 0.043)	1137 (R_{int} = 0.030)
no. of unique data, with $F_o^2 > 2\sigma(F_o^2)$	276	802
no. of variables	13	40
Flack parameter	0.06(4)	0.03(2)
$R(F)$ for $F_o^2 > 2\sigma(F_o^2)$ [a]	0.026	0.026
$R_w(F_o^2)$ [b]	0.066	0.064
goodness of fit	0.93	1.05
$(\Delta\rho)_{max}$, $(\Delta\rho)_{min}$ (e Å^{-3})	1.29, –0.52	1.94, –0.76

[a] $R(F) = \sum||F_o| - |F_c|| / \sum|F_o|$.

[b] $R_w(F_o^2) = [\sum[w(F_o^2 - F_c^2)^2] / \sum wF_o^4]^{1/2}$; $w^{-1} = [\sigma^2(F_o^2) + (Ap)^2 + Bp]$, where $p = [\max(F_o^2,0) + 2F_c^2] / 3$.

Table 5-5. Atomic Coordinates and Equivalent Isotropic Displacement Parameters for $Li_xAg_{1-x}GaSe_2$ and $Li_xAg_{1-x}InSe_2$

atom	Wyckoff position	occupancy	*x*	*y*	*z*	U_{eq} (Å^2)
$Li_{0.25}Ag_{0.75}GaSe_2$ ($I\bar{4}2d$)						
Li/Ag	4*b*	0.350(3) Li, 0.650(3) Ag	0	0	½	0.0366(5)
Ga	4*a*	1	0	0	0	0.0168(3)
Se	8*d*	1	0.2229(1)	¼	⅛	0.0203(2)
$Li_{0.50}Ag_{0.50}GaSe_2$ ($I\bar{4}2d$)						
Li/Ag	4*a*	0.525(3) Li, 0.475(3) Ag	0	0	0	0.0331(6)
Ga	4*b*	1	0	0	½	0.0157(3)
Se	8*d*	1	0.2753(1)	¾	⅛	0.0194(2)
$Li_{0.75}Ag_{0.25}GaSe_2$ ($I\bar{4}2d$)						
Li/Ag	4*b*	0.727(4) Li, 0.273(4) Ag	0	0	½	0.026(1)
Ga	4*a*	1	0	0	0	0.014(1)
Se	8*d*	1	0.2278(1)	¼	⅛	0.017(1)
$LiGaSe_2$ ($I\bar{4}2d$)						
Li	4*a*	1	0	0	0	0.011(2)
Ga	4*b*	1	0	0	½	0.0157(2)
Se	8*d*	1	0.2686(1)	¾	⅛	0.0168(2)
$Li_{0.25}Ag_{0.75}InSe_2$ ($I\bar{4}2d$)						
Li/Ag	4*b*	0.347(4) Li, 0.653(4) Ag	0	0	½	0.0410(8)
In	4*a*	1	0	0	0	0.0252(4)
Se	8*d*	1	0.2461(1)	¼	⅛	0.0245(3)
$Li_{0.75}Ag_{0.25}GaSe_2$ ($Pna2_1$)						
Li/Ag	4*a*	0.799(3) Li, 0.201(3) Ag	0.0883(4)	0.6230(6)	0.125(2)	0.0271(10)
In	4*a*	1	0.0785(1)	0.1258(1)	0.1266(3)	0.0200(2)
Se1	4*a*	1	0.0782(1)	0.1279(2)	0.5031(1)	0.0216(2)
Se2	4*a*	1	0.4150(1)	0.1236(2)	0.0000(2)	0.0219(2)

Table 5-6. Interatomic Distances (Å) in $Li_xAg_{1-x}GaSe_2$ and $Li_xAg_{1-x}InSe_2$

compound	Li/Ag–Se	Ga–Se or In–Se
$Li_xAg_{1-x}GaSe_2$		
$Li_{0.25}Ag_{0.75}GaSe_2$ ($I\bar{4}2d$)	2.6008(5) (×4)	2.4094(4) (×4)
$Li_{0.50}Ag_{0.50}GaSe_2$ ($I\bar{4}2d$)	2.5847(4) (×4)	2.4066(3) (×4)
$Li_{0.75}Ag_{0.25}GaSe_2$ ($I\bar{4}2d$)	2.5624(3) (×4)	2.4070(3) (×4)
$LiGaSe_2$ ($I\bar{4}2d$)	2.5354(4) (×4)	2.4058(4) (×4)
$Li_xAg_{1-x}InSe_2$		
$Li_{0.25}Ag_{0.75}InSe_2$ ($I\bar{4}2d$)	2.6064(6) (×4)	2.5786(5) (×4)
$Li_{0.75}Ag_{0.25}InSe_2$ ($Pna2_1$)	2.549(5), 2.566(6), 2.566(15), 2.580(6)	2.570(1), 2.576(3), 2.578(1), 2.580(1)

The crystallographic analyses confirm the diamond-like structures adopted by these compounds, which are superstructures of the familiar sphalerite (or zincblende) and wurtzite aristotypes of ZnS (Figure 5-3). In the tetragonal $CuFeS_2$-type structure ($I\bar{4}2d$), the *c*-axis is doubled relative to the cubic sphalerite structure ($F\bar{4}3m$), so that nets of close-packed chalcogen anions are now described as lying parallel to the set of {112} planes. These nets are stacked along the <221> directions (and not the [112] direction, as sometimes erroneously reported by others who confuse planes with directions). In the orthorhombic β-$NaFeO_2$-type structure ($Pna2_1$), the unit cell volume is quadrupled relative to the hexagonal wurtzite structure ($P6_3mc$) but the *c*-axis remains unaltered, so that nets of close-packed chalcogen anions still lie parallel to (001) and are stacked along [001]. These superstructures presumably arise from charge ordering of the Li/Ag and the Ga or In cations. The resulting arrangements of metal-centred tetrahedra, which are all corner-sharing, are built from similar slabs (formed between pairs of close-packed anion nets) with identical colouring patterns of the metal cations (Figure 5-4).

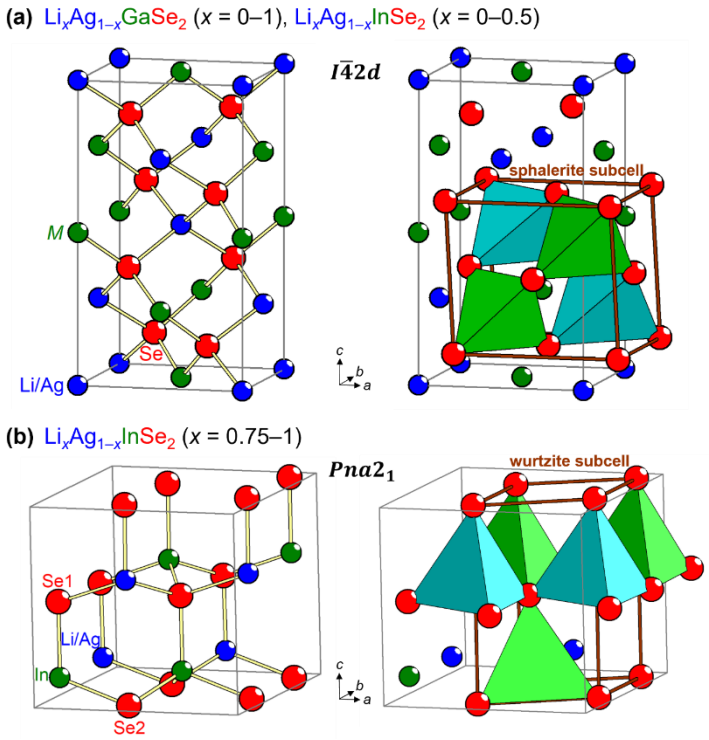

Figure 5-3. Structures of $Li_xAg_{1-x}GaSe_2$ and $Li_xAg_{1-x}InSe_2$. The left panels show the unit cell contents. The right panels highlight the relationships to the cubic sphalerite or hexagonal wurtzite subcells, translated from their conventional settings to place the anions at lattice points.

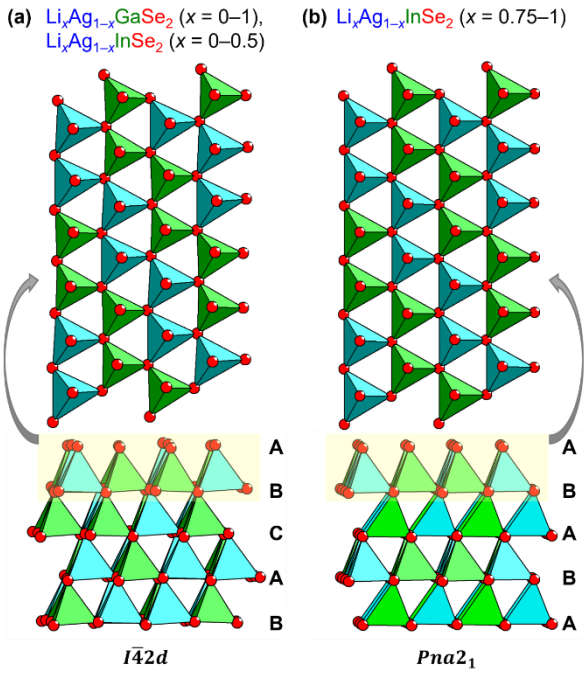

Figure 5-4. Arrangement of metal-centred tetrahedra in $Li_xAg_{1-x}GaSe_2$ and $Li_xAg_{1-x}InSe_2$, contrasting the ccp stacking of anions in the tetragonal $CuFeS_2$-type structure and the hcp stacking of anions in the orthorhombic β-$NaFeO_2$-type structure.

Given the rather disparate sizes of Li^+ and Ag^+ ions, as gauged by the nominal Shannon ionic radii noted earlier, it may seem surprising that they are completely disordered within the solid solution $Li_xAg_{1-x}GaSe_2$. To be sure, partial solid solutions of involving a combination of Li and Ag are well precedented.[16] On progressing from $Li_{0.25}Ag_{0.75}GaSe_2$ to $LiGaSe_2$, the Li/Ag–Se distances decrease gradually from 2.60 Å to 2.54 Å; these are clearly distinguishable from the Ga–Se distances, which remain relatively constant at 2.41 Å (Table 5-6). These distances agree with typical values found for Li–Se (2.45–2.65 Å), Ag–Se (2.60–2.90 Å), and Ga–Se bond lengths (2.35–2.55 Å).[41] This comparison suggests that the Ag atoms are overbonded in $Li_xAg_{1-x}GaSe_2$. Indeed, the bond valence sums are 1.0–1.2 if this site is filled with Li atoms, but 1.6–1.9 if filled with Ag atoms, indicating significant overbonding.[42] The other sites are well behaved, with bond valence sums of 3.0 for Ga and 2.1–2.2 for Se atoms. A similar analysis for the structures determined within the solid solution $Li_xAg_{1-x}InSe_2$ shows the same feature, with bond valence sums of 1.0–1.1 for Li, 1.6–1.8 for Ag, 3.0 for In, and 2.1–2.2 for Se atoms. There is also a further complication that the observed In–Se distances (2.57–2.58 Å) overlap with the Li/Ag–Se distances (2.55–2.61 Å).

Because many conclusions about the properties of diamond-like semiconductors depend on their detailed atomic arrangements, it is somewhat disconcerting that both experimental and computational interpretations have been frequently made on the basis of uncertain structures. For example, chalcopyrite and related structures may exhibit very similar powder XRD patterns that are difficult to distinguish.[43,44] Even when single-crystal structures are determined, there may remain unresolved questions, as presented above. To address this concern, ^{7}Li NMR spectroscopy was performed on several members of $Li_xAg_{1-x}GaSe_2$ and $Li_xAg_{1-x}InSe_2$ (Figure 5-5). The isotropic chemical shifts and linewidths were extracted and are listed in Table A4-2. All spectra

show a narrow single resonance, providing strong evidence that Li atoms occupy a unique site in the structures. The chemical shifts lie in the range that is typical for cationic Li in a low coordinate environment.[45] It is noteworthy that both $LiGaSe_2$ polymorphs have similar spectra, but the chemical shift is found at slightly lower frequency for the orthorhombic form (2.3 ppm) than for the tetragonal form (2.6 ppm), reflecting subtle differences in the short-range local environments around the Li atoms. Introducing more Li tends to increase the linewidths of the NMR resonance within the $Li_xAg_{1-x}GaSe_2$ solid solution due to an enhanced homonuclear (^7Li–^7Li) dipolar coupling, but an apparent break in the trend occurs within the $Li_xAg_{1-x}InSe_2$ solid solution, reflecting the change from the tetragonal to orthorhombic structures (Figure 5-6). This break agrees with the trend in Li–Li distances in $Li_xAg_{1-x}InSe_2$. Within the tetragonal structure, they proceed from 4.209 Å ($x = 0.25$) to 4.193 Å ($x = 0.50$), and within the orthorhombic structure, they proceed from 4.201 Å ($x = 0.75$) to 4.180–4.186 Å ($x = 1$).

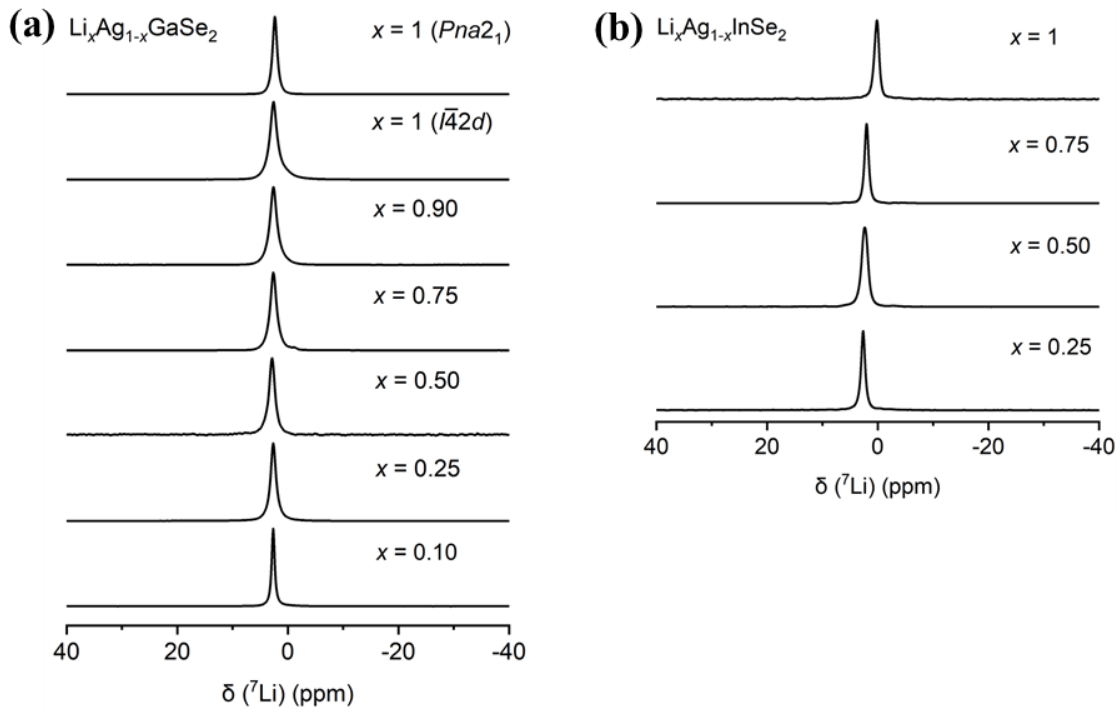

Figure 5-5. ^7Li MAS NMR spectra of $Li_xAg_{1-x}GaSe_2$ and $Li_xAg_{1-x}InSe_2$.

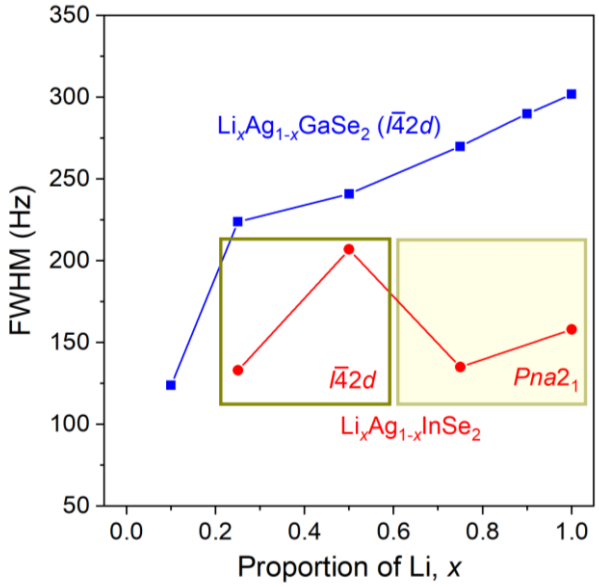

Figure 5-6. Linewidths in ^{7}Li NMR spectra of $Li_xAg_{1-x}GaSe_2$ and $Li_xAg_{1-x}InSe_2$.

5.3.2 Optical Properties

The diffuse reflectance spectra, which were converted to absorption spectra, show prominent edges from which optical band gaps were extrapolated (Figure 5-7). Increasing Li content tends to shift the absorption edges to higher energies, so that the band gap changes roughly linearly from 1.8 to 3.4 eV in $Li_xAg_{1-x}GaSe_2$, and from 1.2 to 2.5 eV in $Li_xAg_{1-x}InSe_2$ (Table A4-3 and Figure 5-8). The band gaps for the end-members ($AgGaSe_2$, $LiGaSe_2$, $AgInSe_2$, and $LiInSe_2$) generally agree well with previously reported experimental values, but even here, variations can occur.[15] For example, reported band gaps of $LiInSe_2$ range from 1.8 to 2.9 eV, the discrepancies being attributed to different degrees of defects.[31] The IR transmission spectra reveal that the absence of features over a wide range from 2.5 to 25 μm, with only weak absorption peaks attributed to atmospheric H_2O and CO_2, as seen in a KBr reference standard (Figure A4-3). However, care has to be taken before conclusions can be made about optical transparency, because this is more properly assessed on large single crystal samples.

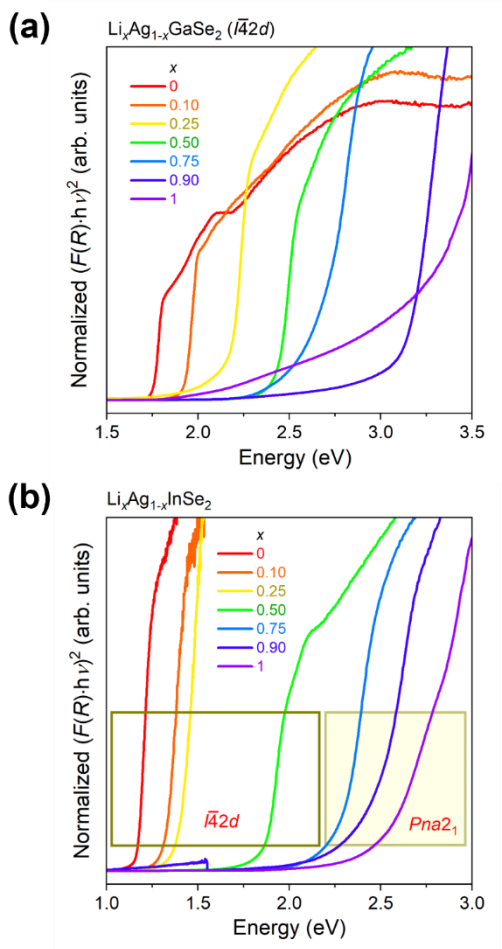

Figure 5-7. Optical diffuse reflectance spectra for $Li_xAg_{1-x}GaSe_2$ and $Li_xAg_{1-x}InSe_2$.

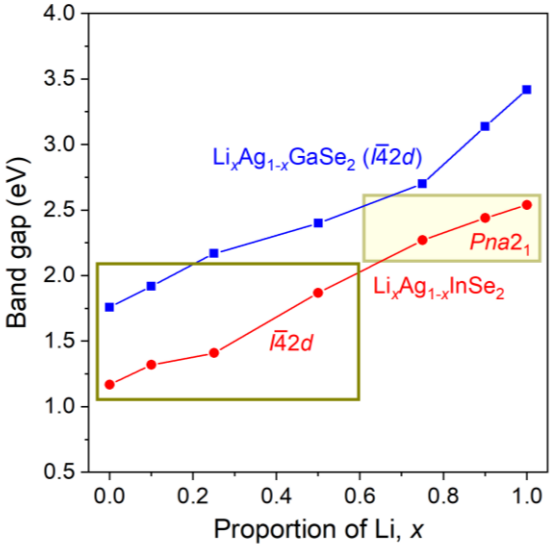

Figure 5-8. Band gaps for $Li_xAg_{1-x}GaSe_2$ and $Li_xAg_{1-x}InSe_2$.

Optical SHG measurements were made on $Li_xAg_{1-x}GaSe_2$ and $Li_xAg_{1-x}InSe_2$ powders using a fundamental laser wavelength of 2090 nm and compared with the benchmark material $AgGaS_2$. The SHG intensities are competitive with $AgGaS_2$ (Table A4-4 and Figure 5-9). At the smallest particle size range of 20–50 μm, the intensities are higher than for $AgGaS_2$ and tend to reach a maximum for the members near the middle of the solid solution (12× $AgGaS_2$ for $Li_{0.50}Ag_{0.50}GaSe_2$ and 10× $AgGaS_2$ for $Li_{0.75}Ag_{0.25}InSe_2$). The dependence of the SHG intensities on particle size ranges is somewhat irregular, but in general, these compounds do not show type-I phase matching behaviour at this wavelength. For comparison, the corresponding sulfide $Li_{0.6}Ag_{0.4}GaS_2$ shows a modest enhancement (1.1× $AgGaS_2$) but is type-I phase matchable at 2100 nm,[16] whereas the selenide $Li_{0.5}Ag_{0.5}GaSe_2$ is not phase matchable at 1910 nm.[17] However, these compounds may be phase matchable in the optical parametric oscillator process, as shown by the two end members $AgGaSe_2$ and $LiGaSe_2$, so it would be worthwhile to conduct measurements on $Li_xAg_{1-x}GaSe_2$ and $Li_xAg_{1-x}InSe_2$ at other wavelengths.

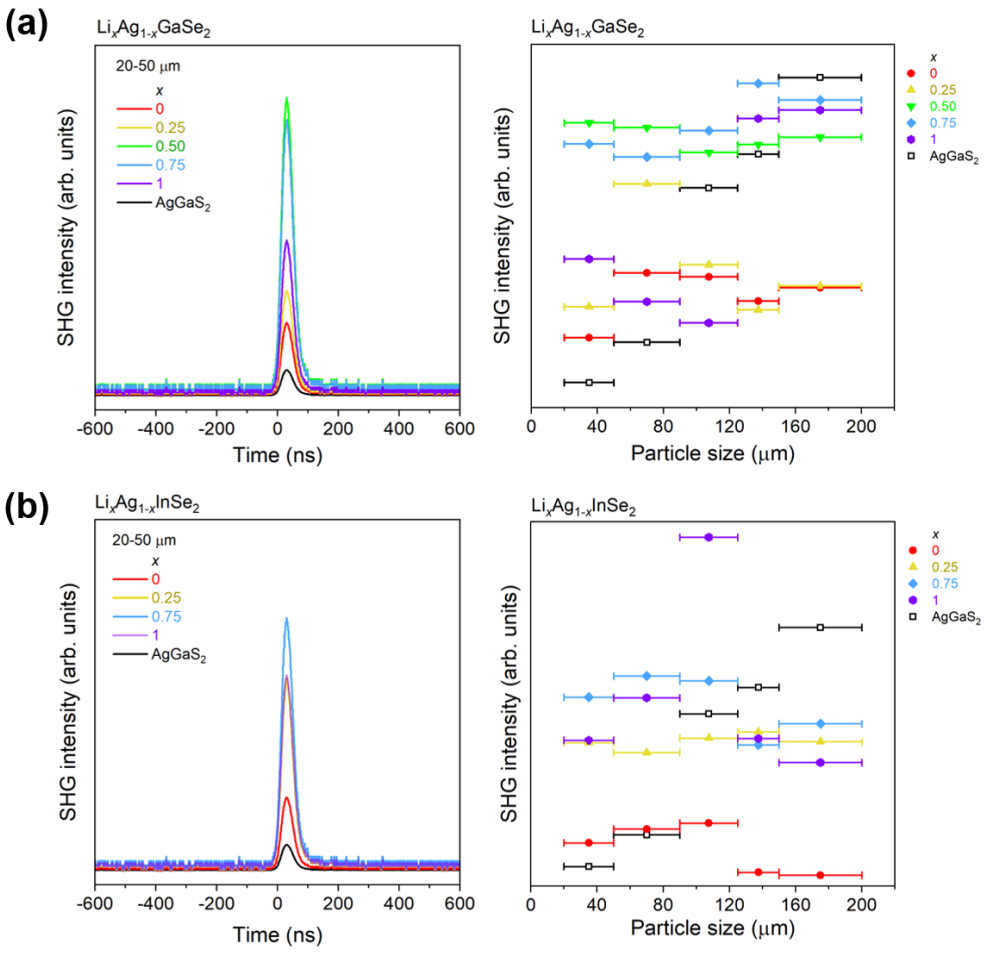

Figure 5-9. SHG intensities within particle sizes of 20–50 μm (left panels) and dependence on particle size ranges (right panels) for $Li_xAg_{1-x}GaSe_2$ and $Li_xAg_{1-x}InSe_2$, measured relative to $AgGaS_2$ using a laser source with a fundamental wavelength of 2090 nm.

Finally, it is worthwhile to compare the optical properties of the two forms of $LiGaSe_2$ more closely (Figure A4-4). Despite their different structures, the reflectance spectra are very similar, with absorption edges corresponding to 3.3 eV for both forms. They show strong SHG intensities (6× $AgGaS_2$ for the tetragonal and 12× $AgGaS_2$ for the orthorhombic form) for 20–50 μm particle sizes (Table A4-5), but do not exhibit type-I phase matching behaviour at 2090 nm. These results contradict reports by Cai et al. of a much lower band gap of 1.7 eV for tetragonal $LiGaSe_2$ and type-I phase matching behaviour at the same wavelength.[23] Given the nearly linear

trend in band gap as a function of Li content in $Li_xAg_{1-x}GaSe_2$ noted earlier (Figure 5-8), it is difficult to reconcile this discrepancy except perhaps to speculate that different synthetic conditions may have led to varying levels of defects. We contend that it is more likely that these polymorphs of $LiGaSe_2$ should have similar magnitudes of band gaps; after all, even the sphalerite and wurtzite forms of ZnS itself have similar band gaps (calculated 3.2–3.3 eV; measured 3.5–3.6 eV).[10]

5.3.3 Thermal Properties

The thermal stability of $Li_xAg_{1-x}GaSe_2$ and $Li_xAg_{1-x}InSe_2$ was assessed by DSC measurements (Figure 5-10). They show clear endothermic peaks upon heating and exothermic peaks upon cooling, with no other thermal events, indicating congruent melting behaviour. The melting points can be estimated from the location of the endothermic peaks, although the onset of melting can be about 20 °C lower. These melting points vary smoothly within the solid solutions (Figure 5-11). For the end-members, they generally agree well with literature values (850–860 °C for $AgGaSe_2$, 846 °C for orthorhombic $LiGaSe_2$, 787 °C for $AgInSe_2$, and 904 °C for $LiInSe_2$).[15,18,46,47] For $Li_xAg_{1-x}GaSe_2$, the melting point stays within a relatively narrow range, in agreement with previous observations (850±50 °C),[18] but it maximizes near $x = 0.75$. It is interesting that the tetragonal form of $LiGaSe_2$ also melts congruently, given that it is presumed to be metastable relative to the orthorhombic form. Further investigation, perhaps using much slower heating rates during the thermal analysis, may be helpful in understanding this behaviour. For $Li_xAg_{1-x}InSe_2$, the melting point varies linearly, increasing from 787 °C for $AgInSe_2$ to 910 °C for $LiInSe_2$. This trend agrees with naïve expectations that the ionic bonding character is enhanced with greater proportions of Li. Altogether, $Li_xAg_{1-x}GaSe_2$ and $Li_xAg_{1-x}InSe_2$ exhibit melting

points that remain relatively low, similar to those of other benchmark IR NLO materials, so that growth of large single crystals by other techniques will be feasible.

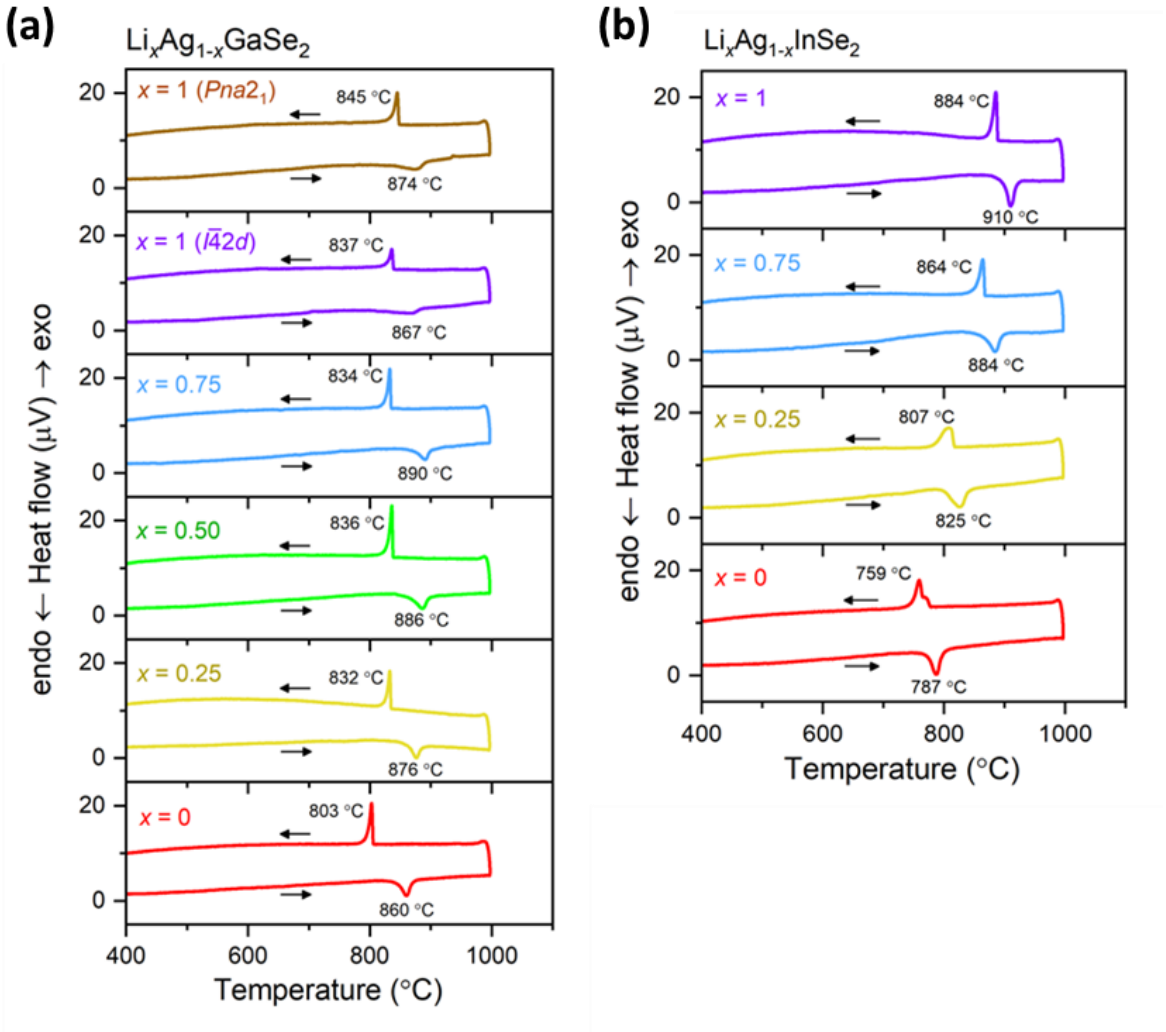

Figure 5-10. DSC curves for $Li_xAg_{1-x}GaSe_2$ and $Li_xAg_{1-x}InSe_2$.

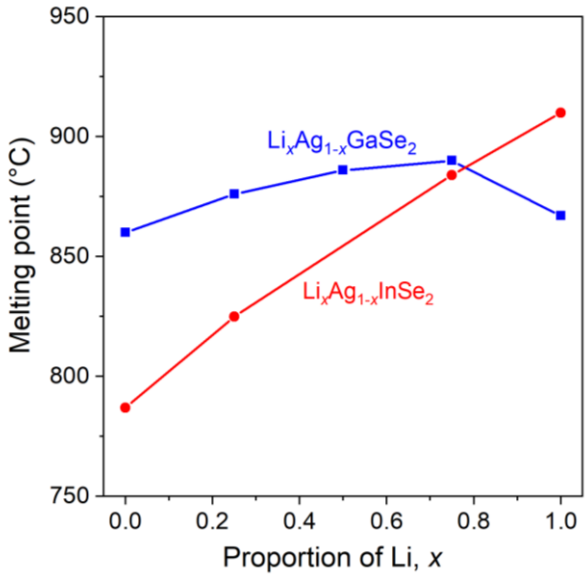

Figure 5-11. Dependence of melting point on Li content for $Li_xAg_{1-x}GaSe_2$ and $Li_xAg_{1-x}InSe_2$.

5.3.4 Electronic Structure

DFT calculations were performed on various ordered models of $Li_xAg_{1-x}GaSe_2$ and $Li_xAg_{1-x}InSe_2$ (Figure A4-5 and Figure A4-6). The electronic structure consists of valence and conduction bands separated by an energy gap which gradually broadens with increasing Li content. The valence band maxima and conduction band minima coincide at the Brillouin zone centre, indicating direct band gaps. The calculated band gaps are significantly underestimated compared to the experimental results (Table A4-3), as anticipated if standard pseudopotentials are used,[48] but the objective here was mainly to discern trends rather than to reproduce band gaps accurately. These calculations show that the band gap gradually increases in a nearly linear fashion as Li replaces Ag atoms, and for a given member (fixed x) of the Ga-containing solid solution $Li_xAg_{1-x}GaSe_2$, it is about 0.5 eV higher than for the In-containing counterpart $Li_xAg_{1-x}GaSe_2$, consistent with the experimental trends (Figure 5-8). Moreover, the computed band gaps are nearly identical (2.01–2.05 eV) for the tetragonal and orthorhombic forms of $LiGaSe_2$, supporting the experimental results noted earlier.

These results corroborate expectations from bonding considerations. The valence band is dominated by metal-chalcogen bonding interactions, whereas the conduction band is dominated by antibonding interactions. Then, gradual substitution of an alkali metal (Li) for a transition metal (Ag) introduces greater ionic character in the overall bonding, thereby weakening orbital interactions, making the bands less disperse, and widening the band gaps. The integrated COHP values (–ICOHP) show that Ga–Se or In–Se interactions form the largest contributions to the covalent bonding stability of these structures (Table A5-5). The integrated COBI (–ICOBI) values, which quantify the degree of covalency on a scale of 0 (ionic) to 1 (covalent), show considerable ionic character for Li–Se (0.14–0.15) and Ag–Se bonds (0.21–0.27), in contrast to the covalent character for Ga–Se (0.81–0.86) or In–Se bonds (0.77–0.81). Accordingly, as evident in the ELF plots, the electron density is highly localized around Li atoms, and to a lesser extent, Ag atoms, whereas it is shared in the region of between Ga and Se atoms, or between In and Se atoms (Figure A4-7).

5.4 Conclusions

A complete Ga-containing solid solution $Li_xAg_{1-x}GaSe_2$ could be prepared with the tetragonal $CuFeS_2$-type structure retained for the entire breadth; a key step in obtaining the tetragonal polymorph of the end-member $LiGaSe_2$ was relatively fast cooling from high temperatures. In contrast, the Li-containing solid solution $Li_xAg_{1-x}InSe_2$ undergoes transformation from the tetragonal $CuFeS_2$-type to the orthorhombic β-$NaFeO_2$-type structure as the Li content increases from $x = 0.50$ to $x = 0.75$. Through a combination of X-ray diffraction and ^{7}Li NMR experiments, the site distribution of metal atoms was confirmed, with Li atoms definitively occupying only one site in the crystal structures. The optical band gaps vary smoothly within these

solid solutions, increasing in a nearly linear fashion with higher Li content, as supported by electronic structure calculations. Contradicting previous reports, our results indicate that the tetragonal and orthorhombic polymorphs of $LiGaSe_2$ have nearly the same band gap of 3.3 eV. Under laser irradiation at 2090 nm, these Li-substituted compounds exhibit SHG intensities that are stronger or similar to those of the benchmark materials $AgGaS_2$ and $AgGaSe_2$, depending on the particle sizes. Given their larger band gaps, it would be worthwhile to measure laser-induced damage thresholds to assess the potential of these compounds as IR NLO materials. These compounds remain congruently melting at temperatures generally between 800 and 900 °C, so that growth of large single crystals, required for practical application, is feasible.

5.5 References

(1) Garmire, E. *Opt. Express* **2013**, *21*, 30532–30544.

(2) Chung, I.; Kanatzidis, M. G. *Chem. Mater.* **2014**, *26*, 849–869.

(3) Guo, S.-P.; Chi, Y.; Guo, G.-C. *Coord. Chem. Rev.* **2017**, *335*, 44–57.

(4) Liang, F.; Kang, L.; Lin, Z.; Wu, Y. *Cryst. Growth Des.* **2017**, *17*, 2254–2289.

(5) Wu, K.; Pan, S. *Coord. Chem. Rev.* **2018**, *377*, 191–208.

(6) Luo, X.; Li, Z.; Guo, Y.; Yao, J.; Wu, Y. *J. Solid State Chem.* **2019**, *270*, 674–687.

(7) Lin, H.; Wei, W.-B.; Chen, H.; Wu, X.-T.; Zhu, Q.-L. *Coord. Chem. Rev.* **2020**, *406*, 213150.

(8) Li, G.; Yang, Z.; Li, J.; Pan, S. *Chem. Commun.* **2020**, *56*, 11565.

(9) Chen, H.; Wei, W.-B.; Lin, H.; Wu, X.-T. *Coord. Chem. Rev.* **2021**, *448*, 214154.

(10) Liang, F.; Kang, L.; Lin, Z.; Wu, Y.; Chen, C. *Coord. Chem. Rev.* **2017**, *333*, 57–70.

(11) Chen, M.-M.; Xue, H.-G.; Guo, S.-P. *Chem. Rev.* **2018**, *368*, 115–133.

(12) Wang, W.; Mei, D.; Liang, F.; Zhao, J.; Wu, Y.; Lin, Z. *Coord. Chem. Rev.* **2020**, *421*, 213444.

(13) Zhou, W.; Zhang, Q.; Yao, W.-D.; Xue, H.; Guo, S.-P. *Inorg. Chem.* **2021**, *60*, 12536–12544.

(14) Yao, W.-D.; Cheng, X.; Guo, S.-P.; Whangbo, M.-H.; Ding, B.; Deng, S. *Chem. Mater.* **2023**, *35*, 1159–1167.

(15) Nikigosyan, D. N. Nonlinear Optical Crystals: A Complete Survey, Springer: New York, 2005.

(16) Zhou, H.-M.; Xiong, L.; Chen, L.; Wu, L.-M. *Angew. Chem. Int. Ed.* **2019**, *58*, 9979–9983.

(17) Yelisseyev, A.; Lobanov, S.; Molokeev, M.; Zhang, S.; Pugachev, A.; Lin, Z.; Vedenyapin, V.; Kurus, A.; Khamoyam, A.; Isaenko, L. *Adv. Opt. Mater.* **2021**, *9*, 2001856.

(18) Isaenko, L.; Dong, L.; Kurus, A.; Lin, Z.; Yelisseyev, A.; Lobanov, S.; Molokeev, M.; Korzhneva, K.; Goloshumova, A. *Adv. Opt. Mater.* **2022**, *10*, 2201727.

(19) Lobanov, S. I.; Korzhneva, K. E.; Gromilov, S. A.; Sukhikh, A. S.; Isaenko, L. I. *J. Cryst. Growth* **2023**, *604*, 127057.

(20) Zhou, W.; Yao, W.-D.; Zhang, Q.; Xue, H.; Guo, S.-P. *Inorg. Chem.* **2021**, *60*, 5198–5205.

(21) Zhou, W.; Wu, J.; Liu, W.; Guo, S.-P. *Coord. Chem. Rev.* **2023**, *477*, 214950.

(22) Bai, T.; Xing, S.; Li, C.; Shi, Z.; Feng, S. *Chem. Commun.* **2016**, *52*, 8581–8584.

(23) Cai, W.; Abudurusuli, A.; Xie, C.; Tikhonov, E.; Li, J.; Pan, S.; Yang, Z. *Adv. Funct. Mater.* **2022**, *32*, 2200231.

(24) Pöhls, J.-H.; Heyberger, M.; Mar, A. *J. Solid State Chem.* **2020**, *290*, 121557.

(25) Coelho, A. A. *TOPAS-Academic*, *version 6; Coelho Software*: Brisbane, Australia, **2007**.

(26) Sheldrick, G. M. *Acta Crystallogr. Sect. A* **2008**, *64*, 112–122.

(27) Gelato, L. M.; Parthé, E. *J. Appl. Crystallogr.* **1987**, *20*, 139–143.

(28) Bloch, F. *Phys. Rev.* **1946**, *70*, 460–474.

(29) Kortüm, G. *Reflectance Spectroscopy*; Springer: New York, 1969.

(30) Kurtz, S. K.; Perry, T. T. *J. Appl. Phys.* **1968**, *39*, 3798–3813.

(31) Clark, D. J.; Zhang, J.-H.; Craig, A. J.; Weiland, A.; Brant, J. A.; Cho, J. B.; Kim, Y. S.; Jang, J. I.; Aitken, J. A. *J. Alloys Compd.* **2022**, *917*, 165381.

(32) Okhotnikov, K.; Charpentier, T.; Cadars, S. *J. Cheminform.* **2016**, *8*, 17.

(33) Hafner, J. *J. Comput. Chem.* **2008**, *29*, 2044–2078.

(34) Perdew, J. P.; Burke, K.; Ernzerhof, M. *Phys. Rev. Lett.* **1996**, *77*, 3865–3868.

(35) Deringer, V. L.; Tchougréeff, A. L.; Dronskowski, R. *J. Phys. Chem. A* **2011**, *115*, 5461–5466.

(36) Maintz, S.; Deringer, V. L.; Tchougréeff, A.L.; Dronskowski, R. *J. Comput. Chem.* **2013**, *34*, 2557–2567.

(37) Grin, Y.; Savin, A.; Silvi, B.; The ELF perspective of chemical bonding. In *The Chemical Bond: Fundamental Aspects of Chemical Bonding*; Frenking, G., Shaik, S., Eds.; Wiley-VCH, Weinheim, 2014, pp. 345−382.

(38) Maintz, S.; Deringer, V. L.; Tchougréeff, A. L.; Dronskowski, R. *J. Comput. Chem.* **2016**, *37*, 1030–1035.

(39) Shannon, R. D. *Acta Crystallogr. Sect. A* **1976**, *32*, 751–767.

(40) Yelisseyev, A.; Liang, F.; Isaenko, L.; Lobanov, S.; Goloshumova, A.; Lin, Z.S. *Opt. Mater.* **2017**, *17*, 795–804.

(41) Villars, P.; Cenzual, K. *Pearson's Crystal Data – Crystal Structure Database for Inorganic Compounds (on DVD)*, Release 2021/22; ASM International: Materials Park, OH, USA.

(42) Brese, N. E.; O'Keeffe, M. *Acta Crystallogr. Sect. B* **1991**, *47*, 192–197.

(43) Lemoine, P.; Guélou, G.; Raveau, B.; Guilmeau, E. *Angew. Chem. Int. Ed.* **2022**, *61*, e202108686.

(44) Frenzel, N.; Frisch, G. *Z. Anorg. Allg. Chem.* **2022**, *648*, e202200148.

(45) Michaelis, V. K.; Levin, K.; Germanov, Y.; Lelong, G.; Kroeker, S. *Chem. Mater.* **2018**, *30*, 5521–5526.

(46) Ivashchenko, I. A.; Zimy, O. F.; Olekseyuk, I. D. *Chem. Met. Alloys* **2008**, *1*, 274–282.

(47) Kamijoh, T.; Kuriyama, K. *J. Cryst. Growth* **1981**, *51*, 6–10.

(48) Xiao, H.; Tahir-Kheli, J.; Godard, W. A., III. *Phys. Chem. Lett.* **2011**, *2*, 212–217.

Chapter 6.

Structure and Optical Properties of $Li_xAg_{1-x}AlSe_2$

Manuscript in preparation.

Jomaa, M.; Mishra, V.; Sarkar, D.; Sun, M.; Yao, J.; Michaelis, V. K.; Mar. A.

6.1 Introduction

Ternary chalcogenides with the general formula A^I–B^{III}–C^{VI}_2 (A = Li, Cu, Ag; B = Al, Ga, In; C = S, Se, Te), which are semiconductors with band gaps ranging from 0.9 to 4.0 eV,[1,2] have emerged as attractive candidates for optoelectronic and infrared nonlinear optical (IR NLO) devices.[3–6] They crystallize in related noncentrosymmetric diamond-like structures built up from metal-centred tetrahedra with different stacking sequences of the anions.[7,8] Most of the Li-containing compounds adopt the orthorhombic β-$NaFeO_2$-type structure ($Pna2_1$), which is a superstructure of the wurtzite-type structure ($P6_3mc$), based on hexagonal closest packing of anions. The Cu- or Ag-containing compounds crystallize exclusively in the tetragonal $CuFeS_2$-type or chalcopyrite structure ($I\bar{4}2d$), which is a superstructure of the sphalerite or zincblende structure ($F\bar{4}3m$), based on cubic closest packing of anions.[9–11]

Most studies on these chalcogenides have focused on the Cu- or Ag-containing compounds: $CuGaSe_2$ and $CuInSe_2$ are well known light-absorbing materials for thin film solar cells, and $AgGaS_2$ and $AgGaSe_2$ are benchmark IR NLO materials.[12,13] In contrast, the Li-containing compounds have been less well investigated, probably because of challenges associated with their synthesis and characterization, including their crystal growth, air sensitivity, and location of Li atoms. The Li-containing compounds tend to have larger band gaps than the Cu- or

Ag-containing ones (e.g., 3.6 eV for $LiGaSe_2$, 1.7 eV for $CuGaSe_2$, 1.8 eV for $AgGaSe_2$).[1,14,15] For practical application of IR NLO materials, a high laser damage induced threshold is desirable and can be achieved with materials with larger band gaps,[2,8] but this usually results in lower NLO efficiencies.[16] Many efforts have been made to substitute alkali or alkaline earth metals to find new candidates that can balance the competing requirements of a high laser damage induced threshold and a large second harmonic generation response.[17–21]

It seems reasonable to expect this balance can be achieved in solid solutions with Li substituting for Cu or Ag atoms, all of which are monovalent and have similar preferences for tetrahedral geometry. Several of these solid solutions have been previously investigated, including $Li_xCu_{1-x}InSe_2$ (x = 0–0.40),[22] $Li_xAg_{1-x}GaS_2$, in which a transition takes place from tetragonal (x = 0–0.60) to orthorhombic structures (past x = 0.70),[23] and $Li_xAg_{1-x}GaSe_2$ (x = 0–0.90).[24] In our own recent work, we demonstrated that a complete solid solution $Li_xAg_{1-x}GaSe_2$ (x = 0–1.00) can be formed and that $Li_xAg_{1-x}InSe_2$ undergoes a transition from tetragonal (x = 0–0.50) to orthorhombic structures (x = 0.60–1.00).

The Al-containing analogues appear to have been less well studied. Given that $AgAlSe_2$ adopts a tetragonal structure and $LiAlSe_2$ adopts an orthorhombic one,[2,25,26] it can be hypothesized that a structural transition will also take place within the solid solution $Li_xAg_{1-x}InSe_2$. Here, we report on the synthesis, structure determination, and optical properties of this solid solution.

6.2 Experimental

6.2.1 Synthesis

Starting materials were Ag powder (99.9%, Aldrich), Li ribbon (99.9%, Aldrich), Al powder (99.5%, Alfa Aesar), and Se powder (99.5%, Onyxmet). The Li ribbon was handled and

cut within an argon-filled glove box, and its surface was carefully scraped to remove any contaminants before use. Various members of the solid solution $Li_xAg_{1-x}AlSe_2$ were prepared from stoichiometric mixtures of the elements with a total mass of 0.400 g. First, Ag, Al, and Se were ground together, pressed into pellets, and loaded them into carbon-coated fused silica tubes. Then, the tubes were transferred to an argon-filled glove box and Li was added to the tubes. The tubes were evacuated, sealed, and placed in a furnace where they were heated to 850 °C at a rate of 15 °C h^{-1}, held at this temperature for 45 h, and cooled down to room temperature at 15 °C h^{-1}.

Powder X-ray diffraction (XRD) patterns of the ground samples were collected on a Bruker D8 Advance powder diffractometer, equipped with a SSD160 detector and a Cu *K*α radiation source operated at 40 kV and 40 mA. The experimental XRD patterns were analyzed with the use of the TOPAS Academic software package.[27] The background was modeled by a twelve-term polynomial function and a Pawley fit was applied.[28] From these patterns, refined cell parameters were extracted.

Samples were examined on a Zeiss Sigma 300 VP field-emission scanning electron microscope, operated with an accelerating voltage of 15 kV and equipped with a Bruker Quantax 600 system with dual X-Flash 6/60 detectors. Energy-dispersive X-ray (EDX) analysis was performed on several points and areas on the samples to determine their elemental composition. However, Li is undetectable by this technique, and the quantification of Al and Se was challenging because their emission peaks (Al *K*α and Se *L*α) overlap. Nevertheless, the combined amounts of Al and Se were consistent with the expected compositions.

6.2.2 Structure determination

Intensity data were collected on suitable crystals of $Li_{0.25}Ag_{0.75}AlSe_2$, $Li_{0.50}Ag_{0.50}AlSe_2$, and $Li_{0.75}Ag_{0.25}AlSe_2$ on a Bruker PLATFORM diffractometer equipped with a SMART APEX II CCD area detector and a graphite-monochromated Mo $K\alpha$ radiation source, using ω scans at various φ angles with a frame width of 0.3° and an exposure time of 15 s per frame. Face-indexed numerical absorption corrections were applied. Structure solution and refinement were carried out with the use of the SHELXTL (version 2018/3) program package.[29] Based on Laue symmetry, intensity statistics, and systematic absences, the tetragonal space group $I\bar{4}2d$ was chosen for $Li_{0.25}Ag_{0.75}AlSe_2$ and $Li_{0.50}Ag_{0.50}AlSe_2$, and the orthorhombic space group $Pna2_1$ was chosen for $Li_{0.75}Ag_{0.25}AlSe_2$. Disorder of Li and Ag atoms within the same site was modeled by constraining the sum of their occupancies to unity. The final refinements led to reasonable atomic displacement parameters, sensible bond lengths, and excellent agreement factors. Atomic positions were standardized using the program STRUCTURETIDY.[30]

6.2.3 Solid-state ^{7}Li NMR spectroscopy

Solid-state ^{7}Li NMR experiments were performed on a Bruker 400 MHz (B_0 = 9.4 T) Avance III HD NMR spectrometer, equipped with a 4 mm double resonance H-X magic angle spinning (MAS) probe with $\omega_0/2\pi(^7\text{Li})$ = 155.6 MHz. Samples with a mass of 50–100 mg were ground and packed into ZrO_2 rotors (4 mm o.d.) sealed with Kel-F caps. The spectra were acquired using a Bloch decay sequence with a 4.0 μs π/2 pulse ($\gamma B_1/2\pi$ = 62.5 kHz), a recycle delay of 10–15 s, 4–128 co-added transients, and a MAS frequency of 14 kHz. All NMR spectra were referenced to 0.0 ppm for a 1.0 M LiCl (aq) solution. The spectra were processed using the Bruker Topspin 4.1.1 software package.

6.2.4 Optical measurements

Optical diffuse reflectance spectra were measured from 200 nm (6.2 eV) to 1500 nm (0.82 eV) on an Agilent Cary 5000 UV-vis-NIR spectrophotometer equipped with a reflectance accessory. A compacted pellet of polytetrafluoroethylene was used as a 100% reflectance standard. The reflectance spectra were converted to optical absorption spectra using the Kubelka–Munk function, $F(R) = \alpha/S = (1–R)^2/2R$, where $F(R)$ denotes the ratio of absorption coefficient α and scattering coefficient S, and R is the reflectance.

Transmission IR spectra were measured from 400 cm^{-1} to 4000 cm^{-1} on an Excalibur 3100 Fourier transform IR spectrometer. The samples were ground with KBr powder in a mass ratio of 1:100.

Optical SHG intensities was estimated by the Kurtz–Perry technique using a fundamental light of 2090 nm with a Q-switch Ho:Tm:Cr:YAG laser.[31] Ground samples were sieved into five particle sizes ranges between 20 and 200 μm. These samples with different particle sizes were then loaded into custom holders with a thickness of 0.5 mm. Microcrystals of the benchmark material $AgGaS_2$ with similar particle sizes served as the reference.

6.2.5 Electronic structure calculations

Ordered models for various members of the solid solution $Li_xAg_{1-x}AlSe_2$ were generated using the program Supercell (version 2.0).[32] Electronic structure calculations were performed using the projected augmented wave (PAW) method as implemented in the Vienna ab initio simulation package (VASP, version 5.4.4).[33–35] Exchange and correlation were treated in this density functional theory (DFT) method by the generalized gradient approximation, as parameterized by Perdew, Burke, and Ernzerhof.[36–38] The recommended PAW potentials (Li_sv, Al, Ag, Se) were used, with the plane-wave basis cut-off energy set to 650 eV. The first Brillouin

zone was sampled by a gamma-centered 17 × 17 × 9 *k*-mesh for density of states (DOS) calculations. The convergence criteria were set to 10^{-8} eV for electronic optimization and $|-2 \times 10^{-2}|$ eV for ionic relaxation. Electron localization functions (ELF), projected crystal orbital Hamilton populations (−pCOHP), and crystal orbital bond indices (COBI) were determined using the program LOBSTER (version 4.1.0).[39–43]

6.3 Results and discussion

6.3.1 Structural analysis

Members of the solid solution $Li_xAg_{1-x}AlSe_2$ were synthesized by reaction of the elements at 850 °C. Powder XRD patterns indicate that all samples are single-phase, corresponding to the tetragonal $CuFeS_2$-type structure for $x = 0$–0.50 and the orthorhombic β-$NaFeO_2$-type for $x = 0.60$–1.00, with gradual shifts in peak positions to higher angles as the Li content x increases (Figure 6-1). From Pawley fittings of these XRD patterns (Figure A5-1), the tetragonal and orthorhombic cell parameters were refined (Table 6-1). Consistent with the relative sizes (cf. Shannon ionic radii of 1.00 Å for Ag^+ and 0.59 Å for Li^+ in CN4), the unit cell contracts nearly linearly with greater Li content, in agreement with Vegard's law (Figure 6-2).

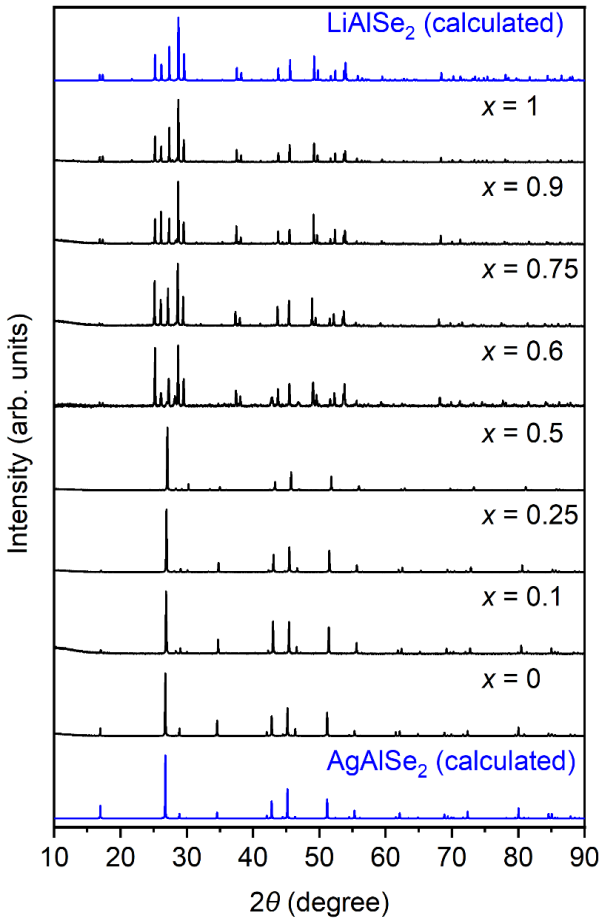

Figure 6-1. Powder XRD patterns for $Li_xAg_{1-x}AlSe_2$.

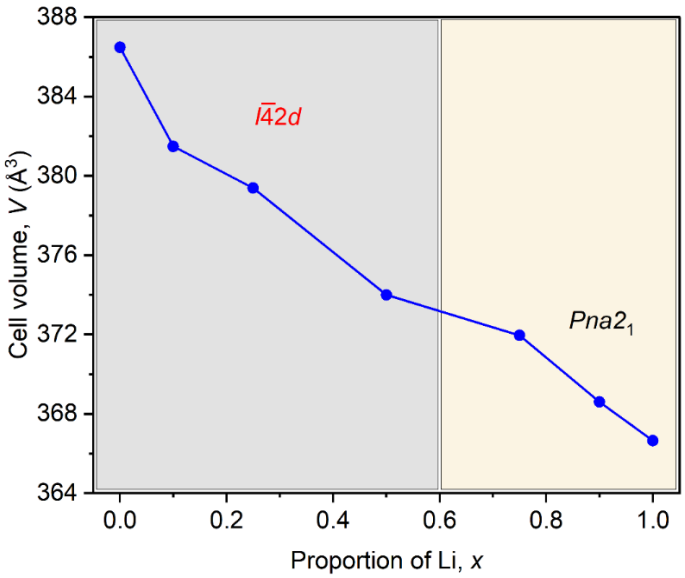

Figure 6-2. Dependence of unit cell volume on Li content for $Li_xAg_{1-x}AlSe_2$.

Table 6-1. Cell Parameters and Refinement Results for $Li_xAg_{1-x}AlSe_2$

Compound	space group	a (Å)	b (Å)	c (Å)	V (Å^3)	R_p	R_{wp}
$AgAlSe_2$	$I\bar{4}2d$	5.974(1)		10.830(1)	386.48	0.094	0.127
$Li_{0.10}Ag_{0.90}AlSe_2$	$I\bar{4}2d$	5.9490(3)		10.7791(2)	381.48	0.102	0.137
$Li_{0.25}Ag_{0.75}AlSe_2$	$I\bar{4}2d$	5.941(1)		10.750(1)	379.38	0.085	0.115
$Li_{0.50}Ag_{0.50}AlSe_2$	$I\bar{4}2d$	5.909(1)		10.7129(1)	374.00	0.084	0.120
$Li_{0.75}Ag_{0.25}AlSe_2$	$Pna2_1$	6.854(5)	8.266(3)	6.5652(7)	371.95	0.083	0.110
$Li_{0.90}Ag_{0.10}AlSe_2$	$Pna2_1$	6.826(1)	8.2687(5)	6.5305(4)	368.60	0.097	0.135
$LiAlSe_2$	$Pna2_1$	6.808(6)	8.264(3)	6.517(5)	366.65	0.098	0.138

To examine structural changes in more detail, single-crystal X-ray diffraction studies were performed on $Ag_{0.75}Li_{0.25}AlSe_2$, $Ag_{0.50}Li_{0.50}AlSe_2$, and $Ag_{0.25}Li_{0.75}AlSe_2$. Table 6-2 lists crystal data, Table 6-3 lists atomic and displacement parameters, and Table 6-4 lists ranges of interatomic distances. The tetragonal structure of $Li_{0.25}Ag_{0.75}AlSe_2$ and $Li_{0.50}Ag_{0.50}AlSe_2$ contains three sites, with disordered Li and Ag atoms at 4*b*, Al atoms at 4*a*, and Se atoms at 8*d*. The orthorhombic structure of $Li_{0.75}Ag_{0.25}AlSe_2$ contains four sites, all in 4a, comprising one disordered Li/Ag site, one Al site, and two Se sites.

Table 6-2. Crystallographic Data for $Li_xAg_{1-x}AlSe_2$

nominal composition	$Li_{0.25}Ag_{0.75}AlSe_2$	$Li_{0.50}Ag_{0.50}AlSe_2$	$Li_{0.75}Ag_{0.25}AlSe_2$
formula mass (amu)	267.54	242.30	217.07
refined composition	$Li_{0.337(5)}Ag_{0.663(5)}AlSe_2$	$Li_{0.595(5)}Ag_{0.405(5)}AlSe_2$	$Li_{0.802(7)}Ag_{0.198(7)}AlSe_2$
space group	$I\bar{4}2d$ (No. 122)	$I\bar{4}2d$ (No. 122)	$Pna2_1$ (No. 33)
a (Å)	5.943(2)	5.9156(6)	6.845(5)
b (Å)	5.943(2)	5.9156(6)	8.305(6)
c (Å)	10.778(6)	10.7295(13)	6.576(5)
V (Å^3)	380.7(4)	375.47(8)	373.8(4)
Z	4	4	4
T (K)	296(2)	296(2)	296(2)
ρ_{calcd} (g cm^{-3})	4.668	4.286	3.857
crystal dimensions (mm)	0.12 × 0.10 × 0.07	0.15 × 0.09 × 0.08	0.10 × 0.10 × 0.08
μ(Mo $K\alpha$) (mm^{-1})	23.14	22.19	21.02
transmission factors	0.056–0.160	0.339–0.481	0.543–0.746
2θ limits	7.84–58.32°	7.86–58.62°	7.72–58.74°
data collected	$-8 \le h \le 8$, $-8 \le k \le 8$, $-14 \le l \le 14$	$-8 \le h \le 8$, $-8 \le k \le 8$, $-14 \le l \le 14$	$-9 \le h \le 9$, $-11 \le k \le 11$, $-9 \le l \le 9$
no. of data collected	2153	5402	8397
no. of unique data, including $F_o^2 < 0$	262 (R_{int} = 0.043)	262 (R_{int} = 0.045)	1024 (R_{int} = 0.080)
no. of unique data, with $F_o^2 > 2\sigma(F_o^2)$	255	256	828
no. of variables	12	12	39
Flack parameter	0.003(4)	0.03(4)	0.06(6)
$R(F)$ for $F_o^2 > 2\sigma(F_o^2)$ [a]	0.023	0.037	0.047
$R_w(F_o^2)$ [b]	0.049	0.099	0.108
goodness of fit	1.10	1.33	1.11
$(\Delta\rho)_{max}$, $(\Delta\rho)_{min}$ (e Å^{-3})	0.56, −0.63	0.89, −0.70	2.2, −2.6

[a] $R(F) = \sum||F_o| - |F_c|| / \sum|F_o|$.

[b] $R_w(F_o^2) = [\sum[w(F_o^2 - F_c^2)^2] / \sum wF_o^4]^{1/2}$; $w^{-1} = [\sigma^2(F_o^2) + (Ap)^2 + Bp]$, where $p = [\max(F_o^2,0) + 2F_c^2]/3$.

Table 6-3. Atomic Coordinates and Equivalent Isotropic Displacement Parameters for $Li_xAg_{1-x}AlSe_2$

atom	Wyckoff position	occupancy	*x*	*y*	*z*	U_{eq} (Å^2)
$Li_{0.25}Ag_{0.75}AlSe_2$						
Li/Ag	4*b*	0.337(5) Li, 0.663(5) Ag	0	0	0	0.033(1)
Al	4*a*	1	0	0	½	0.014(1)
Se	8*d*	1	0.2828(2)	¼	⅛	0.019(1)
$Li_{0.50}Ag_{0.50}AlSe_2$						
Li/Ag	4*b*	0.595(5) Li, 0.405(5) Ag	0	0	0	0.031(1)
Al	4*a*	1	0	0	½	0.015(1)
Se	8*d*	1	0.2790(2)	¼	⅛	0.020(1)
$Li_{0.75}Ag_{0.25}AlSe_2$						
Li/Ag	4*a*	0.802(7) Li, 0.198(7) Ag	0.0839(9)	0.1241(7)	0.1126(8)	0.028(2)
Al	4*a*	1	0.0733(8)	0.6253(6)	0.1155(10)	0.026(2)
Se1	4*a*	1	0.0947(2)	0.1376(2)	0.4774(2)	0.020(1)
Se2	4*a*	1	0.4367(2)	0.1151(2)	0	0.020(1)

Table 6-4. Interatomic Distances (Å) for $Li_xAg_{1-x}AlSe_2$

	$Li_{0.25}Ag_{0.75}AlSe_2$	$Li_{0.50}Ag_{0.50}AlSe_2$	$Li_{0.75}Ag_{0.25}AlSe_2$
Li/Ag−Se	2.617(1) (×4)	2.5905(7) (×4)	2.402(6), 2.501(6), 2.527(6), 2.648(6)
Al−Se	2.3528(8) (×4)	2.3863(6) (×4)	2.332(5), 2.450(6), 2.454(5), 2.531(7)

In both types of structures, all the metal atoms are surrounded by Se atoms in tetrahedral coordination. These tetrahedra share corners to form 3D networks (Figure 6-3). The tetragonal $CuFeS_2$-type structure has a doubled cell relative to cubic sphalerite, whereas the orthorhombic β-$NaFeO_2$-type structure as a quadrupled cell relative to hexagonal wurzite. Correspondingly, the Se atoms are arranged in close packed nets which stack in the sequence ABC (cubic closest

packing) in the $CuFeS_2$-type structure and AB (hexagonal closest packing) in the orthorhombic β-$NaFeO_2$-type structure. The Li/Ag–Se and Al–Se distances are consistent with the sum of ionic radii (IR values of 0.59 Å for Li^{1+} (CN4), 1.0 Å for Ag^{1+} (CN4), 0.39 Å for Al^{3+} (CN4), and 1.98 Å for Se^{2-} (CN4)) and with typical values found for Li–Se (2.45–2.65 Å), Ag–Se (2.60–2.90 Å), and Al–Se bond lengths (2.30–2.43 Å).[44]

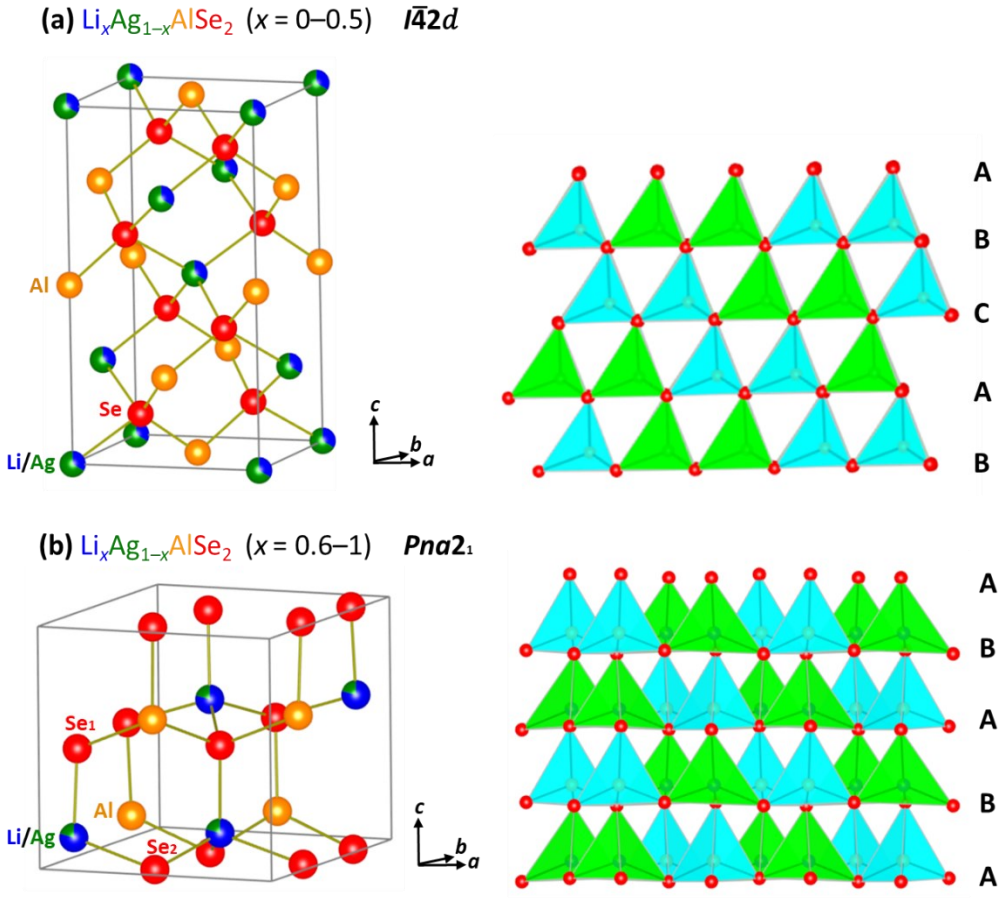

Figure 6-3. Structures of $Li_xAg_{1-x}AlSe_2$. The left panels show the unit cell contents. The right panels contrast the arrangement of metal-centred tetrahedra, with ccp stacking of Se anions in the tetragonal $CuFeS_2$-type structure and hcp stacking in the orthorhombic β-$NaFeO_2$-type structure.

The ^7Li MAS NMR spectra of $Li_xAg_{1-x}AlSe_2$ samples show narrow single resonances, in support of a unique Li site in these compounds (Figure 6-4). The chemical shifts are 0.4 to 2.4 ppm and the linewidths are 203 to 327 Hz (). These spectra are similar to that of $LiAlSe_2$, and the

small chemical shifts relative to LiCl indicate that the Li atoms participate in bonds with ionic character and do not experience any Knight shifts.[45]

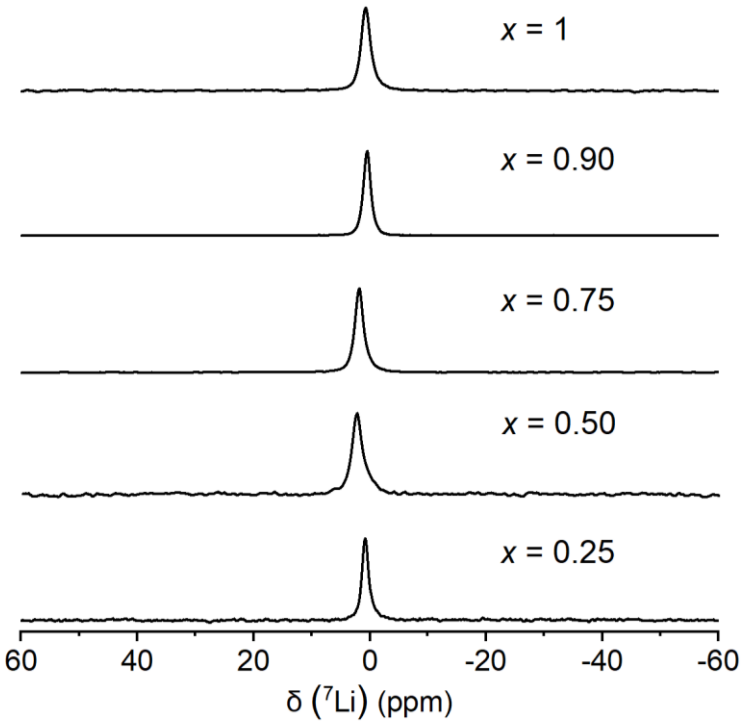

Figure 6-4. ^{7}Li-MAS NMR spectra of $Li_xAg_{1-x}AlSe_2$.

6.3.2 Optical properties

Optical band gaps for $Li_xAg_{1-x}AlSe_2$ were obtained from absorption spectra converted from UV−vis−NIR diffuse reflectance spectra (Figure 6-5). The band gap gradually increases from 2.7 to 3.6 eV on progressing from $AgGaSe_2$ to $LiAlSe_2$ (Table A5-2). For the end-members, these values agree well with previously reported results (2.6 eV for $AgAlSe_2$ and 3.6 eV for $LiAlSe_2$).[26,46] The IR transmission spectra show a wide range of optical transparency from 2.5 to 25 μm (Figure A5-2). Only weak absorption peaks due to atmospheric H_2O and CO_2 are present.

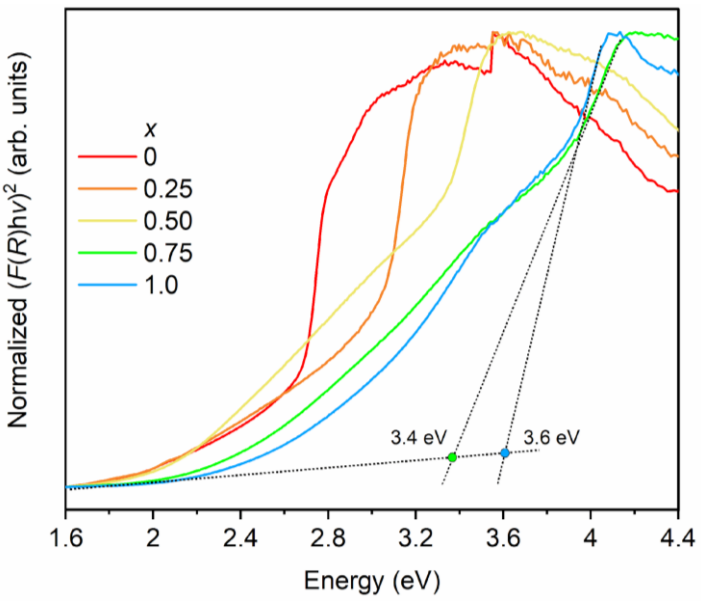

Figure 6-5. Optical diffuse reflectance spectra for $Li_xAg_{1-x}AlSe_2$.

Optical SHG signals of $Li_xAg_{1-x}AlSe_2$ were measured on powder samples using a fundamental laser wavelength of 2090 nm and compared with $AgGaS_2$ as a benchmark (Table A5-3**Table**). At the smallest particle size range of 20–50 μm, the SHG efficiencies are about 0.4 to 2.6 times that of $AgGaS_2$. At other particle sizes, some samples gave weak signals. Some of these data may need to be re-evaluated toJOMAA ensure that samples did not degrade when the measurement was performed. The dependence on particle size is rather irregular, suggesting that these compounds are not type-I phase-matchable at this wavelength. It should be noted that the phase-matching condition is dependent on the wavelength, and thus, these compounds may display phase-matching behaviour in a different wavelength range.

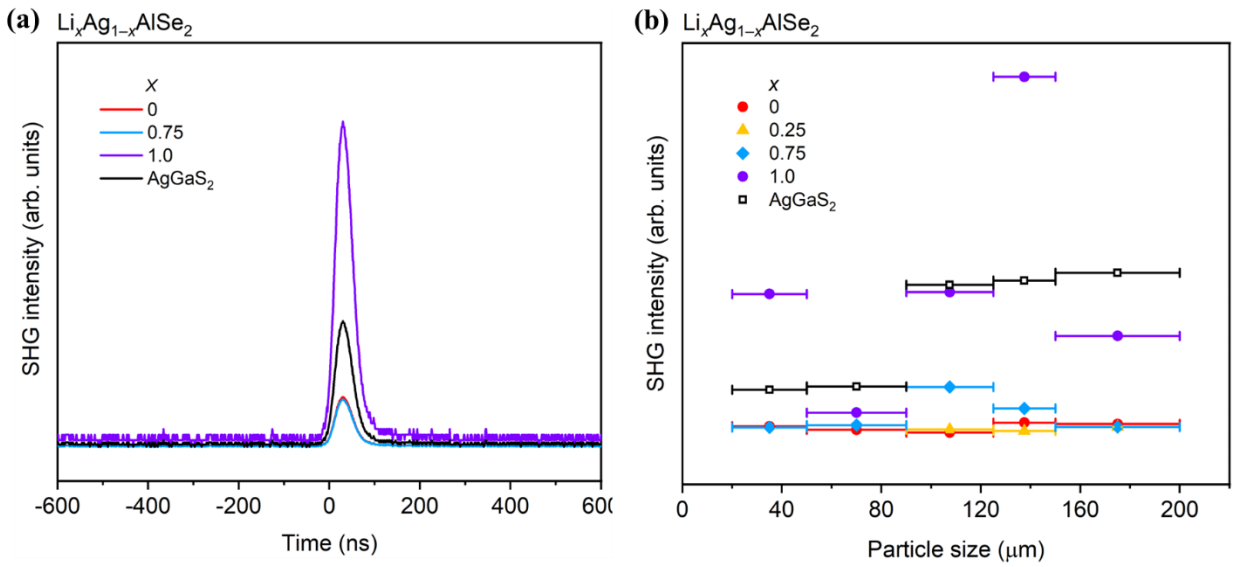

Figure 6-6. (a) SHG intensities of $Li_xAg_{1-x}AlSe_2$ within particle sizes of 20–50 μm relative to $AgGaS_2$ using a laser source with a fundamental wavelength of 2090 nm. (b) Dependence on particle size range.

6.3.3 Electronic structure

To understand the effect of Li substitution on electronic properties of these compounds, DFT calculations were performed on ordered models of $Li_xAg_{1-x}AlSe_2$ (Figure A5-4(a)). The band dispersion diagrams reveal that the band gap remains direct throughout the entire breadth of solid solution, with the valence band maxima and conduction band minima lying at the Brillouin zone center Γ. The calculated band gaps for the $Li_xAg_{1-x}AlSe_2$ are lower than those observed experimentally, as it is well known that they are underestimated if standard pseudopotentials are used (Table A5-2). However, the trend is consistent with the experimental results (Figure 6-7), and the calculated values for the end-members are close to those reported in the literature (1.2–1.7 eV for $AgAlSe_2$, 2.6–3.3 eV for $LiAlSe_2$).[47–51]

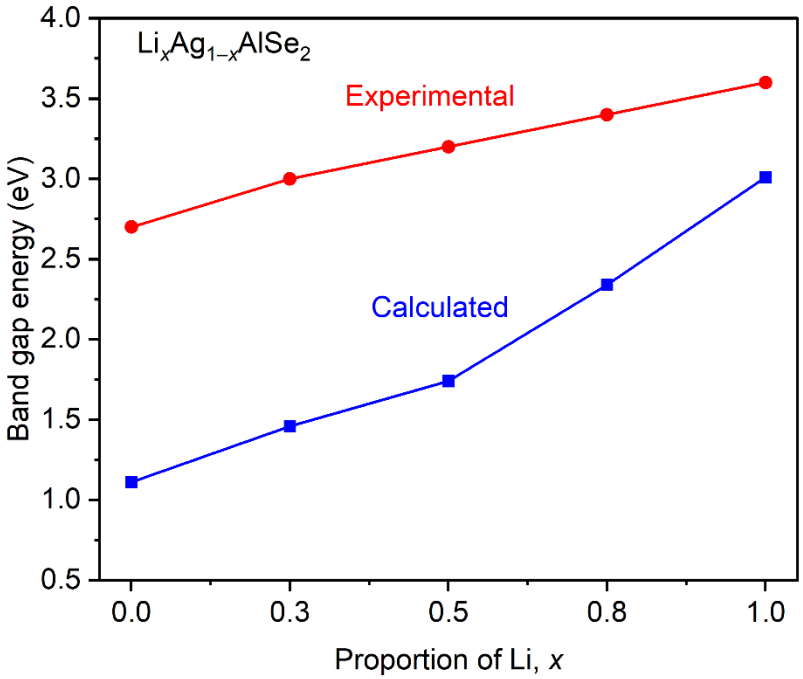

Figure 6-7. Experimental and calculated band gaps for $Li_xAg_{1-x}AlSe_2$.

The DOS and −COHP curves show that the top of the valence band is dominated by Ag 4d and Se 4p antibonding states, and the bottom of the conduction band by Se 4p and Al 3p states (Figure A5-4(b)). The magnitude of the band gap is strongly controlled by demarcation of Ag–Se bonding and antibonding levels. Substitution with smaller Li atoms tends to contract the whole structure, enhancing these Ag–Se interactions so that the energy separation between bonding and antibonding levels becomes even larger.

The integrated −pCOHP values (−IpCOHP) are relatively small for the Li–Se interactions (0.85–0.95 eV/bond) and Ag–Se interactions (1.17–2.44 eV/bond), indicating weakly covalent interactions (Table A5-4). The Al–Se bonds are considerably stronger, with –IpCOHP values of 4.88–5.07 eV/bond. COBI values were evaluated to quantify the bonding character, on a scale of 0 (ionic) to 1 (covalent).[52] Consistent with expectations, Li–Se bonding exhibits the highest degree of ionicity (0.14–0.15 eV/bond), followed by Ag–Se (0.20–0.27 eV/bond), while Al–Se bonds are

highly covalent (0.80–0.84 eV/bond) (Table A5-5). The results are further supported by the ELF plots (Figure A5-5). Electron density is highly concentrated around Se atoms, and the region between Ag and Se atoms shows low electron density (green blue colour). Upon substitution of Ag by Li atoms, the electron Ag by Li, the electron density becomes even more localized around Se, suggesting more ionic Li–Se bonds. In contrast, the electron density between Al and Se atoms is intermediate (yellow green colour), indicating covalent Al–Se bonds.

6.4 Conclusion

The solid solution $Li_xAg_{1-x}AlSe_2$ undergoes a transition from the tetragonal $CuFeS_2$-type (x = 0–0.5) to the orthorhombic β-$NaFeO_2$-type structure (x = 0.6–1.0). They possess large band gaps which increase linearly from 2.7 to 3.6 eV, show wide IR transparency, and exhibit strong SHG responses (up to 12× $AgGaS_2$) within particle sizes of 20–50 μm under laser irradiation at 2090 nm. Further investigation of laser induced damage thresholds, and confirmation of the SHG responses would be worthwhile to evaluate their potential as NLO materials.

6.5 References

(1) Zunger, J. E.; Zunger, A. *J. Phys. Rev. B* **1984**, *29*, 1882–1906.

(2) Kim, J.; Hughbanks, T. *Inorg. Chem.* **2000**, *39*, 3092–3097.

(3) Kim, S.; Lee, M.; Hong, C.; Yoon, Y.; An, H.; Lee, D.; Jeong, W.; Yoo, D.; Kang, Y.; Youn, Y.; Han, S. H. *Sci. Data* **2002**, *7*, 1–6.

(4) Albornoz, J. G.; Rojas L. R. M.; Merino, J. M.; León, M. *J. Phys. Chem. Solids* **2014**, *75*, 1–7.

(5) Zeng, Y.;Chua, S. J.; Wu, P. *Chem. Mater.* **2002**, *14*, 2989–2998.

(6) Khan, A.; Sajjad, M.; Murtaza, G.; Laref, A. *Z. Naturforsch. A* **2018**, *73*, 645–655.

(7) Kodigala, S. R. Optical Properties of I–III–VI2 Compounds. In *Thin Films and Nanostructures*; Kodigala, S.R., Ed. New York, USA, 2010, 35, pp. 195–317.

(8) Isaenko, L.; Yelisseyev, A.; Lobanov, S.; Titov, A.; Petrov, V.; Zondy, J. J.; Krinitsin, P.; Merkulov, A.; Vedenyapin, V.; Smirnova, J. *Cryst. Res. Technol*. **2003**, *38*, 379−387.

(9) Kosobutsky, A. V.; Basalaev, Y. M. *Solid State Commun.* **2014**, *199*, 17–21.

(10) Shewchun, J.; Loferski, J. J.; Beaulieu, R.; Chapman, G. H.;Garside, B. K. *J. Appl. Phys*. **1979**, *50*, 6978– 6985.

(11) Omata, T.; Nagatani, H.; Suzuki, I.; Kita, M. *Sci. Technol. Adv. Mater.* **2015**, *16*, 024902.

(12) Shafarman, W. N.; Klenk, R.; McCandless, B. E. *J. Appl. Phys.* **1996**, *79*, 7324–7328.

(13) Tinoco, T.; Polian, A.; Itié, J. P.; Moya, E.; Gonzalez, J. *J. Phys. Chem. Solids* **1995**, *56*, 481–484.

(14) Petrov, V.; Yelisseyev, A.; Isaenko, L.*;* S. Lobanov, Titov, A.; Zondy, J.-J. *Appl. Phys. B* **2004**, *78*, 543–546.

(15) Jung, S. Il., Yoon, K. H.; Ahn, S.; Gwak, J.; Yun, J. H. *Curr. Appl. Phys.* **2010**, *10*, S395–S398.

(16) Li, S.-F.; Jiang, X.-M.; Fan, Y.-H.; Liu, B.-W.; Zeng, H.-Y.; Guo, G.-C. *Chem. Sci.* **2018**, *9*, 5700–5708.

(17) Orlova, N. S., Kochkarik, O. E.; Bodna, I. V. *Cryst. Res. Technol*. **1994**, *29*, 561–568.

(18) Yelisseyev, A. P.; Molokeev, M. S.; Jiang, X.; Krinitsin, P. G.; Isaenko,L. I.; Lin, Z. *J. Phys. Chem. C* **2018**, *122*, 17413–17422.

(19) Yin, W.; Feng, K.; Hao, W.; Yao, J.; Wu, Y. *Inorg. Chem.* **2012**, *51*, 5839–5843.

(20) Bera, T. K.; Song, J. H.; Freeman, A. J., Jang, J. I.; Ketterson, J. B.; Kanatzidis, M. G. *Angew. Chem. Int. Ed.* **2008**, *47*, 7828–7832.

(21) Yang, H.-D.; Ran, M.-Y.; Zhou, S.-H.; Wu, X.-T.; Lin, H.; Zhu, Q.-L. *Chem. Sci.* **2022**, *13*, 10725–10733.

(22) Huang, R. T.; Zheng, M.; Sui, L. F.; Cai, C. B.; Huang, F. Q. *J. Inorg. Mater.* **2017**, *32*, 101–106.

(23) Zhou, H. M.; Xiong, L.; Chen, L.; Wu, L. M. *Angew. Chem. Int. Ed.* **2019**, *58*, 9979–9983.

(24) Isaenko, L.; Dong, L.; Kurus, A.; Lin, Z.; Yelisseyev, A.; Lobanov, S.; Molokeev, M. *Adv. Opt. Mater*. **2022**, *10*, 2201727.

(25) Kuriyama, K.; Nozaki, T. *J. Appl. Phys*. **1981**, *52*, 6441–6443.

(26) Protasenya, A. M.; Zolotarev, M. L.; Poplavnoi, A. S. *Sov. Phys. J.* **1983**, *26*, 517–520.

(27) Coelho, A. A. *TOPAS-Academic*, *version 6; Coelho Software*: Brisbane, Australia, **2007**.

(28) Pawley, G. S. *J. Appl. Crystallogr.* **1981**, *14*, 357–361.

(29) Sheldrick, G. M. *Acta Crystallogr. Sect. A* **2008**, *64*, 112–122.

(30) Parthé, E.; Gelato, L. M.; Chabot, B. *Acta Crystallogr. Sect. A* **1988**, *44*, 999–1002.

(31) Kurtz, S. K.; Perry, T. T. *J. Quantum Electron.* **1968**, *4*, 333.

(32) Okhotnikov, K.; Charpentier, T.; Cadars, S.; Supercell program. *J. Cheminform.* **2016**, *8*, 1–15.

(33) G. Kresse, J. F. *Phys. Rev. B* **1996**, *54*, 11169–11185.

(34) G. Kresse, D. J. *Phys. Rev. B* **1999**, *59*, 1758–1775.

(35) Blöchl, P. E. *Phys. Rev. B* **1994**, *50*, 17953–17979.

(36) Perdew, J. P.; Burke, K.; Ernzerhof, M. *Phys. Rev. Lett.* **1996**, *77*, 3865–3868.

(37) Hohenberg, P. *Phys. Rev.* **1964**, *136*, B864–B870.

(38) Kohn, W.; Sham, L. J. *Phys. Rev.* **1965**, *140*, A1133–A1138.

(39) Grin, Y.; Savin, A.; Silvi, B. The ELF perspective of chemical bonding. In *The Chemical Bond: Fundamental Aspects of Chemical Bonding*; Frenking, G., Shaik, S., Eds.; Wiley-VCH, Weinheim, 2014, pp. 345–382

(40) Dronskowski, R.; Bloechl, P. E. *J. Phys. Chem.* **1993**, *97*, 8617–8624.

(41) Deringer, V. L.; Tchougréeff, A. L.; Dronskowski, R. *J. Phys. Chem. A* **2011**, *115*, 5461–5466.

(42) Maintz, S.; Deringer, V. L.; Tchougréeff, A. L.; Dronskowski, R. *J. Comput. Chem.* **2013**, *34*, 2557–2567.

(43) Maintz, S.; Deringer, V. L.; Tchougréeff, A. L.; Dronskowski, R. *J. Comput. Chem.* **2016**, *37*, 1030–1035.

(44) Villars, P.; Cenzual, K. *Pearson's Crystal Data – Crystal Structure Database for Inorganic Compounds (on DVD)*, Release 2021/22; ASM International: Materials Park, OH, USA.

(45) Winter, F.; Dupke, S.; Eckert, H.; Rodewald, U. C.; Pöttgen, R. *Z. Anorg. Allg. Chem.* **2013***, 639*, 2790–2795.

(46) Honeyman, W. N.; Wilkinson, K. H. *J. Phys. D* **1971**, *4*, 1182–1185.

(47) Nguimdo, G. M. D.; Joubert, D. P. *Eur. Phys. J. B* **2015**, *88*, 1–10.

(48) Maeda, T.; Takeichi, T.; Wada, T. *Phys. Stat. Solidi* **2006**, *203*, 2634–2638.

(49) Pamplin, B. R.; Kiyosawa, T.;Masumoto, K. *Prog. Cryst. Growth Charact.* **1979**, *1*, 331–387.

(50) Hai, X.; Tahir-Kheli, J.;Goddard, W. A. *J. Phys. Chem. Lett.* **2011**, *2*, 212–217.

(51) Li, L. H.; Li, J. Q.; Wu, L. M. *J. Solid State Chem.* **2008**, *181*, 2462–2468.

(52) Müller, P. C.; Ertural, C.; Hempelmann, J.; Dronskowski, R. *J. Phys. Chem. C* **2021**, *125*, 7959–7970.

Chapter 7.

7.1 Conclusions

Several objectives were successfully achieved in this work, which focuses on the structures and properties of Li-containing intermetallics and chalcogenides. New ternary and quaternary coloured intermetallics were synthesized that contain less expensive elements such as Cu and Zn, while possessing similar crystal and electronic structures as previously known analogues. They adopt cubic structures whose atomic arrangements were determined by a combination of XRD and NMR methods. The colours of these compounds make them attractive candidates for use in decorative coatings, jewelry, and plasmonic materials. Solid solutions were prepared of existing chalcogenides that are well known for their IR NLO properties. By varying the amount of Li, the physical properties can be controlled. Solid-state ^{7}Li NMR spectroscopy was a valuable complementary method to help clarify their occupation within single vs. multiple sites in the crystal structures.

7.1.1 Coloured Li intermetallics

Three research projects have contributed to the evaluation of how colours can be controlled in Li-containing intermetallics by chemical substitution.

In Chapter 2, ternary compounds were targeted that satisfy electron count conditions to obtain coloured intermetallic compounds. Two new compounds were successfully synthesised in as nearly single-phase samples: purple Li_2ZnGa and light blue Li_2ZnIn. They crystallize in the cubic NaTl-type structure (space group $Fd\bar{3}m$). Their colours were initially assessed qualitatively from optical reflectance spectra, and then accurately quantified by extracting CIE1931 x and y

coordinates mapped onto colour space. Band structure calculations revealed no energy gaps, consistent with expectations for metallic behaviour. The results are significant because coloured intermetallic compounds remain quite rare, accounting for less than 1% of all known intermetallic compounds.

In Chapter 3, the goal was to target quaternary coloured intermetallics, which are even more rare than ternary ones. Several combinations of Li, Mg, transition metals, and p-block metals or metalloids were attempted. Two new equiatomic quaternary Heusler phases were discovered, exhibiting visible colours: red-violet LiMgPdGe and light blue LiMgCdGe. Particularly noteworthy, LiMgCdGe is the first quaternary coloured compound containing no precious metals at all. The compounds LiMgPdSn (red-violet) and LiMgPtSn (red), previously known but poorly characterized, were reproduced. The main challenge here is that definitive structural models cannot be determined by their powder XRD patterns alone. It is important to determine the site distribution of LiMgPdSn because it serves as the parent structure type for equiatomic quaternary Heusler compounds. Complementing the diffraction data, evidence from ^{7}Li NMR spectroscopy and electronic structure calculations supports an ordered distribution in which Li occupies one specific site (Li in 4*d*, Mg in 4*b*, Pd in 4*a*, Sn in 4*c*) in both LiMgPdSn and LiMgPtSn. However, for LiMgCdGe, the possibility of disorder between Cd and Ge atoms cannot be ruled out. In contrast, for LiMgPdGe, the evidence suggests that Li atoms occupy more than one site, likely disordering with Mg atoms in 4*d* and 4*b*. The colours of these compounds were quantified using diffuse reflectance spectroscopy and CIE1931 colour space. The band dispersion diagrams reveal pseudogaps which are likely responsible for the optical properties of the compounds. The visible colours are attractive and unusual. There is strong potential that other coloured intermetallics can be discovered among quaternary Li-containing Heusler compounds.

Although the band structure analysis provided some insights into the origin of colour within these ternary and quaternary compounds, it is still not entirely clear if the colour can be varied more precisely. Therefore, in Chapter 3, the effect of mixing two coloured intermetallics was examined, to form series of solid solutions whose chemical compositions can be gradually incremented. Based on the two isoelectronic end-members $LiCu_2Al$ (red) and $LiCu_2Ga$ (yellow), the solid solution $LiCu_2Al_{1-x}Ga_x$ could be prepared, with the colour smoothly varying as Ga substitutes for Al. A compositionally induced phase transition occurred upon replacing Al with Ga beyond $x = 0.3$. Substitutions of different first-row transition metals for Cu in $LiCu_2Ga$ were attempted, but only Ni substitution was successful. Within the solid solution $LiCu_{2-y}Ni_yGa$, replacing Cu with Ni atoms reduced the reflectivity, resulting in a gradual change from yellow to light yellow, as confirmed by optical reflectance measurements. No structural changes occurred in this solid solution. The Cu 3d states lie about 2.5 eV below the Fermi level, which is consistent with the absorption edges (2.4–2.9 eV) of the solid solutions. This suggests that the origin of colour in these compounds is similar to that of elemental copper or gold, which involves interband transition from the filled metal d-states to the empty states above the Fermi level.

These findings suggest that visible colour in intermetallics can arise in two ways. Completely or nearly filled transition-metal d-states must be present below the Fermi level to permit electronic transitions within the visible region (1.5–3.0 eV). Alternatively, there must be pesudogap with an energy level that corresponds to an electronic transition in the visible region of the spectrum.

7.1.2 Quaternary Li-containing chalcogenides as IR NLO materials

This project aims to achieving a suitable balance between strong SHG signals and wide band gaps, which ensure a large laser damage threshold. A secondary goal was to investigate potential transitions from the tetragonal $CuFeS_2$-type structure to the orthorhombic β-$NaFeO_2$-type structure as Ag is substituted by Li in the ternary chalcogenides $AgMSe_2$ (M = Al, Ga, In). The complete solid solution $Li_xAg_{1-x}GaSe_2$ was successfully prepared in which the tetragonal $CuFeS_2$-type structure is adopted within the entire series. This is unusual because most previous studies have reported the end-member $LiGaSe_2$ with an orthorhombic β-$NaFeO_2$ structure. That is, we have demonstrated that it is possible to stabilize the tetragonal $LiGaSe_2$ polymorph, the crucial step being relatively fast cooling from high temperatures.

The other solid solutions $Li_xAg_{1-x}AlSe_2$ and $Li_xAg_{1-x}InSe_2$ undergo the expected transformation from the tetragonal $CuFeS_2$-type to the orthorhombic β-$NaFeO_2$ structure as the Li content increases beyond x = 0.50. Atomic site distributions were confirmed by XRD and ^{7}Li NMR experiments, which reveal that Li atoms occupy only one site. The optical band gaps increase linearly with higher Li content and are nearly the same in the tetragonal and orthorhombic polymorphs of $LiGaSe_2$ at 3.3 eV. These Li-substituted compounds were then examined for their nonlinear optical behaviour; they were found to exhibit SHG intensities that were either stronger or comparable to those of the benchmark materials $AgGaS_2$ and $AgGaSe_2$, depending on the particle sizes. Moreover, these compounds remain congruently melting at temperatures ranging from 800 and 900 °C, making it possible to grow large single crystals, required for practical application.

7.2 Future directions

There remain many unanswered questions about the origin of colour in intermetallic substances and much more to be done. For example, it would be helpful to extend the study of ternary coloured compounds presented in Chapter 2 by preparing solid solutions $Li_2(Zn_{1-x}Ga_x)_2$ and $Li_2(Zn_{1-x}In_x)_2$ to investigate the effect of the electron count on the colours observed. In the literature, many candidates for IR NLO materials have been reported, often with strong SHG responses. However, full characterization is quite tedious, and they include assessment of laser induced damage thresholds, which was not done here because of lack of instrumentation. For practical application of IR NLO materials, large single crystals must be grown, which is also a lengthy endeavour. Although the compounds examined in this thesis exhibited good SHG responses, they were not type-I phase-matchable at the laser wavelengths used. A wavelength-dependent study would be valuable to assess their performance as practical materials.

Bibliography

(1) Castillo, S.; Ansart, F.; Laberty-Robert, C.; Portal, J. *J. Power Sources* **2002**, *112*, 247–254.

(2) Greatbatch, W.; Holmes, C. F. *Pacing Clin. Electrophysiol.* **1992**, *15*, 2034–2037.

(3) Lavernia, E. J.; Grant, N. J. *J. Mater. Sci.* **1987**, *22*, 1521–1529.

(4) Kostrivas, A.; Lippold, J. C. *Int. Mater. Rev*. **1999**, *44*, 217–237.

(5) Schetky, L. M. *MRS Bull.* **1996**, 50–55.

(6) Deevi, S. C.; Sikka, V. K. *Intermetallics* **1996**, *4*, 357–375.

(7) Takano, K. *J. Phys. Soc. Japan* **1969**, *26*, 362–370.

(8) Ohara, S.; Komura, S.; Taked, T. *J. Phys. Soc. Japan* **1973**, *34*, 1472–1476.

(9) Scanlon, W. W. *Science* **1963**, *142*, 1265–1269.

(10) Antolini, E. *Appl. Catal. B Environ*. **2017**, *217*, 201–213.

(11) Jiang, Y.; He, Y.; Liu, C. T. *Intermetallics* **2018**, *93*, 217–226.

(12) Nakamura, M. *MRS. Bull*. **1995**, *20*, 33–39.

(13) Cinca, N.; Lima, C. R. C.; Guilemany, J. M. *J. Mater. Res. Technol*. **2013**, *2*, 75–86.

(14) Herbst, J. F.; Croat, J. J.; Pinkerton, F. E.; Yelon, W. B. *Phys Rev. B* **1984**, *29*, 4176–4178.

(15) Mathias, B. T.; Geballe, T. H.; Geller, S.; Corenzwit, E. *Phys. Rev*. **1954**, *95*, 1435.

(16) Furukawa, S.; Komatsu, T. *ACS. Catal*. **2017**, *7*, 735–765.

(17) Gil, F. J.; Planell, J.A. *J .Eng. Med*. **1998**, *212*, 473–488.

(18) Vishnubhatla, S. S.; Jan, J. P. *Philos. Mag*. **1967**, *16*, 45–50.

(19) Chatterjee, B. Diverse Topics in Science and Technology, AuthorHouse, UK, 2013.

(20) Wang, M.X.; Zhu, H.; Yang, G. J.; Liu, K.; Li, J. F.; Kong, L. T. *Mater. Des*. **2021**, *198*, 109359.

(21) Walter, R. *Nature* **1923**, *112*, 832–834.

(22) Liu, C.; Lu, W.; Xia, W.; Chang Liu, Du, C.; Rao, Z.; Best, J. P.; Brinckmann, S.; Lu, J.; Gault, B.; Dehm, G.; Wu,G.; Li, Z.; Raabe, D. *Nat. Commun*. **2022**, *13*, 1–9.

(23) Zhang, Y.; Zhou, Y. J.; Lin, J. P.; Chen, G. L.; Liaw, P. K. *Adv. Eng. Mater*. **2008**, *10*, 534–538.

(24) Kempter, C. P. *Phys. Status Solidi B* **1966**, *18*, K117–K118.

(25) Steinemann, S. G.; Wolf, W.; Podloucky, R. Color and Optical Properties. In: J. H. Westbrook, R. L. Fleischer (Eds.), *Intermetallic Compounds, Principles and Practice*. Vol 3, Weily, New York, 2002, 231–244.

(26) Mishra, V.; Iyer, A. K.; Mumbaraddi, D.; Oliynyk, A. O.; Zuber, G.; Boucheron, A.; Dmytriv, G.; Bernard, G. M.; Michaelis, V. K.; Mar, A. *J. Solid State Chem*. **2020**, *292*, 121703–121705.

(27) Jomaa, M.; Mishra, V.; Mumbaraddi, D.; Chaudhary, M.; Dmytriv, G.; Michaelis, V. K.; Mar, A. *J. Solid State Chem*. **2022**, *306*, 122792.

(28) Gardam, G. E. *Trans IMF*. **1966**, *44*, 186–188.

(29) Cretu, C.; Van Der Lingen, E. *Gold Bull*. **1999**, *32*, 115–126.

(30) Saeger, K. E.; Rodies, J. *Gold Bull*. 1**977**, *10*, 10–14.

(31) Steinemann, S. G.; Anongba, P. N. B. Podloucky, R. *J. Phase Equilibria* **1997**, *18*, 655–662.

(32) Van Der Lingen, E. *J. South. Afr. Inst. Min. Metall*. **2014**, *114*,137–144.

(33) Nomerovannaya, L. V.; Kirillova, M. M.; Shaikin, A. B. *Phys. Status Solidi B* **1980**, *102*, 715–720.

(34) Ranganathan, S.; Inoue, A. *Acta. Mater*. **2006**, *54*, 3647–3656.

(35) Eberz, U.; Seelentag, W.; Schuster, H.-U. *Z. Naturforsch*. **1980**, *35 b*, 1341–1343.

(36) Drews, J.; Eberz, U.; Schuster, H.-U. *J. Less Common Met.* **1986**, *116*, 271–278.

(37) Czybulka, A.; Petersen, A.; Schuster, H.-U. *J. Less Common Met.* **1990**, *161*, 303–312.

(38) Dmytriv, G.; Pauly, H.; Ehrenberg, H.; Pavlyuk, V.; Vollmar, E. *J. Solid State Chem*. **2005**, *178*, 2825–2831.

(39) Burstein, E.; Brotman, A.; Apell, P. *J. De. Phys*. **1983**, *44*, C10-429–C10-439.

(40) Villars, P.; Cenzual, K. *Pearson's Crystal Data–Crystal Structure Database for Inorganic Compounds*, (on DVD), Release 2022/23, ASM International, Materials Park, OH, USA.

(41) Jeong, Y. B.; Kim, J. T.; Hong, S. H.; Lee, H. D.; Choi, S. Y.; Kim, K. B. *Mater. Des*. **2019**, *175*, 107814.

(42) Supansomboon, S.; Dowd, A.; Van Der Lingen, E.; Keast, V. J.; Cortie, M. B. (Ed.) Howard, P.; Huggett, P.; Evans, D. *Mater. Forum* **2013**, *37*, 1–5.

(43) Seo, M.; Lee, M. *Acta Mater*. **2018**, *159*, 1–7.

(44) Makovicky, E. Rev. *Mineral Geochemistry* **2006**, *61*, 7–125

(45) Bergman, J. G.; Kurtz, S. K.; *Mater. Sci. Eng*. **1970**, *5*, 235–250.

(46) Shcherbakov, M. R.; Neshev, D. N.; Hopkins, B.; Shorokhov, A. S.; Staude, I.; Melik-Gaykazyan, E. V.; Decker, M.; A. Ezhov, A. A.; Miroshnichenko, A. E.; Brener, I.; Fedyanin, A. A.; Kivshar, Y. S. *Nano Lett*. **2014**, *14*, 6488–6492.

(47) Sutherland, R. L.; Mclean, D.G.; Kirkpatrick, S. *Handbook of Nonlinear Optics with Contributions*. Marcel Dekker: New York, 2003.

(48) Boyd, R. W. *Nonlinear Optics*. 3rd ed. Rochester, Elsiver: New York, 2007.

(49) Luo, X.; Li, Z.; Guo, Y.; Yao, J.; Wu.; Y. *J. Solid State Chem*. **2019**, *270*, 674–687.

(50) Galanty, M.; Shavit, O.; Weissman, A.; Aharon, H.; Gachet, D.; Segal, S.; Salomon, A. *Light Sci. Appl*. **2018**, *7*, 1–8.

(51) Guo, S. P.; Chi, Y.; Guo, G. C. *Coord. Chem. Rev*. **2017**, *335*, 44–57.

(52) Halasyamani, P. S.; Rondinelli, J. M. *Nat. Commun*. **2018**, *9*, 1–4.

(53) Liu, B. W.; Zeng, H. Y.; Jiang, X. M.; Guo, G. C. *CCS. Chem*. **2021**, *3*, 964–973.

(54) Kang, L.; Zhou, M.; Yao, J.; Lin, Z.; Wu, Y.; Chen, C. *J. Am. Chem. Soc*. **2015**, *137*, 13049–13059.

(55) Guidotti, D.; Driscoll, T. A.; Gerritsen, H. J. *Solid State Commun*. **1983**, *46*, 337–340.

(56) Zhang, W.; Yu, H.; Wu, H.; Halasyamani, P. S. *Chem. Mater*. **2017**, *29*, 2655–2668.

(57) Ok, K. M.; Chi, E. O.; Halasyamani, P. S. *Chem. Soc. Rev*. **2006**, *35*, 710–717.

(58) Abudurusuli, A.; Li, J.; Pan, S. *Dalt. Trans*. **2021**, *50*, 3155–3160.

(59) Jiang X.-M.; Guo, S.-P.; Zeng, H.-Y.; Zhang, M.-J.; Guo. G.-C. *Structure-Property Relationships in Non-Linear Optical Crystals II: The IR Region*. Springer, Berlin, 2012.

(60) Chen, J.; Jiang, X.; Wu, Q.; Lin, Z.; Luo, M.; Ye, N. *J. Alloys Compd*. **2022**, *901*, 163384.

(61) Lin, H.; Chen, H.; Zheng, Y. J.; Yu, J. S.; Wu, X. T.; Wu, L. M. *Dalt. Trans*. **2017**, *46*, 7714–7721.

(62) Elsaesser, T.; Seilmeier, A.; Kaiser, W.; Koidl, P.; Brandt, G. *Appl. Phys. Lett*. **1984**, *44*, 383–385.

(63) Catella, G. C.; Shiozawa, L. R.; Hietanen, J. R.; Eckardtet R. C.; Route, R. K.; Feigelson, R. S.; Cooper, D. G.; Marquardt, C. L. *Appl. Opt*. **1993**, *32*, 3948–3951.

(64) Boyd, G. D.; Buehler, E.; Storz, F. G. *Appl. Phys. Lett*. **1971**, *18*, 301–304.

(65) Isaenko, L.; Yelisseyev, A.; Lobanov, S.; Petrov, V.; Rotermund, F.; Slekys, G.; Zondy. J. -J. *J. Appl. Phys*. **2002**, *91*, 9475–9480.

(66) Cai, W.; Abudurusuli, A.; Xie, C.; Tikhonov, E.; Li, J. Pan, S.; Yang, Z. *Adv. Funct. Mater.* **2022**, 2200231.

(67) Yin, W.; Feng, K.; He, R.; Mei, D.; Lin, Z.; Yao, J.; Wu, Y. *Dalt. Trans*. **2012**, *41*, 5653–5661.

(68) Geng, L.; Cheng, W. -D.; Lin, C. -S.; Zhang, W. -L.; Zhang, H.; He, Z. -Z. *Inorg. Chem*. **2011**, *50*, 5679–5686.

(69) Guo, Y.; Liang, F.; Li, Z.; Xing, W.; Lin, Z. -S.; Yao, J.; Mar. A.; Wu, Y. *Inorg. Chem*. **2019**, *58*, 10390–10398.

(70) Isaenko, L.; Yelisseyev, A.; Lobanov, S.; Titov, A.; Petrov, V.; Zondy, J. -J.; Krinitsin, P.; Merkulov, A.; Vedenyapin, V.; Smirnova, *J. Cryst. Res. Technol.* **2003**, *38*, 379–387.

(71) Yelisseyev, A.; Liang, F.; Isaenko, L.; Lobanov, S.; Goloshumova, A.; Lin, Z. S. *Opt. Mater*. **2017**, *72*, 795–804.

(72) Kumar, V.; Chandra, S.; Santosh, R. *J. Electron. Mater*. **2018**, *47*, 1223–1231.

(73) Lekse, J. W.; Moreau, M. A.; McNerny, K. L.; Yeon, J.; Halasyamani, P. S.; Aitken, J. A. *Inorg. Chem*. **2009**, *48*, 7516–7518.

(74) Brant, J. A.; Clark, D. J.; Kim, Y.S.; Jang, J. I.; Weiland, A.; Aitken, J. A. *Inorg. Chem*. **2015**, *54*, 2809–2819.

(75) Zhang, J. -H.; Clark, D. J.; Brant, J. A.; Sinagra, C. W.; Kim, Y. S.; Jang, J. I.; Aitken, J. A. *Dalt. Trans.* **2015**, *44*, 11212–11222.

(76) Yin, W.; Feng, K.; Hao, W.; Yao, J.; Wu, Y. *Inorg. Chem.* **2012**, *51*, 5839−5843.

(77) Cheetham, A. K.; Day. P. Solid State Chemistry, Clarendon: Oxford, 1988, 1–398.

(78) Harrison, M. J.; Graebner, A. P.; McNeil, W. J.; McGregor, D. S. *J. Cryst. Growth* **2006**, *290*, 597–601.

(79) Massa, W. *Crystal Structure Determination*, 2nd ed.; Springer: Berlin, 2004.

(80) Lynn, F.; Eyck, T. *Meth. Enzymol.* **1985**, *115*, 324–337.

(81) Cowtan, K. *Phase Problem in X -ray Crystallography, and Its Solution*, in *eLS*, Wiley: Chichester, UK, 2003.

(82) Kraus, W.; Nolze, G. *J. Appl. Crystallogr*. **1966**, *29*, 301–303.

(83) Coelho, A. A. *TOPAS–Academic, Version 6*, Coelho Software, Brisbane, Australia, 2007.

(84) Saghiri, M. A.; Asgar, K.; Lotfi, M.; Karamifar, K.; Saghiri, A. M.; Neelakantan, P.; Gutmann, J. L.; Sheibaninia, A. *Acta. Odontol. Scand*. **2012**, *70*, 603–609.

(85) Kowoll, T.; Müller, E.; Fritsch-Decker, S.; Hettler, S.; Störmer, H.; Weiss, C.; Gerthsen, D. *Scanning* **2017**, *2017*, 1–12.

(86) Heslop-Harrison, J.S. Energy Dispersive X-Ray Analysis. In: Linskens, HF., Jackson, J.F. (eds) *Physical Methods in Plant Sciences. Modern Methods of Plant Analysis*, vol 11, Springer, Berlin, Heidelberg, 1990, 244–277.

(87) Reif, B.; Ashbrook, S. E.; Emsley, L.; Hong, M. *Nat. Rev. Methods Primers* **2021**, *1*, 1–23.

(88) Dupke, S.; Eckert, H.; Winter, F.; Pöttgen, R. *Prog. Solid State Chem*. **2014**, *42*, 57–64.

(89) Youngman, R. *Materials* **2018**, *11*, 1–24.

(90) Lim, A. R.; Yoon, C. S. *Mater. Chem. Phys*. **2014**, *147*, 644–648.

(91) Chandran, C. V.; Heitjans, P. *Annu. Rep. NMR. Spectrosc.* **2016**, *89*, 1–102.

(92) Ganesh, K. N.; *Curr. Sci.* **1982**, *51*, 866–874.

(93) Sakellariou, D. Brown, S. P.; Lesage, A.; Hediger, S.; Bardet, M.; Meriles, C. A.; Pines, A.; Emsley, L. *J. Am. Chem. Soc*. **2003**, *125*, 4376–4380.

(94) Andrew, E. R.; Bradbury, A.; Eades, R. G. *Nature* **1958**, *182*, 4376–4380.

(95) Alia, A.; Ganapathy, S.; de Groot H. J. M. *Photosyn. Res*. **2009**, *102*, 415–425.

(96) Michaelis, V. K.; Levin, K.; Germanov, Y.; Kroeker, S. *Chem. Mater.* **2018**, *30,* 5521−5526.

(97) Janecek, M.; Moses, W. W. *IEEE. Trans. Nucl. Sci*. **2008**, *55*, 2432–2437.

(98) International Commission on Illumination. Commission internationale de l'éclairage, huitième session, Cambridge, Cambridge,1931.

(99) Smith, T.; Guild, J. *Trans. Opt. Soc*. **1931**, *33*, 74–134.

(100) Wright, W. D. *Trans. Opt. Soc.* **1929**, *30*, 141–164.

(101) Guild, J. *Philos. Trans. Royal Soc. A* **1931**, *230*, 149–187.

(102) http://www.brucelindbloom.com/ (Accessed Jan 01, 2021).

(103) Makuła, P.; Pacia, M.; Macyk, W. *J. Phys. Chem. Lett*. **2018**, *9*, 6814–6817.

(104) Dolgonos, A.; Mason, T. O. *J. Solid State Chem*. **2016**, *240*, 43–48.

(105) Kubelka, P.; Munk, F. *Fuer. Tekn. Phys.* **1931**, *12*, 593–609.

(106) Tauc, J.; Grigorovici, R .; Vancu, A. *phys. stat. sol*. **1966**, *15*, 627–637.

(107) Zanatta, A.; Chambouleyron, I. *Phys. Rev. B* **1996**, *53*, 3833–3836.

(108) Kohn, W.; Sham, L. J. *Phys. Rev*. **1965**, *140*, A1133–A1138.

(109) Rindt, C. C. M., Gaastra-Nedea, S. V. Modeling thermochemical reactions in thermal energy storage systems. *Advances in Thermal Energy Storage Systems*. Woodhead Publishing, 2015, 375–415.

(110) Hoffmann, R. *Angew. Chem*. **1987**, *26*, 846–878.

(111) Dronskowski, R.; Blöchl, P. E. *J. Phys. Chem*. **1993**, *97*, 8617–8624.

(112) Deringer, V. L.; Tchougréeff, A. L.; Dronskowski, R. *J. Phys. Chem. A* **2011**, *115*, 5461–5466.

(113) Long, N. H.; Akai, H. *J. Phys. Condens. Matter*. **2007**, *19*, 365232.

(114) Kresse, G.; Furthmüller, J. *Phys. Rev. B* **1996**, *54*, 11169–11185.

(115) Kresse, G.; Joubert, D. *Phys. Rev. B* **1999**, *59*, 1758–1775.

(116) Blöchl, P. E. *Phys. Rev. B* **1994**, *50*, 17953–17979.

(117) Perdew, J. P.; Burke, K.; Ernzerhof, M. *Phys. Rev. Lett*. **1996**, *77*, 3865–3868.

(118) Hohenberg, P. *Phys. Rev*. **1964**, *136*, B864–B870.

(119) Grin, Y.; Savin, A.; Silvi B. The ELF Perspective of Chemical Bonding. *In The Chemical Bond: Fundamental Aspects of Chemical Bonding*, Frenking, G.; Shaik, S., Eds.; Wiley-VCH: Weinheim, 2014, pp 345–382.

(120) Dronskowski, R.; Festkbrperforschung, M.; Blochl, P. E. *J. Phys. Chem*. **1993**, *97*, 8617–8624.

(121) Maintz, S.; Deringer, V. L.; Tchougréeff, A. L. *J. Comput. Chem*. **2013**, *34*, 2557–2567.

(122) Maintz, S.; Deringer, V. L.; Tchougréeff, A. L.; Dronskowski, R. *J. Comput. Chem.* **2016**, *37*, 1030–1035.

(123) Steinemann, S. G.; Wolf, W.; Podloucky; R. *Color and optical properties*, in: J. H. Westbrook, R.L. Fleischer (Eds.), Intermetallic Compounds, Vol. 3, Principles and Practice, Wiley, New York, 2002, 231–244.

(124) Saeger, K. E.; Rodies; J. *Gold Bull*. **1977**, *10*, 10–14.

(125) Cretu, C.; van der Lingen, E. *Gold Bull*. **1999**, *32*,115–126.

(126) Corti, C. W.; Black, blue and purple! The special colours of gold, in: E. Bell (Ed.), The Santa Fe Symposium on Jewelry Manufacturing Technology, *Met-Chem. Research*, Albuquerque, 2004, 121–134.

(127) Hurly, J.; Wedepohl, P. T. *J. Mater. Sci*. **1993**, *28*, 5648–5653.

(128) van der Lingen, E. *J. South. Afr. Inst. Min. Metall.* **2014**, *114*, 137–144.

(129) Jeong, Y. B.; Kim, J. T.; S. Hong, H.; Lee, H. D.; Choi, S.Y.; Kim, K. B. *Mater. Des*. **2019**, *175*, 107814-1–107814-11.

(130) Cahn, R. W. *Nature* **1998**, *396*, 523–524.

(131) Keast, A. V. J.; Birt, K.; Koch, C. T.; Supansomboon, S.; Cortie, M. B. *Appl. Phys. Lett*. **2011**, *99*, 111908-1–111908-3.

(132) Furrer, A.; Seita, M.; Spolenak, R. *Acta Mater.* **2013**, *61*, 2874–2883.

(133) Eberz, U.; Seelentag, W.; Schuster, H.-U. *Z. Naturforsch*. *B* **1980**, *35*, 1341–1343.

(134) Supansomboon, S.; Maaroof, A.; Cortie; M. B. *Gold Bull*. **2008**, *41*, 296–304.

(135) Klotz; U. E. *Gold Bull.* **2010**, *43*, 4–10.

(136) Na, J. H.; Han, K. H.; Garrett, G. R.; Launey, M. E.; Demetriou, M. D.; Johnson, W. L. *Sci. Rep*. **2019**, *9*, 3269-1–3269-8.

(137) Mun, S. C.; Kang, G. C.; Jeong, Y. B.; Park, H. J.; Kim, Y. S.; Hong, S. H.; Song, G.; Kim, K. B. *Mater. Des.* **2021**, *200*, 109449-1–109449-8.

(138) Liu, J.; Liu, Y.; Gong, P.; Li, Y.; Moore, K. M.; Scanley, E.; Walker, F.; Broadbridge, C. C.; Schroers; J. *Gold Bull*. **2015**, *48*, 111–118.

(139) Blaber, M. G.; Arnold, M. D.; Ford, M. J. *J. Phys. Condens. Matter.* **2009**, *21*, 144211-1–144211-8.

(140) Drews, J.; Eberz, U.; Schuster, H.-U. *J. Less Common Met.* **1986**, *116*, 271–278.

(141) Czybulka, A.; Petersen, A.; Schuster, H.-U. *J. Less Common Met.* **1990**, *161*, 303–312.

(142) Dymtriv, G.; Pauly, H.; Ehrenberg, H.; Pavlyuk, V.; Vollmar, E. *J. Solid State Chem*. **2005**. *178*, 2825–2831.

(143) Mishra, V.; Iyer, A. K.; Mumbaraddi, D.; Oliynyk, A. O.; Zuber, G., Boucheron, A.; Dmytriv, G.; Bernard, G. M.; Michaelis, V. K.; Mar, A. *J. Solid State Chem*. **2020**, *292*, 121703-1−121703-5.

(144) Schuster, H.-U.; Mewis, A. *Z. Naturforsch. B* **1969**, *24*, 1190.

(145) Mewis, A.; Schuster, H.-U. *Z. Naturforsch*. *B* **1971**, *26*, 62.

(146) Schuster, H.-U.; Thiedemann, D.; Schonemann, H. *Z. Anorg. Allg. Chem*. **1969**, *370*, 160−170.

(147) Fürtauer, S.; Effenberger, H. S.; Flandorfer, H. *J. Solid State Chem*. **2014**, *220*, 198−205.

(148) Schönemann, H.; Jacobs, H.; Schuster. H.-U. *Z. Anorg. Allg. Chem*. **1971**, *382*, 40−48.

(149) Kraus, W.; Nolze, G. *J. Appl. Crystallogr*. **1996**, *29*, 301–303.

(150) Coelho, A. A. *TOPAS-Academic, version 6, Coelho Software*, Brisbane, Australia, 2007.

(151) Hunt, R. W. G.; Pointer, M. R. Measuring Colour, 4th Ed., Wiley, Chichester, 2011.

(152) Long, N. H.; Akai, H. *J. Phys. Condens. Matter.* **2007**, *19*, 365232-1–365232-8.

(153) Tillard-Charbonnel, M.; Chahine, A.; Belin, C. *Mater. Res. Bull*. **1993**, *28*, 1285−1294.

(154) Tillard-Charbonnel, M.; Chouaibi, N.; Belin, C. *Eur. J. Solid State Inorg. Chem*. **1992**, *29*, 347−359.

(155) Kinzhibalo, V. V.; Mel'nyk, E. V.; Petrus, I. L. *Visn. L'viv. Derzh. Univ., Ser. Khim*. **1981**, *23*, 23−26.

(156) Pauling, L.; Kamb, B. *Proc. Natl. Acad. Sci*. *USA.* **1986**, *83*, 3569−3571.

(157) Villars, P.; Cenzual, K. *Pearson's Crystal Data – Crystal Structure Database for Inorganic Compounds*, (on DVD), Release 2021/22, ASM International, Materials Park, OH, USA.

(158) Bekaert, E.; Robert, F.; Lippens, P. E.; Menetrier, M. *J. Phys. Chem.* **2010**, *C114,* 6749−6754.

(159) Trease, N. M.; Zhou, L.; Chang, H. J.; Zhu, B. Y.; Grey, C. P. *Solid State Nucl. Magn. Reson*. **2012**, *42*, 62–70.

(160) Winter, F.; Dupke, S.; Eckert, H.; Rodewald, U. Ch.; Pöttgen, R. *Z. Anorg. Allg. Chem*. **2013**, *639*, 2790–2795.

(161) Dupke, S.; Eckert, H.; Winter, F.; Pöttgen, R. *Prog. Solid State Chem*. **2014**, *42*, 57–64.

(162) Hu, J. Z.; Zhao, Z.; Hu, M. Y.; Feng, J.; Deng, X.; Chen, X.; Xu, W.; Liu, J.; Zhang, J.-G. *J. Power Sources* **2016**, *304*, 51–59.

(163) Michaelis, V. K.; Levin, K.; Germanov, Y.; Lelong, G.; Kroeker, S. *Chem. Mater*. **2018**, *30*, 5521–5526.

(164) Dmytriv, G.; Pavlyuk, V.; Ehrenberg, H. *Unpublished results*.

(165) Graf, T.; Felser, C.; Parkin, S. S. P. *Prog. Solid State Chem*. **2011**, *39*, 1–50.

(166) Felser, C.; Hirohata, A. (Eds.). Heusler Alloys: Properties, Growth, Applications, Springer, Cham, Switzerland, 2016.

(167) Eberz, U.; Seelentag, W.; Schuster, H.-U. *Z. Naturforsch. B* **1980**, *35*, 1341–1343.

(168) Drews, J.; Eberz, U.; Schuster, H.-U. *J. Less Common Met*. **1986**, *116*, 271–278.

(169) Steinemann, S. G.; Wolf, W.; Podloucky, R. Color and optical properties, in: Westbrook, J. H.; Fleischer, R. L. (Eds.), *Intermetallic Compounds, Principles and Practice*, vol. 3, Wiley, New York, 2002, 231–244.

(170) Cretu, C.; van der Lingen, E. *Gold Bull*. **1999**, *32*, 115–126.

(171) Klotz, U. E. *Gold Bull*. **2010**, *43*, 4–10.

(172) Supansomboon, S.; Dowd, A.; van der Lingen, E.; Keast, V. J.; Cortie, M. B. *Mater. Forum* **2013**, *37*, 1–6.

(173) van der Lingen, E. *J. South. Afr. Inst. Min. Metall*. **2014**, *114*, 137–144.

(174) Liu, J.; Liu, Y.; Gong, P.; Li, Y.; Moore, K. M.; Scanley, E.; Walker, F.; Broadbridge, C. C.; Schroers, J. *Gold Bull*. **2015**, *48*, 111–118.

(175) Jeong, Y. B.; Kim, J. T.; Hong, S. H.; Lee, H. D.; Choi, S. Y.; Kim, K. B. *Mater. Des*. **2019**, *175*, 107814-1–107814-11.

(176) Prandini, G.; Rignanese, G.-M.; Marzari, N. *npj. Comput. Mater*. **2019**, *5*, 129-1–129-12.

(177) Mecking, O. *J. Archaeol. Sci*. **2020**, *121*, 105199-1–105199-16.

(178) Hong, S. H.; Mun, S. C.; Kang, G. C.; Park, H. J.; Jeong, Y. B.; Song, G.; Ki, K. B. *Prog. Mater. Sci*. **2022**, *123*, 100811-1–108111-18.

(179) Seo, M.; Lee; M. *Acta Mater*. **2018**, *159*, 1–7.

(180) Na, J. H.; Han, K. H.; Garrett, G. R.; Launey, M. E.; Demetriou, M. D.; Johnson, W. L. *Sci. Rep*. **2019**, *9*, 3269-1–3269-8.

(181) Mun, S. C.; Kang, G. C.; Jeong, Y. B.; Park, H. J.; Kim, Y. S.; Hong, S. H.; Song, G.; Kim, K. B. *Mater. Des*. **2021**, *200*, 109449-1–109449-8.

(182) Heletta, L.; Stein, S.; Pottgen, R. *Z. Naturforsch*. *B* **2018**, *73*, 739–747.

(183) Mishra, V.; Iyer, A. K.; Mumbaraddi, D.; Oliynyk, A. O.; Zuber, G.; Boucheron, A.; Dmytriv, G.; Bernard, G. M.; Michaelis, V. K.; Mar, A. *J. Solid State Chem*. **2020**, *292*, 121703-1–121703-5.

(184) Jomaa, M.; Mishra, V.; Mumbaraddi, D.; Chaudhary, M.; Dmytriv, G.; Michaelis, V. K.; Mar, A. *J. Solid State Chem*. **2022**, *306*, 122792.

(185) Villars, P.; Cenzual, K. *Pearson's Crystal Data – Crystal Structure Database for Inorganic Compounds*, (On DVD), Release 2021/22, ASM International, Materials Park, OH, USA.

(186) Özdoğan, K.; Şaşıoğlu, E.; Galanakis, I. *J. Appl. Phys*. **2013**, *113*, 193903-1–193903-5.

(187) Bainsla, L.; Suresh, K. G. *Appl. Phys. Rev*. **2016**, *3*, 031101-1–031101-21.

(188) Barman, C. K.; Mondal, C.; Pathak, B.; Alam, A. *Phys. Rev*. *B* **2019**, *99*, 045144-1–045144-6.

(189) Gzyl, A. S.; Oliynyk, A. O.; Mar, A. *Cryst. Growth Des*. **2020**, *20*, 6469–6477.

(190) He, J.; Naghavi, S. S.; Hegde, V. I.; Amsler, M.; Wolverton, C. *Chem. Mater*. **2018**, *30*, 4978–4985.

(191) Kim, K.; Ward, L.; He, J.; Krishna, A.; Agrawal, A.; Wolverton, C. *Phys. Rev*. *B* **2018**, *2*, 123801-1–123801-9.

(192) Gao, Q.; Opahle, I.; Zhang, H. *Phys. Rev. Mater*. **2019**, *3*, 024410-1–024410-12.

(193) Jiang, S.; Yang, K. *J. Alloys Compd*. **2021**, *867*, 158854-1–158854-14.

(194) Burdett, J. K.; Lee, S. L.; McLarnan, T. J. *J. Am. Chem. Soc*. **1985**, *107*, 3083–3089.

(195) Miller, G. J. *Eur. J. Inorg. Chem*. **1998**, 523–526.

(196) Gzyl, A. S.; Oliynyk, A. O.; Adutwum, L. A.; Mar, A. *Inorg. Chem*. **2019**, *58*, 9280–9289.

(197) Kraus, W.; Nolze, G. *J. Appl. Crystallogr*. **1996**, *29*, 301–303.

(198) Hunt, R. W. G.; Pointer, M. R. *Measuring Colour*, 4th ed., Wiley, Chichester, 2011.

(199) Kresse, G.; Furthmüller, J. *Phys. Rev*. *B* **1996**, *54*, 11169–11186.

(200) Kresse, G.; Joubert, D. *Phys. Rev*. *B* **1999**, *59*, 1758–1775.

(201) Blochl, P. E. *Phys. Rev*. *B* **1994**, *50*, 17953–17979.

(202) Perdew, J. P.; Burke, K.; Ernzerhof, M. *Phys. Rev. Lett*. **1996**, *77*, 3865–3868.

(203) Webster, P. J. *Contemp. Phys*. **1969**, *10*, 559–577.

(204) Webster, P. J.; Ziebeck, K. R. A. *J. Phys. Chem. Solid* **1973**, *34*, 1647–1654.

(205) Michaelis, V. K.; Levin, K.; Germanov, Y.; Lelong, G.; Kroeker, S. *Chem. Mater*. **2018**, *30*, 5521–5526.

(206) Steinemann, S. G.; Wolf, W.; Podloucky; R. Color and optical properties, in: J. H. Westbrook, R.L. Fleischer (Eds.), *Intermetallic Compounds*, Vol. 3, Principles and Practice, Wiley, New York, 2002, 231–244.

(207) Jeong, Y. B.; Kim, J. T.; S. Hong, H.; Lee, H. D.; Choi, S.Y., Kim, K. B. *Mater. Des.* **2019**, *175*, 107814-1–107814-11.

(208) Prandini, G.; Rignanese, G. M.; Marzari, N. *npj. Comput. Mater.* **2019**, *5*, 129.

(209) Wu, H.; Fan, G. *Prog. Mater. Sci.* **2020**, *113*, 100675.

(210) Hong, S. H.; Mun, S. C.; Kang, G. C.; Park, J. J.; Jeong, Y. B.; Song, G.; Ki Buem Kim,K. B. *Prog. Mater. Sci.* **2021**, *113*, 100811.

(211) Esparza-Contro, C.; Berthomé, G.; Renou, G.; Robaut, F.; Coindeau, S.; Vachey, C.; Cambin, J.; Mantel, M.; Latu-Romain. L. *Surf. Coatings .Technol.* **2020**, *389*, 125643.

(212) Runge, J. M. The Metallurgy of Anodizing Aluminum: Connecting Science to Practice. Chicago, IL, USA, 2018, 1–473.

(213) Caicedo, J. C. *J. Alloys Compd.* **2019**, *770*, 875–885.

(214) Niyomsoan, S.; Grant, W.; Olson, D. L.; Mishra, B. *Thin Solid Films* **2002**, *415*, 187–194.

(215) Ma, J.; Yi, J.; Zhao, D. Q.; Pan, M. X.; Wang, W. H. *J. Appl. Phys.* **2012**, *112*, (2012).

(216) Pfaff, G. *ChemTexts.* **2022**, *8*, 1–17.

(217) Supansomboon, S.; Dowd, A.; van der Lingen, E.; Keast, V. J.; Cortie, M. B. **2013**, *37*, 1–5.

(218) Seo, M.; Lee, M. *Acta Mater.* **2018**, *159*, 1–7.

(219) Vishnubhatla, S. S.; Jan, J. P. *Philos. Mag.* **1967**, *16*, 45–50.

(220) Pauly, H.; Weiss, A.; Witte, H. *Int. J. Mater. Res.* **1968**, *59*, 47–58.

(221) Czybulka, A.; Petersen, A.; Schuster, H.-U. *J. Less Common Met.* **1990**, *161*, 303–312.

(222) Drews, J.; Eberz, U.; Schuster, H.-U. *J. Less Common Met.* **1986**, *116*, 271–278.

(223) Jomaa, M.; Mishra, V.; Mumbaraddi, D.; Chaudhary, M.; Dmytriv, M.; Michaelis, V. K. Mar. A. *J. Solid State Chem.* **2022**, *306*, 122792.

(224) Jomaa, M.; Mishra, V.; Chaudhary, M.; Mumbaraddi, D.; Michaelis, V. K. Mar. A. *J. Solid State Chem.* **2022**, *314*, 123372.

(225) Mishra, V.; Iyer, A. K.; Mumbaraddi, D.; Oliynyk, A. O.; Zuber, G., Boucheron, A.; Dmytriv, G.; Bernard, G. M.; Michaelis, V. K.; Mar, A. *J. Solid State Chem*. **2020**, *292*, 121703.

(226) Coelho, A. A. *TOPAS-Academic, version 6, Coelho Software*, Brisbane, Australia, 2007.

(227) Kraus, W.; Nolze, G. *J. Appl. Crystallogr.* **1996**, *29*, 301–303.

(228) Allouche, A. *J. Comput. Chem.* **2012**, *32*, 174–182.

(229) Perdew, J. P.; Burke, K.; Ernzerhof, M. *Phys. Rev. Lett.* **1996**, *77*, 3865–3868.

(230) Slater, J. C. *J. Chem. Phys.* **1964**, *41*, 3199–3204.

(231) Talik, E.; Heimann, J.; Chelkowski, A. *J. Less Common Met.* **1986**, *124*, L13–L16.

(232) Kimura, H.; Maeda, H.; Sato, M. *J. Cryst. Growth* **1986**, *74*, 187–190.

(233) Yamane, H.; Sakamoto, T.; Kubota, S.; Shimada, M. *J. Mater. Sci.* **2001**, *36*, 307–311.

(234) Fang, M. H., Fang, M-H.; Meng, S.-Y.; Majewska, N.; Leśniewski, T.; Mahlik, S.; Marek Grinberg, M.; Sheu, H.-S.; Liu, R.-S. *Chem. Mater.* **2019**, *31*, 4614–4618.

(235) Kominami, H.; Imagawa, K.; Matsuura, T.; Hara, K.; Kurowasa, S. *1st Int. Vac. Nanoelectron Conf.* **2018**, 1–2.

(236) Kumar, G. R.; Kumar, K. V.; Venudhar, Y. C. *Mater. Sci. Appl.* **2012**, *3*, 87–91.

(237) Kaleva, G. M.; Politova, E. D.; Ivanov, S. A.; Mosunov, A. V.; S. Stefanovich, Y. Sadovskaya, N. V.; Mathieu, R.; Nordblad, P. *Inorg. Mater.* **2011**, *47*, 1132–1140.

(238) Michaelis, V. K.; Levin, K.; Germanov, Y.; Lelong, G.; Kroeker, S. *Chem. Mater.* **2018***, 30*, 5521–5526.

(239) Bekaert, E.; Robert, F.; Lippens, P. E.; Ménétrier, M. *J. Phys. Chem. C* **2010**, *114*, 6749–6754.

(240) Trease, N. M.; Zhou, L.; Chang, H. J.; Zhu, B. Y.; Grey, C. P. *Solid State Nucl. Magn. Reson.* **2012**, *42*, 62–70.

(241) Winter, F.; Dupke, S.; Eckert, H.; Rodewald, U. C.; Pöttgen, R. *Z. Anorg. Allg. Chem.* **2013***, 639*, 2790–2795.

(242) Dupke, S.; Eckert, H.; Winter, F.; Pöttgen, R. *Prog. Solid State Chem.* **2014**, *42*, 57–64.

(243) Hu, J. Z.; Zhao, Z.; Hu, M. Y.; Feng, J.; Deng, X.; Chen, X.; Xu, W.; Liu, J.; Zhang, J.-G. *J. Power Sources* **2016**, *304*, 51–59.

(244) Saeger, K. E.; Rodies, J. *Gold Bull.* **1977**, *10*, 10–14.

(245) Arrowsmith, D. J. *Gold Bull.* **1986**, *19*, 117–122.

(246) Garmire, E. *Opt. Express* **2013**, *21*, 30532–30544.

(247) Chung, I.; Kanatzidis, M. G. *Chem. Mater.* **2014**, *26*, 849–869.

(248) Guo, S.-P.; Chi, Y.; Guo, G.-C. *Coord. Chem. Rev.* **2017**, *335*, 44–57.

(249) Liang, F.; Kang, L.; Lin, Z.; Wu, Y. *Cryst. Growth Des.* **2017**, *17*, 2254–2289.

(250) Wu, K.; Pan, S. *Coord. Chem. Rev.* **2018**, *377*, 191–208.

(251) Luo, X.; Li, Z.; Guo, Y.; Yao, J.; Wu, Y. *J. Solid State Chem.* **2019**, *270*, 674–687.

(252) Lin, H.; Wei, W.-B.; Chen, H.; Wu, X.-T.; Zhu, Q.-L. *Coord. Chem. Rev.* **2020**, *406*, 213150.

(253) Li, G.; Yang, Z.; Li, J.; Pan, S. *Chem. Commun.* **2020**, *56*, 11565.

(254) Chen, H.; Wei, W.-B.; Lin, H.; Wu, X.-T. *Coord. Chem. Rev.* **2021**, *448*, 214154.

(255) Liang, F.; Kang, L.; Lin, Z.; Wu, Y.; Chen, C. *Coord. Chem. Rev.* **2017**, *333*, 57–70.

(256) Chen, M.-M.; Xue, H.-G.; Guo, S.-P. *Chem. Rev.* **2018**, *368*, 115–133.

(257) Wang, W.; Mei, D.; Liang, F.; Zhao, J.; Wu, Y.; Lin, Z. *Coord. Chem. Rev.* **2020**, *421*, 213444.

(258) Zhou, W.; Zhang, Q.; Yao, W.-D.; Xue, H.; Guo, S.-P. *Inorg. Chem.* **2021**, *60*, 12536–12544.

(259) Yao, W.-D.; Cheng, X.; Guo, S.-P.; Whangbo, M.-H.; Ding, B.; Deng, S. *Chem. Mater.* **2023**, *35*, 1159–1167.

(260) Nikigosyan, D. N. Nonlinear Optical Crystals: A Complete Survey, Springer: New York, 2005.

(261) Zhou, H.-M.; Xiong, L.; Chen, L.; Wu, L.-M. *Angew. Chem. Int. Ed.* **2019**, *58*, 9979–9983.

(262) Yelisseyev, A.; Lobanov, S.; Molokeev, M.; Zhang, S.; Pugachev, A.; Lin, Z.; Vedenyapin, V.; Kurus, A.; Khamoyam, A.; Isaenko, L. *Adv. Opt. Mater.* **2021**, *9*, 2001856.

(263) Isaenko, L.; Dong, L.; Kurus, A.; Lin, Z.; Yelisseyev, A.; Lobanov, S.; Molokeev, M.; Korzhneva, K.; Goloshumova, A. *Adv. Opt. Mater.* **2022**, *10*, 2201727.

(264) Lobanov, S. I.; Korzhneva, K. E.; Gromilov, S. A.; Sukhikh, A. S.; Isaenko, L. I. *J. Cryst. Growth* **2023**, *604*, 127057.

(265) Zhou, W.; Yao, W.-D.; Zhang, Q.; Xue, H.; Guo, S.-P. *Inorg. Chem.* **2021**, *60*, 5198–5205.

(266) Zhou, W.; Wu, J.; Liu, W.; Guo, S.-P. *Coord. Chem. Rev.* **2023**, *477*, 214950.

(267) Bai, T.; Xing, S.; Li, C.; Shi, Z.; Feng, S. *Chem. Commun.* **2016**, *52*, 8581–8584.

(268) Cai, W.; Abudurusuli, A.; Xie, C.; Tikhonov, E.; Li, J.; Pan, S.; Yang, Z. *Adv. Funct. Mater.* **2022**, *32*, 2200231.

(269) Pöhls, J.-H.; Heyberger, M.; Mar, A. *J. Solid State Chem.* **2020**, *290*, 121557.

(270) Coelho, A. A. *TOPAS-Academic*, *version 6; Coelho Software*: Brisbane, Australia, **2007**.

(271) Sheldrick, G. M. *Acta Crystallogr. Sect. A* **2008**, *64*, 112–122.

(272) Gelato, L. M.; Parthé, E. *J. Appl. Crystallogr.* **1987**, *20*, 139–143.

(273) Bloch, F. *Phys. Rev.* **1946**, *70*, 460–474.

(274) Kortüm, G. *Reflectance Spectroscopy*; Springer: New York, 1969.

(275) Kurtz, S. K.; Perry, T. T. *J. Appl. Phys.* **1968**, *39*, 3798–3813.

(276) Clark, D. J.; Zhang, J.-H.; Craig, A. J.; Weiland, A.; Brant, J. A.; Cho, J. B.; Kim, Y. S.; Jang, J. I.; Aitken, J. A. *J. Alloys Compd.* **2022**, *917*, 165381.

(277) Okhotnikov, K.; Charpentier, T.; Cadars, S. *J. Cheminform.* **2016**, *8*, 17.

(278) Hafner, J. *J. Comput. Chem.* **2008**, *29*, 2044–2078.

(279) Perdew, J. P.; Burke, K.; Ernzerhof, M. *Phys. Rev. Lett.* **1996**, *77*, 3865–3868.

(280) Deringer, V. L.; Tchougréeff, A. L.; Dronskowski, R. *J. Phys. Chem. A* **2011**, *115*, 5461–5466.

(281) Maintz, S.; Deringer, V. L.; Tchougréeff, A.L.; Dronskowski, R. *J. Comput. Chem.* **2013**, *34*, 2557–2567.

(282) Grin, Y.; Savin, A.; Silvi, B.; The ELF perspective of chemical bonding. In *The Chemical Bond: Fundamental Aspects of Chemical Bonding*; Frenking, G., Shaik, S., Eds.; Wiley-VCH, Weinheim, 2014, pp. 345−382.

(283) Maintz, S.; Deringer, V. L.; Tchougréeff, A. L.; Dronskowski, R. *J. Comput. Chem.* **2016**, *37*, 1030–1035.

(284) Shannon, R. D. *Acta Crystallogr. Sect. A* **1976**, *32*, 751–767.

(285) Yelisseyev, A.; Liang, F.; Isaenko, L.; Lobanov, S.; Goloshumova, A.; Lin, Z.S. *Opt. Mater.* **2017**, *17*, 795–804.

(286) Villars, P.; Cenzual, K. *Pearson's Crystal Data – Crystal Structure Database for Inorganic Compounds (on DVD)*, Release 2021/22; ASM International: Materials Park, OH, USA.

(287) Brese, N. E.; O'Keeffe, M. *Acta Crystallogr. Sect. B* **1991**, *47*, 192–197.

(288) Lemoine, P.; Guélou, G.; Raveau, B.; Guilmeau, E. *Angew. Chem. Int. Ed.* **2022**, *61*, e202108686.

(289) Frenzel, N.; Frisch, G. *Z. Anorg. Allg. Chem.* **2022**, *648*, e202200148.

(290) Michaelis, V. K.; Levin, K.; Germanov, Y.; Lelong, G.; Kroeker, S. *Chem. Mater.* **2018**, *30*, 5521–5526.

(291) Ivashchenko, I. A.; Zimy, O. F.; Olekseyuk, I. D. *Chem. Met. Alloys* **2008**, *1*, 274–282.

(292) Kamijoh, T.; Kuriyama, K. *J. Cryst. Growth* **1981**, *51*, 6–10.

(293) Xiao, H.; Tahir-Kheli, J.; Godard, W. A., III. *Phys. Chem. Lett.* **2011**, *2*, 212–217.

(294) Zunger, J. E.; Zunger, A. *J. Phys. Rev. B* **1984**, *29*, 1882–1906.

(295) Kim, J.; Hughbanks, T. *Inorg. Chem.* **2000**, *39*, 3092–3097.

(296) Kim, S.; Lee, M.; Hong, C.; Yoon, Y.; An, H.; Lee, D.; Jeong, W.; Yoo, D.; Kang, Y.; Youn, Y.; Han, S. H. *Sci. Data* **2002**, *7*, 1–6.

(297) Albornoz, J. G.; Rojas L. R. M.; Merino, J. M.; León, M. *J. Phys. Chem. Solids* **2014**, *75*, 1–7.

(298) Zeng, Y.;Chua, S. J.; Wu, P. *Chem. Mater.* **2002**, *14*, 2989–2998.

(299) Khan, A.; Sajjad, M.; Murtaza, G.; Laref, A. *Z. Naturforsch. A* **2018**, *73*, 645–655.

(300) Kodigala, S. R. Optical Properties of I–III–VI2 Compounds. In *Thin Films and Nanostructures*; Kodigala, S.R., Ed. New York, USA, 2010, 35, pp. 195–317.

(301) Isaenko, L.; Yelisseyev, A.; Lobanov, S.; Titov, A.; Petrov, V.; Zondy, J. J.; Krinitsin, P.; Merkulov, A.; Vedenyapin, V.; Smirnova, J. *Cryst. Res. Technol*. **2003**, *38*, 379−387.

(302) Kosobutsky, A. V.; Basalaev, Y. M. *Solid State Commun.* **2014**, *199*, 17–21.

(303) Shewchun, J.; Loferski, J. J.; Beaulieu, R.; Chapman, G. H.;Garside, B. K. *J. Appl. Phys*. **1979**, *50*, 6978– 6985.

(304) Omata, T.; Nagatani, H.; Suzuki, I.; Kita, M. *Sci. Technol. Adv. Mater.* **2015**, *16*, 024902.

(305) Shafarman, W. N.; Klenk, R.; McCandless, B. E. *J. Appl. Phys.* **1996**, *79*, 7324–7328.

(306) Tinoco, T.; Polian, A.; Itié, J. P.; Moya, E.; Gonzalez, J. *J. Phys. Chem. Solids* **1995**, *56*, 481–484.

(307) Petrov, V.; Yelisseyev, A.; Isaenko, L.*;* S. Lobanov, Titov, A.; Zondy, J.-J. *Appl. Phys. B* **2004**, *78*, 543–546.

(308) Jung, S. Il., Yoon, K. H.; Ahn, S.; Gwak, J.; Yun, J. H. *Curr. Appl. Phys.* **2010**, *10*, S395–S398.

(309) Li, S.-F.; Jiang, X.-M.; Fan, Y.-H.; Liu, B.-W.; Zeng, H.-Y.; Guo, G.-C. *Chem. Sci.* **2018**, *9*, 5700–5708.

(310) Orlova, N. S., Kochkarik, O. E.; Bodna, I. V. *Cryst. Res. Technol*. **1994**, *29*, 561–568.

(311) Yelisseyev, A. P.; Molokeev, M. S.; Jiang, X.; Krinitsin, P. G.; Isaenko,L. I.; Lin, Z. *J. Phys. Chem. C* **2018**, *122*, 17413–17422.

(312) Yin, W.; Feng, K.; Hao, W.; Yao, J.; Wu, Y. *Inorg. Chem.* **2012**, *51*, 5839–5843.

(313) Bera, T. K.; Song, J. H.; Freeman, A. J., Jang, J. I.; Ketterson, J. B.; Kanatzidis, M. G. *Angew. Chem. Int. Ed.* **2008**, *47*, 7828–7832.

(314) Yang, H.-D.; Ran, M.-Y.; Zhou, S.-H.; Wu, X.-T.; Lin, H.; Zhu, Q.-L. *Chem. Sci.* **2022**, *13*, 10725–10733.

(315) Huang, R. T.; Zheng, M.; Sui, L. F.; Cai, C. B.; Huang, F. Q. *J. Inorg. Mater.* **2017**, *32*, 101–106.

(316) Zhou, H. M.; Xiong, L.; Chen, L.; Wu, L. M. *Angew. Chem. Int. Ed.* **2019**, *58*, 9979–9983.

(317) Isaenko, L.; Dong, L.; Kurus, A.; Lin, Z.; Yelisseyev, A.; Lobanov, S.; Molokeev, M. *Adv. Opt. Mater*. **2022**, *10*, 2201727.

(318) Kuriyama, K.; Nozaki, T. *J. Appl. Phys*. **1981**, *52*, 6441–6443.

(319) Protasenya, A. M.; Zolotarev, M. L.; Poplavnoi, A. S. *Sov. Phys. J.* **1983**, *26*, 517–520.

(320) Coelho, A. A. *TOPAS-Academic*, *version 6; Coelho Software*: Brisbane, Australia, 2007.

(321) Pawley, G. S. *J. Appl. Crystallogr.* **1981**, *14*, 357–361.

(322) Sheldrick, G. M. *Acta Crystallogr. Sect. A* **2008**, *64*, 112–122.

(323) Parthé, E.; Gelato, L. M.; Chabot, B. *Acta Crystallogr. Sect. A* **1988**, *44*, 999–1002.

(324) Kurtz, S. K.; Perry, T. T. *J. Quantum Electron.* **1968**, *4*, 333.

(325) Okhotnikov, K.; Charpentier, T.; Cadars, S.; Supercell program. *J. Cheminform.* **2016**, *8*, 1–15.

(326) G. Kresse, J. F. *Phys. Rev. B* **1996**, *54*, 11169–11185.

(327) G. Kresse, D. J. *Phys. Rev. B* **1999**, *59*, 1758–1775.

(328) Blöchl, P. E. *Phys. Rev. B* **1994**, *50*, 17953–17979.

(329) Perdew, J. P.; Burke, K.; Ernzerhof, M. *Phys. Rev. Lett.* **1996**, *77*, 3865–3868.

(330) Hohenberg, P. *Phys. Rev.* **1964**, *136*, B864–B870.

(331) Kohn, W.; Sham, L. J. *Phys. Rev.* **1965**, *140*, A1133–A1138.

(332) Grin, Y.; Savin, A.; Silvi, B. The ELF perspective of chemical bonding. In *The Chemical Bond: Fundamental Aspects of Chemical Bonding*; Frenking, G., Shaik, S., Eds.; Wiley-VCH, Weinheim, 2014, pp. 345–382

(333) Dronskowski, R.; Bloechl, P. E. *J. Phys. Chem.* **1993**, *97*, 8617–8624.

(334) Deringer, V. L.; Tchougréeff, A. L.; Dronskowski, R. *J. Phys. Chem. A* **2011**, *115*, 5461–

5466.

(335) Maintz, S.; Deringer, V. L.; Tchougréeff, A. L.; Dronskowski, R. *J. Comput. Chem.* **2013**, *34*, 2557–2567.

(336) Maintz, S.; Deringer, V. L.; Tchougréeff, A. L.; Dronskowski, R. *J. Comput. Chem.* **2016**, *37*, 1030–1035.

(337) Villars, P.; Cenzual, K. *Pearson's Crystal Data – Crystal Structure Database for Inorganic Compounds (on DVD)*, Release 2021/22; ASM International: Materials Park, OH, USA.

(338) Winter, F.; Dupke, S.; Eckert, H.; Rodewald, U. C.; Pöttgen, R. *Z. Anorg. Allg. Chem.* **2013**, *639*, 2790–2795.

(339) Honeyman, W. N.; Wilkinson, K. H. *J. Phys. D* **1971**, *4*, 1182–1185.

(340) Nguimdo, G. M. D.; Joubert, D. P. *Eur. Phys. J. B* **2015**, *88*, 1–10.

(341) Maeda, T.; Takeichi, T.; Wada, T. *Phys. Stat. Solidi* **2006**, *203*, 2634–2638.

(342) Pamplin, B. R.; Kiyosawa, T.;Masumoto, K. *Prog. Cryst. Growth Charact.* **1979**, *1*, 331–387.

(343) Hai, X.; Tahir-Kheli, J.;Goddard, W. A. *J. Phys. Chem. Lett.* **2011**, *2*, 212–217.

(344) Li, L. H.; Li, J. Q.; Wu, L. M. *J. Solid State Chem.* **2008**, *181*, 2462–2468.

(345) Müller, P. C.; Ertural, C.; Hempelmann, J.; Dronskowski, R. *J. Phys. Chem. C* **2021**, *125*, 7959–7970.

Appendix 1:

Supplementary data for Chapter 2

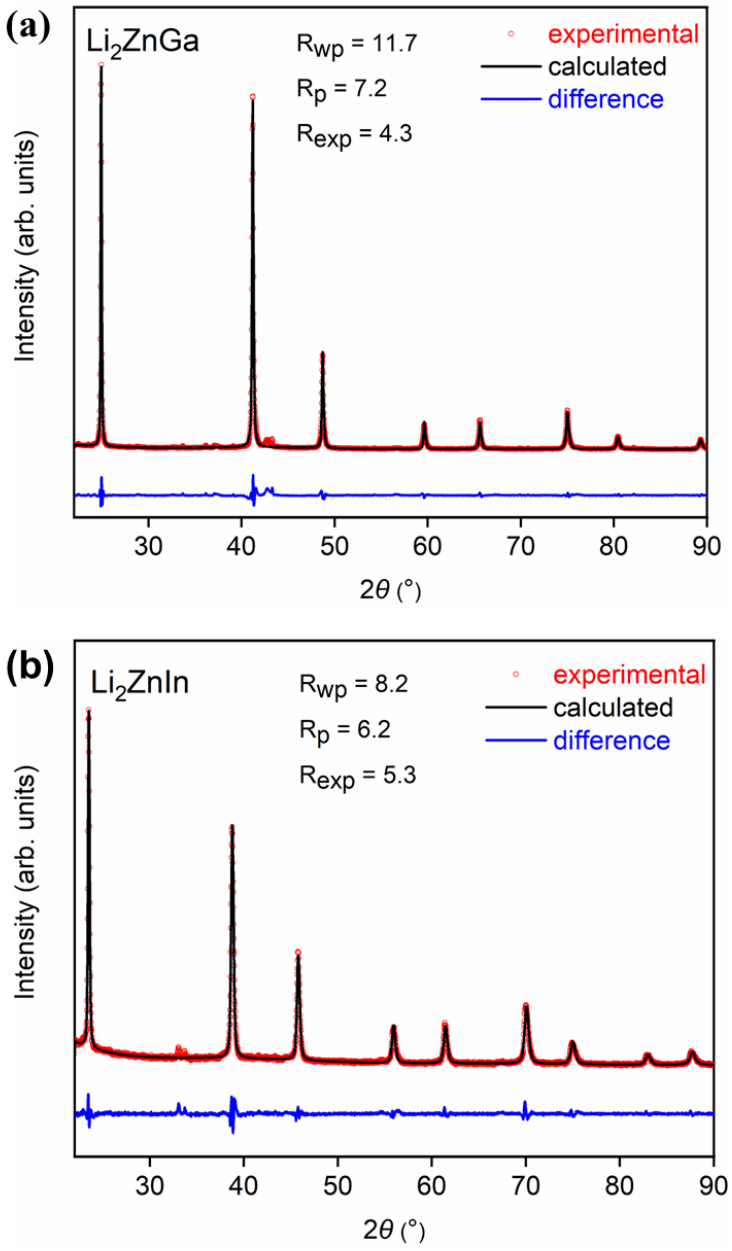

Figure A1-1. Pawley fittings of powder XRD patterns for (a) Li_2ZnGa and (b) Li_2ZnIn

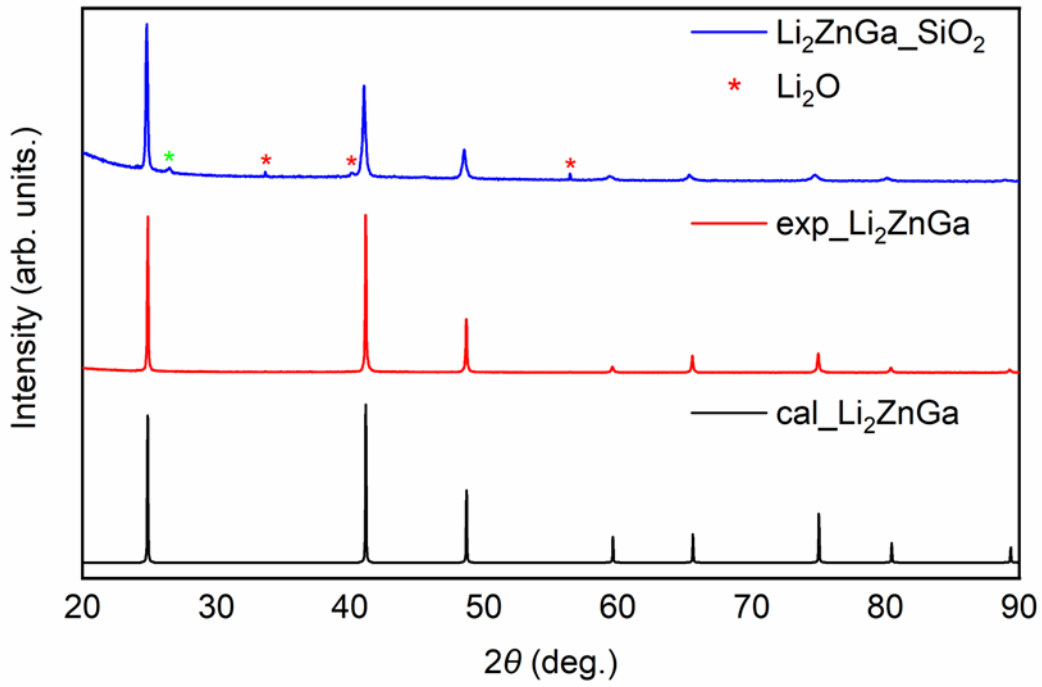

Figure A1-2. Powder XRD patterns for Li_2ZnGa, after (top) and before (middle) NMR measurements, in comparison to simulated pattern (bottom).

Appendix 2:

Supplementary data for Chapter 3

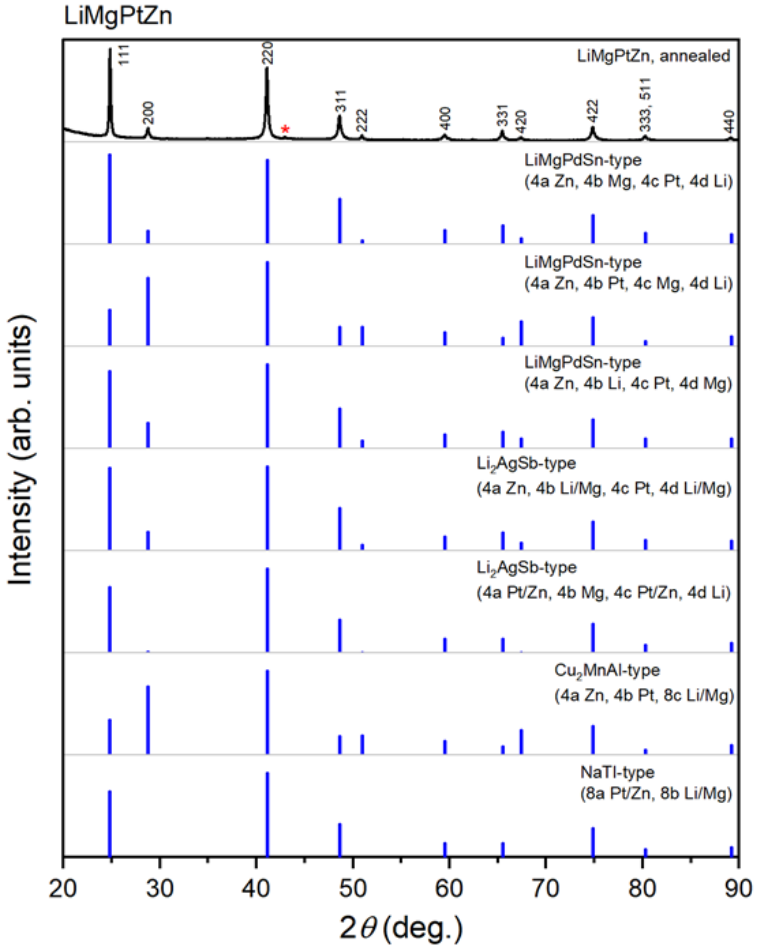

Figure A2-1. Experimental powder XRD pattern for LiMgPtZn compared with simulated patterns based on different structural models.

Appendix 3:

Supplementary data for Chapter 4

Table A3-1. Elemental analysis (mol. %) for $LiCu_2Al_{1-x}Ga_x$ and $LiCu_{2-y}Ni_yGa$

Compound	Cu	Ni	Ga	Al
$LiCu_2Al_{1-x}Ga_x$				
$LiCu_2Al$	68.5	-	-	31.5
$LiCu_2Al_{0.9}Ga_{0.1}$	67.5	-	3.0	29.5
$LiCu_2Al_{0.7}Ga_{0.3}$	69.0	-	11.8	19.2
$LiCu_2Al_{0.5}Ga_{0.5}$	73.5	-	13.4	13.1
$LiCu_2Al_{0.3}Ga_{0.7}$	71.8	-	20.6	7.5
$LiCu_2Ga$	72.8	-	27.2	-
$LiCu_{2-y}Ni_yGa$				
$LiCu_2Ga$	72.8	-	27.2	-
$LiCu_{1.8}Ni_{0.2}Ga$	63.0	6.6	30.4	-
$LiCu_{1.6}Ni_{0.4}Ga$	56.9	11.6	31.4	-
$LiCu_{1.5}Ni_{0.5}Ga$	56.0	17.7	26.3	-
$LiCu_{1.6}Ni_{0.6}Ga$	50.7	21.5	27.8	-
$LiCu_{1.2}Ni_{0.8}Ga$	41.8	26.4	31.7	-
$LiCuNiGa$	28.7	40.4	30.9	-

Table A3-2. Unit cell and refinement parameters for $LiCu_2Al_{1-x}Ga_x$ and $LiCu_{2-y}Ni_yGa$

Compound	Space group	*a*(Å)	Volume (Å^3)	R_p	R_{wp}
$LiCu_2Al_{1-x}Ga_x$					
$LiCu_2Al$	$Pm\bar{3}m$	2.9415(0)	25.45(0)	0.049	0.032
$LiCu_2Al_{0.9}Ga_{0.1}$	$Pm\bar{3}m$	2.9439(2)	25.51(6)	0.066	0.050
$LiCu_2Al_{0.7}Ga_{0.3}$	$Fm\bar{3}m$	5.8494(6)	200.1(2)	0.04.9	0.036
$LiCu_2Al_{0.5}Ga_{0.5}$	$Fm\bar{3}m$	5.8538(2)	200.59(6)	0.057	0.038
$LiCu_2Al_{0.3}Ga_{0.7}$	$Fm\bar{3}m$	5.8602(8)	201.2(2)	0.051	0.036
$LiCu_2Al_{0.1}Ga_{0.9}$	$Fm\bar{3}m$	5.8756(6)	202.8(2)	0.041	0.055
$LiCu_2Ga$	$Fm\bar{3}m$	5.8843(3)	203.74(9)	0.039	0.030
$LiCu_{2-y}Ni_yGa$					
$LiCu_2Ga$	$Fm\bar{3}m$	5.8843(3)	203.74(9)	0.039	0.030
$LiCu_{1.8}Ni_{0.2}Ga$	$Fm\bar{3}m$	5.8762(1)	202.90(3)	0.030	0.029
$LiCu_{1.6}Ni_{0.4}Ga$	$Fm\bar{3}m$	5.8646(6)	201.7(2)	0.035	0.027
$LiCu_{1.5}Ni_{0.5}Ga$	$Fm\bar{3}m$	5.8553(4)	200.8(1)	0.028	0.020
$LiCu_{1.4}Ni_{0.6}Ga$	$Fm\bar{3}m$	5.8485(1)	200.05(3)	0.043	0.030
$LiCu_{1.2}Ni_{0.8}Ga$	$Fm\bar{3}m$	5.8334(1)	198.50(3)	0.068	0.043
$LiCuNiGa$	$Fm\bar{3}m$	5.8207(2)	197.21(6)	0.040	0.028

Table A3-3. ^{7}Li NMR data for $LiCu_2Al_{1-x}Ga_x$

Compound	Space group	Chemical shift (ppm)	FWHM (kHz)
$LiCu_2Al$	$Pm\bar{3}m$	48.8	2.18
$LiCu_2Al_{0.9}Ga_{0.1}$	$Pm\bar{3}m$	50.6	2.38
$LiCu_2Al_{0.5}Ga_{0.5}$	$Fm\bar{3}m$	53.0	3.04
$LiCu_2Al_{0.1}Ga_{0.9}$	$Fm\bar{3}m$	52.3	2.26
$LiCu_2Ga$	$Fm\bar{3}m$	51.0	1.91

Table A3-4. CIE Coordinates for $LiCu_2Al_{1-x}Ga_x$ and $LiCu_{2-y}Ni_yGa$

sample	CIE 1931 *x*	CIE 1931 *y*
$LiCu_2Al_{1-x}Ga_x$		
$LiCu_2Al$	0.5367	0.4068
$LiCu_2Al_{0.9}Ga_{0.1}$	0.5623	0.4250
$LiCu_2Al_{0.5}Ga_{0.5}$	0.5208	0.4478
$LiCu_2Al_{0.1}Ga_{0.9}$	0.5099	0.4497
$LiCu_2Ga$	0.4768	0.4686
$LiCu_{2-y}Ni_yGa$		
$LiCu_2Ga$	0.4768	0.4686
$LiCu_{1.8}Ni_{0.2}Ga$	0.4946	0.4506
$LiCu_{1.6}Ni_{0.4}Ga$	0.4689	0.4469
$LiCu_{1.6}Ni_{0.6}Ga$	0.4776	0.4388
$LiCu_{1.2}Ni_{0.8}Ga$	0.4620	0.4324
$LiCuNiGa$	0.4518	0.4153

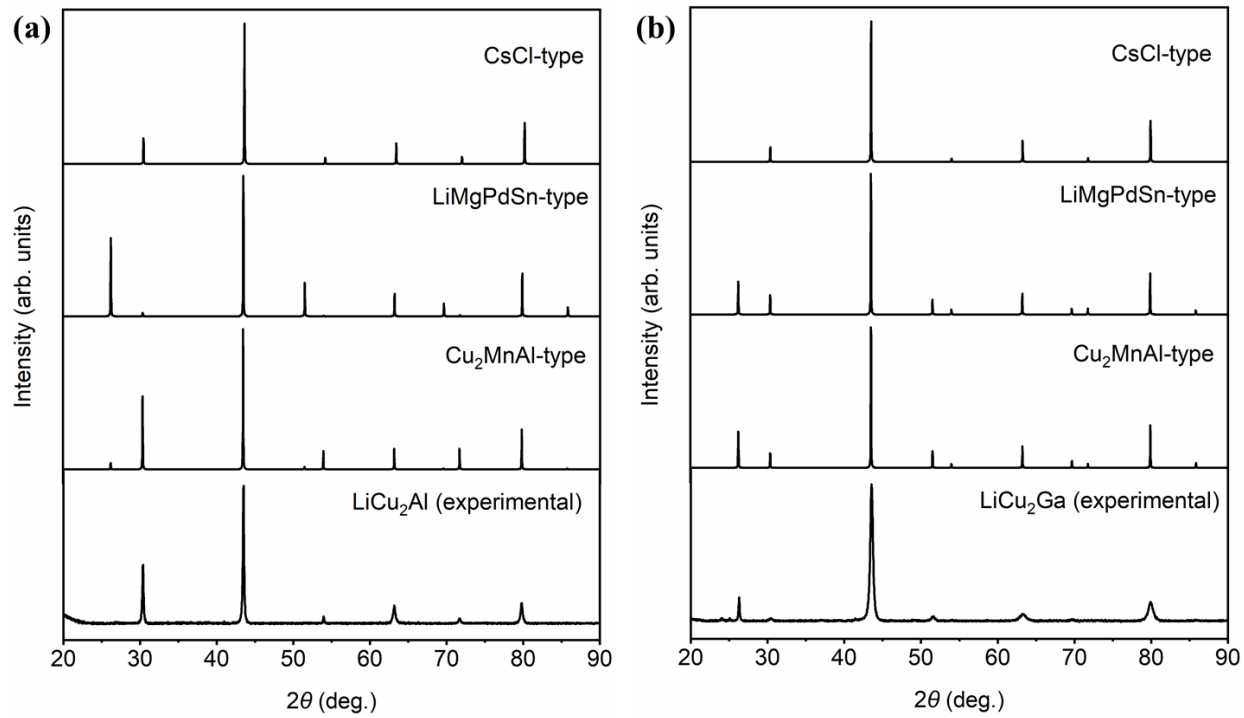

Figure A3-1. Structures models of (a) $LiCu_2Al$ (b) $LiCu_2Ga$ compounds based on possible arrangements of atoms within a cubic cell in space group $Fm\bar{3}m$ (for Cu_2MnAl-type), $F\bar{4}3m$ for (LiMgPdSn-type) and $Pm\bar{3}m$ (for CsCl-type).

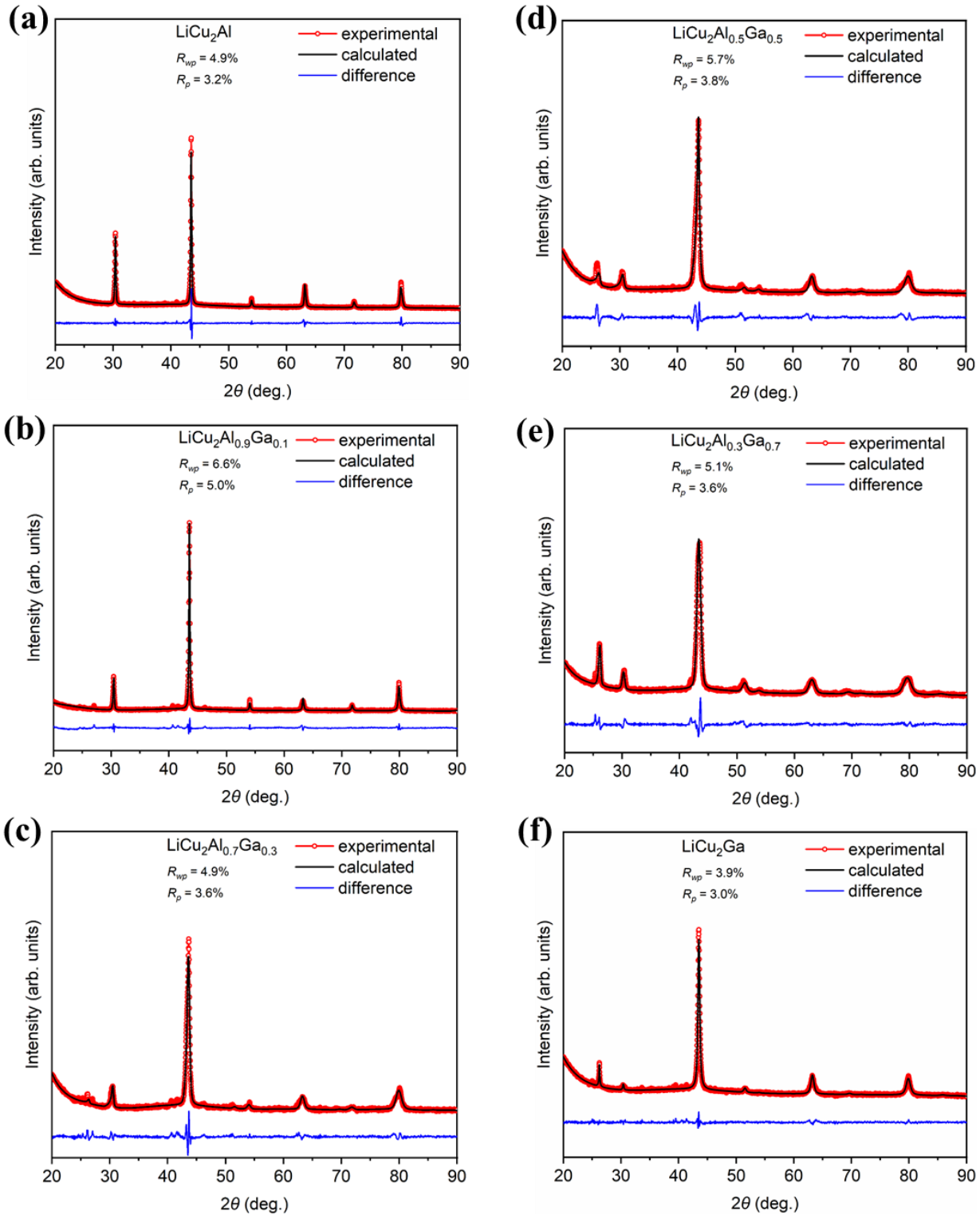

Figure A3-2. Pawley refinements for $LiCu_2Al_{1-x}Ga_x$.

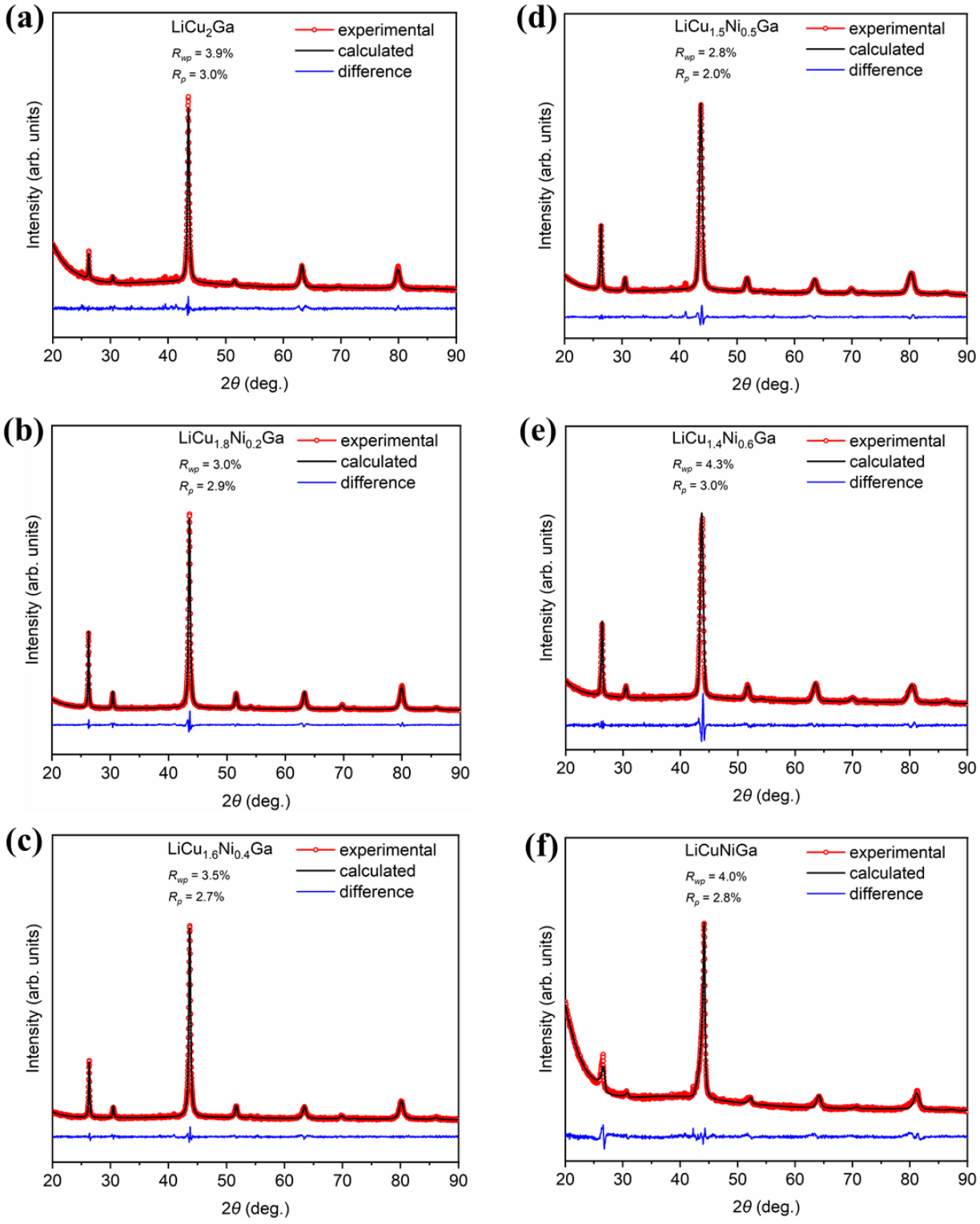

Figure A3-3. Pawley refinements for $LiCu_{2-y}Ni_yGa$.

Appendix 4:

Supplementary data for Chapter 5

Table A4-1. EDX Analyses (mol. %) for $Li_xAg_{1-x}GaSe_2$ and $Li_xAg_{1-x}InSe_2$ Samples [a]

sample	observed			expected		
	Ag	Ga or In	Se	Ag	Ga or In	Se
$Li_xAg_{1-x}GaSe_2$						
$AgGaSe_2$	26	25	49	25	25	50
$Li_{0.10}Ag_{0.90}GaSe_2$	24	26	50	23	26	51
$Li_{0.25}Ag_{0.75}GaSe_2$	19	28	53	20	27	53
$Li_{0.50}Ag_{0.50}GaSe_2$	15	29	56	14	29	57
$Li_{0.75}Ag_{0.25}GaSe_2$	8	31	61	8	31	61
$Li_{0.90}Ag_{0.10}GaSe_2$	1	33	66	3	32	65
$LiGaSe_2$ ($I\bar{4}2d$)		34	66		33	67
$LiGaSe_2$ ($Pna2_1$)		30	70		33	67
$Li_xAg_{1-x}InSe_2$						
$AgInSe_2$	25	26	49	25	25	50
$Li_{0.10}Ag_{0.90}InSe_2$	23	27	50	23	26	51
$Li_{0.25}Ag_{0.75}InSe_2$	20	29	52	20	27	53
$Li_{0.50}Ag_{0.50}InSe_2$	13	30	57	14	29	57
$Li_{0.75}Ag_{0.25}InSe_2$	7	33	60	8	31	61
$Li_{0.90}Ag_{0.10}InSe_2$	3	33	64	3	32	65
$LiInSe_2$		34	66		33	67

[a] Li is too light to detect by EDX analyses. Estimated uncertainties are within 1–3%.

Table A4-2. Isotropic Chemical Shifts and Linewidths of ^{7}Li NMR Spectra for $Li_xAg_{1-x}GaSe_2$ and $Li_xAg_{1-x}InSe_2$

compound	δ_{iso} (ppm)	FWHM (Hz)
$Li_xAg_{1-x}GaSe_2$		
$Li_{0.10}Ag_{0.90}GaSe_2$ ($I\bar{4}2d$)	2.64(1)	124(2)
$Li_{0.25}Ag_{0.75}GaSe_2$ ($I\bar{4}2d$)	2.65(1)	224(3)
$Li_{0.50}Ag_{0.50}GaSe_2$ ($I\bar{4}2d$)	2.83(1)	241(3)
$Li_{0.75}Ag_{0.25}GaSe_2$ ($I\bar{4}2d$)	2.62(1)	270(3)
$Li_{0.90}Ag_{0.10}GaSe_2$ ($I\bar{4}2d$)	2.59(1)	290(4)
$LiGaSe_2$ ($I\bar{4}2d$)	2.59(1)	302(5)
$LiGaSe_2$ ($Pna2_1$)	2.34(1)	186(4)
$Li_xAg_{1-x}InSe_2$		
$Li_{0.25}Ag_{0.75}InSe_2$ ($I\bar{4}2d$)	2.65(2)	133(2)
$Li_{0.50}Ag_{0.50}InSe_2$ ($I\bar{4}2d$)	2.35(2)	207(3)
$Li_{0.75}Ag_{0.25}InSe_2$ ($Pna2_1$)	2.01(2)	135(2)
$LiInSe_2$ ($Pna2_1$)	2.32(2)	158(2)

Table A4-3. Optical Band Gaps for $Li_xAg_{1-x}GaSe_2$ and $Li_xAg_{1-x}InSe_2$

compound	experimental band gap (eV)	calculated band gap (eV)
$Li_xAg_{1-x}GaSe_2$		
$AgGaSe_2$ ($I\bar{4}2d$)	1.76	0.21
$Li_{0.10}Ag_{0.90}GaSe_2$ ($I\bar{4}2d$)	1.92	
$Li_{0.25}Ag_{0.75}GaSe_2$ ($I\bar{4}2d$)	2.17	0.62
$Li_{0.50}Ag_{0.50}GaSe_2$ ($I\bar{4}2d$)	2.40	0.98
$Li_{0.75}Ag_{0.25}GaSe_2$ ($I\bar{4}2d$)	2.70	1.47
$Li_{0.90}Ag_{0.10}GaSe_2$ ($I\bar{4}2d$)	3.14	
$LiGaSe_2$ ($I\bar{4}2d$)	3.39	2.01
$LiGaSe_2$ ($Pna2_1$)	3.37	2.05
$Li_xAg_{1-x}InSe_2$		
$AgInSe_2$ ($I\bar{4}2d$)	1.17	0.18
$Li_{0.10}Ag_{0.90}InSe_2$ ($I\bar{4}2d$)	1.32	
$Li_{0.25}Ag_{0.75}InSe_2$ ($I\bar{4}2d$)	1.41	0.30
$Li_{0.50}Ag_{0.50}InSe_2$ ($I\bar{4}2d$)	1.87	0.64
$Li_{0.75}Ag_{0.25}InSe_2$ ($Pna2_1$)	2.27	1.08
$Li_{0.90}Ag_{0.10}InSe_2$ ($Pna2_1$)	2.44	
$LiInSe_2$ ($Pna2_1$)	2.54	1.61

Table A4-4. Powder SHG Intensities as a Function of Particle Sizes for $Li_xAg_{1-x}GaSe_2$ and $Li_xAg_{1-x}InSe_2$ [a]

compound	20–50 μm	50–90 μm	90–125 μm	125–150 μm	150–200 μm
$Li_xAg_{1-x}GaSe_2$					
$AgGaSe_2$ ($I\bar{4}2d$)	2.8	2.0	0.60	0.40	0.40
$Li_{0.25}Ag_{0.75}GaSe_2$ ($I\bar{4}2d$)	4.0	3.4	0.65	0.39	0.37
$Li_{0.50}Ag_{0.50}GaSe_2$ ($I\bar{4}2d$)	11.4	4.3	1.2	1.0	0.82
$Li_{0.75}Ag_{0.25}GaSe_2$ ($I\bar{4}2d$)	10.5	3.8	1.3	1.3	0.93
$LiGaSe_2$ ($I\bar{4}2d$)	5.9	1.6	0.37	1.1	0.90
$LiGaSe_2$ ($Pna2_1$)	12.1	4.2	1.2	1.0	0.44
$Li_xAg_{1-x}InSe_2$					
$AgInSe_2$ ($I\bar{4}2d$)	2.2	1.1	0.36	0.07	0.04
$Li_{0.25}Ag_{0.75}InSe_2$ ($I\bar{4}2d$)	7.3	2.6	0.86	0.78	0.56
$Li_{0.75}Ag_{0.25}InSe_2$ ($Pna2_1$)	9.6	4.1	1.2	0.71	0.63
$LiInSe_2$ ($Pna2_1$)	7.4	3.7	2.0	0.74	0.48

[a] Relative to $AgGaS_2$ serving as a reference.

Table A4-5. Integrated –COHP and COBI for Bonding Interactions in $Li_xAg_{1-x}GaSe_2$ and $Li_xAg_{1-x}InSe_2$

compound	–ICOHP (eV/bond)			ICOBI (eV/bond)		
	Li–Se	Ag–Se	Ga–Se or In–Se	Li–Se	Ag–Se	Ga–Se or In–Se
$Li_xAg_{1-x}GaSe_2$						
$AgGaSe_2$ ($I\bar{4}2d$)		1.22	4.85		0.21	0.81
$Li_{0.25}Ag_{0.75}GaSe_2$ ($I\bar{4}2d$)	0.88	1.17–1.22	4.83–4.88	0.14	0.21–0.22	0.81–0.83
$Li_{0.50}Ag_{0.50}GaSe_2$ ($I\bar{4}2d$)	0.87–0.88	1.32–1.42	4.82–4.89	0.14	0.22–0.23	0.82–0.84
$Li_{0.75}Ag_{0.25}GaSe_2$ ($I\bar{4}2d$)	0.90–0.91	1.77	4.84–4.88	0.14	0.24	0.83–0.84
$LiGaSe_2$ ($I\bar{4}2d$)	0.93		5.38–5.39	0.14		0.86
$LiGaSe_2$ ($Pna2_1$)	0.93–0.97		4.81–4.91	0.14–0.15		0.83–0.85
$Li_xAg_{1-x}InSe_2$						
$AgInSe_2$ ($I\bar{4}2d$)		1.22	4.15		0.22	0.77
$Li_{0.25}Ag_{0.75}InSe_2$ ($I\bar{4}2d$)	0.88	1.18–1.24	4.14–4.20	0.14	0.21–0.23	0.77–0.78
$Li_{0.50}Ag_{0.50}InSe_2$ ($I\bar{4}2d$)	0.87–0.88	1.46–1.52	4.15–4.20	0.14–0.15	0.22–0.24	0.77–0.79
$Li_{0.75}Ag_{0.25}InSe_2$ ($Pna2_1$)	0.88–0.93	2.29–2.69	4.16–4.28	0.14–0.15	0.26–0.27	0.77–0.80
$LiInSe_2$ ($Pna2_1$)	0.92–0.99		4.16–4.26	0.14–0.15		0.79–0.81

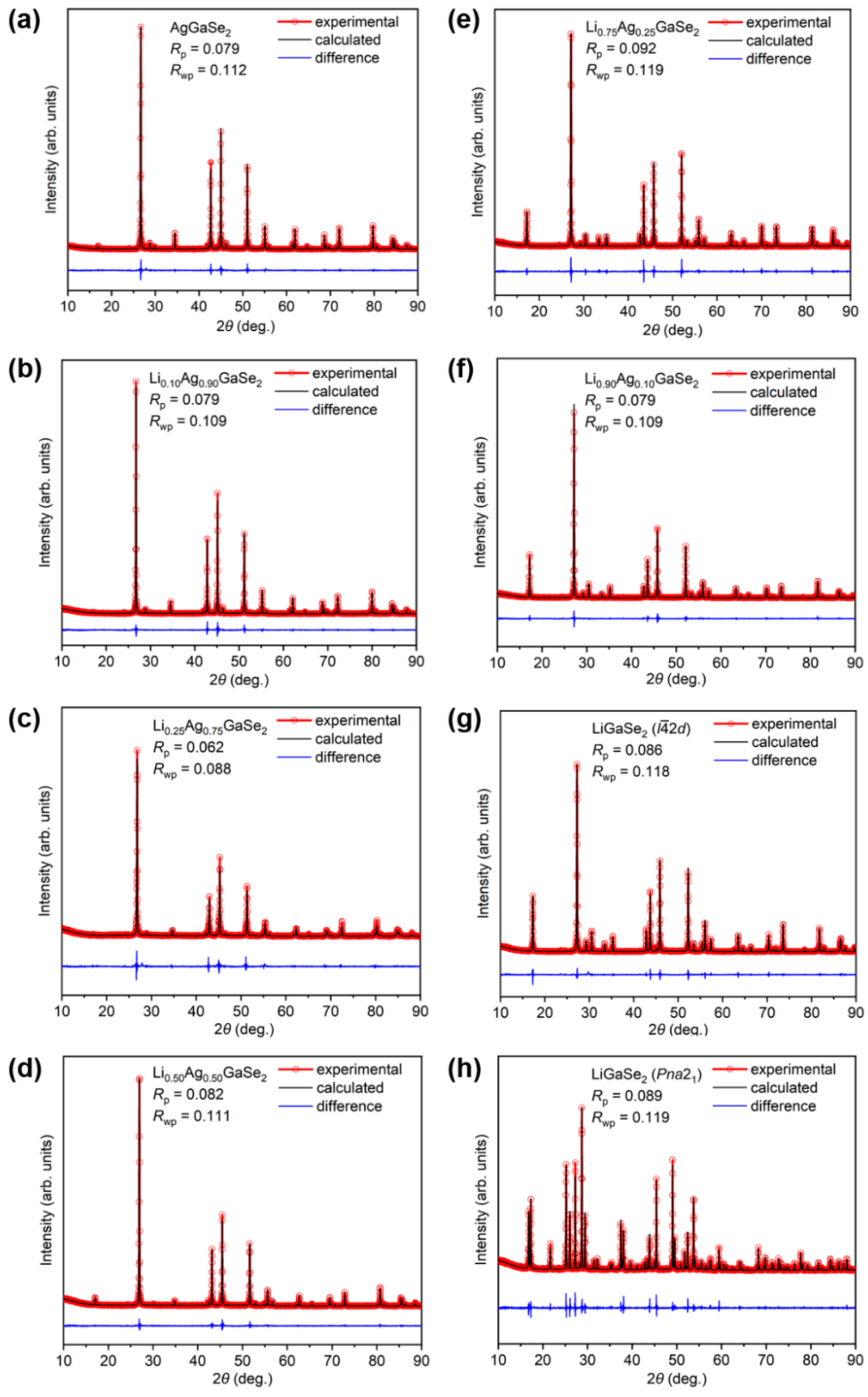

Figure A4-1. Pawley refinements for $Li_xAg_{1-x}GaSe_2$, including tetragonal and orthorhombic polymorphs of $LiGaSe_2$.

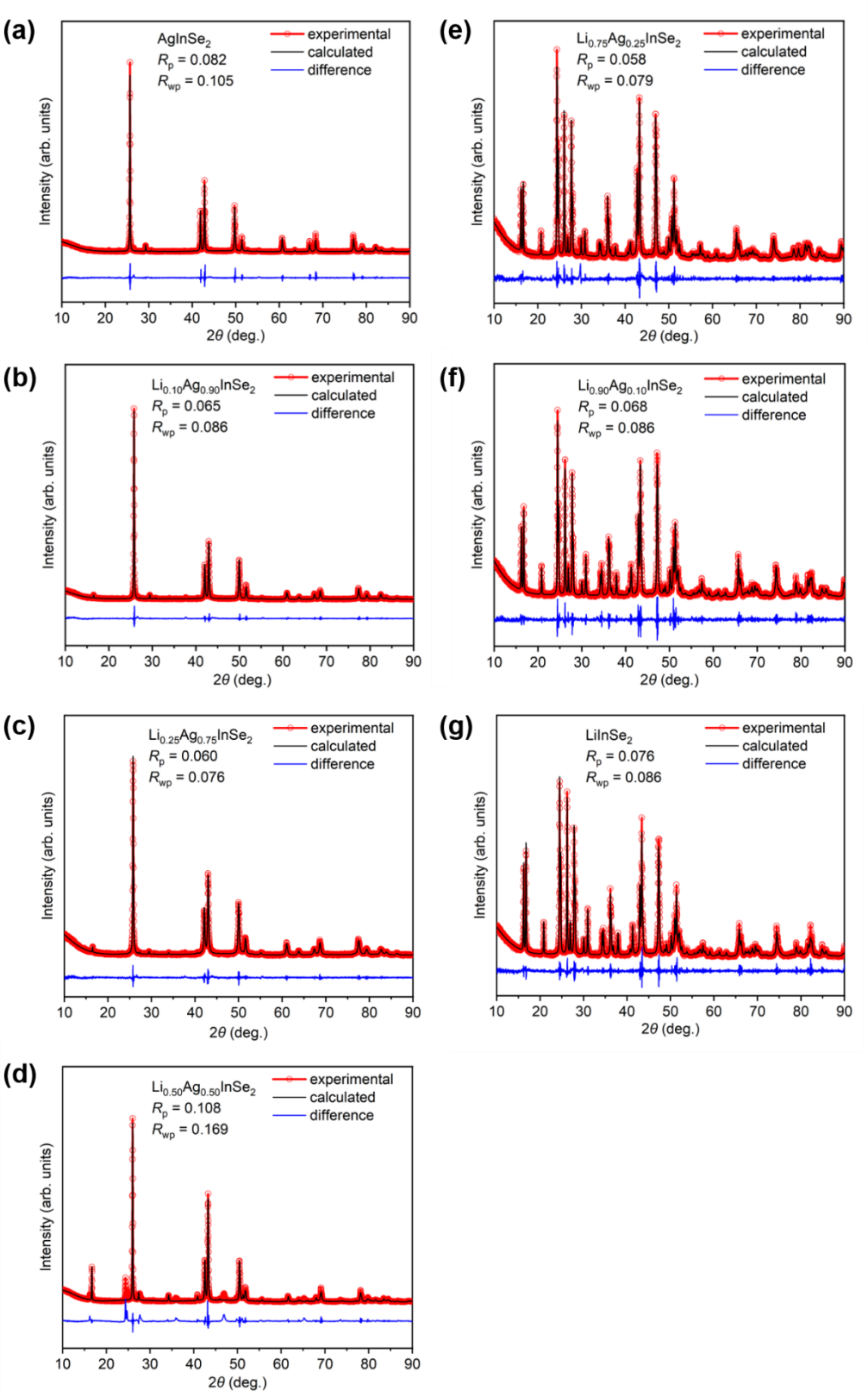

Figure A4-2. Pawley refinements for $Li_xAg_{1-x}InSe_2$.

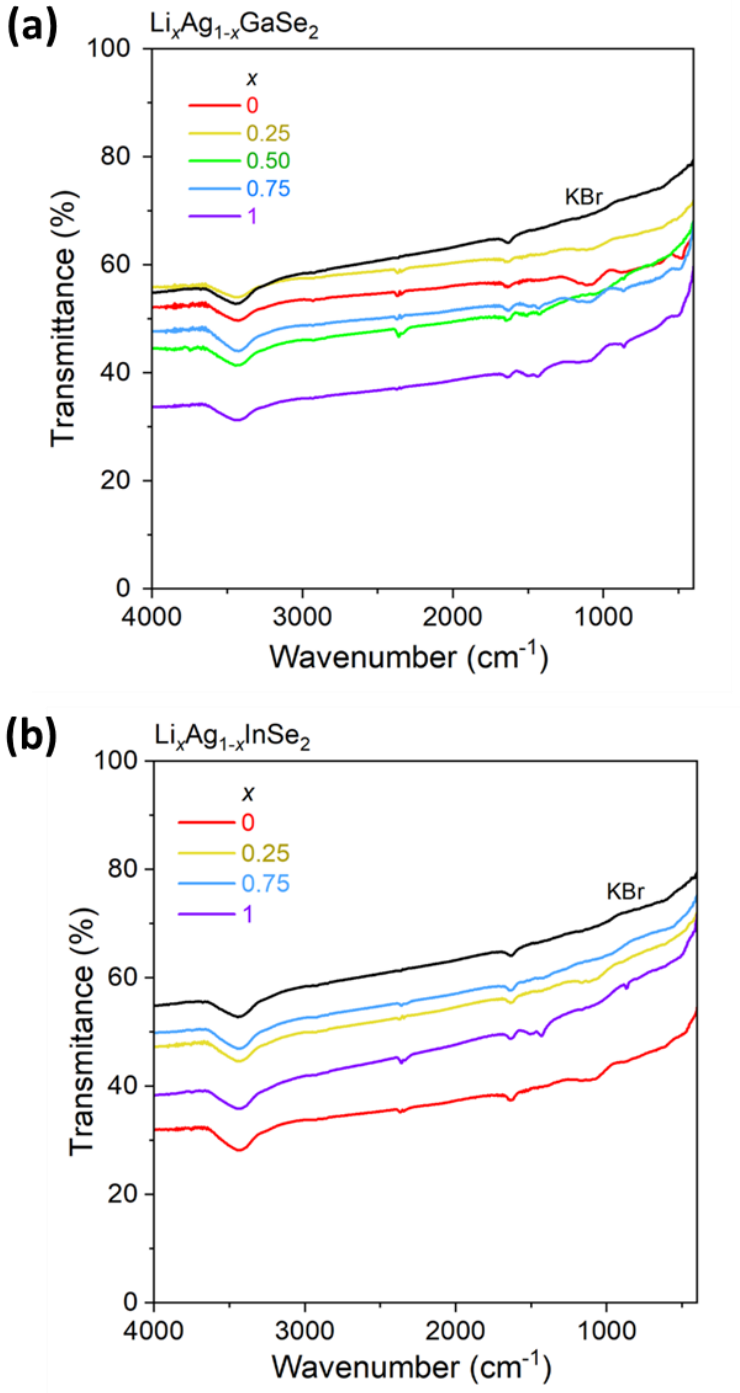

Figure A4-3. IR transmission spectra for $Li_xAg_{1-x}GaSe_2$ and $Li_xAg_{1-x}InSe_2$.

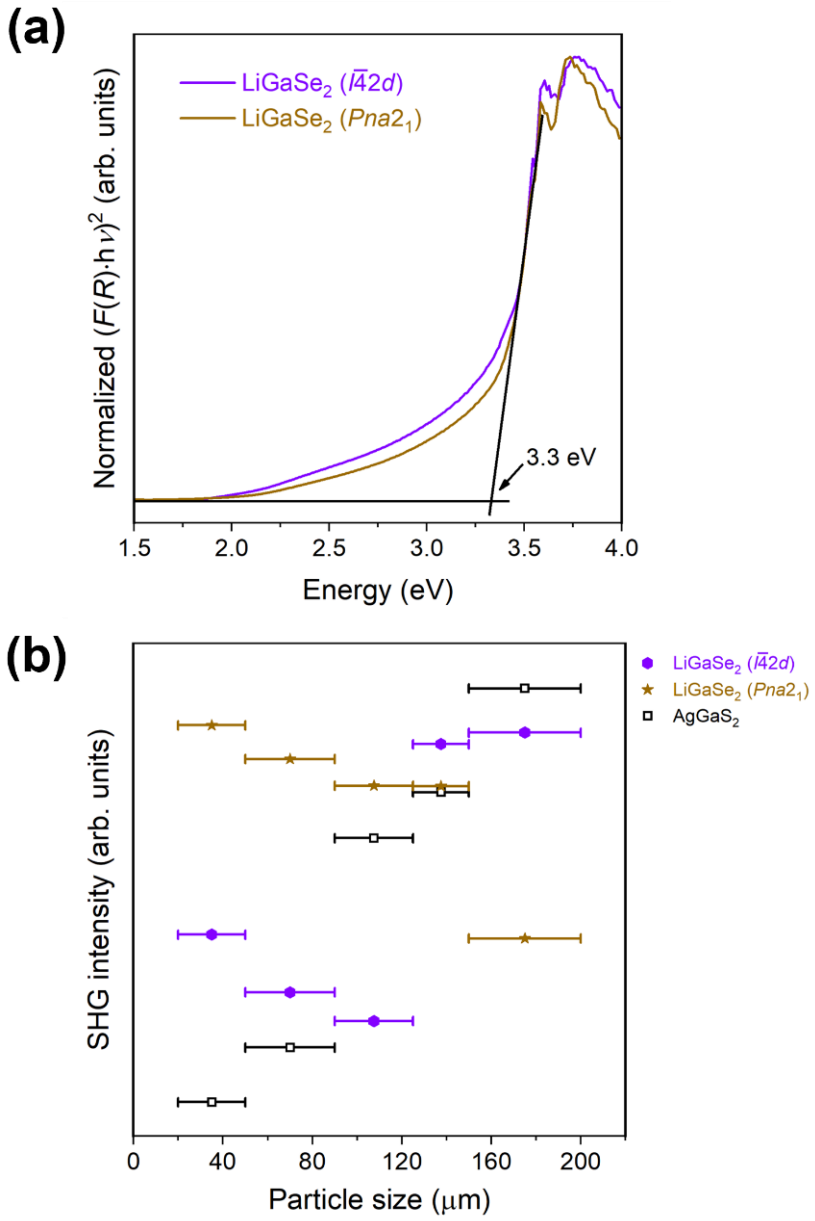

Figure A4-4. (a) Diffuse reflectance spectra and (b) dependence of SHG intensity on particle size ranges (at 2090 nm laser wavelength) for tetragonal vs. orthorhombic forms of $LiGaSe_2$.

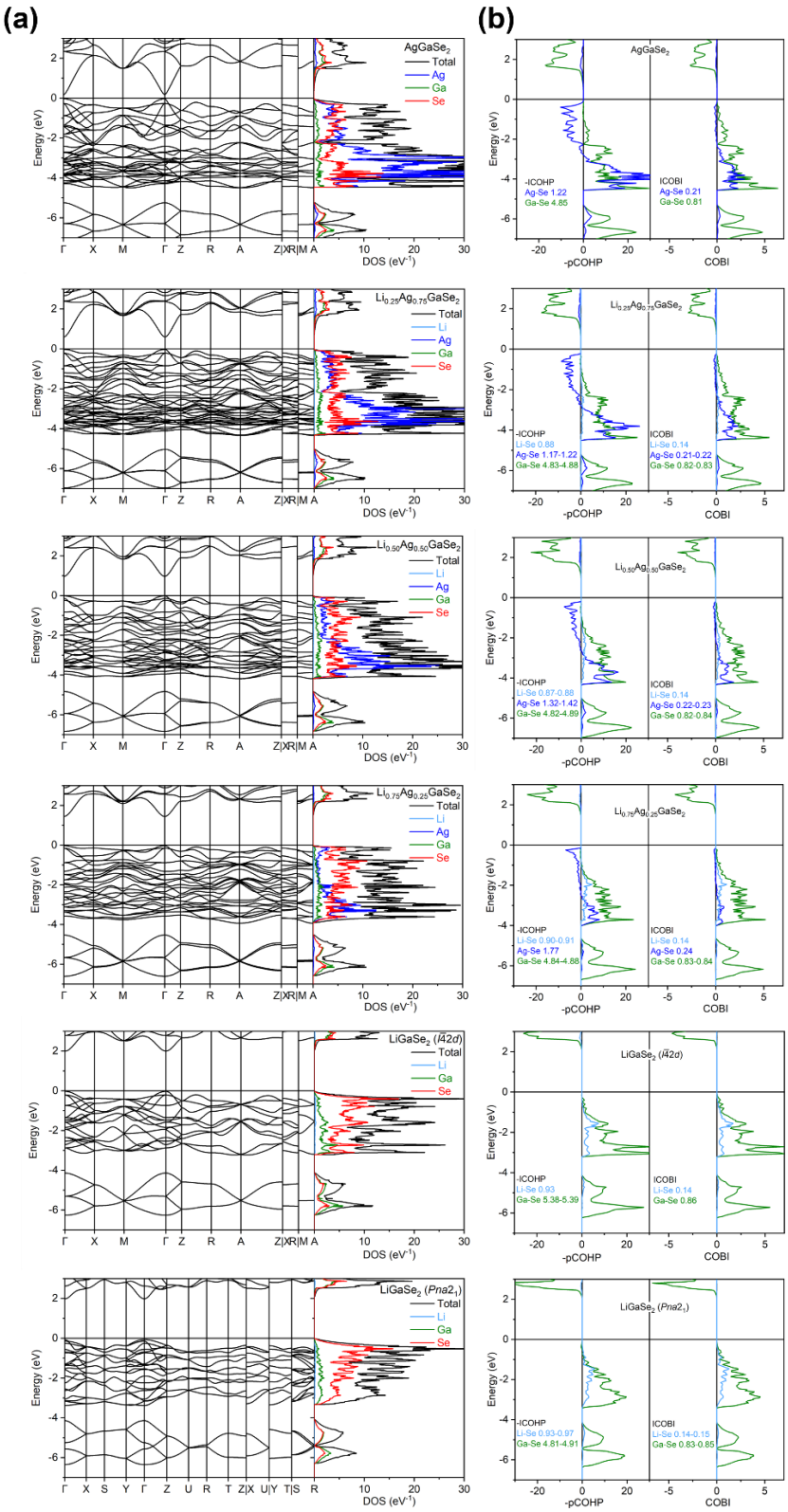

Figure A4-5. (a) Band dispersion and DOS plots; and (b) COHP and COBI plots for models of $Li_xAg_{1-x}GaSe_2$.

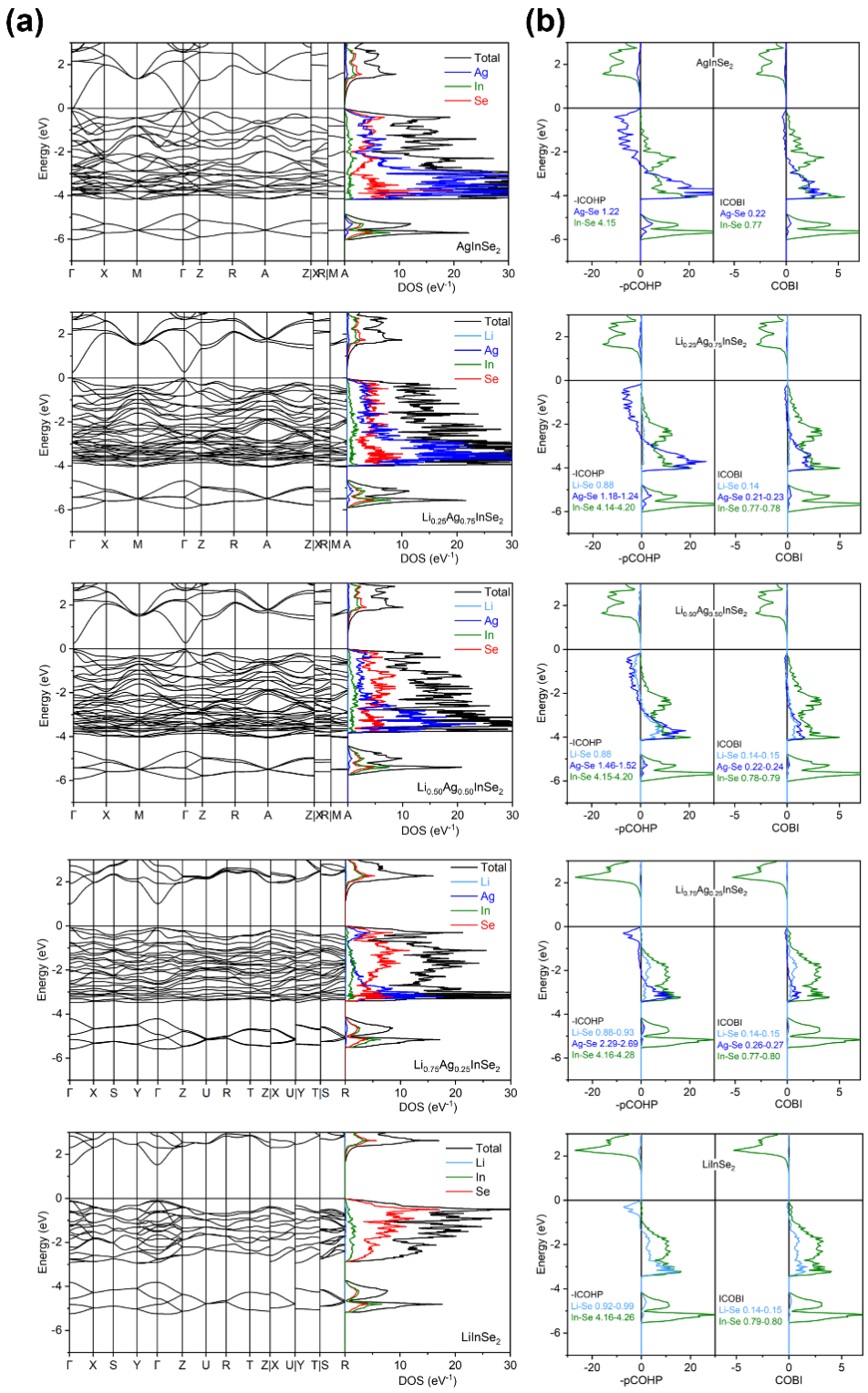

Figure A4-6. (a) Band dispersion and DOS plots; and (b) COHP and COBI plots for models of $Li_xAg_{1-x}InSe_2$.

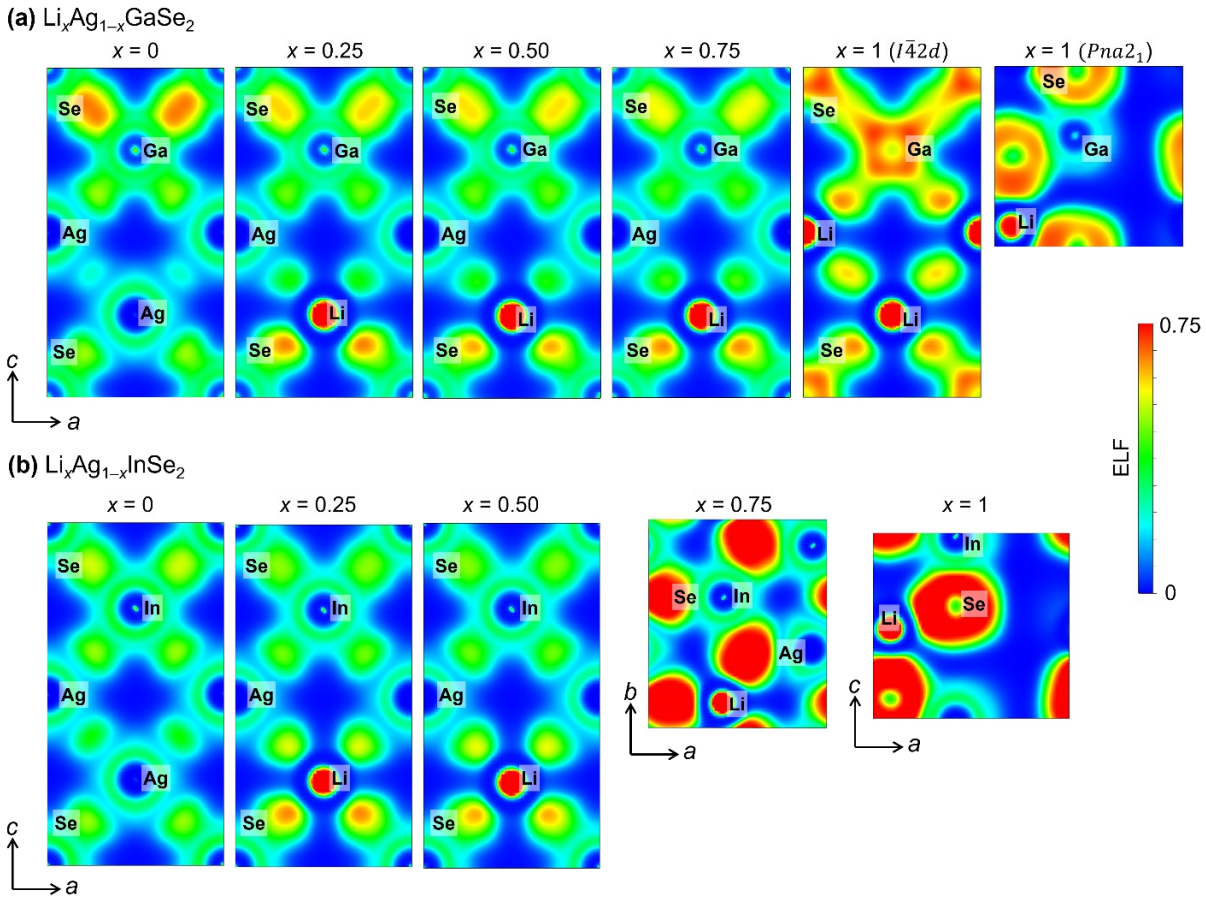

Figure A4-7. ELF plots for $Li_xAg_{1-x}GaSe_2$ and $Li_xAg_{1-x}InSe_2$.

Appendix 5:

Supplementary data for Chapter 6

Table A5-1. Isotropic Chemical Shifts and Linewidths of ^{7}Li NMR Spectra for $Li_xAg_{1-x}AlSe_2$

Compound	Chemical shift (ppm)	FWHM (Hz)
$Li_{0.25}Ag_{0.75}AlSe_2$	0.78(2)	203(9)
$Li_{0.5}Ag_{0.5}AlSe_2$	2.36(2)	327(3)
$Li_{0.75}Ag_{0.25}AlSe_2$	1.81(2)	268(2)
$Li_{0.9}Ag_{0.1}AlSe_2$	0.43(2)	230(4)
$LiAlSe_2$	0.71(2)	294(5)

Table A5-2. Optical Band Gaps (eV) for $Li_xAg_{1-x}AlSe_2$

Compound	experimental band gap (eV)	calculated band gap (eV)
$AgAlSe_2$	2.66	1.11
$Li_{0.25}Ag_{0.75}AlSe_2$	2.99	1.46
$Li_{0.5}Ag_{0.5}AlSe_2$	3.14	1.74
$Li_{0.75}Ag_{0.25}AlSe_2$	3.37	2.34
$LiAlSe_2$	3.60	3.01

Table A5-3. Powder SHG Intensities as a Function of Particle Sizes for $Li_xAg_{1-x}AlSe_2$ [a]

Compound	20–50 μm	50–90 μm	90–125 μm	125–150 μm	150–200 μm
$AgAlSe_2$	0.4	0.32	0.11	0.16	0.15
$Li_{0.25}Ag_{0.75}AlSe_2$			0.13	0.12	0.13
$Li_{0.75}Ag_{0.25}AlSe_2$	0.4	0.37	0.38	0.25	0.13
$LiAlSe_2$	2.6	0.59	0.96	2.2	0.64

[a] Relative to $AgGaS_2$ serving as a reference.

Table A5-4. Integrated COHP (eV/bond) for Bonding Interactions in $Li_xAg_{1-x}AlSe_2$

Compound	Li–Se	Ag–Se	Al–Se
$AgAlSe_2$		1.17	5.00
$Li_{0.25}Ag_{0.75}AlSe_2$	0.86	1.15	4.96
$Li_{0.5}Ag_{0.5}AlSe_2$	0.85–0.87	1.33–1.45	4.94–4.99
$Li_{0.75}Ag_{0.25}AlSe_2$	0.87–0.92	1.93–2.44	4.88–5.07
$LiAlSe_2$	0.91–0.95		4.88–5.01

Table A5-5. Integrated COBI (eV/bond) for Bonding Interactions in $Li_xAg_{1-x}AlSe_2$

Compound	Li–Se	Ag–Se	Al–Se
$AgAlSe_2$		0.21	0.81
$Li_{0.25}Ag_{0.75}AlSe_2$	0.14	0.20–0.22	0.81–0.82
$Li_{0.5}Ag_{0.5}AlSe_2$	0.14	0.21–0.23	0.81–0.82
$Li_{0.75}Ag_{0.25}AlSe_2$	0.14–0.15	0.24–0.27	0.80–0.84
$LiAlSe_2$	0.14–0.15		0.81–0.84

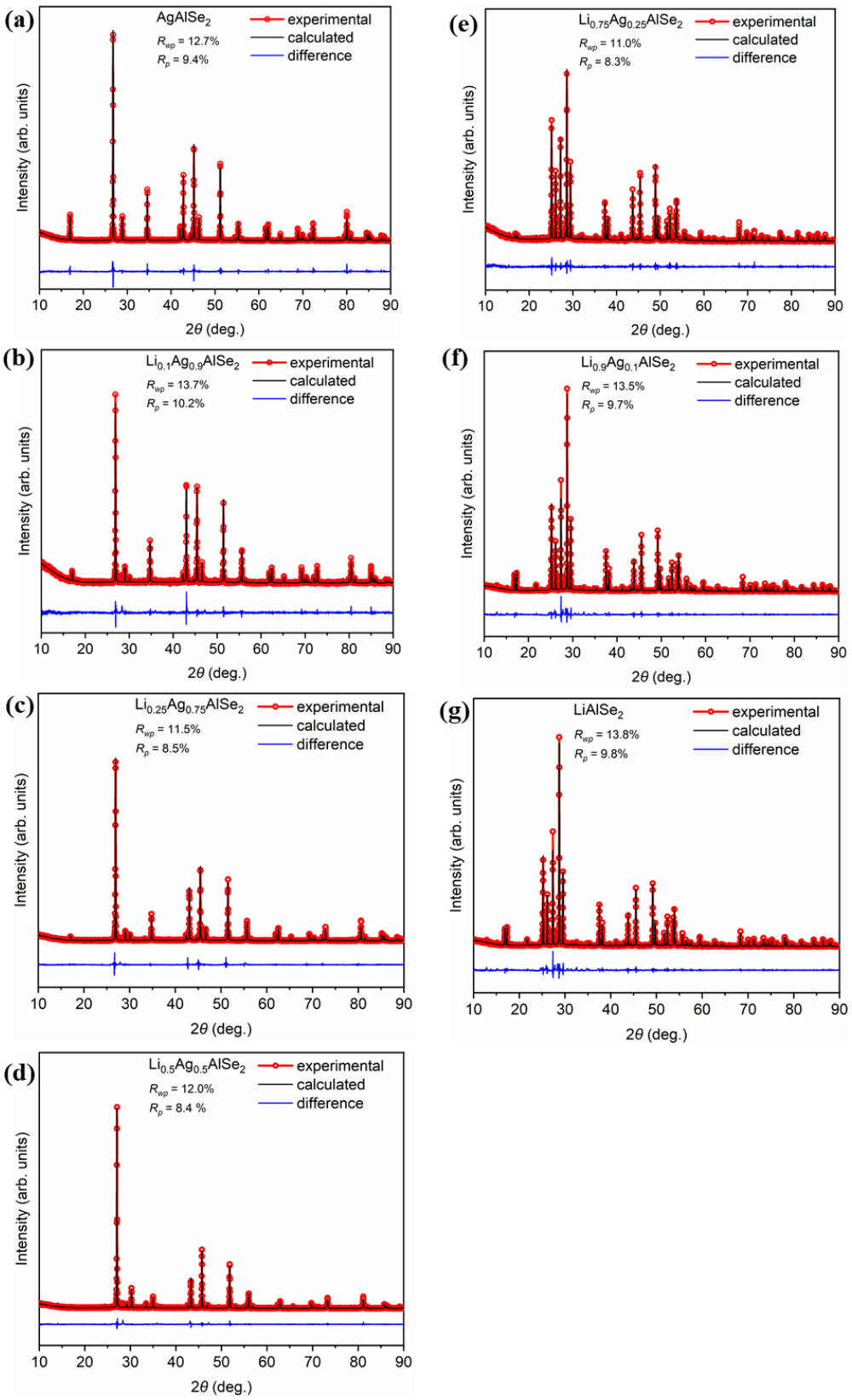

Figure A5-1. Pawley refinements for $Li_xAg_{1-x}AlSe_2$.

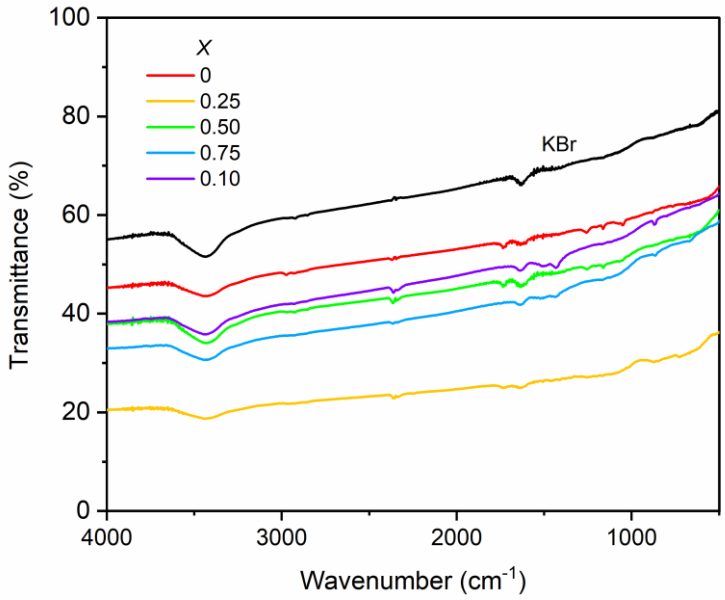

Figure A5-2. IR transmission spectra for $Li_xAg_{1-x}AlSe_2$.

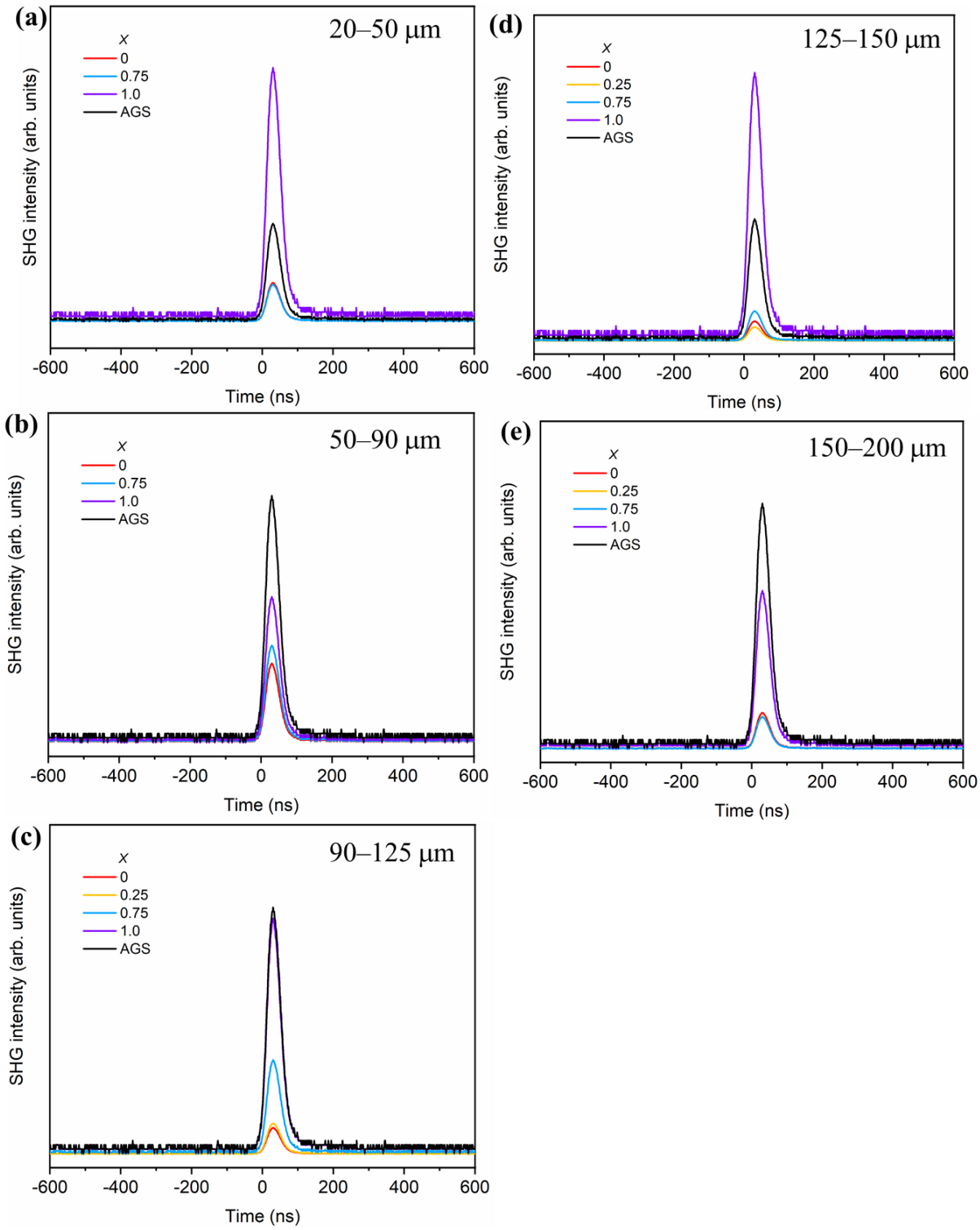

Figure A5-3. SHG intensities for $Li_xAg_{1-x}AlSe_2$ within particle sizes of 20–200 μm.

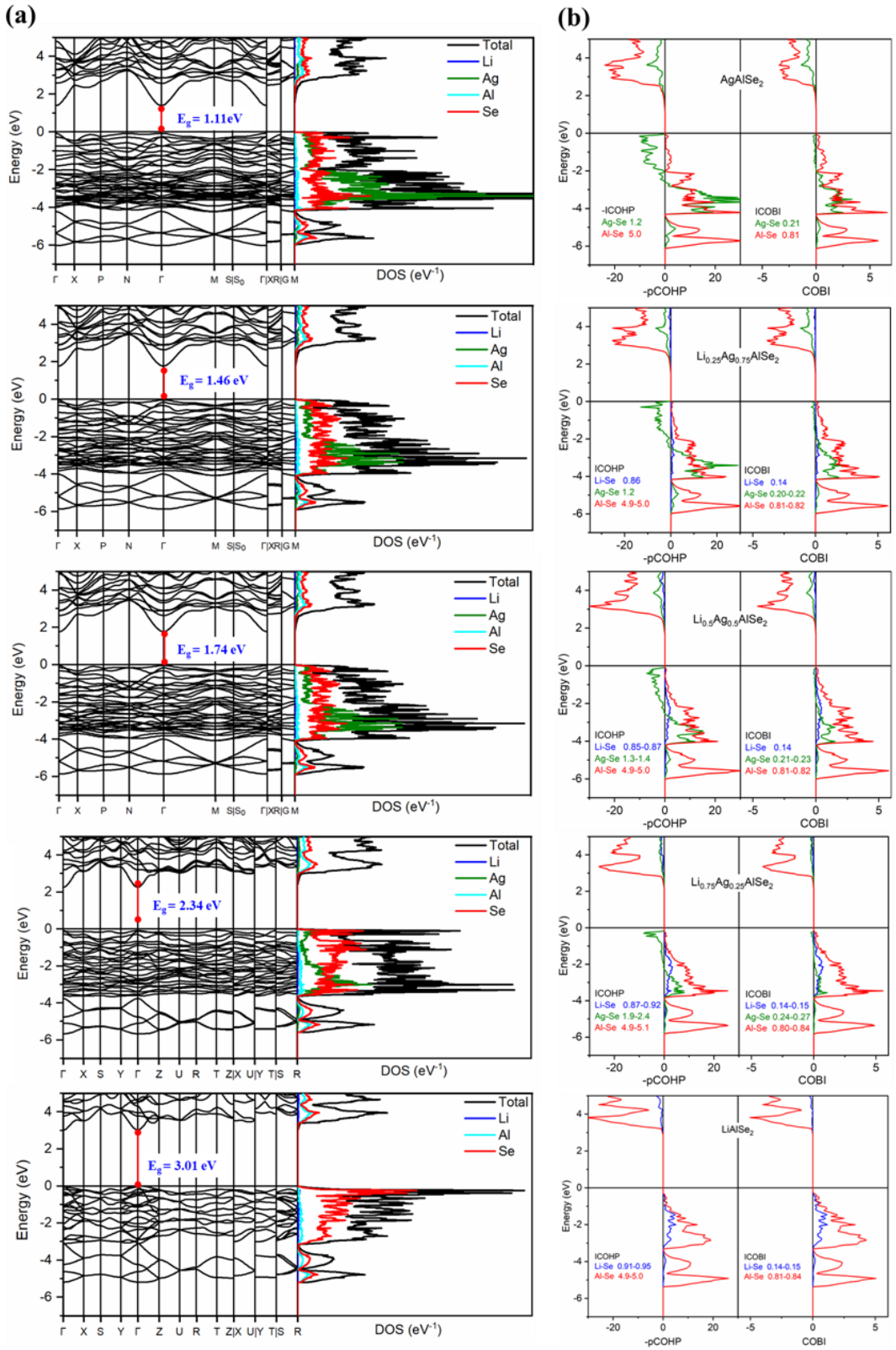

Figure A5-4. (a) Band dispersion and DOS plots; and (b) COHP and COBI plots for models of $Li_xAg_{1-x}AlSe_2$.

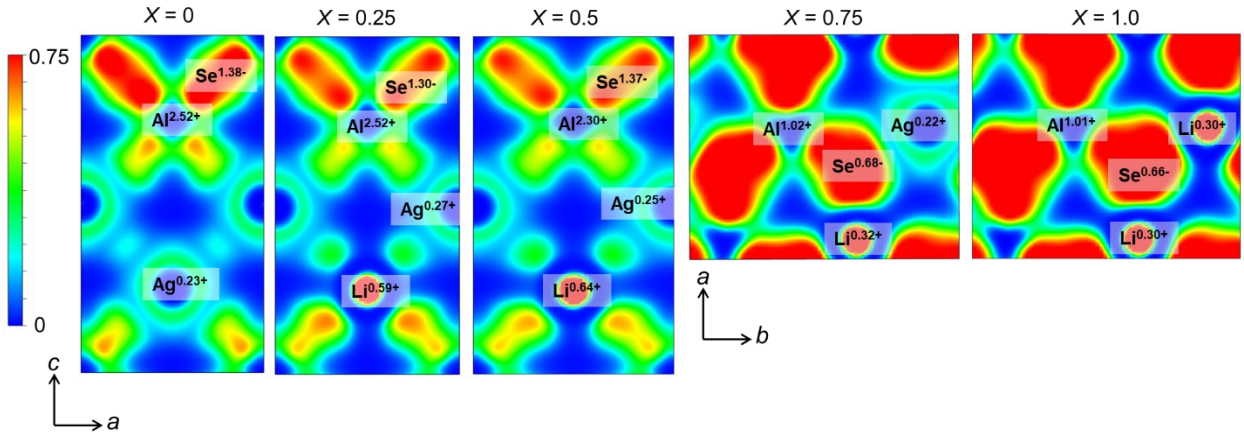

Figure A5-5. ELF plots for $Li_xAg_{1-x}AlSe_2$.